METHODOLOGY FOR A DYNAMIC ASSESSMENT OF MULTIPLE AIRCRAFT TETHERED TO A SHARED PAYLOAD

A Thesis
Presented to
The Academic Faculty

by

Etienne Demers Bouchard

In Partial Fulfillment
of the Requirements for the Degree
Doctor of Philosophy in the
School of Aerospace Engineering

Georgia Institute of Technology
May 2020

METHODOLOGY FOR A DYNAMIC ASSESSMENT OF MULTIPLE AIRCRAFT TETHERED TO A SHARED PAYLOAD

Approved by:

Professor Dimitri Mavris, Advisor
School of Aerospace Engineering
Georgia Institute of Technology

Professor JVR Prasad
School of Aerospace Engineering
Georgia Institute of Technology

Professor Mark Costello
School of Aerospace Engineering
Georgia Institute of Technology

Dr. Elena Garcia
School of Aerospace Engineering
Georgia Institute of Technology

Professor David Rancourt
Mechanical Engineering
Université de Sherbrooke

Date Approved: September 26, 2019

Mobilis in mobili - Moving within the moving element

Jules Verne, 20,000 Leagues Under the Sea

To my wife, Maria

ACKNOWLEDGEMENTS

First and foremost, I would like to thank Dr. Mavris, my advisor. Thank you for the support through the whole process, the academic guidance and the opportunity to work with you.

I would like to thank the other members of my thesis committee: Prof. Costello, Prof. Prasad, Prof. Rancourt and Dr. Garcia for their precious technical insights and perspective needed to accomplish this thesis.

The Aerospace Systems Design Lab and the School of Aerospace Engineering have provided me with countless opportunities and great personal and professional meetings, that have influenced in one way or another this work. Among them, I would like to thank Francois Bolduc-Teasdale, Michael Cormier, Claudel Lessard-Therrien, Christian Perron, Alek Gavrilovski, Eva Kallou, Paola Zanella, Mohit Gupta, Emre Yılmaz, Caleb Harris, Tim Chin, Sylvester Ashok, Kyle Collins, Imon Chakraborty, Olivia Fisher and Christopher Frank.

I will forever be grateful for the support that my family has shown through my academic journey.

Finally, I would like to thank my wife, Maria, for her unconditional loving support. Thank you.

TABLE OF CONTENTS

LIST OF TABLES

LIST OF FIGURES

SUMMARY

Vertical Takeoff and Landing (VTOL) aircraft play an important role in our society by accomplishing a wide range of missions. Many concepts have been introduced to increase the maximum speed of helicopters. This characteristic has usually been conflicting with hover endurance due to the high disk loading typical to high-speed vehicles. However, there has also been interest in long endurance flight, highlighted by the AHS International Igor I. Sikorsky 24 Hour Hover Challenge.

The use of tethered fixed-wing aircraft to lift a shared payload constitutes a promising configuration to provide long endurance VTOL capabilities. Preliminary studies suggested that the system is expected to perform long endurance missions efficiently, due to the possible low empty weight fraction and the very low equivalent disk loading.

Previous studies analyzed the use of manned aircraft to perform this operation. While they provide the core lifting capabilities, the performance is limited by the type of aircraft, and the flight path limitations imposed by having a pilot on board: limited centrifugal loading, long tethers and large flight path radius, as well as high pilot workload imposed by aircraft coordination. The recent advances in autonomy and electric propulsion are enablers to the use of unmanned aircraft to perform multiple aircraft load lifting.

In 2016, Rancourt presented multiple advanced flight paths that efficiently use the degrees of freedom unique to the tethered aircraft to further reduce the power required in hover and to perform advancing flight at high equivalent advance ratio. The inverse dynamic analysis included the dynamic characteristics relevant to the

identification of the power required. However, important epistemic uncertainty still remains on the dynamic behavior of the system.

The present dissertation aims at presenting a methodology to select dynamic influenced design parameters for the system. Among them, the attachment of the tether on the aircraft and the nominal flight path parameters of the systems are identified as new design and operational degrees of freedom that have an important impact on the dynamics of the system. The effects of important variations in suspended mass throughout the mission due to fuel burn are also considered. In order to inform decisions about these parameters, a dynamics-influenced design framework is presented.

First, a lower-complexity performance evaluation module is implemented as a means to rapidly differentiate between the various flight path combinations. This module is based on a quasi-steady formulation with only the wing used as lifting surface. Second, a dynamic simulation environment that incorporates the main characteristics of the system is developed, while consideration is given to complexity and runtime. This model is used to evaluate a trimmed-constrained tether attachment region. Linearization about the trim condition and a conversion to multi-blade coordinates are used to create a dynamic model with a minimal level of complexity, while representing the fundamental motion of the system during the circular hover flight phase. The open-loop characteristics of the system are then evaluated for the system in hover, and requirements on the open-loop further constrain the tether attachment point. An approximation of the states, control input and lift coefficient during an operation with a constant wind velocity allows to differentiate between feasible configurations by evaluating a performance criterion. This procedure is repeated for multiple flight path parameters and can be used to differentiate between the optimal configurations. Analogously, for configurations with variable suspended mass, different flight paths are compared, and an evaluation function is used to find

an attachment point that represents an appropriate compromise between the different suspended masses while meeting all the constraints. Finally, a closed-loop formulation in multi-blade coordinates is proposed to demonstrate the time-marching simulation results.

NOMENCLATURE

Acronyms

EPR2	Electric-Powered Reconfigurable Rotor
CSR	Centrifugally Stiffened Rotor
IBC	Individual Blade Coordinate
MBC	Multi Blade Coordinate
PBH	Popov-Belevitch-Hautus controllability Test
cg	Center of Gravity
nr	Nonrotating Frame
AC	Aircraft

Variables

g	Gravitational Constant
k	Tether spring Stiffness
L	Nominal Tether Length
$\tilde{L}$	Deformed Tether Length
ϕ, θ, ψ	Aircraft Euler angles
p, q, r	Aircraft Angular Rates in the Body Frame
ζ	Tether Elevation Angle
ξ	Tether Azimuth Angle
u, v, w	Velocity in the Body Frame
$\tilde{u}, \tilde{v}, \tilde{w}$	Airspeed in the Body Frame
$\mathrm{w}_1, \mathrm{w}_2, \mathrm{w}_3$	Wind Components
q	Position Degrees of Freedom
$\dot{q}$	Velocity Degrees of Freedom
$\vec{x}$	State Vector

$\vec{u}$	Control Input Vector
α	Aerodynamic Angle of Attack
β	Aerodynamic Sideslip Angle
Ψ	Virtual Hub Azimuth Angle
Ω	Virtual Hub Angular Velocity
δ_r	Rudder Control Input
δ_e	Elevator Control Input
δ_a	Aileron Control Input
δ_P	Propeller Control Input
Φ	Cost Function

Notation

Ⓘ	Reference Frame I
$\vec{M}^I$	Vector $\vec{M}$ Expressed in the Reference Frame Ⓘ
$\vec{r}^{\,I}_{O\to A}$	Position Vector Between Point O and Point A, Expressed in the Reference Frame I
$\mathtt{w_i}$	i_{th} Eigenvector

CHAPTER I

MOTIVATION

1.1 Vertical Takeoff and Landing

Since the first production helicopters in the 1940s, helicopters have played an important role in society: the possibility to takeoff from unprepared terrain and fly at a wide range of speed differentiate helicopters from any other vehicle and allowing them to take on unique missions in civil, commercial and military applications. While the state-of-the-art in vertical flight technology evolved continuously, some performance characteristics saw disruptive advances.

First, motivated by the Future Vertical Lift (FVL) initiative and the objective to fly at 230 knots, new concepts have been proposed to enable this paradigm shift in forward speed. These include the use of advanced coaxial and tilt rotor systems aimed at mitigating the limitations related to the use of conventional rotors in advancing flight [49].

Second, propelled by the advances in electric propulsion and autonomy, there is a new strong effort to support the development of electric VTOL vehicles. Electric propulsion allows the use of multiple small electric motors that do not see the weight penalty due to size related limitations typically affecting internal combustion engines or turbines. This allows the use of many motors which render the concept space infinite.

1.1.1 Endurance

Endurance in hover, however, remains an important limit for Vertical Takeoff Landing (VTOL) concepts. The simplest demonstration of this limit is the equation for momentum theory relating to the power required to hover [56]:

$$\frac{P}{T} = \frac{1}{FM}\sqrt{\frac{1}{2\rho}\frac{T}{A}} \tag{1}$$

With T, the thrust in hover being the weight of the vehicle, A, the disk area, P, the required power and FM, the Figure of Merit. Figure of merit covers the other loss mechanisms, not represented by momentum theory and has a typical value of 0.7-0.9 [63]. For a given weight, a greater rotor area decreases disk loading (T/A), in return decreases the power to weight required to hover.

Helicopters typically have a lower power at a non-zero advancing velocity, and endurance is not expressed for hover, but rather at the best endurance speed.

For the purpose of demonstration an equation is derived for the endurance of a helicopter in hover based on momentum theory. Assuming that fuel burn is a function of the specific fuel consumption (SFC) and power to hover, the variation of weight as a function of time becomes $\dot{W} = -SFC \cdot P$ [8]. This differential equation can be used to find the endurance E:

$$\int_0^E dt = \int_{W_i}^{W_f} \frac{1}{-P \cdot SFC} dW \tag{2}$$

Assuming a constant figure of merit, the endurance equation becomes:

$$E = \frac{2\sqrt{2\rho}FM}{SFC}\left(\frac{W_i}{A}\right)^{-1/2} \frac{1}{(1-\sqrt{\frac{W_f}{W_i}})} \tag{3}$$

Based on this equation, it can be seen that the disciplines required to achieve long hover endurance are the following: aerodynamic efficiency of the rotor system through FM, propulsion system efficiency through SFC, light structure leading to low empty weight fraction $\frac{W_f}{W_i}$ and finally a low disk loading $\frac{W_i}{A}$.

1.1.2 AHS International Igor I. Sikorsky 24 Hour Hover Challenge and the Need for Endurance

The endurance limitations of existing helicopters have motivated the most recent Sikorsky Competition: AHS International Igor I. Sikorsky 24 Hour Hover Challenge [3, 10], unveiled in May 2016.

The success criteria for the 24 Hour Hover Challenge are the following:

- Hover for 24 hours, in winds smaller than 5 m/s
- Be unmanned, and lift an 80 kg payload, a weight that notionally represents a pilot
- Transit to three waypoints that are 1 km apart
- During hover, a reference point on the vehicle must stay within a 20 m diameter sphere.

An analysis presented by Strauss [89] was aimed at evaluating the feasibility of achieving the objective based on existing configurations. While the endurance of existing production helicopters is typically in the order of 6 hours, the same helicopters with no pilots and with the totality of their useful weight assumed as fuel can be up to 16 hours. The author identified three parameters that can be optimized on existing configurations consistent with the analysis of the endurance equation: disk loading, fuel consumption and fuel weight fraction.

The competition objectives are to inspire the next generation of engineers and the public, but also to stimulate the development of VTOL technology. The scope of the 24 hour hover challenge is the following : "The challenge is designed to stretch the efficiency and reliability of vertical flight aircraft by demonstrating 24 hours of continuous hovering flight" [3, 59].

Even if the mission proposed in the Challenge guidelines remains conceptual, long

endurance VTOL flight presents opportunities for multiple applications. Among others, the use of a hovering vehicle can be a interesting platform for communication relays [72]. In the event of natural disasters, the use of temporary communication towers can be vital to the safety of nearby population. The use of both small remote controlled helicopters and large helium balloons have been demonstrated as platforms to carry communication antennas [92]. While both concepts show great advantages, they also have limitations inherent to their designs: The balloons have an extreme long endurance, but their deployment is complicated by their sizes and their position control is dependant on the winds. In counterparts, the small remote control helicopter in counterpart are easy to deploy, but have limited endurance and payload capacity. This comparison illustrates the relevance of a vehicle capable of performing 24 hour hover.

1.2 Multiple Aircraft Tethered to a Shared Load

The 24 Hour Hover Challenge represents the opportunity to generate new VTOL concepts. Among possible concepts, the use of Multiple Tethered Fixed-Wing Aircraft presents possible interesting advantages.

The configuration of interest has been introduced as the Electric Powered Reconfigurable Rotor (EPR2) concept [27]. An illustration of the physical components of the system is shown in Figure 1. The name reconfigurable rotor comes from the comparison between the aircraft flying over the payload in a circular manner, akin to a rotor. The reconfigurable aspect is related to the fact that equivalent "rotor parameters" such as the radius and angular velocity can be adjusted or reconfigured throughout the flight to operate in an optimal regime.

1.2.1 Physical Decomposition

The system is comprised of multiple fixed-wing aircraft that are tethered to a shared fuselage, or payload.

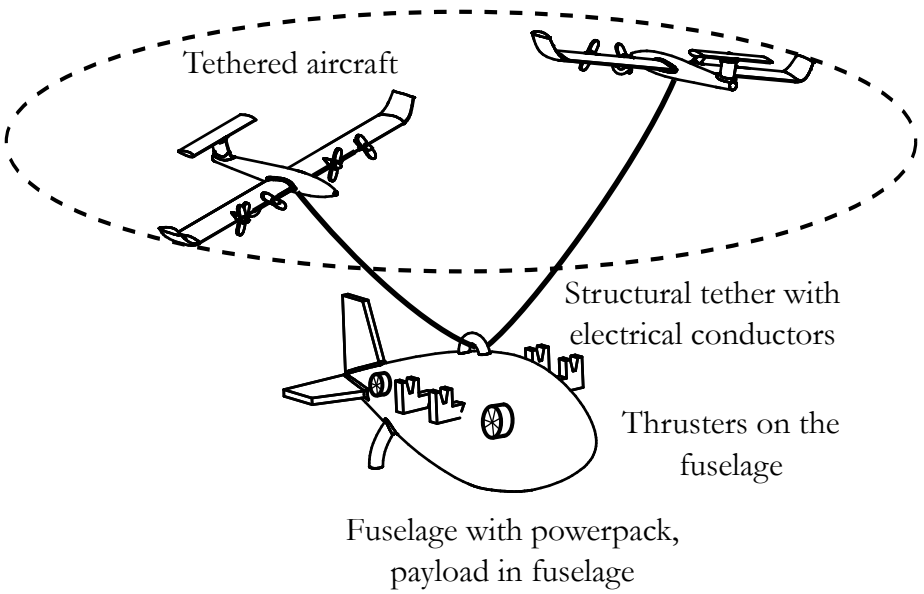

Figure 1: EPR2 concept schematic representation

1.2.1.1 Fuselage

The fuselage represents the body lifted by the aircraft. It contains the useful load, as well as an electrical power source: either a battery, an engine-generator system or a hybrid power source. Control surfaces can be positioned on the fuselage body, along with thrusters to control its motion.

1.2.1.2 Tether

The tethers are the link between the fuselage and the aircraft. They must bear tension loads as well as transmit electric power.

1.2.1.3 Fuselage-Tether Interface

Since the aircraft are flying in cyclic motion above the fuselage, the tether-fuselage interface represents an important component of the system. It must be able to transfer the loads and the electric power from the fuselage frame to the rotating frame of the tethers.

Figure 2: Makani *Wing 7* Aircraft

1.2.1.4 Aircraft

Unmanned electric aircraft are used to provide lift. The Makani *Wing 7* [65], illustrated in Figure 2 is an aircraft used for airborne wind power generation that could be utilized for this application.

1.2.2 Phases of Flight

The concept is characterized by the phases of flight illustrated in Figure 3. First the aircraft takeoff in a tailsitting configuration. During this phase, the aircraft use the thrust of their propellers to stay in a stationary flight. At this point, the aircraft only lift themselves and the tethers.

Second, the aircraft transition to a circular flight path above the fuselage. Note that the fuselage is still on the ground at this point. The aircraft increase their speed and angle of attack until enough tension in the tether is provided to lift the payload off the ground. Hover is the phase of flight where the aircraft fly in circular or near circular flight path above a stationary fuselage.

The next phase of flight, the advancing circular flight, is described by a relatively slow motion of the fuselage with respect to the ground. This is accomplished by

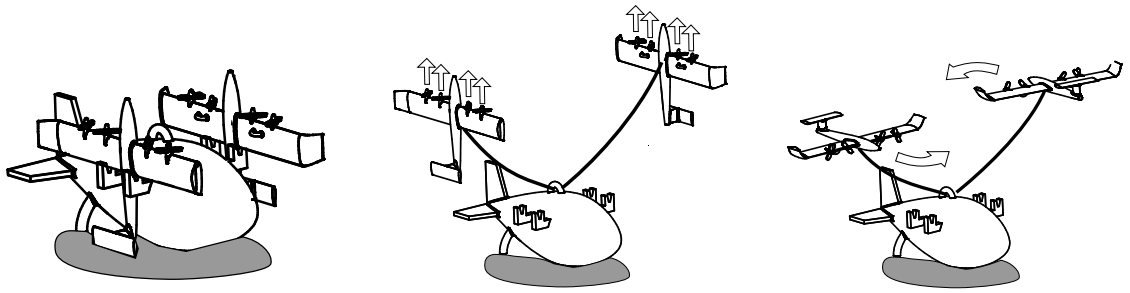

(a) System on the ground

(b) Tailsitting takeoff of the aircraft

(c) Circular flight path of the aircraft

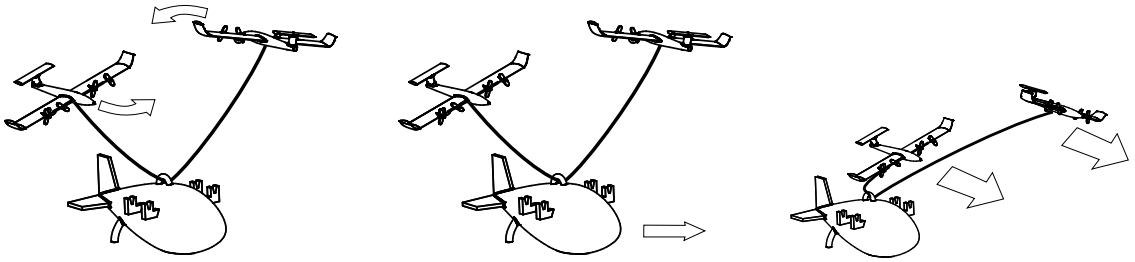

(d) Takeoff of the fuselage

(e) Advancing circular flight

(f) Side-by-side forward flight reconfiguration

Figure 3: Phases of flight of the EPR2 concept

modifying the flight path of the aircraft to generate more tension towards one side or another.

Finally, the last phase of flight is a side-by-side cruise of the aircraft. This is accomplished after a transition from the circular flight phase to a linear flight regime. This flight phase could allow for a more efficient cruise operation. All the phases of flight are reversed for landing.

1.2.3 Expected Advantages

This system is expected to provide interesting cost, structural, aerodynamic and propulsive advantages over traditional helicopters.

First, the power required in hover is expected to be greatly reduced compared to conventional helicopters. This is due to the equivalent disk area being not constrained to a circle, but rather a large annulus. Preliminary analyses showed an order of magnitude decrease in disk loading [27, 28].

Also, the system is constituted of relatively simple components already widely used in different applications. The use of high-speed electrical motors reduces the weight of the propulsion system by avoiding the need to include a heavy gearbox and increases the reliability of the system. For example, *Makani* developed a very lightweight aircraft capable of similar flight conditions with the objective of flying over extended periods of time to extract wind power.

Finally, an aircraft wing is not subjected to the same loading as rotor blades. For example, bending moments along the length of a helicopter blade are important loads and can increase the required strength of the rotor blade. For the concept of interest in this paper, the lift on the wing is transferred to tethers that can be attached at different locations on the wings, hence reducing the bending moment. Moreover, the wing-mounted propellers eliminate the rotor torque.

1.3 Previous Studies of the EPR2 Concept

The author [27] proposed a methodology to optimize the system level characteristic in hover to minimize the power required for a given payload weight. It was noted that this system presented important interdisciplinary coupling, as shown in the selection of the tether length: On one side, a short tether is light and has small electric losses. However, a short tether does not necessarily allow a flight radius large enough to have a good hovering efficiency. A multidisciplinary environment was created to capture the tradeoffs of such parameters.

In order to address the interdisciplinary coupling highlighted by [27], a subsystem decomposition is performed and the components are used in an integrated optimization formulation. The different forces acting on the vehicle are summed over a quasi-static equilibrium formulation. A free-body diagram of the system is exposed on Figure 4. Not shown on the image are the equivalent drag force from the tether, the drag of the aircraft and the propulsive force of the propellers, all assumed tangent

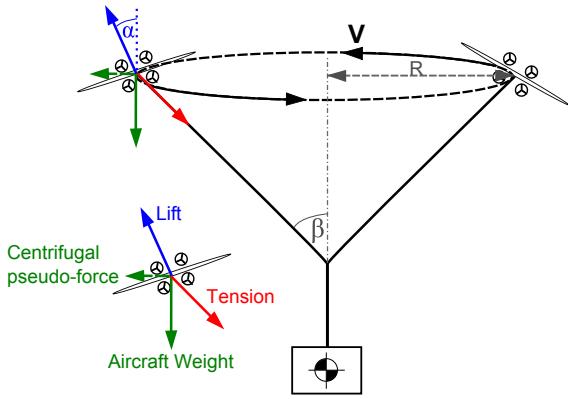

Figure 4: The forces acting on the aircraft during the hover phases.

to the flight path.

The sub-models developed for the analysis environment were the following:

Propulsion Efficiency A fixed 80% propulsion efficiency was assumed for the motor and propeller.

Wing Aerodynamics In order to account for aircraft wake interaction, blade-element-momentum theory (BEMT) was used to calculate the lift and induced drag coefficients on the wings.

Power Production In order to provide power to the aircraft, a power production unit was integrated to the payload. The power production was sized based on a power density assumption.

Tether The tether model assumed a conductor weight model and an insulation layer. In order to efficiently assess the drag over the tether, the simplified, quasi-static analytical formulation is used. The deformation of the tether is omitted, and the shape of the tether is assumed as a straight line. The equivalent drag force and centrifugal pseudo-force are applied at the upper end of the cable during the hover

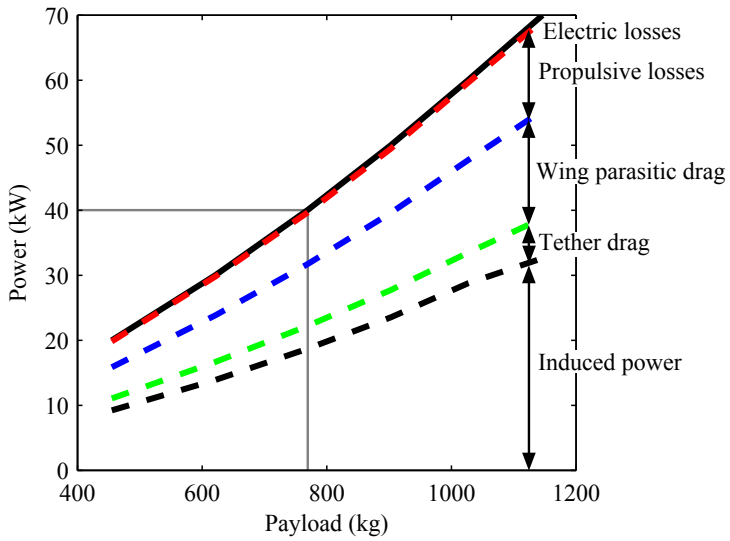

Figure 5: The optimization results of the power required and payload lifting capabilities (solid line) and power breakdown (dashed lines).

phase. The equation for both drag and centrifugal pseudo-force can be found in Demers Bouchard [27].

The optimization problem for the hovering phase was posed as follows:

Maximize:	Payload mass
Given:	Aircraft Characteristics
With Respect to:	α, β, Conductor Diameter , l, $V_{Aircraft}$
Subject to:	$C_l \leq C_{l_{max}}$, $P_{req} \leq P_{available}$

The results of the power curve for a system comprised of 2 Makani aircraft are illustrated in Figure 5. It was observed that this concept presents new loss mechanisms: propulsive losses associated with the propeller efficiency and tether drag. The preliminary results, however, illustrated that the power to a lift a payload is a lot smaller than for conventional helicopters, mainly due to the reduced induced power due to the low disk loading.

For a system operating at the Makani's aircraft nominal power of 40 kW (20 kW each), the payload could be 700 kg. For comparison, the Bell 206 helicopter, capable of lifting a slung load of 907 kg, is powered by a 310 kW engine.

1.4 Observations

The preliminary analysis showed that the EPR2 concept presents interesting capabilities, specifically with respect to the power to payload weight ratio. Rancourt also presented interesting ways to make use of the new degrees of freedom to perform efficiently the various phases of flight.

In order to focus on the factors that are likely to play an important role on the power curve, the existing analyses assumed simplified aircraft dynamics and assumed trajectory tracking. Consequently, important uncertainty remains related to its dynamic characteristics and how it can respond to disturbances. Observations on the characteristics of the systems and comparison to existing vehicles outline this uncertainty:

Disk Loading As discussed in the previous section, the low power requirement in hover of the EPR2 system can be linked to the very low equivalent disk loading proper to the circular flight path. In counterpart, helicopters that have a low disk loading are typically more sensitive to environmental disturbances such as gusts.

Mass Ratio One of the advantages of this proposed configuration is the low empty weight fraction, explained by the use of lightweight aircraft. This leads to a particular weight ratio between the aircraft and the stationary load, where neither of the elements' contribution to the dynamics can be omitted.

Degrees of Freedom The flight path leads to multiple flight conditions that can be used to minimize the power requirement. From a dynamic point of view, the degrees of freedom can also be used advantageously to control the system and achieve a desired flight state.

Collaboration Unlike for the pitch motion of helicopter blades that is dictated by the swash plate, the tethered aircraft perform independent maneuvers that must be coordinated by an external means. This allows for more degrees of freedom, but increases the complexity of a possible control system.

In light of the previous observations, this present work intends to provide a framework which enables informed design decision for the development of the tethered aircraft influenced by unusual dynamics:

Research Objective:

Provide a framework to analyze the dynamics-driven design decisions of a system comprised of multiple aircraft tethered to a shared load during hovering, circular flight.

The rest of this document is organized as follows:

- Chapter 2 presents the literature review of systems presenting analogous characteristics
- Chapter 3 describes the research objective and research questions
- Chapter 4 defines the methodology utilized to fulfill the research objectives
- Chapter 5 presents the implementation of the methodology and the salient results
- Chapter 6 contains the conclusions, contributions and future work based on this dissertation.

CHAPTER II

BACKGROUND AND LITERATURE REVIEW

Chapter 1 introduced the use multiple tethered aircraft to lift a shared payload as a potential architecture to perform long endurance VTOL missions. However, it was identified that the dynamic characteristics and their impact on the design decisions are not clearly understood.

To gain insight on the system dynamics, the first part of this chapter will provide an overview of existing tethered systems. The second part of this chapter will present details on dynamics considerations for the design of aerospace systems.

2.1 Tethered Systems Review

2.1.1 Single Fixed-Wing Aircraft Deployment

Existing work has been done to assess the use of tethered manned aircraft to vertically lift a payload. First, the use of single aircraft payload deployment has been proposed. To provide VTOL capability, the aircraft can fly over a circular flight path and use the verticallity property of the tether to obtain a limited tether tip displacement.

Williams developed dynamic tether models to analyze the single aircraft configuration [101, 104, 105]. In a first analysis, he evaluated the combinations of tether length, flight path radius and aircraft angular velocity around the orbit center that minimize the tether tip displacement. This allowed to find optimal configurations based on practical aircraft limitations. The models were also used to study the fundamental modes of motion of the cable system, and the solutions were compared to experimental simulations.

For a payload pickup mission, the single aircraft can transition from a cruise condition to a pickup maneuver, during which the aircraft will turn, reducing the

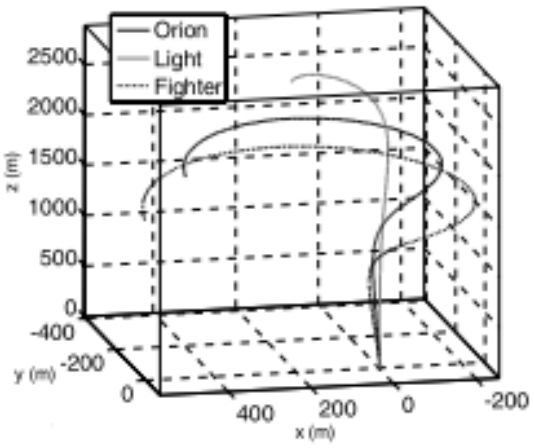

(a) Cable shape that minimizes tip displacement

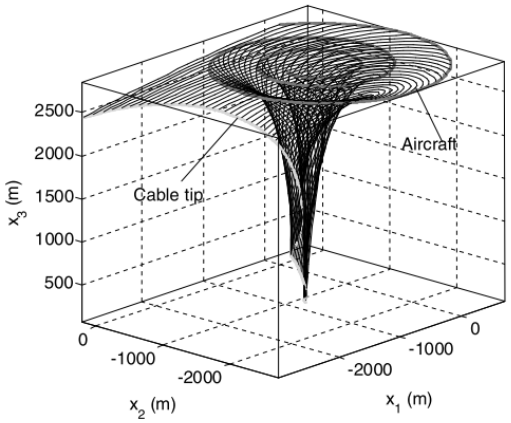

(b) Cable shape composite image during a tow in maneuver

Figure 6: Single aircraft deployment [104, 105]

tether tip velocity and altitude. Williams proposed flight a path during the transition to minimize the tether tip displacement.

In order to obtain the verticality property of the tether, a long tether is required. Williams studied tether lengths in the order of 1-5 km. This system is very simple, however, the limited displacement at the tip relies on the aerodynamic damping of the tether. Consequently, this system presents high sensitivity to wind gusts, and does not allow rapid maneuverability of the cable tip.

Multiple solutions were also proposed to reduce the tip displacement, such as the inclusion of a drogue chute at the tip, or the installation of masses and rigid body along the tether length to modify the tether dynamics [9, 20, 23, 86, 87, 90, 91].

2.1.2 Multiple Manned Aircraft Deployment

The use of multiple aircraft has also been proposed to perform load lifting [5, 6, 40, 41, 53, 73, 102, 107]. Since the aircraft do not perform VTOL, they typically do not start the mission tethered to each other, which poses a challenge for the rendezvous of multiple tethers. Multiple solutions were proposed to attach the tethers once the aircraft are in the air which represents a complex task.

Williams and Ockels [102,103] also developed a numerical simulation environment for a multiple aircraft system lifting a shared payload. Similar to the work on a single aircraft, the models were used to find optimal configuration and study the dynamic modes. Due to the use of long tethers, the dynamic modes include important contributions of the cable motion.

In 1983, the use of multiple manned aircraft to lift a payload vertically was demonstrated in a flight test reported by Wilson [106]. Two general aviation aircraft, flying over a circular flight radius of 600 ft were used to lift a 60 lb payload. The author's analysis showed that larger aircraft can be used for the task, and that the slung load could weigh up to 15-20% of the aircraft gross weight. Additional visual aids were installed on the inner wingtip of each aircraft, including a mirror and flight instruments to help the pilot fly without having to look inside the cockpit.

This flight test underlined the potential of the concept. However, the use of manned aircraft imposes limitations on the capability. The coordination of the aircraft imposes a great workload on the pilots. The tethered load introduces particular dynamics in the system new to aircraft pilots. Moreover, the operation in advancing flight (or stationary flight with respect to the ground in a windy condition) might be very difficult to realize due to the complex coordination between the aircraft, and the cyclic control input typical to the quasi-circular flight path.

2.1.3 Previous analyses on the EPR2

2.1.3.1 SWARM: System Level Design and Analysis

In 2017, the American Helicopter Society student design competition's topic was the Sikorsky 24 hour hover challenge [4]. The joint Georgia Tech and Universite de Sherbrooke graduate submission, the *Swarm* aircraft, utilized the ERP2 concept [13]. The fuselage designed by the student team is shown in 7. The concept utilized a diesel engine as the power source, coupled to an electric generator to send the electrical power to the aircraft. The study approximated the hover endurance to 28 hours.

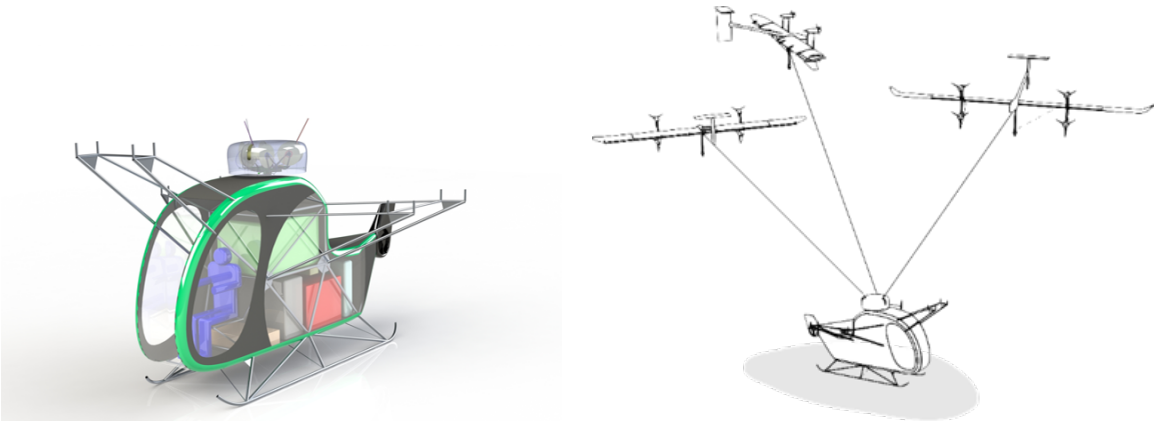

(a) (b)

Figure 7: The submission of the joint Georgia Tech and Universite de Sherbrooke graduate team for the 2017 AHS student design competition: the *Swarm* aircraft

2.1.3.2 Higher Level of Fidelity Analysis and Advanced Flight Path

Due to the presence of a flexible flight path, the system has an infinite number of degrees of freedom. To take advantage of those degrees of freedom, Rancourt proposed the use of advanced flight paths to minimize the power to hover and maximize the load lifting capability in forward flight [77–79].

2.1.3.3 Flight Path Optimization Framework

The aerodynamic interaction of the aircraft was identified as an important aspect of the performance of the system. Rancourt proposed an environment that takes into account the aerodynamic interaction and allows an optimization of the flight path for various operating conditions.

The environment is a multidisciplinary flight path optimization tool that also leverages multifidelity analyses. The flight path of the aircraft was parametrized by a Fourier series. This allows to take into account a varying aircraft velocity and radial position as a function of the azimuthal angle.

The aircraft flight path is analyzed by a dynamic tether model coupled to a fuselage aerodynamic model. The aircraft velocities and the required aircraft aerodynamic

forces as a function of time are then extracted. This formulation removes the requirement of an iterative dynamic solver because all the forces are imposed to follow the prescribed motions.

An aerodynamic model of the wing was then used to provide the required forces. Two models were used: a lifting-line aerodynamic approximation, and a lifting line with wake consolidation model for the far wake. Given the required aerodynamic forces, the aircraft orientation is found, as well as the aileron deflection leading to no rolling moment. Finally, a propeller model is used to find the instantaneous propeller angular velocity that gives the required thrust.

Within the dynamic solution, some assumptions were used to allow this inverse dynamics simulation:

1. This is possible only for the use of 3 tethered aircraft, as the forces acting the fuselage must be at equilibrium at each timestep. More than 3 aircraft lead to a dynamic indetermination and less than 3 aircraft does not assure equilibrium of the fuselage.

2. The aircraft are assumed as a point mass, so there is no rigid body rotational dynamics calculation. Instead, the body angles are imposed at each time step without external moments applied. The pitch and roll angles are assumed so that the required lift force is applied on the aircraft. The yaw angle is assumed so that there is no sideslip.

3. Only the aircraft wings are assumed as lifting surfaces.

4. Only the differential aileron deflection is analyzed as a control input. The deflections are assumed so that there is no rolling moment at the center of mass of the aircraft. The nominal rolling moment on the wing is a product of multiple factors, including the influence of the wake, the non-uniform apparent wind velocity on the wing due to the high turn rate as well as roll rate.

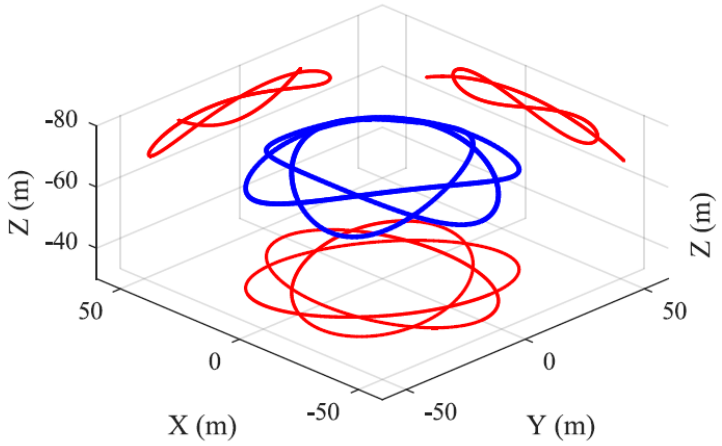

Figure 8: Flight path in hover that limits the negative impact of induced velocity on power required [77].

2.1.3.4 Optimized flight path

In hover, flying over a circular flight path creates a downwash over the area where the aircraft fly, which impacts the performance of the system negatively. The proposed flight path shown in Figure 8 includes cyclic radial variation of the flight path. This operation creates an apparent increase in effective disk area and it was evaluated as allowing a 10-15% reduction of power required compared to a circular flight path.

In advancing flight, a circular flight path leads to the typical limitations seen by helicopter of retreating blade stall: the aircraft on the advancing side sees high apparent wind velocity which translate to high dynamic pressure and consequently a great potential to generate lift. On the retreating side, the opposite is true: the apparent wind velocity is decreased, and so is the potential to generate lift. Due to the requirement to have lateral force balance, this can limit the load lifting capability in forward flight or limit advance ratio. This problem is amplified for the EPR2, as the low aircraft velocity leads to very high advance ratios for relatively low fuselage velocity.

In order to get past this limitation, the proposed flight path by Rancourt was a

non-circular flight path with a tilt of the equivalent tip-path plane, the plane which holds the aircraft flight path. Figure 9 sows the optimal flight path for a system with an advancing velocity of 15 m/s.

The lateral force balance is accomplished by having the retreating part of the flight path being farther out than the advancing side, and changing the equivalent angular velocity as a function of the azimuthal angle. The Figure 10 shows the associated aircraft states.

2.1.3.5 Observations on the Flight Path Optimization Framework

Many observations can be made from the results in [77]:

- It can be noted that the lift coefficient has a maximal value of 2. This is a large value for a fixed wing aircraft, but it was reported that Makani aircraft for example, were able to operate at such high lift coefficient value, namely due to the presence of a flapped airfoil. It was noted in the other preliminary analysis that operation as close to the maximum lift coefficient as possible leads to less power required.

- The aircraft true airspeed varies between approximately 20 to 36 m/s, which is a relatively low variation for a condition where the fuselage flies at 15 m/s. This relatively low airspeed variation is achieved by adjusting the advanced flight path.

- During a period, there is tether tension variations of a factor of 2.

- One of the observations made by Rancourt was that if a flight path following approach is used to control the aircraft, a very small error in the position of the aircraft in the direction of the tether length will result in a very large force mismatch. The recommendation was to include a tether force sensor as a sensor part of the control system.

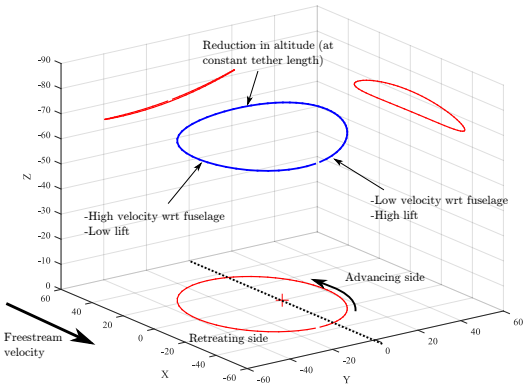

(a) Isometric view of the flight path in the moving frame

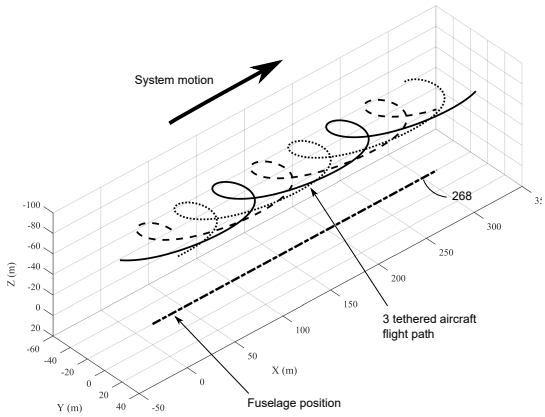

(b) Isometric view of the flight path in the fixed frame

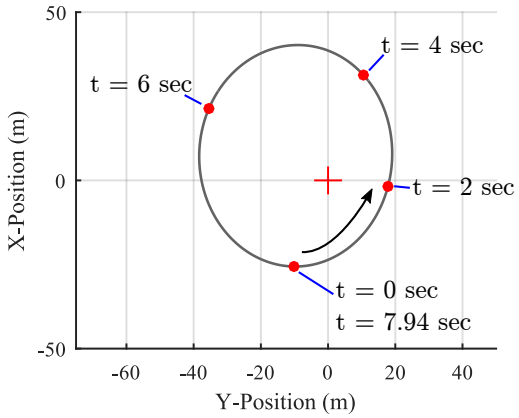

(c) Top view of the flight path in the moving frame

Figure 9: Optimal flight path for a 15 m/s advancing flight proposed by Rancourt. [77]

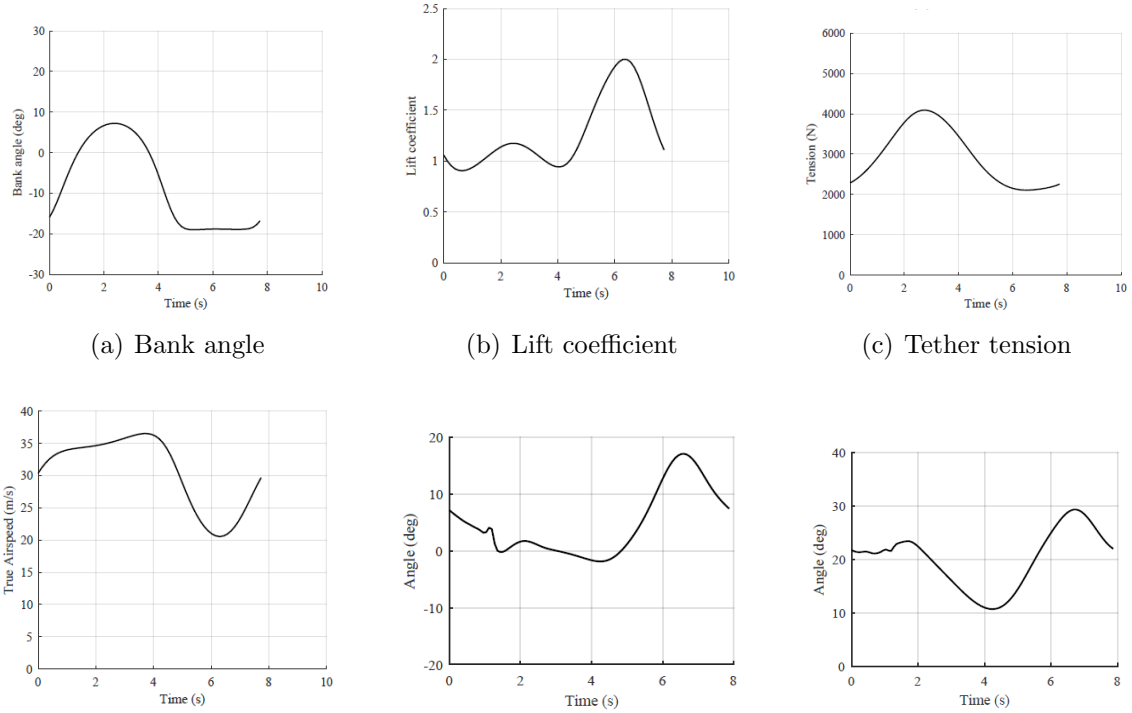

(a) Bank angle (b) Lift coefficient (c) Tether tension

(d) Aircraft true airspeed (e) Aileron deflection (f) Aircraft pitch angle

Figure 10: Salient characteristics of the advancing flight path proposed by Rancourt [77].

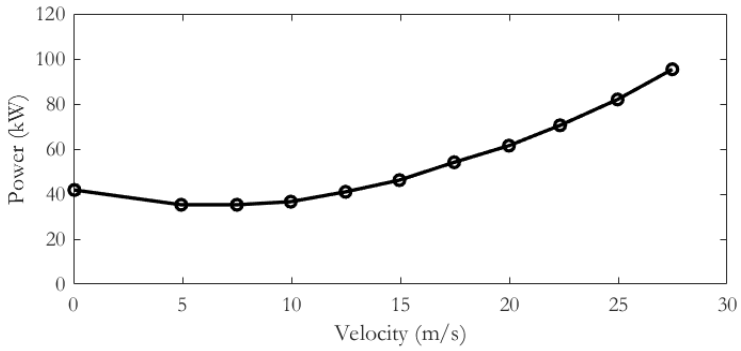

Figure 11: Power curve of the 3 Makani aircraft system lifting a 800 kg fuselage [77].

This environment optimized the flight path for various advancing speeds, and extracted the related power curve. The power curve for the use of 3 Makani *Wing 7* aircraft lifting a 800 kg fuselage is illustrated in Figure 11.

These flight paths allow efficient advancing flight. Because the system allows a continuous operation from hover to higher speed advancing flight, this allows for a transition to a side-by-side forward flight with no variation in fuselage speed. In order to perform the side-by-side forward flight, the fuselage has to be accelerated to at least a velocity greater than the one associated with the stall of the aircraft. Because the fuselage can be accelerated while the aircraft are still in a quasi-circular flight regime, the transition to side-by-side does not require a large thrust impulse during the transition. These characteristics make the EPR2 configuration very attractive.

2.1.3.6 Experimental Demonstration

In its paper, Chapdelaine [19] presented the lifting capabilities of a single remote controlled aircraft tethered to a fixed load cell on the ground. The analysis explored different operating conditions, incorporated experimental results for the benefit of performance modeling. The author demonstrated successfully the high lift to empty weight capacity of a single tethered aircraft.

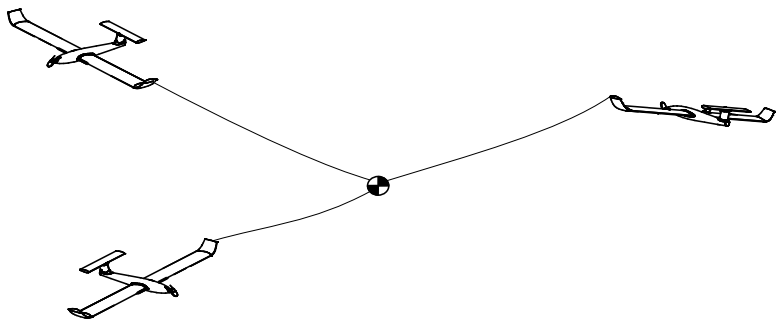

Figure 12: Schematic representation of the centrifugally stiffened rotor (CSR)

2.1.3.7 Forward Flight Configuration

The performance in forward flight has been studied by Cormier [22]. The analysis used an optimizer to find the operating parameters that lead to minimal power required. The model included aerodynamic interaction between two aircraft in a side-by-side formation, lifting a shared tethered load.

2.1.4 Centrifugally Stiffened Rotor

The centrifugally stiffened rotor (CSR), also referred to as Tethered Uni-Rotor Network (TURN) is a concept proposed in various articles, notably Selfridge and Moore [70, 81–83] and by Gamzon [40, 41]. Aircraft are tethered from their wingtips, and fly in a circle to lift a payload. as shown on Figure 12. Some authors proposed the use of conventional aircraft, and Selfridge and Moore [83] also presented a design with specifically tailored aircraft to be used in the concept.

The concept is similar to the EPR2, where multiple unmanned aircraft are used to lift a tethered load. The important difference lies in the impact of the attachment point on the mode of flight. Due to the attachment point located on the wingtip, the roll dynamics are tightly coupled with the tether tension.

Selfridge performed the development of a dynamic model of the system, including a discretized dynamic tether model. Selfridge proposed an interesting analogy for the dynamic assessment of the system: the multiple moving parts constitute a complex

problem to analyze when the vehicle is considered as a whole, similar to how the busy traffic on a highway can be mesmerizing when viewed from the air. However, the traffic behavior can be understood a lot easier if each car is considered independently, if all drivers follow a set of predefined rules. This analogy motivated the multi-level structure of the controller.

The outermost control level, referred to as Outer-Loop control, controls the motion of the payload, by generating the desired forces acting on the hub in the inertial frame. To perform a vertical translation, a collective command in z-component of the force vector is supplied to the four aircraft, and is distributed equally:

$$F_{i_{vert}} = \frac{F_{vert}}{4} \tag{4}$$

To perform a translation in plane, a command of the in inplane force is supplied to the four aircraft based on their azimuthal position:

$$F_{i_{horz}} = \frac{F_{horz}}{2} \cos\left[(\phi + \frac{i\pi}{2})\right] \tag{5}$$

The second layer of control is the Inner-Loop, which aims at tracking the desired individual tether forces. This controller was based on output feedback tracking and is applied for each aircraft.

Selfridge identified two modes of generating both vertical forces and in-plane forces, each with their respective response speed. Additional vertical forces on the tether can be generated by increasing the pitch of the aircraft (rapid time constant), as well as increasing the velocity of the aircraft (slower time constant). Similarly, the horizontal component of the tether force in can be modified by rudder actuation (rapid time constant) as well as a tilt of the aircraft flight path plan (slower time constant). The actuation modes were mixed based on their response time by complementary filtering.

Finally, the innermost controller level is the aircraft attitude controller, that aims

at tracking the aircraft states. This controller is a based on state feedback. The author identified that uncertainty in the tether dynamic model model might affect the performance of the closed-loop system and included a model reference adaptive control.

The motivation behind the choice of this controller architecture is that it effectively removes the requirement to assess the coupling between the different parts of the system in the development of the controller.

Numerical implementation of the of the aircraft attitude controller and the Inner-Loop were published [70,83] with the aircraft attached to a fixed point on the ground and submitted to wind disturbance. However, to the knowledge of the author, there is no available simulation results of the whole system, i.e. there is no demonstration of the Outer-Loop controller guiding the motion of a payload supported by the aircraft.

2.1.5 Helicopter Dual Lift

The use of multiple helicopter to lift a shared load, referred to as Dual Lift, has been analyzed since the 1970's [57].

The main expected advantages of using multiple aircraft is to expand the lift capabilities of a helicopter fleet without having to design and build a larger and expansive helicopter to complete a small number of flights.

Two concepts were proposed to lift the system: the pendant and the spreader bar configurations as shown in Figure 13, each having their advantages and drawbacks. Due to the action of the load to pull the helicopters together, the pendant configuration sees a penalty in lift available due to the need for the helicopter to counter balance the inward force. The Spreader Bar configuration allows the helicopters to keep their thrust vector vertical. However, the truss structure used to keep the helicopters apart can be relatively large and heavy compared. The dynamic characteristics of each configuration are also different due to the presence or absence

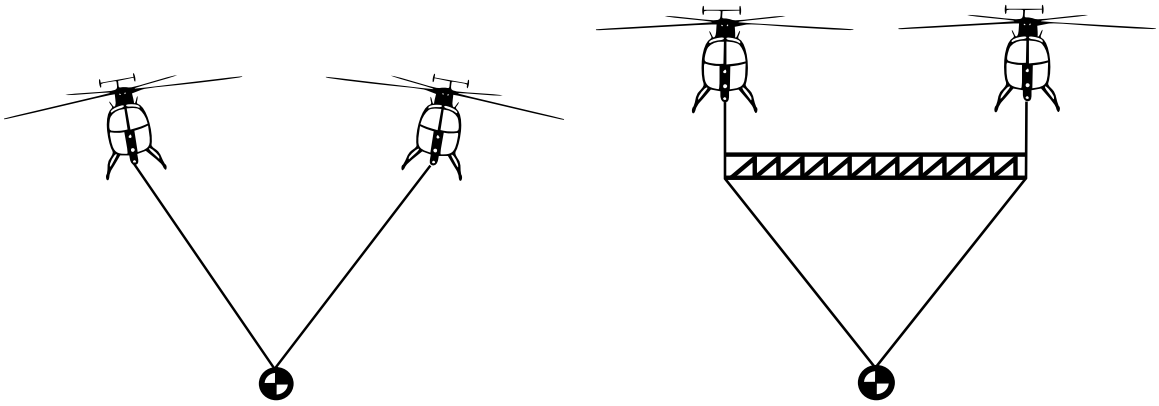

(a) Pendant configuration (b) Spreader bar configuration

Figure 13: Dual lift helicopter configurations

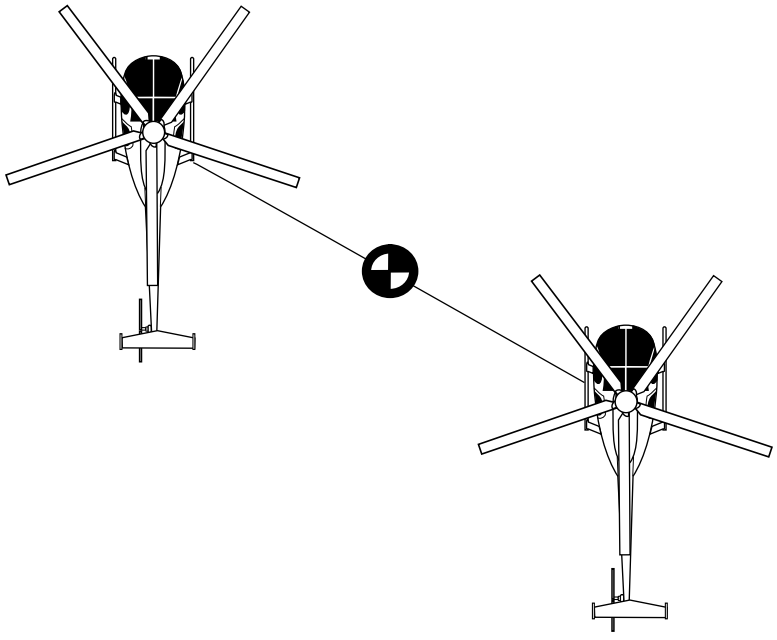

Figure 14: Dual lift configuration with formation angle

of the spreader bar.

Among the wide body of reasearch on the dual-lift helicopter concept [21,67], some authors presented different method to control the pendant configuration, highlighted in the present section.

First, Mittal [69] presented an approach to control a system in the pendant configuration. A nonlinear plant inversion controller was used as an external loop to the existing Flight Control System. A dynamic simulation environment based on Newton dynamics was used to retrieve equations of motion. The equations of motion were simplified and symmetry was used to perform a reduced-order modal analysis for both the pendant and spreader bar configurations.

Mittal then proposed a controller for the payload position. He used a non-linear plant inversion controller as an outer loop to the existing stability augmentation system. This new outer loop was aimed at controlling the average longitudinal and lateral position of the helicopters and the vertical position of the load. An additional output was used in the proposed formulation: the difference between the payload longitudinal position and the average helicopter longitudinal position, as well as the difference between the payload lateral position and the average helicopter lateral position. Due to the presence of parametric uncertainty, such as the uncertainty on the load weight, the nonlinear model was also developed as an adaptatively plant inversion controller.

Second, Kondak et al. [62] proposed a different approach for the controller for multiple unmanned rotorcraft lifting a tethered load in 2007. The proposed formulation is a cascade control, with a nonlinear plant inversion of the multiple helicopters system. In order to overcome the limitations due to parameter uncertainties, a reading of the tether tension and tether orientation with respect to the helicopter was used as part of the controller. In 2007, a system comprised of 3 unmanned helicopters was used to lift a payload of 5kg over a distance of 53.7m.

Finally, Berrios et al. [14] studied the implementation of a controller on R-MAX unmanned helicopters, in 2014. Nonlinear equation of motion of the pendant configuration were developed using Newton-Euler method, keeping the option of having elastic or inelastic cable, as well the option to model the load as a point mass or a rigid body. The linearized equations of motion allowed the author to identify the dynamic modes of the pendant system. Different formation angles of the helicopter as shown in Figure 14 were studied.

Each R-MAX helicopter was already individually equipped with a flight control system (FCS). The author developed a new control loop that builds upon the existing FCS control signal. The new control block uses aircraft states such as aircraft attitude, aircraft attitude rate, vertical velocity, as well as new information specific to the system such as roll and pitch angle of the cables, roll and pitch angular rate of the cables, lateral and longitudinal helicopter separation and lateral and longitudinal helicopter separation rate. The new control loop was developed using the multi-objective optimization tool CONDUIT, based on the ADS33 stability and performance specifications [97].

In addition to the dynamics and control assessment, Berrios et al. [14] proposed a metric that quantify the loss of thrust due to the pendant configuration geometry: *pendant penalty fraction (PPF)*. It represents "the ratio of the helicopter's non-vertical thrust to the percentage of the load weight the helicopter is required to lift" [14]. For their analysis, a separation distance of 2 rotor diameter, with individual cable length of 2 rotor diameters led to a PFF of 5%.

2.1.6 Airborne Wind Energy and Tethered Kites

Tethered aircraft have been used for many other applications than load lift in including airborne wind energy. Airborne wind energy (AWE) uses various flying systems to extract wind power, including tethered aircraft [31]. Two main categories can be used

to classify them: on-board power generation, ground based generation and providing a tethered forces to a moving anchoring vehicle. Regardless of the classes, the dynamics and control represents an important of the analysis.

2.1.6.1 Dynamic Modeling

Most of the dynamic models were used for simulation, a study of the open loop characteristics of an inflatable tethered aircraft was carried out by Terink [93]. The aircraft has no control surfaces, and is attached to the ground through a single line, attached to a two-line bridle. Terink modeled the tethered aircraft as a 6 DOF system, a rigid, massless tether, strip theory to evaluate aerodynamics forces and moments, and the equations of motion were solved with Lagrange dynamics.

The analysis of the system includes the longitudinal and lateral dynamics of the tethered aircraft independently. It was noted for static stability analysis, the tether tension plays a important part in the stability. The tether tension was compared as moving the equivalent center of gravity. Due to the contribution of the tether tension on the equilibrium condition, the stability of that system is affected by the wind speed.

Finally, the impact of the aircraft physical parameters were evaluated on the open-loop behavior, including the inertia, the vertical tail area, the length of the tailboom, the dihedral angle, wind velocity and attachment location.

2.1.6.2 Controls

Many projects studied the controls of tethered aircraft, with some including experimental results. [12, 17, 18, 34, 36–39, 44, 45, 51, 64, 68, 100].

Among the systems of interest, Makani Power [99] developed a system based on the use of a single aircraft tethered to a ground station that flies over a quasi-circular flight path, in the plane perpendicular to the wind. The wind powers the aircraft on its flight path, while the propellers extract some power which is sent through the

Figure 15: The Makani Wing 7 in Flight [99]. Top picture is a superposition of multiple images from the flight

tether to the ground station.

This concept presents similarity to the EPR2 system since similar aircraft fly over a relatively complex flight path, which can be reconfigured as a function of the operating conditions such as the wind speed and orientation to optimize the operation. However, the use of a single aircraft introduces an important difference in the objective of the system, as there is no need to perform collaborative control of an external body.

Zanon and Gros [46, 99, 110, 111] proposed an architecture based on a non-linear Model Predictive Controller, and a Moving Horizon Estimator for the control and state estimation for an this type of AWE. This system was aimed at optimizing the operation to maximize the power output.

2.2 Dynamic considerations in the design of aerospace systems

The dynamics and controls of aerospace vehicle are an important aspects of their overall design since their inception. Single main rotor helicopter, for example, were successful flights once the Bell stabilizer bar was included on the main rotor and provided the pilot a system that he could adequately control.

Since then, a lot of knowledge has been gained on aircraft dynamics, and on the operator's ability to pilot an aircraft. Moreover, advances in electronics has allowed to create systems that are highly augmented and even unmanned. The following section will provide a background in the handling qualities of manned aircraft and dynamic considerations in the design of highly augmented and unmanned aircraft.

2.2.1 Handling Qualities

2.2.1.1 Manned Aircraft Handling

Extensive knowledge has been developed over the year on the required handling qualities for rotorcraft. The *Aeronautical Design Standard Performance Specification Handling Quality Requirement for Military Rotorcraft* [29,50,58,97] contains the handling requirements for piloted helicopters. The Level of handling qualities shall be a combination of the two distinct methods of assessment, Predicted Levels and Assigned Levels. An example are the limits on pitch oscillations, as shown in Figure 16.

The assigned levels are determined by test pilots who complete a series of mission-tasks elements, or maneuver, and use the Cooper-Harper Handling Qualities Rating.

The Predicted Levels are obtained by comparing the predicted helicopter dynamics to a series of requirements. These requirements take many forms: response bandwidth and time delay, closed-loop eigenvalues, large amplitude nonlinear responses, and inter-axis coupling, among others. The requirements differ on the different axes, and on the aircraft primary missions: scout, attack, utility and cargo.

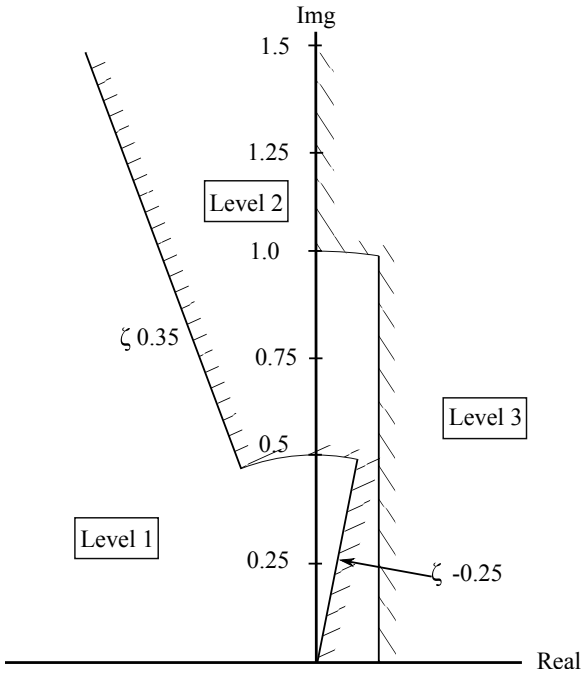

Figure 16: Limits on pitch oscillations, adapted from ADS-33 [97]

Analogous requirements for fixed-wing aircraft are developed in the Military Specification Flying Qualities of Piloted Airplanes (Mil-F-8785) [1, 71].

2.2.1.2 Highly Augmented Aircraft and Unmanned Aircraft Control Systems Requirements

The use of augmented flight controls opened the possibility to modify the tailor the aircraft characteristics by including stability augmentation system. The handling requirements are now applied to the combined aircraft and stability augmentation system.

Using augmentation systems and relaxing the aircraft open-loop dynamic requirement and has opened to many vehicle-level performance, including, but not limited to [30, 33, 80]:

- Load alleviation
- Structural mode control
- Reduced trim drag

- Smaller empennage
- Enhanced maneuverability

Multiple methods have been proposed to generate a stability augmentation system that lead to adequate handling qualities. Some methods in particular pose the gain tuning problem as as a optimization problem: minimize the performance metrics of crossover frequency and actuator activity, while maintaining level 1 design criteria [94–96, 109].

Some methods have also been proposed to simultaneously size physical design features concurrently with generating the control law.

The use of highly augmented aircraft and unmanned aircraft introduces a different approach: The control law it not governed by matching handling qualities, but they are governed by aircraft-level requirements.

In the book chapter *Command and Control of Autonomous Unmanned Vehicles*, How et at. [52] note that fundamental challenge in the design of unmanned control system remains the same : *determine what are the design objectives*. Moreover, the authors note that the design and control strategies developed for manned aircraft may be overly conservative for unmanned system.

Among other considerations for the development of the augmented systems other others have noted: [30, 80]

- Actuator magnitude and rate saturation
- Excessive feedback of sensor noise and bias
- Maximum aerodynamic coefficient
- Structural limit during a maneuver

The design of the control systems has to be done concurrently with the aircraft design.

2.3 Observations from Literature

Previous work on the use of multiple aircraft tethered to a shared payload has shown that this concept has the potential for efficient, long endurance load lifting. Moreover, manned aircraft flight tests have already been performed on this concept. The use of lighter unmanned aircraft, supported by the advances in autonomy, might be an enabler for higher performance, long endurance flight. Detail analysis of the flight paths and the aerodynamic interaction between the aircraft has underlined the load lifting capabilities of such a concept.

Aircraft used for airborne wind energy generation have demonstrated capabilities and flight phase similar to the the one required by shared load lifting: lightweight, electric powered system with autonomous flight capabilities. While those concepts have been studied in details, the dynamics of the the system lifting a shared payload presents new characteristics: the motion of the aircraft are coupled through the load motion. The framework developed for the CSR, an analogous concept using tethered aircraft, aimed at limiting the contribution of the tethered load by including a controller that would negate its motion. However, this process does not allow to understand the dynamic modes of the system, hence limiting the understanding. Finally, the study of manned aircraft lifting a shared load lead to long tethers, with very large flight radius. The equilibrium configurations are characterized by large tether deflection, and the dynamic modes of the system are dominated by tether motion.

This review of the existing literature shows a gap in the understanding of the dynamic related considerations for systems comprised of multiple aircraft lifting a tethered payload over relatively small flight path radius.

CHAPTER III

PROBLEM FORMULATION

As described in the previous sections and as demonstrated in the literature, the EPR2 concept presents interesting expected advantages. However, the lack of knowledge on the dynamic behavior needs to be addressed. While in the literature approaches were presented to evaluate and optimize the flight path to minimize power, there is a fundamental gap in the understanding of the dynamic behavior of the system.

3.1 Research Objective

The overarching research objective of the present research is the following:

Research Objective:

Provide a framework to analyze the dynamics-driven design decisions of a system comprised of multiple aircraft tethered to a shared load during hovering, circular flight.

The system has multiple dynamics-related objectives - the following list outlines some of the most important, and Figure 17 illustrates schematically some of them:

- Assure stability of both the aircraft and the fuselage
- Control the payload position in hover
- Provide disturbance rejection to wind gust and sensor noise
- Enable aircraft coordination and avoid collision

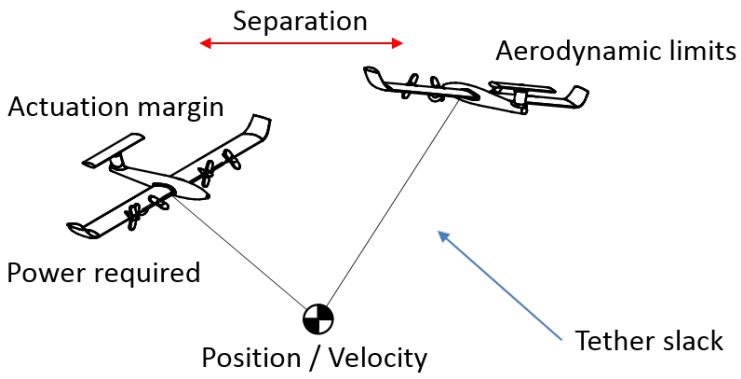

Figure 17: Controller constraints and objectives

- Minimize power required
- Respect actuation margin: Control surface maximum deflection and propeller RPM
- Maintain the tether under tension
- Respect aerodynamic coefficients limit and avoid stall

Some of the objectives might be conflicting. For example, it might be possible that a maneuver which minimizes the fuselage displacement requires more power than a maneuver that induces more fuselage motion. One of the additional observations made on the system is that there is no explicit aircraft state requirement.

The key disciplines at the heart of the research objective are *dynamics, design* and *control.*

Dynamics The first important discipline involved in the research objective is dynamics. This discipline is required namely to model the system and to evaluate the open loop characteristics of the system. While previous analyses outlined in the literature review attempted to evaluate and optimize the power of the system, some dynamic considerations were omitted.

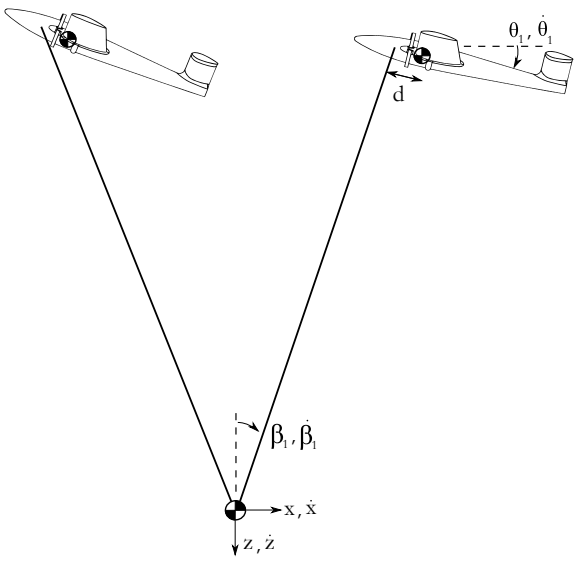

Figure 18: Schematic representation of the canonical problem

Design The system presents new degree of freedom in the design of the system. In the context of a long endurance hover vehicle, the performance consideration for the new design variables have to be part of the overall system design.

Control As illustrated in the presentation of the concept, the aircraft have to be unmanned in order to be able to perform complex and coordinated flight. Consequently, the discipline of control is an important part of the dynamic performance of the system.

3.2 Canonical Problem

In order to understand some of the dynamics, control and design considerations, a simpler problem, referred to as the canonical problem is being proposed, as shown in Figure 18.

The problem of interest consists of a load shared by two aircraft for which only the longitudinal motion is considered. The nominal geometric characteristics of the system are shown in Table 4. This problem allows to perform exploration of the analysis method with reduced complexity, while maintaining some relevant dynamic

Table 4: Canonical problem parameters

System characteristics	**Description**
Tether length	15 m
Nominal Fuselage velocity ($-\dot{x}$)	20 m/s
Aircraft mass (each)	1 kg
Fuselage mass	2 kg
Span	2 m
Chord	0.3 m
Pitch inertia	0.5 kgm^2

characteristics.

There are 6 degrees of freedom : the payload position x and z, the β angle for each cable (2) and one pitch angle θ per aircraft (2). This adds to 12 states when considering their time derivatives. Each aircraft has 2 control input: propeller RPM and elevator deflection δ_e for a total of 4 control input. The equations of motions were obtained by solving the Lagrange equations.

3.2.0.1 Open-Loop Characteristics

A linearization of the equations of motion of the canonical example system was performed around the trimmed condition. The system is characterized by the following equation, expressed in the form $\dot{x} = Ax + Bu$. Coefficients of the matrices can be found in A.

The natural frequency and a schematic representation of the associated eigenvectors are shown in Figure 19 and Table 5.

It can be seen, first, that all modes are stable. Moreover, there are two sets of modes: a low-frequency set and a high-frequency set. The lowest frequency mode is comprised of an up-and-down motion of the whole system, similar to a phugoid mode. The second is characterized by an opening-and closing of the tether angle, analogous to the motion of a pair of scissors. This mode was also identified in the Dual-Lift Helciopter concept. Finally, the third mode is similar to a pendulum motion of the

Table 5: Dynamic modes characteristics of the canonical problem

Mode Description	Eigenvalue	Frequency (rad/s)
Mode 1: Phugoid approx	$-0.1809 - 0.2399i$	0.0478
Mode 2: Scissor	$-0.3793 + 1.0553i$	1.1214
Mode 3: Pendulum	$-0.1551 + 1.6213i$	1.6287
Aircraft Mode A	$-10.8862 - 18.7129i$	21.6491
Aircraft Mode B	$-19.6761 + 14.1385i$	24.229

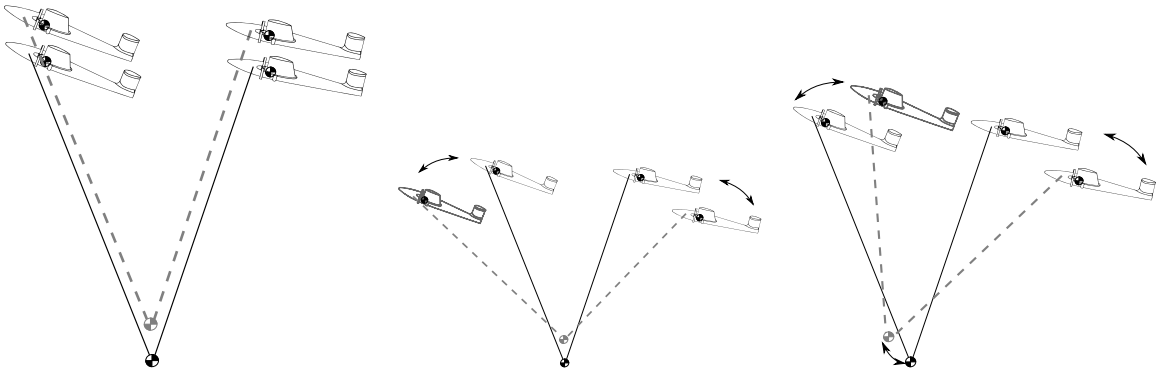

(a) Mode 1 (b) Mode 2 (c) Mode 3

Figure 19: Schematic representation of the eigenvectors

suspended mass.

The two high-frequency modes are characterized mainly by aircraft pitching motion, either in phase or out-of-phase. The two sets of modes have a large spectral separation: a factor of 10 separates the low and the high frequency modes.

3.3 Assumptions

The following assumptions are included in this thesis in order to provide an adequate modeling framework to fulfill the research objective.

Number of aircraft The number of aircraft will be kept constant through the analysis. Rancourt studied the use of 3 aircraft due to the constraint imposed by the inverse dynamic analysis. Selfridge used 4 aircraft as he noted that an even number of rotor represented an interesting option for his cyclic control implementation.

For the current analysis, the smallest number of aircraft is desirable to limit the complexity. As highlighted in the review of existing concepts, the use of a single aircraft is not of interest for this thesis as it requires very long tethers to achieve a stationary payload.

The use of two aircraft was also discarded, as it presents fundamental differences in the analysis compared to a three or more aircraft systems [54]. The explanation relies in the fact that the dynamic of a system with three or more aircraft can be analyzed in the nonrotating frame by decomposing the motion in a series of nonrotating degrees of freedom including a sine and cosine modes (cyclic), while the motion of a system with only two aircraft is done differently. The absence of sine and cosine modes creates a different requirement when analyzing the motion of the aircraft coupled to the load. Details about the non rotating degrees of freedom are provided in the next chapters.

In other words, the analysis of a system with three aircraft has more in common with the system that has four aircraft than the system that has only two. For the remainder of this thesis, the number of aircraft is assumed to be three.

Fixed aircraft configuration The aircraft design is assumed as constant. The design and analysis of the system will be with respect to the new design degree of freedom allowed by the configuration, not from the typical aircraft parameters.

Fuselage design As represented in Figure 1, the fuselage can take multiple shapes and include features like aerodynamic control surfaces or thrusters. However, for the scope of this work, the payload is assumed to have no actuation devices.

Tether length As described in Chapter 1, optimal operating conditions will vary based on the payload mass. Having an adjustable tether length throughout the mission can present possible advantages. However, for the scope of this thesis, the tether length is assumed as fixed once the system is off the ground. This assumption limits

the number of variables, as well as supports a simpler design for the fuselage-tether interface, which already represents a complex mechanical system.

Autonomy and Control Architecture The 24 hour hover challenge [3] allows flexibility on the autonomy level: "During a Prize Flight, the Aircraft shall fly autonomously and/or receive commands from a Controller."

Many definitions exist for the different levels of autonomy. The following list was proposed by Dalamagkidis [25] and is compatible with the four operational modes described in the Federal Agencies Ad Hoc Autonomy Levels for Unmanned Systems (ALFUS) Working Group (WG) report [7]:

- **Remotely piloted:** A certified pilot remotely controls the system either within LOS or with feedback from the UA sensors.
- **Remotely operated (semiautonomous):** The UA is given high-level commands (waypoints, objects to track, etc.), and its performance is monitored by a trained operator. In this case the flying is performed by the UA itself, but all the decision making is delegated to a human.
- **Fully autonomous:** The UA is given general tasks and is capable of determining how to accomplish them, even at the face of unforeseen events. It can also monitor its health and take remedial action after the occurrence of faults.

For the scope of this thesis, the system is assumed to be *remotely operated (semiautonomous)*. An operator on the ground would provide the system with way points to follow via a remote control station [24]. This would be used to fly the triangular flight pattern required to fulfill the 24 Hover Challenge.

Coherent with the level of autonomy of the system, it is assumed that a controller on board will assure a controlled and stable flight. As presented in the previous chapters, there exist multiple control architectures for a system with multiple aircraft.

The control architecture assumed for this system is a centralized controller [66,98]. This assumption is supported by the fact that the aircraft are dynamically coupled together. The information about their current state is relevant to the other aircraft beyond achieving a mission-type requirement: it is needed to maintain flight.

3.4 Research Questions

3.4.1 Tether attachment point

The first observation arouse from the physical decomposition of the system: As described in the previous section, the tether attachment point on the aircraft represents a new design degree of freedom when compared to the design of a single fixed wing aircraft. Moreover, because the aircraft are operating on circular flight paths, there is no more need to keep the parameters symmetric about the x-z plane.

With this new degree of design freedom, there is a need to understand the underlying limitations of the attachment point:

Research Question 1:

What are the benefits of placing the tether attachment point off the center of gravity?

As a thought experiment, the longitudinal static stability of three configurations are compared: a typical fixed-wing aircraft in cruise, a fixed-wing aircraft in cruise lifting a tethered load, and finally, a fixed-wing aircraft, tethered to the ground. The three cases are illustrated on Figure 20

Conventional Fixed-Wing Configuration The aircraft center of gravity envelop can be expressed as a function of the static margin, which is defined as the distance between the neutral point and the center of gravity of the aircraft [35]. A typical value for the location of the center of gravity is $10-25\%$ in front of the neutral point.

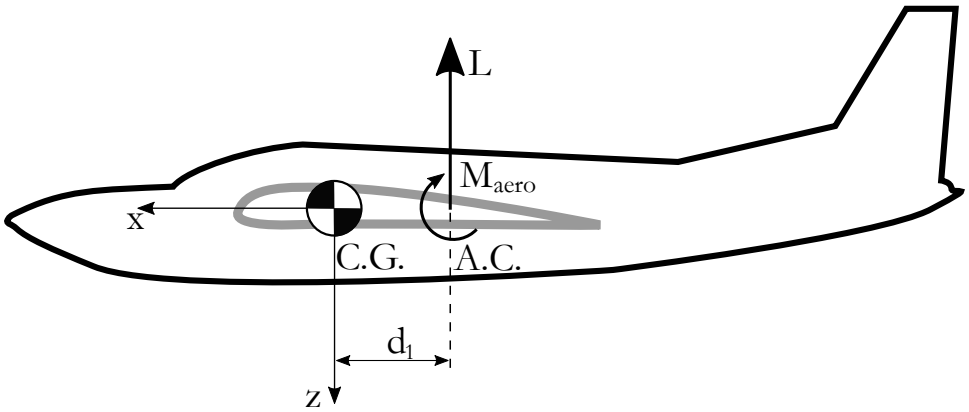

(a) Configuration 1: Conventional fixed wing aircraft in steady-level flight

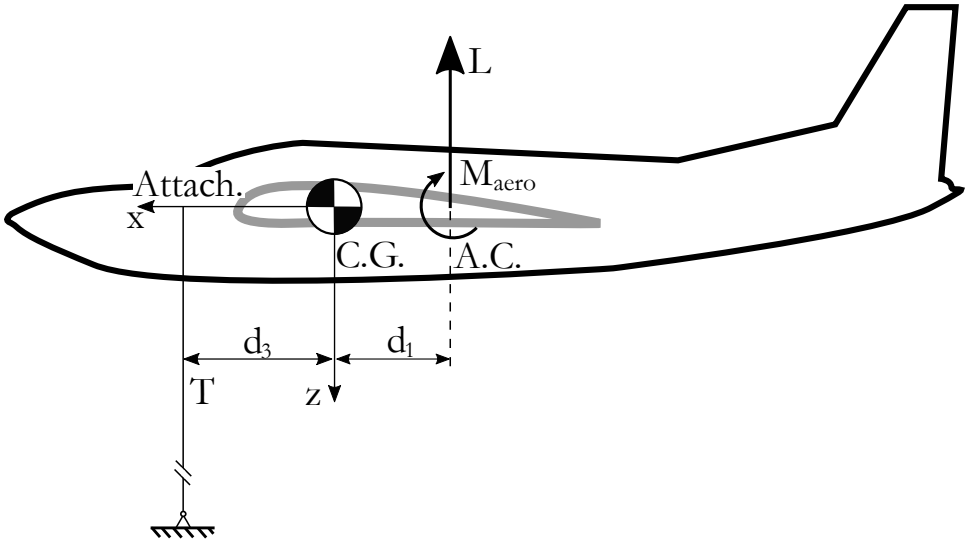

(b) Configuration 2: Fixed wing aircraft tethered to the ground

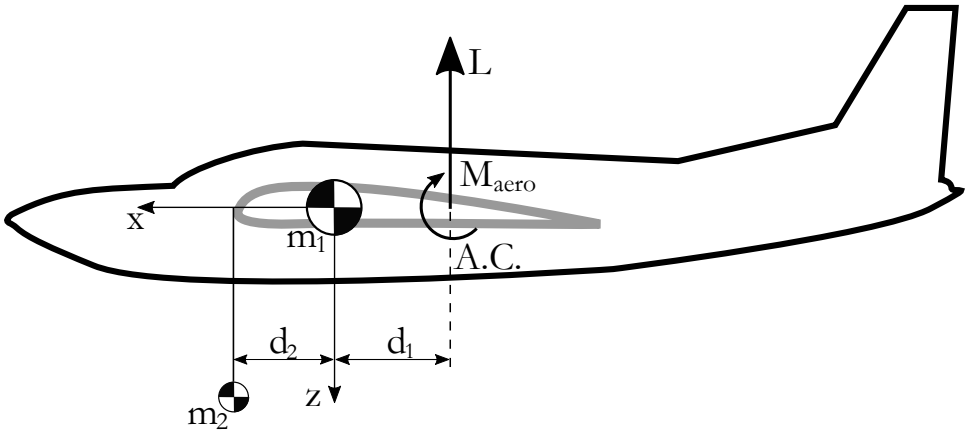

(c) Configuration 3: Fixed wing aircraft lifting a tethered load

Figure 20: Comparison of three configurations: conventional fixed-wing aircraft, fixed-wing aircraft tethered to the ground and fixed wing aircraft lifting a tethered load

Having the center of gravity in front the neutral point allows the aircraft to have positive longitudinal stability. The demonstration of longitudinal stability involves the summation of moment about the center of gravity around the longitudinal axis y, as shown noon Figure 20.

$$\sum M_{y_{cg}} = M_{aero} - Ld_1 \tag{6}$$

Where d_1 denotes the distance between the center of gravity and the aircraft aerodynamic center. The aircraft aerodynamic center is defined as the location where there is no variation of coefficient of aerodynamic moment with angle of attack $\partial C_{m_{aero}}/\partial\alpha = 0$ for the whole aircraft. Assuming that $L = qsC_L$, and that the differentiation of C_L can be expressed locally by $\partial C_L/\partial\alpha$ the static stability is demonstrated by:

$$\frac{\partial M_y}{\partial\alpha} = -qs\frac{\partial C_L}{\partial\alpha}d_1 \tag{7}$$

For a positive static stability, there is a need to have a negative value of $\partial M_y/\partial\alpha$, hence a center of gravity forward of the aerodynamic center ($d_1 > 0$).

Fixed-Wing Aircraft Tethered to the Ground For an aircraft tethered to ground, the location of the attachment point also impacts the dynamics of the aircraft. As a thought experiment, the case represents an aircraft attached to the ground by an infinitely long, inelastic, massless tether. The balance of forces and moments on the center of gravity of the aircraft is carried in the following equations:

$$\sum F_z = T + mg - L \tag{8}$$

$$\sum M_{y_{cg}} = M_{aero} - Ld_1 - Td_3 \tag{9}$$

Assuming static equilibrium, Equation 12 allows to substitute T by $-mg+L$ and carrying the differentiation on Equation 9:

$$\frac{\partial M_y}{\partial \alpha} = -qs\frac{\partial C_L}{\partial \alpha}(d_1 + d_3) \tag{10}$$

The condition for static stability now becomes that $(d_1 + d_3) > 0$. This illustrates that for this configuration, the location of the center of gravity does not play a role in the static longitudinal stability, but the location of the aerodynamic center and the attachment point do: the tether attachment point must be in front of the aerodynamic center.

Fixed-Wing Aircraft Lifting a Tethered Load The second configuration of interest is the aircraft lifting a tethered load. The longitudinal motion is akin to the analysis the configuration 1, but with a modification of the apparent center of gravity of the whole system:

$$x_{cg} = \frac{m_2 d_2}{m_1 + m_2} \tag{11}$$

The condition for static stability, which indicates that the center of gravity must be in front of the aerodynamic center now translates to :

$$\frac{m_2 d_2}{m_1 + m_2} > -d_1 \tag{12}$$

Rearranging, the condition on d_2 is : $d_2 > -d_1 \frac{m_1+m_2}{m_2}$.

On one extreme of the weight ratios, the case of aircraft lifting a heavy load ($m_2 >> m_1$), the condition for static stability approaches the one of the aircraft tethered to the ground $(d_1 + d_2) > 0$.

This thought experiments illustrates how a tether attached to an aircraft can influence the condition for longitudinal static stability. However, it is understood that the attachment point introduces other considerations.

Moreover, for the case of multiple aircraft tethered to a shared payload, the analysis is complicated by many factors. First the static stability has to be performed for all the axes of an aircraft. The circular flight path introduces multiple terms in the summation of forces and moments on each aircraft. Additionally, the aircraft are all attached to the shared fuselage which creates a large coupled problem: the forces induced on the payload by one aircraft affects the motion of the other aircraft.

The static stability is an important criteria in the definition of a manned aircraft. However, for the case of an autonomous system, as presented in the literature, positive static stability is not necessarily required.

The hypothesis for the research question 1 is the following: **Allowing the tether attachment point to be a design variable can increase the actuation margin during the circular hover flight phase.**

In order to prove the hypothesis, the following method is proposed:

STEP 1 Identify the geometric constraints of the attachment point based on the trim conditions;

STEP 2 In the volume identified previously, identify the region that leads to desirable open loop dynamic characteristics of a single aircraft tethered to the ground;

STEP 3 In the volume identified previously, identify the region that leads to desirable open loop dynamic characteristics of the multiple aircraft tethered to a shared payload;

STEP 4 In the volume identified previously, identify the region that leads to a system that is capable of sustaining a steady-state wind gust;

STEP 5 In the volume identified previously, rank the possible attachment locations based on the actuators and lift coefficient margins.

3.4.2 Nominal Flight Path Parameters

In the previous subsection, the tether attachment point on the aircraft was identified as a new design freedom for this system. Additional new degrees of freedom for the design of operation are the aircraft flight parameters. In hover, the circular flight path is described by the tether length, the angle that the tether makes with the horizontal plane and the aircraft velocity. From the observation of the presence of new operating conditions, the second research question arises:

Research Question 2:

What are the benefits of selecting a circular flight path radius and velocity different than the one defining the minimum power required?

As presented in Chapter 1 and Chapter 2, Rancourt and Demers Bouchard presented two different methods to find the flight path parameters that minimize the power required to lift a given payload. The lower-fidelity analysis of Demers Bouchard that uses BEMT in circular flight path is adapted for the analysis of three aircraft to allow to perform the exploration of additional configurations.

The methodology presented in Chapter 1 included the tether electrical conductor as a design variable in the overall optimization process of the system. For the $40kW$ system, the electric losses in the tether were in the order of 1% of the overall power. Consequently, for the purpose of the exploration of different configurations and to limit the number of factors in the equation, the tether properties are assumed as constant and the electrical losses are neglected. The new optimization problem is posed as follows, with the assumptions related to the vehicle of interest shown in the Table 6.:

Table 6: Vehicle characteristics and assumptions for the Makani Power *Wing 7* prototype

Maximum lift coefficient	0.8
Number of aircraft	3
Tether linear density	0.11 kg/m

Minimize: Power required

Given: Payload mass

With Respect to: α, ζ , L, $V_{Aircraft}$

Subject to: $C_l \leq C_{l_{max}}$

The optimal design variables and operating conditions for systems comprised of 3 aircraft are shown in Figure 21. This figure shows the minimum power required, as well as the optimal operating conditions. The variable ζ is illustrated in Figure 30 and is the angle between the cable and the horizontal plane.

Two different maximum coefficient of lift are allowed in the simulation: 0.8 and 1. It can be seen that having a system that can operate at higher lift coefficient reduces the power required. This trend was also shown in Rancourt work, as most of the optimization cases ran on the complex flight paths that would include a portion with maximal lift coefficient, as shown in Figure 10. For the remainder of the analyses, the maximum lift coefficient of 0.8 is assumed.

While minimizing the power required is of great importance for the operation of the system, variation around the optimal operating conditions might represent an appropriate trade-off if other characteristics are achieved on the dynamics point of view. In order to assess a tradeoff, the optimization process was performed for the system lifting a 500 kg payload, while imposing different values of tether angle ζ. The optimization process can be described as follows:

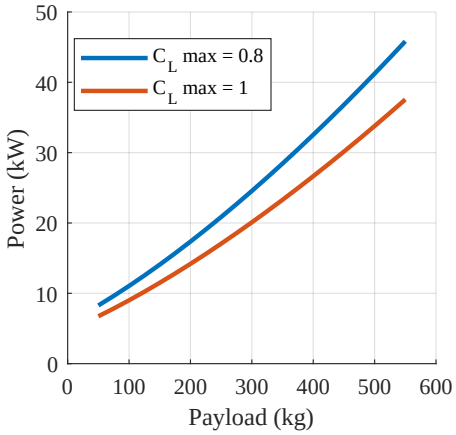

(a) Power required for a given payload

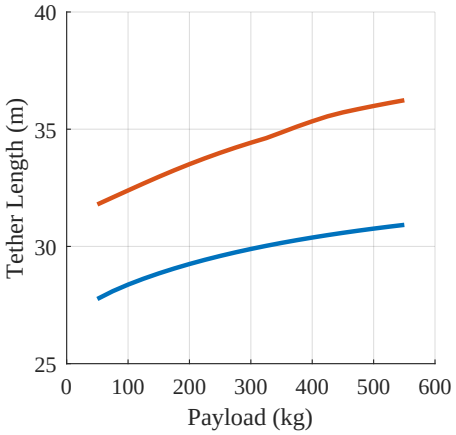

(b) Optimal tether length

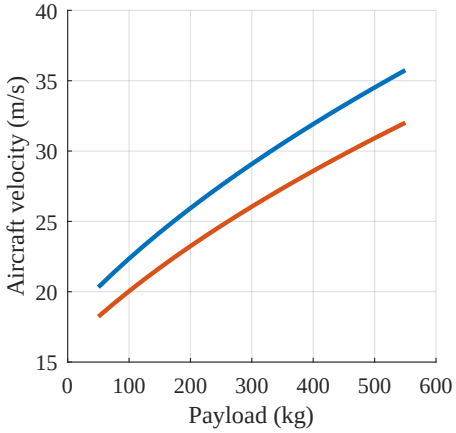

(c) Optimal aircraft velocity

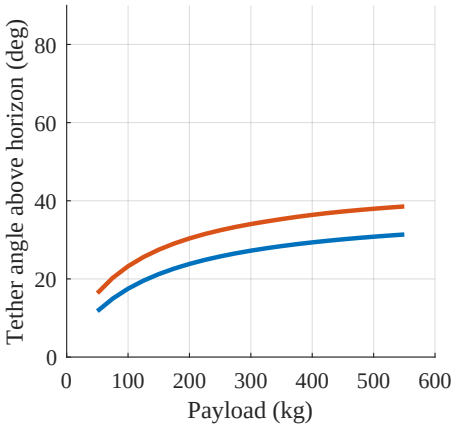

(d) Tether angle ζ

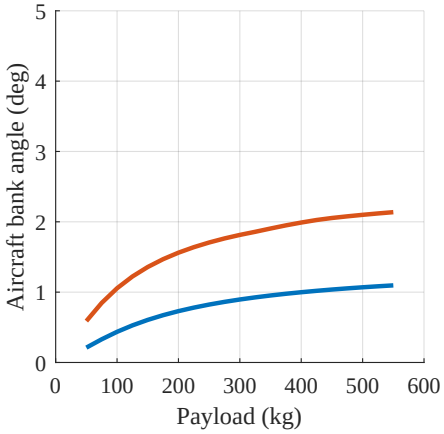

(e) Bank angle

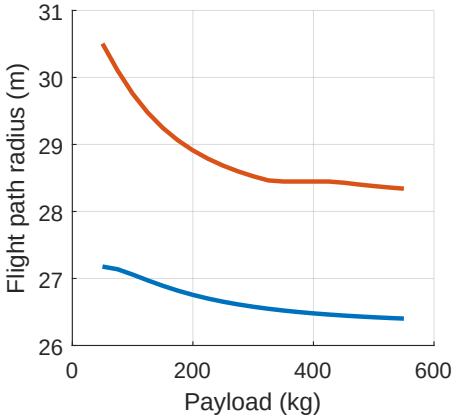

(f) flight path radius

Figure 21: Optimal design variables and operating conditions for systems lifting various suspended mass

Minimize:	Power required
Given:	Payload mass, ζ
With Respect to:	α , L, $V_{Aircraft}$
Subject to:	$C_l \leq C_{l_{max}}$

The results of the optimization process when the tether angle is prescribed are presented in Figure 22. While the optimal angle ζ for a system lifting 500 kg is 32^o, there is a relatively limited increase of power required around it.

In order to limit the number of variables, a similar optimization process was performed with a given tether length of 55 m. The optimization process can be described as follows.

Minimize:	Power required
Given:	Payload mass, ζ, L
With Respect to:	α, $V_{Aircraft}$
Subject to:	$C_l \leq C_{l_{max}}$

The tether length was imposed as 55m and the results of the off design optimization are shown in Figure 23.

Rancourt also performed a similar analysis with the free vortex model. The results of the optimization are shown in 24: for a given tether length and suspended mass, the figure illustrates the power required as a function of the flight path radius for three different aerodynamic modeling assumptions. It can be seen that there is also a similar region of the operating space defined by the flight path radius, or analogously tether angle, that allows a relatively small variation of power required. Within this range, the exploration of different paths does not lead to large power required penalty.

From theses analyses, it can be seen that given a relatively small variation of power required compared to the optimal power, large changes of flight path parameters, and consequently bank angle, are possible. Consequently, the hypothesis for the second research question is the following:

Selecting a set of nominal flight path parameter that differ from the

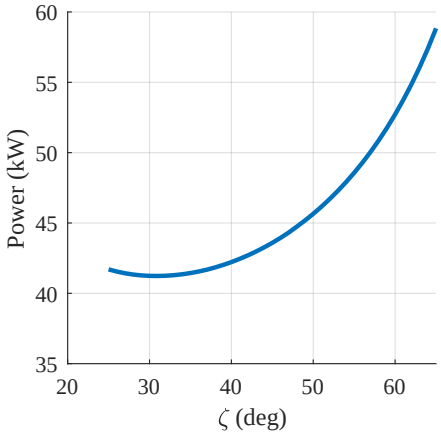

(a) Power required

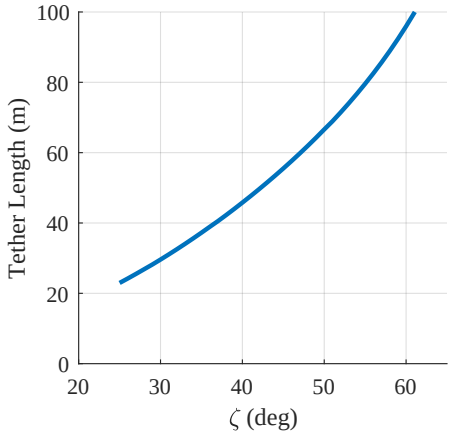

(b) Optimal tether length

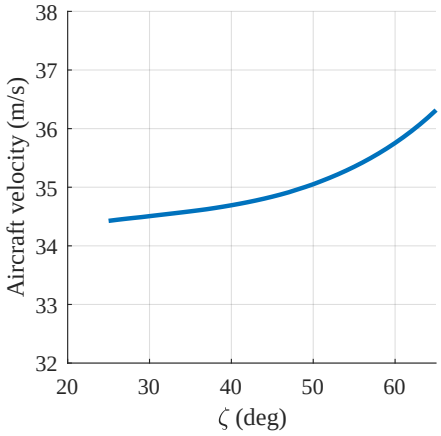

(c) Optimal aircraft velocity

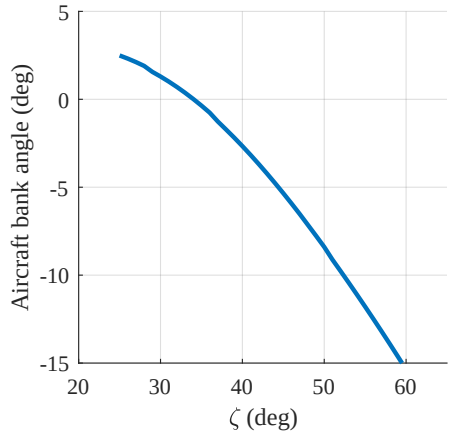

(d) Bank angle

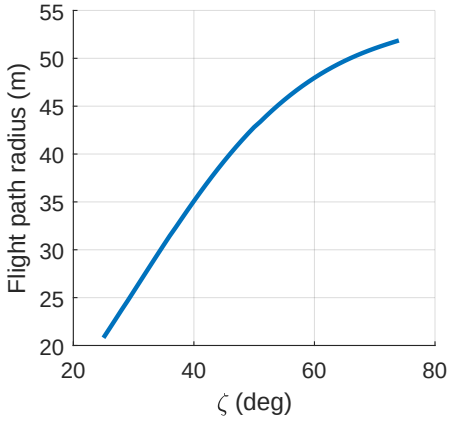

(e) Flight path radius

Figure 22: Optimal design variables and operating conditions for systems lifting 500 kg as a function of the tether angle ζ

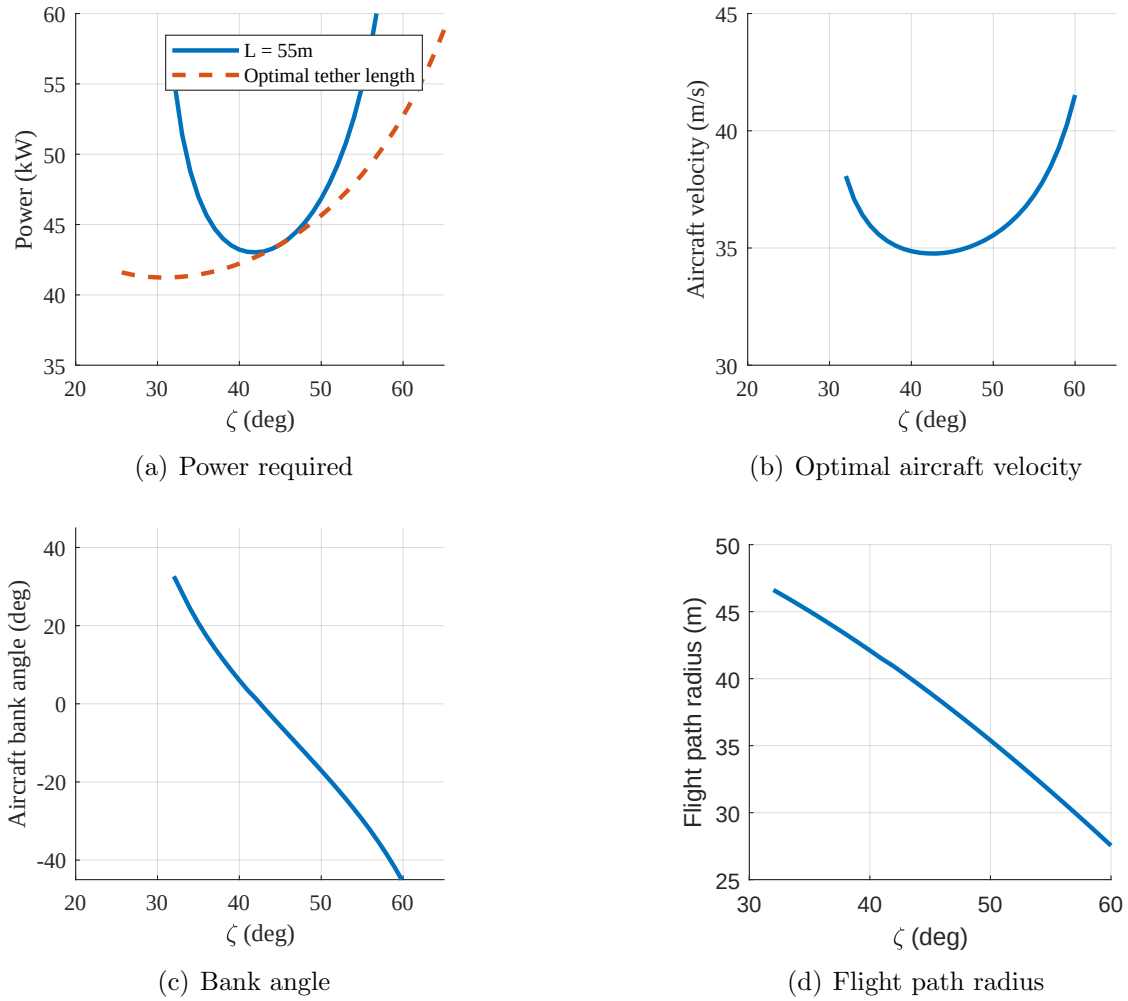

(a) Power required

(b) Optimal aircraft velocity

(c) Bank angle

(d) Flight path radius

Figure 23: Optimal design variables and operating conditions for systems with an imposed tether length $L = 55\ m$ and tether angle ζ

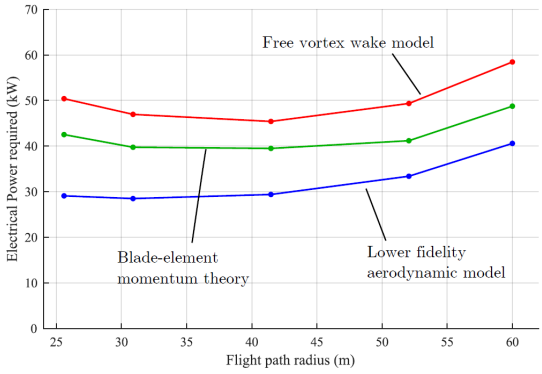

Figure 24: Power required as a function of the flight path radius from Rancourt [79]

power-optimal point can increase the actuation margin during the circular hover flight phase.

In order to prove the hypothesis, the following method is proposed:

STEP 1 Identify possible flight path parameters from the flight path optimization environment ;

STEP 2 Identify the tether attachment locations that lead to an appropriate system performance by using the procedure described for R.Q. 1 for each flight ;

STEP 3 Compare the optimal attachment point of each configuration based on their actuator and aerodynamic coefficient margins.

The nominal flight path parameters of interest are shown in Figure 25. The nominal case has a tether angle $\zeta_0 = 45^o$, and the two variations around the nominal configuration, each with $\zeta = \zeta_0 \pm 5^o$.

These cases were selected are deemed appropriate based on comparison with existing vehicles. First, the angle ζ_0 set to 45^o represents the best estimate for a starting point for the analysis of the system. Second, as shown on Figure 25 and 23, the nominal bank angle is 7.2^o inwards. This represents an interesting first estimate of a bank angle that leads to appropriate dynamic characteristics. For the analysis helicopter rotors, the coning of the rotor provide some static stability. Similarly, fixed wing aircraft dihedral typically increases static stability. Consequently, until more knowledge of the system is available, these parameters represent a good starting point.

The two other cases, with $\zeta = \zeta_0 \pm 5^o$ propose relatively different trim conditions due to the presence of coupling between the various forces acting on the aircraft, while still having relatively similar value of required power. In comparison, the case with $\zeta = 40^o$ has a slight outward bank angle.

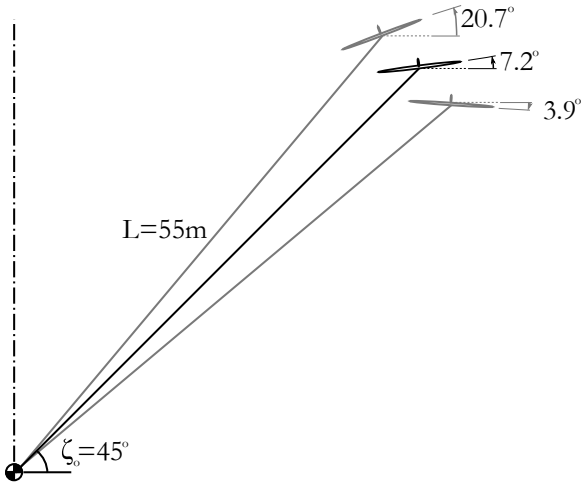

Figure 25: Schematic representation of the three flight paths of interest

3.4.3 Impact of Variable Mass

In the context of a long endurance mission, the mass of the tethered load is expected to vary greatly. This introduces a requirement on the operating capability of the system: it must be able to operate at various values of tethered weight. The third research question is the following:

Research Question 3:
How does the operation over a varying suspended mass influence the selection of the tether attachment point?

Some of the results presented in the Figures of the previous subsections included results with optimal tether lengths. However, if the assumption is that the tether cannot be reeled in, the tether length must be the same for various values of tethered mass. Moreover, the attachment point must remain the same throughout the mission, even with a changing suspended mass.

A study of the performance of the system with a fixed tether length of 55 m with a variable suspended mass was performed. In order to find the optimal condition, the

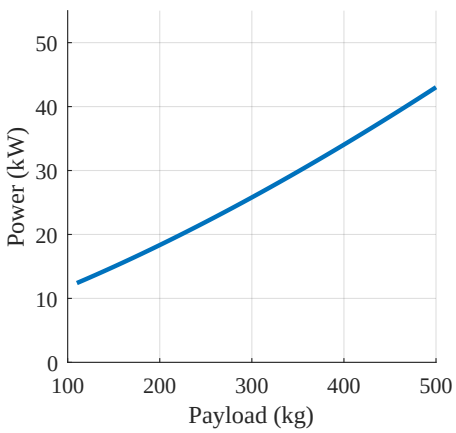

(a) Power required

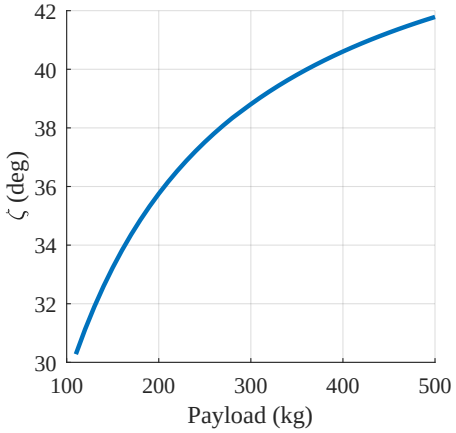

(b) Tether angle ζ

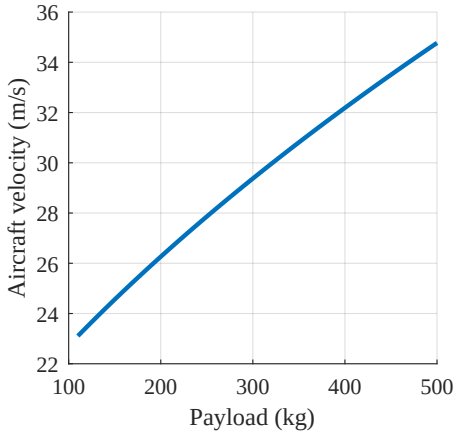

(c) Optimal aircraft velocity

Figure 26: Comparison of optimal design variables and operating conditions for systems lifting various suspended mass with a fixed tether length of 55 m

optimization problem is posed as follows:

Minimize:	Power required
Given:	Payload mass, L
With Respect to:	α, $V_{Aircraft}$,ζ
Subject to:	$C_l \leq C_{l_{max}}$

The optimal operating conditions for a fixed tether length are presented in Figure 26. It can be observed that there are large variations of tether angle ζ.

The hypothesis for the third research question is the following:

The selection of the tether attachment point must take into account

the actuation margin and open-loop response constraints imposed by the varying suspended mass.

STEP 1 Identify possible flight path parameters from the flight path optimization environment for a series of suspended masses covering the mass ratios seen in the mission;

STEP 2 Identify the tether attachment locations using the procedure described for R.Q. 2 for each flight path parameters;

STEP 3 Identify the tether attachment locations that meets the constraints for each values of suspended mass. Identify the optimal attachment location based on an aggregated cost function across the different values of suspended mass.

The cases of interest for a variable suspended mass system will be the operating conditions a 200 kg, 350 kg and the nominal case 500 kg, which are shown in Figure 26

In order to test this approach and subsequent hypothesis, there is a need to formalize the methodology, as well as to develop an experimental apparatus. In this case, a numerical dynamic modeling environment will be described in detail in the next chapter.

CHAPTER IV

METHODOLOGY

This chapter details the method and tools required to fulfill the research objective and answer the research questions. First the overall methodology is outlined. As described in the previous chapter, an experimental apparatus is required to test the method. The apparatus is comprised of a high-level, quasi-steady flight path analysis module, and a non-linear dynamic simulation environment. Once the apparatus is presented, a detailed application of the methodology to the three research questions is developed.

4.1 Methodology Overview

As described in the previous chapter, all three research questions involve finding the set of attachment points on the aircraft that lead to interesting performance of the system. Based on the attachment locations, conclusions can be found on the desirable flight path parameters as well as the feasibility of operating with a variable suspended mass. Consequently, the method presented in this section will detail the analysis of the attachment point for one configuration.

The overall methodology is presented on the Figure 27. Three different models are required, and are expressed with different colors. The first model is the quasi-steady flight path generation module. The module was presented in Chapter 3 and is a modification of the model presented in [27], used to find the nominal flight path parameters of that lead to minimal power required. Once the flight path is generated, it is analyzed in the two dynamics models: one which is comprised of a single aircraft tethered to the ground, and one which is comprised of the three aircraft tethered to a shared load. The following sections will detail the different modules in detail.

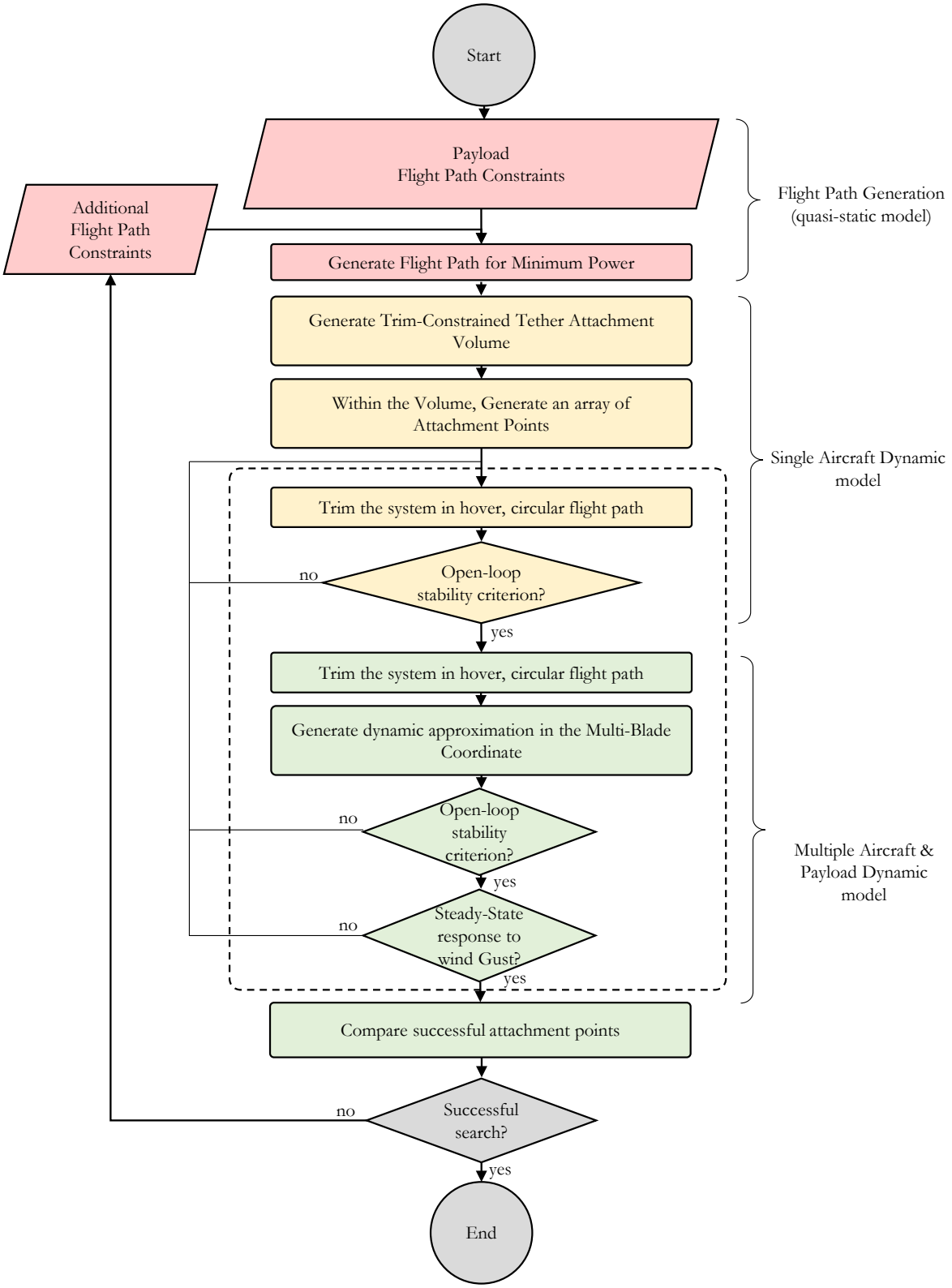

Figure 27: Overall methodology

4.2 Generation of Nominal Flight Path

The first step of the methodology proposed in section 4.1 is to define appropriate flight path parameters. As discussed in the previous sections, the flight path parameters during the circular, hover phase are the tether length, the angle that the tether makes with respect to the horizon and the aircraft velocity. Because of the multiple forces acting on the aircraft, the selection of the flight parameters is not trivial and has consequences on the power required.

4.2.1 Optimization Module

The method selected for the generation of the flight path is the analysis presented in the section 3.4.2, which is a simplified version of the method presented in [27].

The method consists of representing the aircraft as a point-mass, with the quasi-steady forces acting on it. The aerodynamic forces are calculated on the wing only, and a blade-element momentum theory is used for the induced inflow and aerodynamic coefficient calculations. The optimizer converges on cases that minimize the power required, while achieving quasi-static equilibrium on the aircraft.

This module is formulated as an optimization problem, posed as follows:

Minimize:	Power required
Given:	Payload mass
With Respect to:	ζ, α , L, $V_{Aircraft}$
Subject to:	$C_l \leq C_{l_{max}}$

4.2.2 Additional constraints

The optimization problem described in the previous section aims at minimizing the power required to hover. However, in some cases, it can be beneficial, or required to include additional flight path constraints.

4.2.2.1 Flight Path Parameters Exploration

The first instance where it is required to impose additional flight path constraints is related to the second research question, which aims at exploring different flight path parameters. For this question, it is required to use the optimizer to find the operation parameters that are not strictly defined by minimal power required. For this analysis, the tether length, and the tether angle ζ can be used as constraints.

4.2.3 Variable Suspended Mass Analysis

The second instance where it is required to impose additional flight path constraints is to study the second research question, which aims at exploring the feasibility of operating the system with variable suspended mass. For this case, it was assumed that the tether length cannot vary through the mission. Consequently, the tether length must be imposed as a constant parameter for different analyses.

4.3 Dynamic Model

At the heart of the analysis methodology developed in section 4.1, many tasks require the use of a dynamic model of the system. The following section will describe the development of the dynamic simulation framework.

4.3.1 Dynamic Modeling Requirements

The modeling framework selection is dependent on the dynamic model requirement. In order to answer the questions of interest, the modeling methodology was the following: The dynamic model must be as simple as possible while still representing the appropriate level of fidelity able to provide the tools to answer the questions of interest. The following section will provide the dynamic modeling requirements.

Aircraft representation Since the first research question involves identifying the impact of the tether attachment location on the aircraft, there is a need to include

aircraft-level dynamic models and considerations. A 6-DOF rigid body model of the aircraft motion is then required.

Relevant physical parameters must also be modified. Consequently, there is a need to use a flexible definition of the aircraft center of gravity, aerodynamic reference location and tether attachment point.

In order to be consistent with the 6-DOF aircraft representation, the aircraft needs to include the appropriate control input. The required control inputs are the ones typical to small fixed wing aircraft: aileron, rudder, elevator and propeller angular velocity.

Fuselage representation Based on the previous analyses, it is uncertain what type of fuselage could be used for this mission. Many shapes and sizes are possible and they can include different dynamic consideration. In order to limit the number of variables, the fuselage is represented as a point-mass located at the position where the three tethers are attached. No control input is assumed on the fuselage, and only a drag is assumed as the aerodynamic force.

Multibody Representation Because the system includes multiple bodies: one fuselage and three aircraft, the dynamics might not be easy to understand. The representation must be able to provide insight in the coupled motion characteristics. [11, 84, 85]

Framework Flexibility Finally, because this concept offers multiple opportunities for design variations, flexibility in the analysis environment would allow to study new configurations, such as changing the number of aircraft. Consequently, keeping the environment flexible could be beneficial.

Tether dynamics

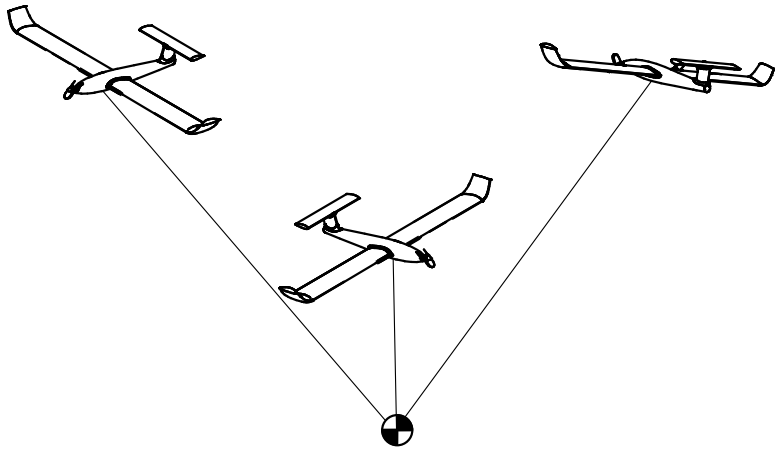

Figure 28: Schematic representation of the idealized dynamic system

4.3.2 Dynamics Model Idealization

In light of the dynamic model requirements, the schematic representation of the idealized dynamic model is represented in Figure 28. The dynamic model can be described as follows:

- The fuselage is described as a point-mass attached at its center of gravity with no rotational dynamics. The only external force applied to the fuselage is an aerodynamic drag.
- The aircraft are represented as rigid, 6 degrees of freedom bodies. Aerodynamic forces are applied on the aircraft's center of gravity.
- The aircraft and the fuselage are attached together by a rigid, massless connection;

4.3.3 Overall System Model: Modular Dynamic Model

Simulating the motion of a rigid body involves calculating the forces and moments acting on it and propagating the equations of motion through time. However, the dynamics of the idealized system comprised of tethered aircraft presents particular

challenges. Among them, there is a need to include the interaction between the different aircraft and the payload. Moreover, there is a need to express the motion of the multiple aircraft in a reference frame that is common to all the bodies. The following section will describe the methodology to successfully accomplish those objectives.

A notional representation of the overall methodology is shown in Figure 29 and can be described as follows:

- The methodology starts from the top. The states are passed and converted from one reference frame to another, as shown by the downward arrows, until the aircraft states are expressed in the inertial frame;
- Solve the equations of motion of the multiple bodies in the inertial reference frame: this involves computing the coupling forces by treating the tether as a massless spring;
- Translate the states derivatives from the inertial, Cartesian coordinate to the spherical-like H-coordinate reference frame by making a kinematic conversion;
- Remove the elastic degree of freedom of the tether by the singular perturbation method;
- If necessary, linearize the equations of motion and express the dynamics in the multi-blade coordinates.

The different modules part of the dynamic model are detailed in the following section.

4.3.4 Reference Frames

The reference frames used for the analysis of the system are shown in Figures 30 and 31.

The leftmost frame Ⓘ is the earth-fixed reference frame. For the purpose of this analysis, this reference frame is attached to the surface of the Earth. Because of

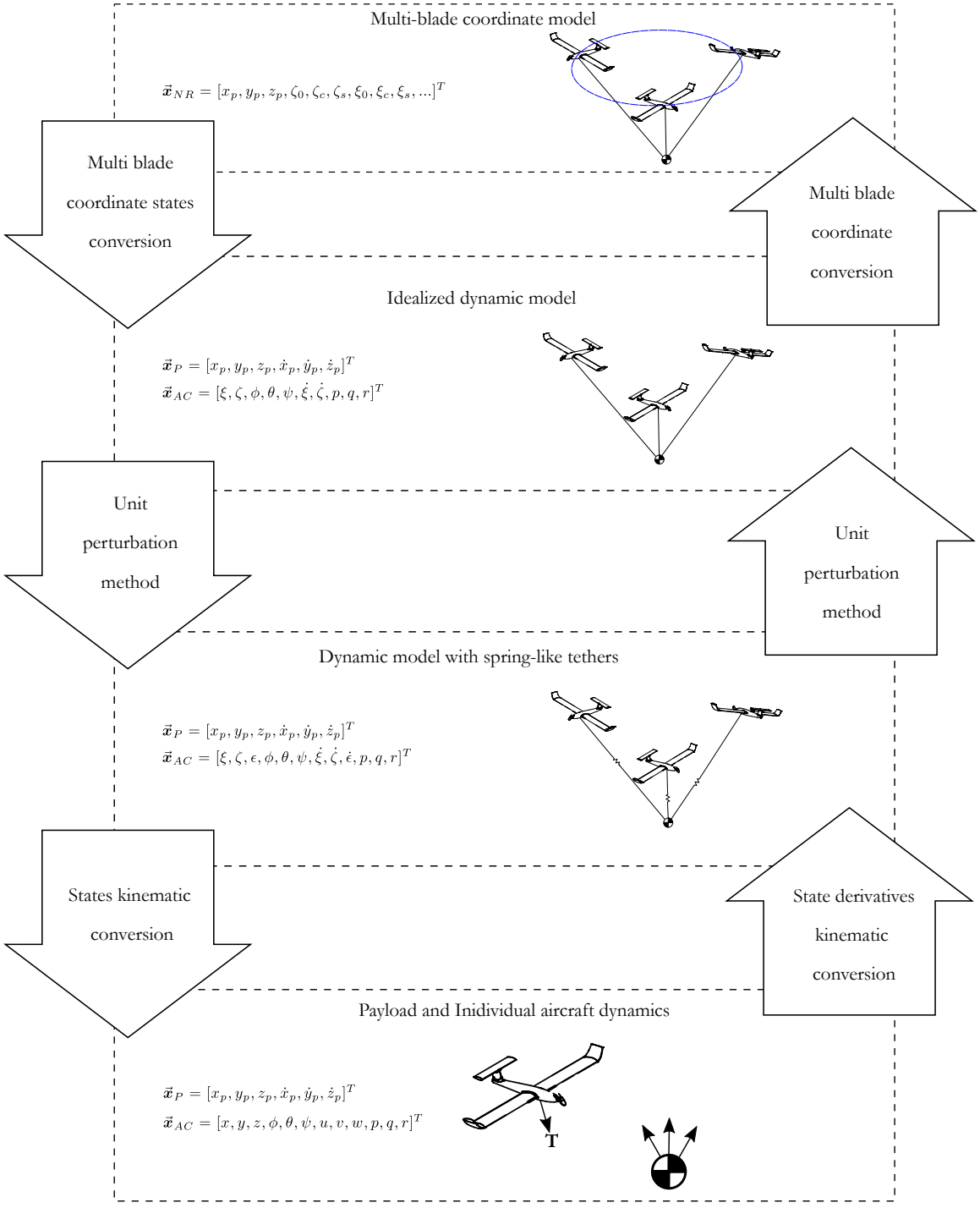

Figure 29: Schematic representation of the overall dynamic modeling methodology

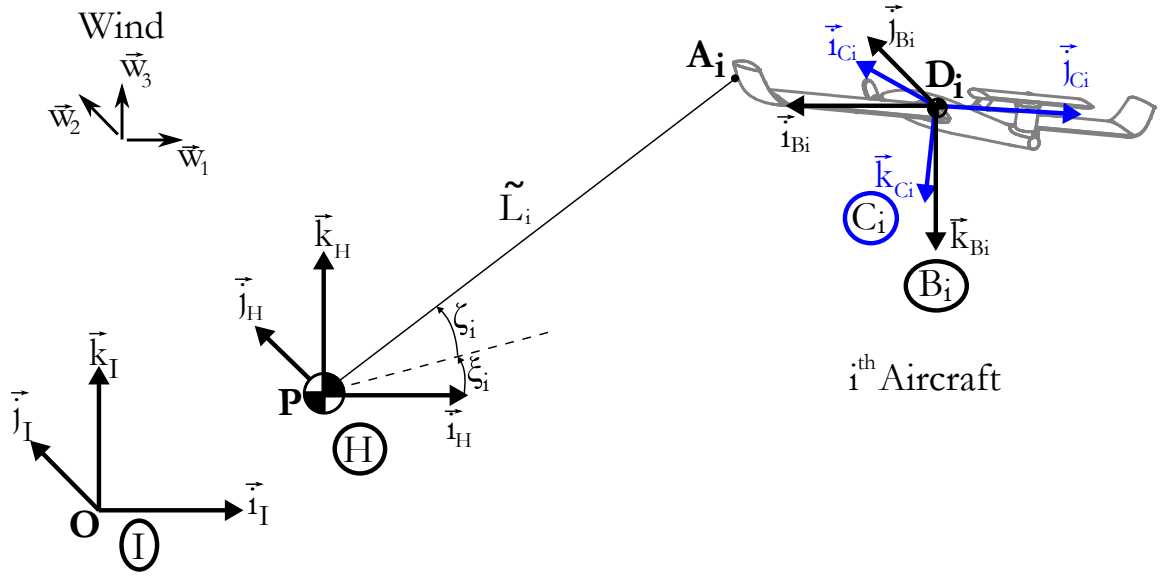

Figure 30: Reference frames used for the analysis of the system. The subscript i denotes that the variables describe the i^{th} aircraft. The frames are identified by letters inscribed in a circle.

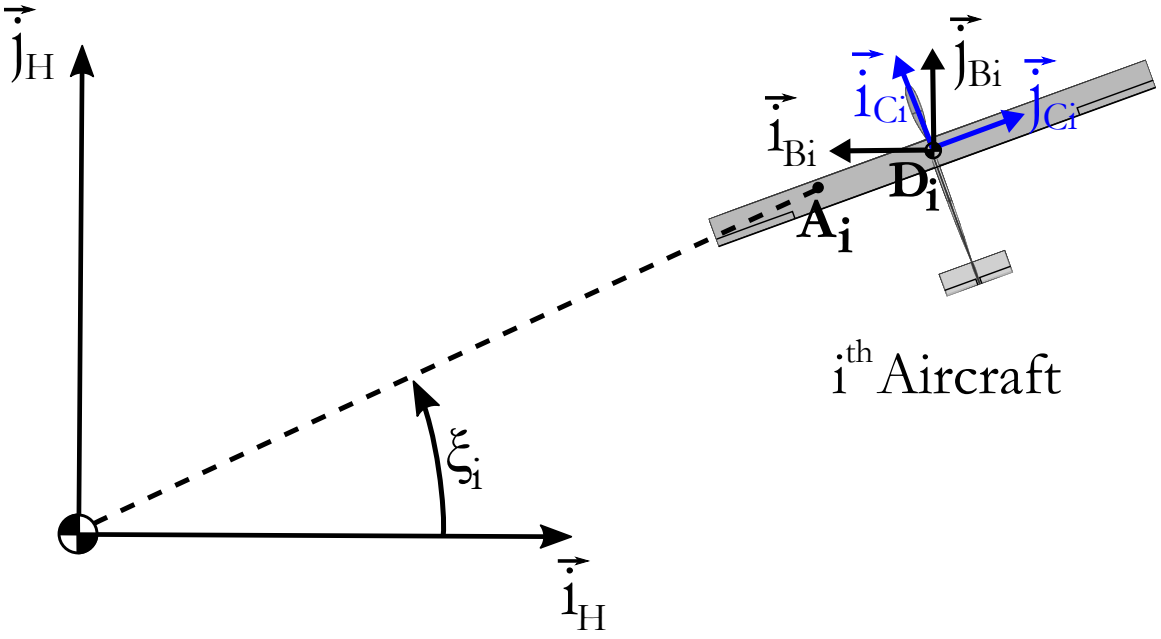

Figure 31: Top-View of the reference frames H, B and C.

the time and geometric scale of this study, the earth is considered as flat. The wind velocity is expressed in the inertial frame, and are represented by the vectors $\vec{w}_1$, $\vec{w}_2$ and $\vec{w}_3$, along the unit vectors $\vec{i}_I$, $\vec{j}_I$ and $\vec{k}_I$.

The second frame, (**H**), is the payload carried reference frame. It is attached at the center of gravity of the payload. There is no rotational dynamics associated with this frame, and (**H**) is always aligned with (**I**).

The third frame (**B$_i$**) is the i^{th} aircraft carried frame, centered at point D, the aircraft center of gravity. There are as many aircraft carried frames as there are aircraft. This framed is attached to the i^{th} aircraft center of gravity, but does not rotate with it. However, the aircraft carried frame uses the North East Down convention, and consequently, the axes of (**B$_i$**)are rotated from (**H**) by 180° about $\vec{j}_h$. The direction cosine matrix from the payload carried frame (**H**) to the aircraft carried frame (**B$_i$**) is the following:

$$\mathbf{T}_{H\to B_i} = \mathbf{L}_2(\pi) = \begin{bmatrix} -1 & 0 & 0 \\ 0 & 1 & 0 \\ 0 & 0 & -1 \end{bmatrix} \tag{13}$$

The fourth frame is the i^{th} aircraft body frame (**C$_i$**). this frame is centered at the i^{th} aircraft center of gravity and rotates with the aircraft through the three body angles ϕ, θ and ψ. The direction cosine matrix from the aircraft carried frame (**B$_i$**) to the aircraft body frame (**C$_i$**) is the following:

$$\mathbf{T}_{B_i\to C_i} = \mathbf{L}_1(\phi)\mathbf{L}_2(\theta)\mathbf{L}_3(\psi) = \begin{bmatrix} 1 & 0 & 0 \\ 0 & c_\phi & s_\phi \\ 0 & -s_\phi & c_\phi \end{bmatrix} \begin{bmatrix} c_\theta & 0 & -s_\theta \\ 0 & 1 & 0 \\ s_\theta & 0 & c_\theta \end{bmatrix} \begin{bmatrix} c_\psi & s_\psi & 0 \\ -s_\psi & c_\psi & 0 \\ 0 & 0 & 1 \end{bmatrix} \tag{14}$$

The location of the aircraft tether attachment point A_i is an important point for the dynamics of the system. For each aircraft, the attachment point can be described

in the (H) frame as follows, with $\tilde{L}_i$ the deformed tether length:

$$\vec{r}^{H}_{P\to A_i} = \tilde{L}_i \mathbf{L}_2(\zeta_i)\mathbf{L}_3(\xi_i) = \tilde{L}_i \begin{bmatrix} \cos\xi_i \cos\zeta_i \\ \sin\xi_i \cos\zeta_i \\ \sin\zeta_i \end{bmatrix} \tag{15}$$

The position of the tether attachment point with respect to the fuselage position is represented in a spherical-like coordinate system, in which the angles ξ is the azimuthal angle, the angle ζ is the elevation angle and the deformed tether length $\tilde{L}_i$ is the radial distance.

For this analysis, all of the systems of interest operate with the aircraft flying in the counter-clockwise direction above the payload. A notional representation is illustrated in the Figures 30 and 30: The aircraft is flying on a circular path which leads to $\dot{\xi}_i > 0$. For the azimuthal position represented in the figure (ξ_i small) $\vec{i}_{C_i}$ is close to being aligned with $\vec{j}_{B_i}$.

An additional reference frame is required for the calculation of the aerodynamic forces. This frame is based at aerodynamic reference location on the aircraft and is aligned with the local aerodynamic velocity. Taking into account the wind velocity expressed in the inertial frame $[\mathrm{w}_1, \mathrm{w}_2, \mathrm{w}_3]^T$, the aerodynamic velocity of the i^{th} aircraft is given by:

$$\begin{bmatrix} \tilde{u}_{ACi} \\ \tilde{v}_{ACi} \\ \tilde{w}_{ACi} \end{bmatrix} = \begin{bmatrix} u_{ACi} \\ v_{ACi} \\ w_{ACi} \end{bmatrix} + \mathbf{T}_{H\to B_i}\mathbf{T}_{B_i\to C_i} \begin{bmatrix} \mathrm{w}_1 \\ \mathrm{w}_2 \\ \mathrm{w}_3 \end{bmatrix} \tag{16}$$

This allows to representing the aerodynamic angles α and sideslip β defined, which are defined by:

$$\frac{\tilde{w}}{\tilde{u}} = \tan\alpha \tag{17}$$

$$\frac{\tilde{v}}{\sqrt{\tilde{u}^2 + \tilde{v}^2 + \tilde{w}^2}} = \sin\beta \tag{18}$$

4.3.5 Payload, Tethers and Individual Aircraft Dynamics

In the bottom section of the dynamic methodology shown in Figure 29 is where the dynamic equations are solved. The different components are modeled independently in their respective coordinate frames. The description of each model is described in the following subsections.

4.3.5.1 Individual Aircraft Modeling

As described in the idealized system definition, the aircraft are modeled as rigid bodies independent of each other, on which a tether tension is applied. The following subsection describes the aircraft modeling.

Aircraft Description The inspiration for the aircraft model is the Makani Wing 7 aircraft. This choice is motivated by the fact that other projects used this aircraft as the platform for the analysis of multiple tethered aircraft. The second motivating aspect is that this aircraft has been flown for airborne wind energy extraction. While the objective of the mission differs, some of its characteristics and core capabilities are the same: tailsitting VTOL, tethered operation and high lift coefficient wing. The assumptions on the aircraft geometry were generated in order to create a model of the aircraft are presented in Figure 32. The neutral point of the whole aircraft is located at the mid-chord, and the center of gravity is located at a quarter chord in front the neutral point.

Aerodynamic Forces and Moments As illustrated in the literature, there are many methods to calculate the aerodynamic forces and moments. For this model, there is a need for efficient calculation, while still representing the required level of

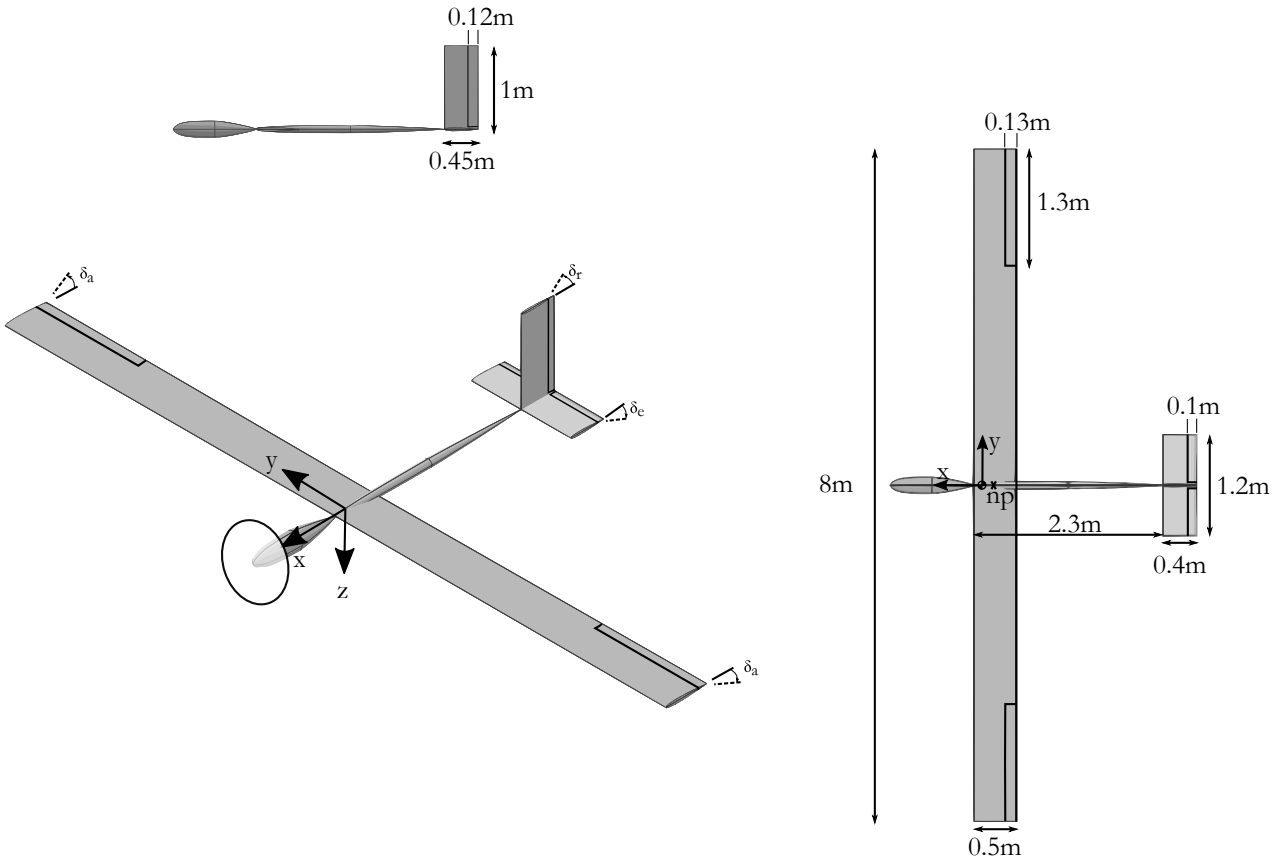

Figure 32: Geometric assumptions of the aircraft

modeling fidelity. As detailed in the dynamic model requirement, the model must include the contribution of the control deflection.

The selected method was the use of a vortex lattice method. An existing code was selected for its proven capabilities, AVL. A representation of the discretized geometry model is shown in Figure 35.

Since the dynamic environment requires multiple aerodynamic evaluations, the aerodynamic model needs to be computationally fast. Consequently, a regression model of the aerodynamic forces and moments of the aircraft has been generated for a range of operating conditions and control input. The regression model is based on neural network.

The aerodynamic forces and moments are represented as non-linear functions:

$$C_L = C_L(\alpha, \beta, \tilde{p}, \tilde{q}, \tilde{r}, \delta_e, \delta_r, \delta_a) \tag{19}$$

$$C_D = C_D(\alpha, \beta, \tilde{p}, \tilde{q}, \tilde{r}, \delta_e, \delta_r, \delta_a) \tag{20}$$

$$C_Y = C_Y(\alpha, \beta, \tilde{p}, \tilde{q}, \tilde{r}, \delta_e, \delta_r, \delta_a) \tag{21}$$

$$C_L = C_L(\alpha, \beta, \tilde{p}, \tilde{q}, \tilde{r}, \delta_e, \delta_r, \delta_a) \tag{22}$$

$$C_M = C_M(\alpha, \beta, \tilde{p}, \tilde{q}, \tilde{r}, \delta_e, \delta_r, \delta_a) \tag{23}$$

$$C_N = C_N(\alpha, \beta, \tilde{p}, \tilde{q}, \tilde{r}, \delta_e, \delta_r, \delta_a) \tag{24}$$

Where the angular rates are normalized quantity.

Moreover, because the maximum lift coefficient on the aircraft is of interest for the study of the maneuvers, the maximum lift coefficient of each surface is also modeled with a regression model.

$$max(C_l) = C_{l_{max}}(\alpha, \beta, \tilde{p}, \tilde{q}, \tilde{r}, \delta_e, \delta_r, \delta_a) \tag{25}$$

Additionally, in order to avoid extrapolation, a classifier function based on the input is used to ensure that the functions are within the sampled space.

Tether Forces and Moments The tether force vector acting on the aircraft is provided by the tether modeling module. For dynamic simulation of the aircraft, the resulting forces and moments from the tether acting on the aircraft are calculated at the center of gravity and are transformed in the body frame.

Propeller The choice of propeller type and geometry, as well as the method of analysis plays an important role in the performance of the system, as shown by Rancourt [79]. For this environment, the important characteristics are the contributions to the dynamics of the system. Since the aircraft have a significant high turn rate, the propeller assemblies can generate important moments on the aircraft. However, this effect can be mainly cancelled if an even number of counter-rotating propellers would be mounted on the aircraft, in which case, the main resulting action on the aircraft would be the thrust. In order to simplify the modeling requirements, the multiple propellers are represented as a single propeller assumed to be installed on the aircraft nose, and only the thrust calculation is included in the dynamics.

The proposed methodology is to generate a thrust coefficient curve as a function of advance ratio. The method includes generating a propeller geometry applicable to the nominal flight path, and generating the thrust coefficient by analyzing off-design operations of the propeller. The tool used for this task is the QMIL-QPROP, developed by Drela [32]. Both tools use an extension of the classical blade-element/vortex formulation. QMIL generates propeller for minimum induced losses, and QPROP subsequently analyzes the geometry.

The approximation of the thrust coefficient allows to calculate the thrust for the flight condition of interest :

$$T = C_T \frac{4}{\pi^2} \rho \omega^2 R^4 \tag{26}$$

Where the advance ratio is given by:

$$J = \frac{\pi V_T}{\omega R} \tag{27}$$

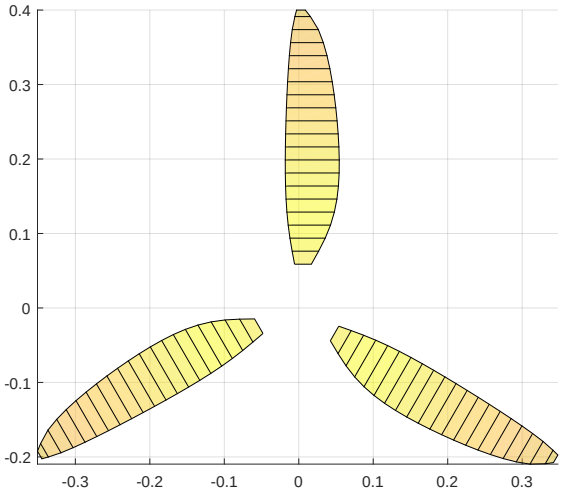

Figure 33: Propeller geometry

The velocity V_T is the velocity in the axis of the propeller. Since the propeller is assumed to be installed in the axis of the aircraft $V_T \simeq u$.

The propeller geometry developed is shown in Figure 33 and the propeller geometry is detailed in the Appendix B. The off-design characteristics of the propeller is shown in Figure 34.

Actuator dynamics The actuators have a limit on their actuation rate $\dot{u}_{i_{MAX}}$.

Kinematic and Equations of motion The aircraft motion is described by its position with respect to the inertial frame x, y and z, the velocity expressed in the body frame u, v and w, the body angles and the body angular rates p, q and r.

The equations of motion for the individual aircraft are the following. First in translation, the acceleration in the body frame is described as follow:

$$\dot{u} = rv - qw + \frac{X}{m} - g\sin\theta \tag{28}$$

$$\dot{v} = pw - ru + \frac{Y}{m} - g\cos\theta\sin\phi \tag{29}$$

$$\dot{w} = qu - pv + \frac{Z}{m} - g\cos\theta\cos\phi \tag{30}$$

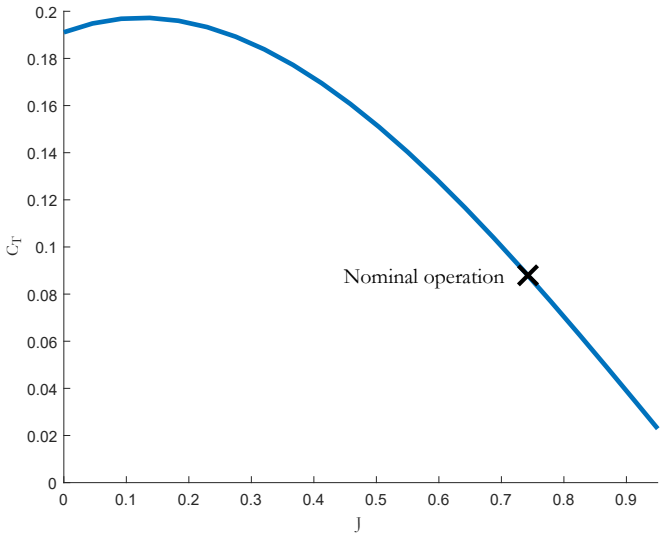

Figure 34: Propeller coefficient of thrust and advance ratio curve

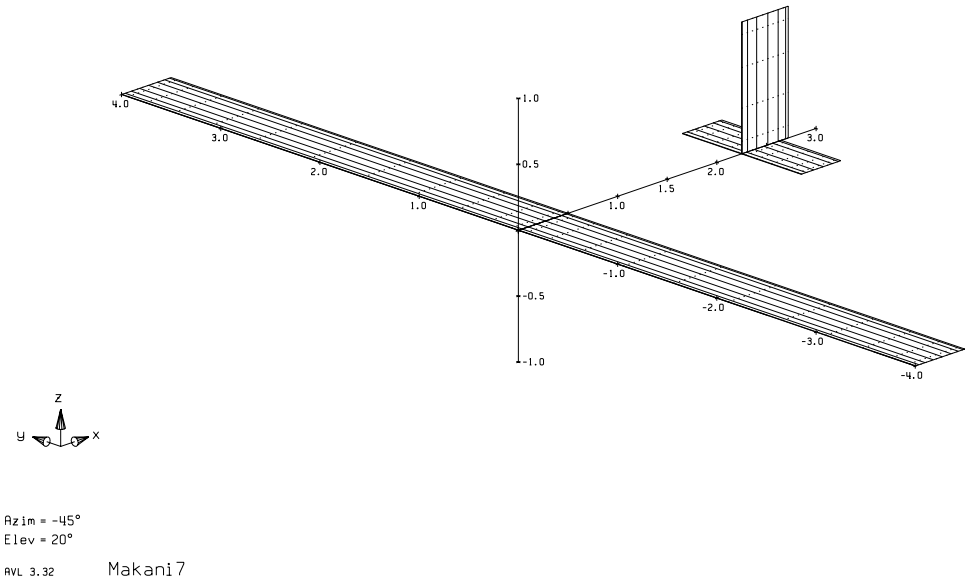

Figure 35: Illustration of the aerodynamic lifting surfaces in AVL

The rotational inertial of the aircraft about the center of gravity is evaluated with the help of openVSP. The various components have been assigned a portion of the mass: wing, tailboom, vertical stabilizer, horizontal stabilizer and fuselage pod. Assuming that the mass is distributed evenly in the volume of each component, the inertia matrix is evaluated numerically. Due to the symmetry about the x-z plane and due to the overall shoe of the aircraft, the off-diagonal components of the inertia matrix are very small, and are assumed as zero for simplicity. The inertia matrix is evaluated as:

$$\mathbf{I} = \begin{bmatrix} 161 & 0 & 0 \\ 0 & 42.7 & 0 \\ 0 & 0 & 202 \end{bmatrix} \tag{31}$$

The diagonal inertia matrix allows to formulate the rotational equations of motion as follows:

$$L = I_{xx}\dot{p} - (I_{yy} - Izz)qr \tag{32}$$

$$M = I_{yy}\dot{q} - (I_{zz} - Ixx)rp \tag{33}$$

$$N = I_{zz}\dot{r} - (I_{xx} - Iyy)pq \tag{34}$$

4.3.5.2 Payload

The payload is represented as a point mass. Consequently, there is no rotational dynamics to be included, and the payload carried frame is always aligned with the inertial reference frame. The states of the payload are the following:

$$\vec{x}_p = [x, y, z, \dot{x}, \dot{y}, \dot{z},]^T \tag{35}$$

The forces applied to the fuselage, X, Y, Z are composed of the gravitational force,

the tension of the three tethers, and aerodynamic force. The tension forces are generated by the tethers and are applied at the center of gravity of the payload.

The aerodynamic forces are applied on the fuselage, by using an equivalent flat plate drag area coefficient $\frac{D}{q}$.

$$\begin{bmatrix} X_{aero} \\ Y_{aero} \\ Z_{aero} \end{bmatrix} = -\frac{1}{2}\frac{D}{q}\rho\sqrt{\tilde{u}_p^2 + \tilde{v}_p^2 + \tilde{w}_p^2}\begin{bmatrix} \tilde{u}_p \\ \tilde{v}_p \\ \tilde{w}_p \end{bmatrix} \tag{36}$$

With $\tilde{u}_p$, $\tilde{v}_p$ and $\tilde{w}_p$ represents the components of the apparent velocity unit vector:

$$\begin{bmatrix} \tilde{u}_p \\ \tilde{v}_p \\ \tilde{w}_p \end{bmatrix} = \begin{bmatrix} u_p \\ v_p \\ w_p \end{bmatrix} + \begin{bmatrix} \mathrm{w}_1 \\ \mathrm{w}_2 \\ \mathrm{w}_3 \end{bmatrix} \tag{37}$$

The equations of motion of the payload are expressed in the inertial frame:

$$\ddot{x}_p = \frac{X}{m} \tag{38}$$

$$\ddot{y}_p = \frac{Y}{m} \tag{39}$$

$$\ddot{z}_p = \frac{Z}{m} - g \tag{40}$$

With X, Y and Z the sum of the forces acting in the $\vec{i}_h$, $\vec{j}_h$ and $\vec{k}_h$ direction, comprised of the tether tension and aerodynamic forces.

4.3.5.3 Tether

As described in the introduction section, the modeling environment will model the tether as a massless, rigid link between the payload and the aircraft. However, the modeling environment requires an elastic degree of freedom between the rigid bodies, that is subsequently removed during the system modeling.

During the initial modeling phase, the tether is modeled as having an initial length L. The elongation ϵ is calculated by:

$$\epsilon = \frac{|\tilde{L}| - L}{L} \tag{41}$$

The force vector is proportional to the elongation and is aligned with the axis of the tether with k being the axial spring constant of the tether.

$$F = k\epsilon \tag{42}$$

It is important to note that because the elastic degree of freedom is removed subsequently, the choice of k is more related to the stability of the computation than the actual physical representation of the cable.

This simple tether model has an important and unfortunate pitfall: if the tether were to go slack, a compressing force would be induced in the tether, which is not representative of the physics. Consequently, checks on the simulation process will have to be introduced so that a tether slack cannot happen. As mentioned previously, a slack in the tether would be an undesirable condition for the operation of the system as well.

4.3.6 Kinematic Conversion of Aircraft Motion

The objective of this module is twofold:

- Convert the states of the aircraft from the spherical coordinates around the payload to the vehicle carried frame in order to solve equations of motion of the aircraft;

- Convert the derivatives of the states of the aircraft from the vehicle carried frame to the derivatives of the states expressed in the spherical coordinates.

4.3.6.1 Aircraft states conversion

The objective is to transform the states describing the motion of the aircraft based on the geometry of the tether, ξ, ϵ, to the states typical to an aerospace vehicle: position expressed in the inertial frame and velocity expressed in the body frame. During this step, the fuselage states remain unchanged.

The position of the aircraft center of gravity with respect to the inertial frame is expressed by:

$$\vec{r}^{I}_{0\to D} = \vec{r}^{I}_{0\to P} + \vec{r}^{I}_{P\to A} + \vec{r}^{I}_{A\to D} \tag{43}$$

With

$$\vec{r}^{I}_{O\to P} = \begin{bmatrix} x_p \\ y_p \\ z_p \end{bmatrix} \tag{44}$$

$$\vec{r}^{I}_{P\to A} = L(1+\epsilon) \begin{bmatrix} \cos\xi_i \cos\zeta_i \\ \sin\xi_i \cos\zeta_i \\ \sin\zeta_i \end{bmatrix} \tag{45}$$

The vector between the aircraft attachment point and the aircraft center of gravity involves rotation between the reference frames:

$$\vec{r}^{I}_{A\to D} = \mathbf{T}_{C\to B}\mathbf{T}_{B\to H}\vec{r}^{C}_{A\to D} \tag{46}$$

With $\mathbf{T}_{B\to H}$ and $\mathbf{T}_{C\to B}$ the inverse of the matrices described in Equations 13 and 14.

The location of the attachment point A_i with respect to the aircraft cg, or point D, is defined in the body frame of the aircraft:

$$\vec{r}^{C}_{A\to D} = \begin{bmatrix} x_{A\to D} \\ y_{A\to D} \\ z_{A\to D} \end{bmatrix} \tag{47}$$

The velocity of the cg of each aircraft in its body frame is expressed by:

$$\vec{V}^{C}_{D} = (\mathbf{T}_{C\to B}\mathbf{T}_{B\to H})^{-1}\frac{d}{dt}\vec{r}^{I}_{0\to D} \tag{48}$$

Propagating time derivative on (48), the aircraft velocity expressed in the body frame is the following:

$$\begin{bmatrix} u \\ v \\ w \end{bmatrix} = (\mathbf{T}_{C\to B}\mathbf{T}_{B\to H})^{-1}\Bigg(\begin{bmatrix} \dot{x}_p \\ \dot{y}_p \\ \dot{z}_p \end{bmatrix} + \begin{bmatrix} Lc_\xi c_\zeta & -L(1+\epsilon)s_\xi c_\zeta & -L(1+\epsilon)c_\xi s\zeta \\ Ls_\xi c_\zeta & L(1+\epsilon)c_\xi c_\zeta & -L(1+\epsilon)s_\xi s_\zeta \\ Ls_\zeta & 0 & L(1+\epsilon)c_\zeta \end{bmatrix} \begin{bmatrix} \dot{\epsilon} \\ \dot{\xi} \\ \dot{\zeta} \end{bmatrix} + \frac{d}{dt}(\mathbf{T}_{C\to B}\mathbf{T}_{B\to H}) \begin{bmatrix} x_{A\to D} \\ y_{A\to D} \\ z_{A\to D} \end{bmatrix} \Bigg) \tag{49}$$

4.3.6.2 Aircraft state derivatives kinematic conversion

Once the aircraft and the payload state derivatives are calculated independently, the aircraft state derivatives initially calculated in the body frame need to be converted to the spherical-like coordinates.

Propagating time derivative on (49), and isolating the second derivatives of ξ, ζ, ϵ, the conversion can be expressed by:

$$
\begin{aligned}
\begin{bmatrix} \ddot{\epsilon} \\ \ddot{\xi} \\ \ddot{\zeta} \end{bmatrix} = & \begin{bmatrix} Lc_\xi c_\zeta & -L(1+\epsilon)s_\xi c_\zeta & -L(1+\epsilon)c_\xi s\zeta \\ Ls_\xi c_\zeta & L(1+\epsilon)c_\xi c_\zeta & -L(1+\epsilon)s_\xi s_\zeta \\ Ls_\zeta & 0 & L(1+\epsilon)c_\zeta \end{bmatrix}^{-1} \\
& \left(-\frac{d}{dt} \begin{bmatrix} Lc_\xi c_\zeta & -L(1+\epsilon)s_\xi c_\zeta & -L(1+\epsilon)c_\xi s\zeta \\ Ls_\xi c_\zeta & L(1+\epsilon)c_\xi c_\zeta & -L(1+\epsilon)s_\xi s_\zeta \\ Ls_\zeta & 0 & L(1+\epsilon)c_\zeta \end{bmatrix} \begin{bmatrix} \dot{\epsilon} \\ \dot{\xi} \\ \dot{\zeta} \end{bmatrix} \right. \\
& + \frac{d}{dt}(\mathbf{T}_{C\to B}\mathbf{T}_{B\to H}) \begin{bmatrix} u \\ v \\ w \end{bmatrix} + (\mathbf{T}_{C\to B}\mathbf{T}_{B\to H}) \begin{bmatrix} \dot{u} \\ \dot{v} \\ \dot{w} \end{bmatrix} - \begin{bmatrix} \ddot{x}_p \\ \ddot{y}_p \\ \ddot{z}_p \end{bmatrix} \\
& \left. - \frac{d^2}{dt^2}(\mathbf{T}_{C\to B}\mathbf{T}_{B\to H}) \begin{bmatrix} x_{A\to D} \\ y_{A\to D} \\ z_{A\to D} \end{bmatrix} \right)
\end{aligned} \tag{50}
$$

The components of Equation (50) can be found in Appendix C. With Equations (48) and (50), the conversion between the different frames is completed.

4.3.6.3 Removing the elastic degree of freedom through singular perturbation method

As mentioned previously, there is a need to remove the tether elastic degree of freedom: while the elastic degree of freedom was required to simulate the motion of the multiple bodies independently, it is also important for this research that the elastic degree of freedom be removed.

For this step, the method used is the singular perturbation method. This method consists of assuming a linear representation of the motion around a condition of interest, and removing specific degrees of freedom [11, 60, 61]. This process is carried out at every step of the simulation.

For the condition of interest, a linear approximation of the dynamics of the form

$\dot{\bar{x}} = A\bar{x} + f$ is generated, where $\bar{x}$ represents the perturbation about the condition of interest. At the beginning of the simulation step, $\bar{x} = 0$.

The state vector is rearranged to regroup the states to keep $\bar{x}_1$ and the states to eliminate, $\bar{x}_2$ together. In this case, the states to remove are the following:

$$\bar{x}_2 = [\epsilon_{t1}, \dot{\epsilon}_{t1}, \epsilon_{t2}, \dot{\epsilon}_{t2}\epsilon_{t3}, \dot{\epsilon}_{t3}]^T \tag{51}$$

The linear dynamics representation about $\bar{x}$ becomes:

$$\begin{bmatrix} \dot{\bar{x}}_1 \\ \hdashline \dot{\bar{x}}_2 \end{bmatrix} = \begin{bmatrix} A_{11} & A_{12} \\ \hdashline A_{21} & A_{22} \end{bmatrix} \begin{bmatrix} \bar{x}_1 \\ \hdashline \bar{x}_2 \end{bmatrix} + \begin{bmatrix} f_1 \\ \hdashline f_2 \end{bmatrix} \tag{52}$$

Where f represents the current values of $\dot{\bar{x}}$, given that $\bar{x} = 0$.

By suppressing the dynamics the blocked degrees of freedom, $\dot{\bar{x}}_2 = 0$, substitution allows to find:

$$\bar{x}_2 = A_{22}^{-1} f_2 \tag{53}$$

The dynamics of the states of interest $\dot{\bar{x}}_1$ becomes:

$$\dot{\bar{x}}_1 = A_{11}\bar{x}_1 + A_{12}A_{22}^{-1} f_2 + f_1 \tag{54}$$

This effectively represents a reduced order dynamic model which has the following degrees of freedom:

- 3 fuselage positions x_p, y_p, z_p and 3 fuselage velocities $\dot{x}_p, \dot{y}_p, \dot{z}_p$;
- Each tether has 2 angular states described by the spherical angles of ζ, ξ and the associated angular rates $\dot{\zeta}$ and $\dot{\xi}$;
- Each aircraft has 3 angular states ϕ, θ, ψ with respect to the inertial frame, and three angular rates p, q, r in their body frame.

The system has the following control input:

- One propeller angular velocity (RPM) per aircraft;
- One elevator deflection per aircraft;
- One rudder deflection per aircraft;
- And one differential aileron deflection per aircraft.

For a total of 36 states, and 12 control input. This model fulfills the requirements of the model as described in the idealization section.

4.3.7 Multi-Blade Coordinates

The dynamic of the system is being expressed in different reference frames: the payload states are expressed in the inertial frame, while the motion of the different aircraft is expressed in their respective frames, which are rotating around the payload. The nature of this problem poses the following two challenges: the analysis of the dynamics of the system requires taking into account the rotation of the aircraft, and each aircraft state's contribution to the dynamics is diluted by the contribution of the other coupled aircraft.

The problem that stems from the interaction between the fix and rotating reference frames is illustrated by the following example: if a single aircraft was tethered to the ground, it represents a steady state motion around equilibrium. Classical analysis tools can be applied for the analysis of the system. However, if a steady wind was coming from the North, its impact on the aircraft dynamics would depend on the aircraft azimuthal position, and might be approximated by a periodic response with pulsation Ω. Similarly, if a load cell was placed between the lower extremity of the tether and the ground, the tether tension force in the x or y direction is dependent on the aircraft states and control input in a periodic fashion. For the analysis of aircraft

tethered to a shared payload, the aircraft have a periodic impact on the dynamics of the payload states $x, y, \dot{x}, \dot{y}$. This periodicity has to be accounted for in the analysis.

Second, the aircraft states are more meaningful if they are expressed together. Am example arise from the study of the impact of a wind gust on the system. If a wind gust were to be applied on the system, the individual aircraft response is hard to interpret. However, the study of the overall, coupled response of the 3 aircraft, seems more insight-full. For example, does the disk on which the aircraft fly tilt towards or away from the gust?

Multi-blade coordinates have been used to address both of these limitations. This method has been widely used in the fields of rotorcraft and wind turbines, for many applications, including dynamic analysis and controls. [15,16,48,53,55,74,75,88,108].

In order to transform the dynamics equations from the rotating frame to a fixed frame, the multi-blade coordinate transformation is used. In the process, a new set of coordinates is created. The coordinates in the rotating frame, used up to this point, are the individual blade coordinates, IBC. The coordinates in the fixed frames are the multi-blade coordinates, MBC.

The degree of freedom of the i^{th} aircraft is q_i in the IBC. For a system with N aircraft, the new degrees of freedom in the nonrotating frame are the following:

$$q_0 = \frac{1}{N}\sum_{i=1}^{N} q_i \tag{55}$$

$$q_{od} = \frac{2}{N}\sum_{i=1}^{N} (-1)^i q_i \tag{56}$$

$$q_{jc} = \frac{2}{N}\sum_{i=1}^{N} q_i \cos j\Psi_i \tag{57}$$

$$q_{js} = \frac{2}{N}\sum_{i=1}^{N} q_i \sin j\Psi_i \tag{58}$$

In which q_{od} exists only for an even number of aircraft.

The inverse transformation can be applied to retrieve the IBC for the k^{th} aircraft:

$$q_k = q_0 + q_{od}(-1)^k + \sum_{j=1}^{J} q_{jc} \cos j\Psi_k + \sum_{j=1}^{J} q_{js} \sin j\Psi_k \tag{59}$$

For rotorcraft analysis, the MBC associated with the flapping degree of freedom β are very useful in the analysis of the rotor response. β_0, referred to as coning, illustrates the average flapping angle of the rotor blade. β_{od}, the differential coning, expresses the difference in coning between blades 1, 3 and blades 2 and 4. $\beta_1 c$ is longitudinal disk tilt, or fore-aft tilt and $\beta_1 s$ is the lateral disk tilt.

Johnson, in the description of the MBC for the analysis of helicopter rotors commented the following [55]:

> The use of multi-blade coordinates is crucial for problems involving the rotor motion coupled with the fixed frame, such as hub motion, swash plate control, or dynamic inflow. MBC are a physically relevant, non-rotating frame representation of the rotor motion; for example, coning and tip-path-plane tilt for blade flapping. Consequently, introduction of MBC separates the coupling of the rotor and fixed frame into subsets and, most importantly eliminates periodic coefficients (except for two-bladed rotors). MBC also reduce the periodicity of the equations resulting from edgewise flight aerodynamics.

In this passage, Johnson illustrated the usefulness of the MBC in the treatment of the interaction between the fixed and the rotating degrees of freedom.

For the case of interest, there are 3 aircraft, so q_{od} will not be used. In order to keep the same number of degrees of freedom in the MBC as in the IBC, the cos and sin expansion will only be performed for the case of $j = 1$. The aircraft IBC q_{ac1}, q_{ac2}, q_{ac3}, will be represented in MBC with q_0, q_c and q_s.

In order to study the present system with the multi-blade coordinates, the concept of *virtual hub* is introduced, as shown in Figure 36. For the purpose of analysis, a

three-arm hub is included in the model. The arms are separated by 180°, and are turning at a constant rate of Ω, such that their angular position in the reference frame (H) with respect to the z-axis are:

$$\Psi_1 = \Psi = \Omega t \tag{60}$$

$$\Psi_2 = \Psi + 120^\circ \tag{61}$$

$$\Psi_3 = \Psi + 240^\circ \tag{62}$$

This virtual hub allows to represent the azimuthal position of the aircraft ξ_i as a differential value from the virtual hub. This concept is analogous to the lead-lag motion of conventional helicopter blades. This differential value, represented by $\overline{\xi}_i$ is expressed by:

$$\overline{\xi}_i = \xi_i - \Psi_i \tag{63}$$

The same concept is applied to the aircraft body angle ψ: The angle $\overline{\psi}_i$ represents the variation from the body angle if the aircraft would have been turning at a constant rate Ω. The initial value at time 0, $\psi_i(t_0)$, is not necessarily 0 as per the trim definition. Finally, for the convention chosen, $\dot{\Omega} > 0$ and $\dot{\psi} < 0$, which leads to the following definition:

$$\overline{\psi}_i = \psi_i - \psi_i(t_0) + \Psi_i \tag{64}$$

The aircraft degrees of freedom were initially expressed in IBC:

$$\vec{q}_{IBC} = [\zeta_1, \zeta_2, \zeta_3, \overline{\xi_1}, \overline{\xi_2}, \overline{\xi_3}, \phi_1, \phi_2, \phi_3, \theta_1, \theta_2, \theta_3, \overline{\psi_1}, \overline{\psi_2}, \overline{\psi_3}]^T \tag{65}$$

With the transformation previously described, the degrees of freedom are converted the nonrotating frame:

$$\vec{q}_{NR} = [\zeta_0, \zeta_c, \zeta_s, \xi_0, \xi_c, \xi_s, \phi_0, \phi_c, \phi_s, \theta_0, \theta_c, \theta_s, \psi_0, \psi_c, \psi_s]^T \tag{66}$$

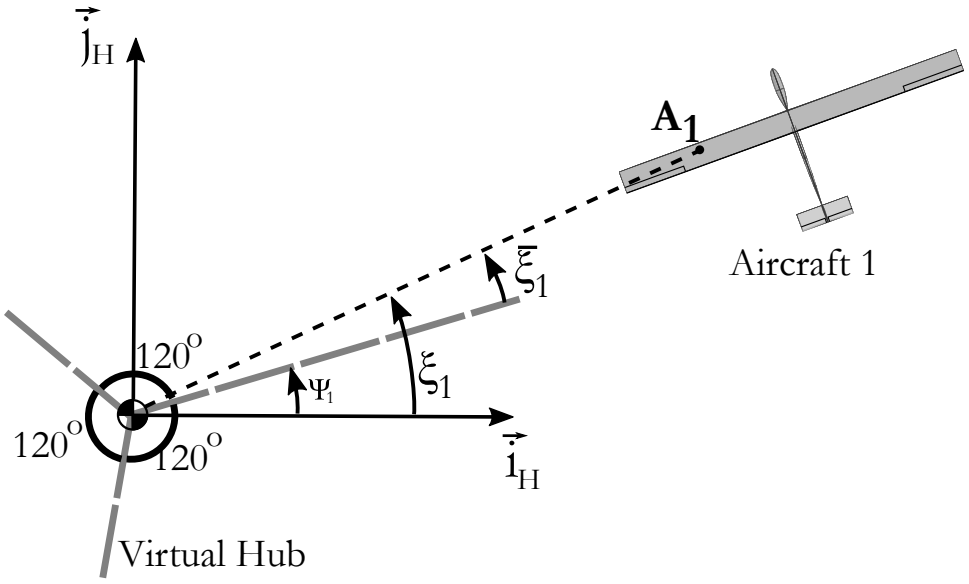

Figure 36: Top view of aircraft 1 and the virtual hub.

The state vector includes the degree of freedom and their derivatives:

$$\vec{x} = \begin{bmatrix} \vec{q} \\ \cdots \\ \dot{\vec{q}} \end{bmatrix} \tag{67}$$

The payload states however, remain unchanged as they are already expressed in the nonrotating frame:

$$\vec{x}_p = [x_p, y_p, z_p, \dot{x}_p, \dot{y}_p, \dot{z}_p]^T \tag{68}$$

The control input of the aircraft can be converted in a similar fashion. Initially, the control input vector illustrated the control input of the individual aircraft:

$$\delta_{IBC} = [\delta_{r1}, \delta_{r2}, \delta_{r3}, \delta_{e1}, \delta_{e2}, \delta_{e3}, \delta_{a1}, \delta_{a2}, \delta_{a3}, \delta_{t1}, \delta_{t2}, \delta_{t3}]^T \tag{69}$$

Equation 55 to 58 and 59 allow the conversion to a set of control input in the nonrotating frame.

$$\delta_{NR} = [\delta_{r0}, \delta_{rc}, \delta_{rs}, \delta_{e0}, \delta_{ec}, \delta_{es}, \delta_{a0}, \delta_{ac}, \delta_{as}, \delta_{t0}, \delta_{tc}, \delta_{ts}]^T \tag{70}$$

The control input δ_0 corresponds to an averaged change of control input for the three aircraft and δ_c ans δ_s corresponds to cyclic variation of control input along Ω.

This is analogous to how the control of the helicopter blade pitch is expressed as cyclic and collective input.

4.3.7.1 Dynamic Approximation in MBC

It is possible to generate an approximate model of the dynamics in MBC given an approximate model of the dynamic model of the system in IBC. The following subsection is based on the work or Bir [16].

The model of the dynamics in IBC is the following:

$$\dot{x} = Ax + Bu + B_d w \tag{71}$$

$$y = Cx + Du + D_d w \tag{72}$$

The state-space representation of the dynamics in MBC is the following:

$$\dot{x}_{nr} = A_{nr} x_{nr} + B_{nr} u_{nr} + B_{dnr} w \tag{73}$$

$$y_{nr} = C_{nr} x_{nr} + D_{nr} u_{nr} + D_{dnr} w \tag{74}$$

The differences matrices A, B,B_d C, D and D_d are approximate by unit perturbation method in the IBC. Transformations are applied to the matrices describing the IBC system and the MBC system is generated. The process is the following. The definition of the transformation matrices T_x can be found in Bir [16].

$$A_{NR} = \left[\begin{array}{c|c} T^{-1} & 0 \\ \hline 0 & T^{-1} \end{array}\right] \left\{ A \left[\begin{array}{c|c} T_1 & 0 \\ \hline \Omega T_2 & T_1 \end{array}\right] - \left[\begin{array}{c|c} \Omega T_2 & 0 \\ \hline \Omega^2 T_3 & 2\Omega T_2 \end{array}\right] \right\} \tag{75}$$

$$B_{NR} = \left[\begin{array}{c|c} T^{-1} & 0 \\ \hline 0 & T^{-1} \end{array}\right] B T_{1c} \tag{76}$$

$$C_{NR} = T_{10}^{-1} \left[\begin{array}{c|c} C_1 T_1 + \Omega C_2 T_2 & C_2 T_1 \end{array}\right] B T_{1c} \tag{77}$$

$$D_{NR} = T_{10}^{-1} D T_{1c} \tag{78}$$

The equations developed allow to study systems with variable angular velocity. In the analysis of the multiple aircraft tethered to a shared payload, the simultaneous acceleration of the aircraft with respect to the initial velocity can be included as $\dot{\Omega}$, or as $\dot{\xi}$. For the current implementation, the equivalent *hub angular velocity*, Ω, is assumed constant, and the acceleration of the aircraft on their path is represented by $\dot{\xi}$, a collective lead-lag motion.

In order to limit the contribution of possible nonlinear components, the MBC creation process defined in Equations 75 - 78 is performed for multiple azimuthal positions and the average matrices are used.

4.3.8 Trim

As described in the previous sections, the equations of motion are governed by a series of non-linear equations. Trim consists of finding the control inputs and the states that minimize the residuals of those equations for a prescribed flight condition. The solution of the trim routine allows to study the flight condition of interest by performing dynamic approximations around it for example, as well as initiating a simulation by providing the initial condition.

For the specific cases of this study, trim will be performed around hover, for which the aircraft fly over a circular flight path above the payload at a constant velocity. Moreover, because the flight parameters are prescribed, these will be imposed as part of a constraint on the trim routine.

The system states and control input can be decomposed as follows: the payload has 6 states, and each aircraft (3 aircraft total) has 10 states and 4 control input, for a total of 48 unknown. In counterparts, there are 18 equations of motion.

The following simplifications and constraints are applied to the problem:

- The aircraft states and control input will be the same, with only a rotational symmetry through an azimuthal separation of 120°. Consequently, the problem

is comprised of 20 unknowns: 6 payload states, 10 aircraft states and 4 control input. Only 8 equations of motion are left.

- Because rotational symmetry is applied and the hover simulation is sought after, the payload states x, $\dot{x}$, y and $\dot{x}$ must be assumed as zero, along with the 2 equations of motion associated. There are only 2 payload states left, 10 aircraft states and 6 equations of motion.

- The payload altitude is selected as a design variable for the altitude of the system. There are only 1 payload states left, 10 aircraft states, 4 control input and 6 equations of motion.

- The azimuthal position of the aircraft is irrelevant for the trim, and can be selected arbitrarily between 0° and 360°. There are only 1 payload states left, 9 aircraft states, 4 control input and 6 equations of motion.

- In hover with steady banked turn, some states are assumed as zero. This is the case of the payload vertical velocity $\dot{z}$ and the tether elevation rate. There are no payload states left, 8 aircraft states, 4 control input and 6 equations of motion.

- The flight path parameters are imposed for the trim problem: The aircraft azimuthal state derivative and the tether elevation are imposed. There are no payload states left, 6 aircraft states, 4 control input and 6 equations of motion.

Additional constraints are applied on the system in hover. The kinematic relationships between the aircraft angular rates in the body reference frame and in the inertial frame need to be respected. This constitutes an additional set of 3 equations.

The problem has 9 equations and 10 unknowns: the aircraft angles (3), the aircraft angular rates (3), the 4 control inputs. This constitutes an unconstrained problem.

Previous methods have been proposed to solve this unconstrained problem. Rancourt [77] in his work imposed no side slip $\beta = 0$ as an extra constraint on the trim solution. This represents a viable alternative when an aircraft is modeled as a wing alone. However, for an aircraft with multiple lifting surfaces in a tight turn, having no sideslip at a point of interest (for example aircraft center of gravity, tether attachment point or aerodynamic center) might introduce a large horizontal component of apparent wind on the tail due to the angular velocity of the aircraft. Similarly, imposing no apparent wind on the tail might introduce an unnecessary constraint that can lead to extreme control input to compensate.

This problem appears as well in the system with more actuation surfaces than required to maintain equilibrium, such as a blended wing body aircraft with distributed trailing edge control surfaces. Garmendia [42, 43] in his work proposed alternative strategies to solution this problem: control allocation and drag minimization.

The objective of the environment is not to find the minimum operating power, but to evaluate disturbance rejection. Consequently, the additional degree of freedom will be used to maximize the margin with respect to the various constraints that could be potentially violated during a maneuver.

A limit on the sideslip angle is also included on the as as side constraint in order to avoid exploring unrealistic flight condition, as well as limiting the unnecessary drag penalty due to high slideslip conditions.

The trim problem is posed as the following optimization problem:

Maximize:	Actuation and lift coefficient margins
Given:	Flight path parameters
With Respect to:	θ, ϕ, ψ , p, q, r, δ_r, δ_e, δ_a, δ_t
Subject to:	$[\ddot{z_p}, \ddot{\zeta}, \ddot{\xi}, \dot{p}, \dot{q}, \dot{r},] = 0$
	$\vec{R}_K = 0$
	$Cl_i \leq Cl_{max}$, $\delta_i \leq \delta_{max_i}$, $\beta \leq \beta max$

Where $\vec{R}_K$, the kinematic residual, is the error between a constant body rotation about the hub z-axis equal to the flight path angular velocity $\dot{\xi}$. The components of the residual vector are calculated from the following equation:

$$\begin{bmatrix} p \\ q \\ r \end{bmatrix} = \begin{bmatrix} 1 & 0 & -s_\theta \\ 0 & c_\phi & s_\phi c_\theta \\ 0 & s_\phi & c_\phi c_\theta \end{bmatrix} \begin{bmatrix} \dot{\phi} \\ \dot{\theta} \\ \dot{\psi} \end{bmatrix} \tag{79}$$

with:

$$\begin{bmatrix} \dot{\phi} \\ \dot{\theta} \\ \dot{\psi} \end{bmatrix} = \begin{bmatrix} 0 \\ 0 \\ -\dot{\xi} \end{bmatrix} \tag{80}$$

4.3.9 Single Aircraft Model

As discussed in the description of the methodology, the use of a dynamic model including a single aircraft tied to the ground has the advantages of having fewer states and presenting simpler dynamics. Consequently, a dynamic model representing this configuration is derived.

The dynamic equations are formulated using the same dynamic modeling environment. However, the kinematic conversation is a simplification of the large problem, as there is no motion of the payload.

The states of this model are the following:

$$\vec{x}_{1AC} = [\zeta, \xi, \phi, \theta, \psi, \dot{\zeta}, \dot{\xi}, p, q, r]^T \tag{81}$$

Trimming the single aircraft model is also a variation on the trim problem of the three aircraft system. The main difference lies in the fact that the payload states are not included in the routine, as they are not present in the dynamic model. Instead, a target tether tension is included in the formulation: The vertical component of the tether tension must be the one third of the payload weight.

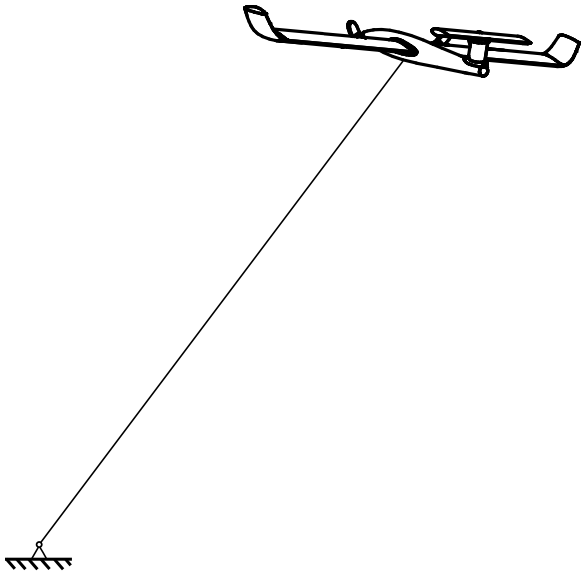

Figure 37: Single aircraft model

The trim problem is posed as the following optimization problem:

Maximize:	Actuation and lift coefficient margins
Given:	Flight path parameters
With Respect to:	θ, ϕ, ψ , p, q, r, δ_r, δ_e, δ_a, δ_t
Subject to:	$T_z = \frac{m_{pay}g}{3}$, $[\ddot{\zeta}, \ddot{\xi}, \dot{p}, \dot{q}, \ddot{r}, \ddot{\psi}] = 0$
	$\vec{R}_K = 0$
	$Cl_i \leq Cl_{max}$, $\delta_i \leq \delta_{max_i}$, $\beta \leq \beta max_i$

4.4 Trim-Constrained Optimization

4.4.1 Introduction

In the section 4.3.9, a method was suggested to trim a given configuration in order to find a set of states and control input that lead to quasi-steady-state equilibrium. However, the ability to trim a configuration or not can also be used to provide information about the design. The following section will recast the trimming problem in order to find constraints on some design parameters. The first variable of interest is the tether attachment location on the aircraft. The simplest approach is to

generate a grid of points on which to evaluate whether trim can be achieved within constraints limits. However, even if this approach is simple, identifying the boundary might require many function calls. Moreover, this approach does not give insight as for which constraint would define a given boundary. Consequently, an optimization-based approach is proposed. The algorithm will answer the question: what is the spatial boundary that defines whether the attachment location will lead to a feasible steady state trim condition that does not violate the constraints?

It is important to note that within that trim-defined feasible space, there is still a need to trim the vehicle before starting a simulation, or linearizing the equations of motion for example, by using the trim method of section 4.3.9.

4.4.2 Optimization Based Boundary Definition

Finding the limit of the attachment location is posed as an optimization problem as follows: given an initial feasible attachment point, how far is trim still feasible? If this problem is solved for many search directions, a 2-D or 3-D boundary can be found. This optimization approach is similar to an Epsilon-Constraint Method in the cylindrical coordinates [47].

The first step involves finding an initial feasible attachment location, represented by x_0, y_0, z_0. While many points are adequate, evaluating the attachment point at aircraft center of gravity is deemed a good option.

The second step is to define a search direction θ. The domain is discretized in a series of azimuthal search directions θ_i.

Finally, the maximum distance s from the origin x_0, y_0, z_0 is found using a numerical optimizer. The Matlab-based SQP is used for this application.

The optimization problem formalized as follows:

Maximize:	s
Given:	x_0, y_0, z_0, θ
With Respect to:	s, θ, ϕ, ψ , p, q, r, δ_r, δ_e, δ_a, δ_t
Subject to:	$s \geq 0$
	$T_z = \frac{m_{pay}g}{3}$, $[\ddot{\zeta}, \ddot{\xi}, \dot{p}, \dot{q}, \ddot{r}, \ddot{\psi}] = 0$
	$\vec{R}_K = 0$
	$C_{l_i} \leq C_{l_{max}}$, $\delta_i \leq \delta_{max_i}$, $\beta \leq \beta max_i$

The solution along each search direction gives a radial distance s, as well as it returns which constraints are active on the boundary. This process is repeated along multiple search directions, which generates a 2-D or 3-D surface.

4.5 Open-Loop Dynamic Characteristics

As presented in the literature, dynamic characteristics play an important role in the design of aerospace systems. However, when using unmanned aircraft, the typical assumptions linked to open-loop dynamics of piloted aircraft do not apply as a requirement. Consequently, there is a need to define a criteria to evaluate dynamics behavior of a configuration.

The criteria is based on the observations made on the canonical problem. The three aircraft problem presents very different dynamics, and many more states when compared to the two aircraft, in-plane model. However, the canonical problem showed that some key characteristics are present that can potentially be applied on the full system. Based on the observation about spectral separation between the aircraft modes and the suspended mass modes, the following hypothesis is formulated.

The system presents multiple degrees of freedom, and defining a dynamic requirement for each axis is a daunting task. Moreover, without knowledge of the actual control and sensing architecture, imposing an open-loop requirement on each axis becomes arbitrary.

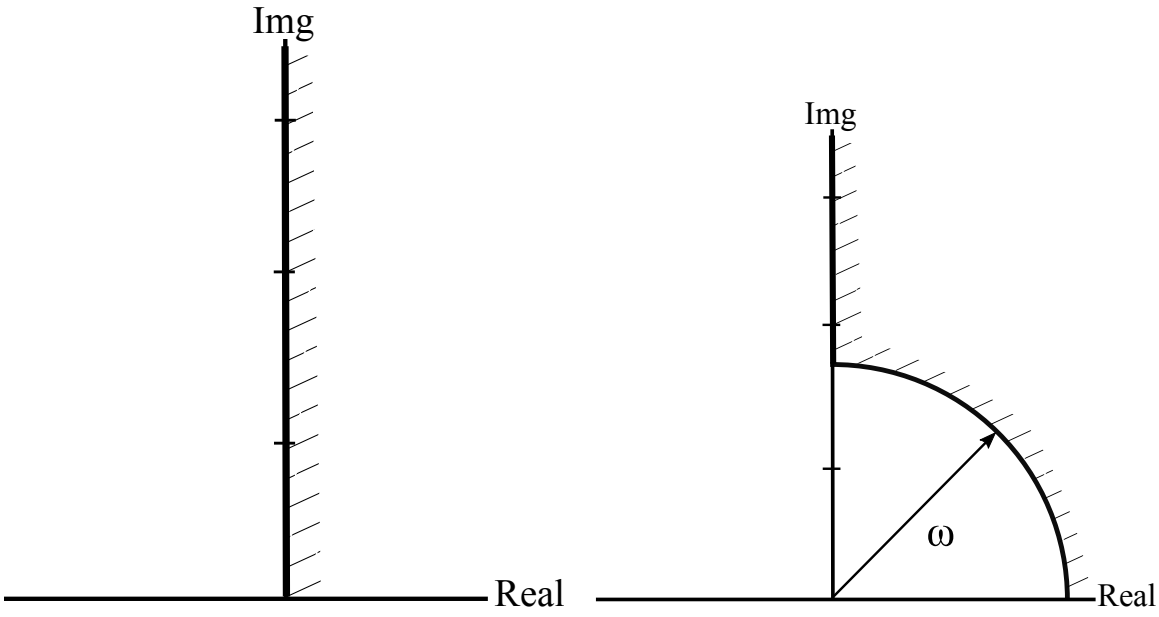

Figure 38: Open-loop requirement: constraint on the pole placement of the aircraft modes (left) and on the system overall modes (right).

Based on the observation about spectral separation between the aircraft modes and the suspended mass modes, the following hypothesis is formulated.

Hypothesis: *The system will have multiple modes unique to the multi-aircraft tethered system with spectral separation between the payload motion (low-frequency) governed modes and the aircraft motion (high-frequency) governed modes.*

Based on this hypothesis, the open-loop requirements are formulated as constraints on the location of the poles of the linear approximation of the dynamic system, illustrated in Figure 38.

- The aircraft-governed modes must stable;
- The other modes must either be stable or have a fundamental frequency slower than the angular velocity of the aircraft.

4.6 Constant Wind Trim Constraint

The last criterion for the assessment of a configuration feasibility is the steady-wind operation. The objective is to assess whether the configuration can operate at a given wind condition while respecting the feasibility related criterion.

The formulation of the advancing flight trim constraint will include

4.6.1 Pseudo-Trim in Steady-Wind Operation

The tools detailed of the previous sections allows to create a linear model of the dynamics in the MBC, about the circular hover trim condition, with no wind:

$$\dot{x}_{nr} = A_{nr}\tilde{x_{nr}} + B_{u_{nr}}\tilde{u_{nr}} + B_{w_{nr}}w \tag{82}$$

$$\tilde{y}_{nr} = C_{nr}\tilde{x_{nr}} + D_{u_{nr}}\tilde{u_{nr}} + D_{w_{nr}}w \tag{83}$$

Where variables marked with a *tilde* are the deviations from circular hover trim conditions z_t. Since the linear model is performed around trim, the physical states (x), control input(u) and output(y) of the system are a sum of this solution and the trim conditions:

$$\begin{bmatrix} z_0 \\ z_c \\ z_s \end{bmatrix} = \begin{bmatrix} z_t \\ - \\ - \end{bmatrix} + \begin{bmatrix} \tilde{z_0} \\ \tilde{z_c} \\ \tilde{z_s} \end{bmatrix} \tag{84}$$

It is important to note that the trim in circular hover only led to non-zero z_0 components expressed in MBC, as there were no cyclic variations, as per the definition of the previously defined trim problem.

Finding the trim condition includes finding the states and control input that lead to no acceleration, $\ddot{x}_{nr} = 0$.

Because the state vector x_{nr} includes the states and their derivatives $x = [q, \dot{q}]^T$, all the velocity states are imposed as zero, $\dot{q} = 0$.

Additionally, some of the position states were imposed as being zeros. This is the case of the payload position x, y and z. Moreover, because the state variables ξ_0 and the aircraft angle about the axis z, ψ can represent together a rigid body motion of the system, the state variable ξ_0 is imposed as zero.

Finally, in order to keep the configurations similar to their nominal operating condition, the averaged coning angle ζ_0 is imposed as zeros.

4.6.2 Constraints

Additional constraints are imposed to ensure that the condition is feasible. These include maximum and minimum limits on actuators and on output, as well as on the aerodynamic coefficients.

The variation value for one of the time marching actuation deflection will be of the form :

$$z(\Psi) = z_0 + z_c \cos(\Psi) + z_c \cos(\Psi) \tag{85}$$

The maximum and minimum of this function are :

$$z_{max} = z_0 + \sqrt{z_c^2 + z_s^2} \tag{86}$$

$$z_{min} = z_0 - \sqrt{z_c^2 + z_s^2} \tag{87}$$

A notional representation of the evolution of a parameter is shown in Figure 39. The margins can be calculated based on the predicted maximum and minimum from the solution of the pseudo-trim calculation.

4.6.3 Cost

Finally, it is possible that multiple conditions lead to a feasible trim solution. Consequently, a cost function is be used as a means to differentiate between them.

The objective is to find conditions that leave some actuation margin. Consequently, a cost function is used to find the most desirable condition.

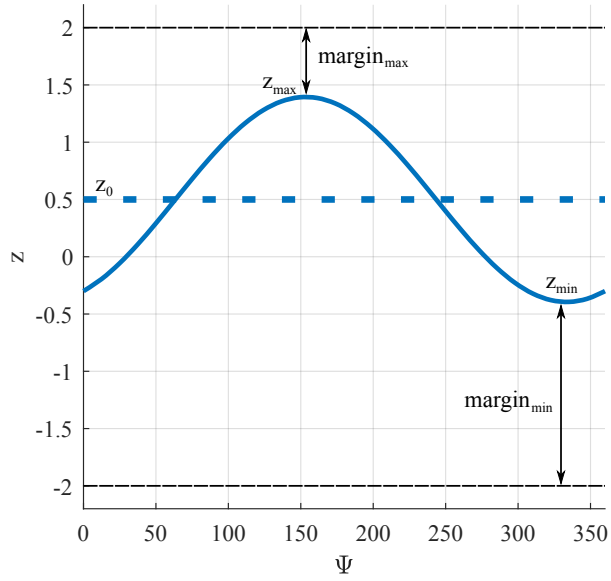

Figure 39: Notional representation of the cyclic variation of a parameter z and the margins

A weighted sum of the inverse squared of the actuation and output margin represents a simple way to ensure that the different margins are considered:

$$\Phi = \sum_{i=1}^{N_{margin}} w_{1_i} \frac{1}{margin_i^2} \tag{88}$$

The margins included are on the four actuators: elevator, rudder, aileron and propeller and the lift coefficient of the vehicle C_L, and they have both a positive and negative value.

The weights w_{1_i} represent a degree of freedom for the designer, depending on which margin is more important. The weighting scheme that will be used as a starting point for the nominal case will be maximum admissible value of the parameter of interest. For example, for the elevator margin: $w_{\delta_e} = max(\delta_e)^2$.

Evaluating the ability to perform under a steady wind condition includes finding a condition that minimizes the cost function while satisfying the feasibility constraints. This task is performed as an optimization problem as follows:

Minimize:	Φ
With Respect to:	$\tilde{u}_{nr}$, $\tilde{q}_{nr}$
Given:	$[y,z,x,\zeta_0,\ \xi_0 = 0]$, wind
Subject to:	$\ddot{x}_{nr} = 0$, $margin(\delta_e, \delta_r, \delta_a, C_L) > 0$

The solution of the optimization problem will inform whether the configuration of interest can operate in the imposed wind condition, and will provide an approximation for the states, control input and lift coefficient that lead to periodic equilibrium.

4.7 Assessment of Feasibility of the Configuration

The previous sections illustrated how the different configurations can be analyzed for feasibility. However, in the case that there are multiple feasible attachment points, there is a need to differentiate between them.

4.7.1 Configuration Evaluation

Similar to the definition of the evaluation criteria in the previous sections, multiple factors are of interest for the comparison of the configuration. The evaluation factors that is coherent with the architecture will be the same as defined in Equation 89: Φ. It allows to the study the actuation and lift coefficient margins. A lower value of Φ is related to an overall combined greater margin.

Two different cases are of interest for the evaluation: the circular hover case, and the constant wind operation. For each tether attachment point, there are two different costs: Φ_{hover} and Φ_{wind}. The two cost can be considered independently, or aggregated in a combined evaluation parameter:

$$\Phi_{config} = \Phi_{hover} + \Phi_{wind} \tag{89}$$

4.7.2 Varying Mass Configuration Evaluation

As discussed in the previous chapters, the use of the tethered aircraft is advantageous for long endurance operations, during which the suspended mass varies through time. The previous section detailed the procedure to evaluate a single configuration. However, the analysis of the system with varying mass effectively represents the analysis of a system operating at different conditions. Consequently, there is a need to consider the multiple conditions in a single evaluation scheme.

As expressed in the assumptions, the tether length and the tether attachment location stay constant throughout the flight. The approach needs to find a common attachment point that satisfies the evaluation criteria for multiple value of suspended mass.

The proposed approach is to find the union of the attachment area that satisfy the trim, open-loop and constant wind velocity trim constraints defined for a series of discretized suspended mass.

Within the combined feasible attachment area, an evaluation criteria is defined to evaluate the cost cost to operate across all of the values of mass evaluated.

$$\Phi_{total} = \sum_{i=1}^{N} w_i \Phi_{config_i} \tag{90}$$

Where Φ_{config_i} represents the combine actuation and lift coefficient cost for one value of mass. The weights w_i can be used to more emphasis on specific mass parameter. An initial guess for the weight would be an equal distribution, or unity for each configuration.

The evaluation criteria can be used to make an informed decision on the attachment point that leads to a combined maximum actuation margin and aerodynamic coefficient margin. While the attachment point that minimizes the individual costs Φ_{config_i} might differ from one suspended mass value to another, the attachment point that minimizes the combined cost Φ_{total} can be seen as an adequate compromise.

CHAPTER V

RESULTS

5.1 Introduction

This chapter presents the implementation of the methodology presented in the previous chapter. First, the details of the operating conditions of the nominal flight path will be demonstrated, including details on the open-loop characteristics. Then, the implementation of the methodology to study the tether attachment point on the aircraft are presented. Once the tether attachment point for one configuration has been found, the methodology to compare between configurations defined by different flight path parameters and by a variable suspended mass is presented. Finally, the implementation of a controller on the system subjected to a wind profile will be demonstrated.

5.2 Baseline configuration

This section presents the results of the implementation of the methodology on the baseline configuration, which is characterized by a suspended mass of 500 kg and a tether angle of $\zeta = 45°$.

In order to study a nominal configuration, the tether attachment point is assumed to be at the aircraft center of gravity, located at the quarter chord.

5.2.1 Trimming results

The trimming algorithm was implemented on the system. However, in order to show the internal trade-off that the sideslip angle β introduces on the selection of the trim condition, an exploration of the condition with fixed sideslip angle was performed. From the development of the trim algorithm, if sideslip is imposed, there is only

	Trim states
ζ	45°
ξ	0°
ϕ	7.7°
θ	4.1°
ψ	92.5°
$\dot{\zeta}$	0 $^\circ/s$
$\dot{\xi}$	51.2 $^\circ/s$
p	3.65 $^\circ/s$
q	6.9 $^\circ/s$
r	-50.7 $^\circ/s$

	Trim control input
δ_r	0.2°
δ_e	$-4.2°$
δ_a	3.23°
δ_P	3.53 $kRPM$

Table 7: Nominal flight path trim results

vector of body angles and control deflection possible to achieve trim.

With β imposed a constraint, the trim problem is now a root finding problem:

Solve for: $\ddot{z_p}$, $\ddot{\xi_1}$, $\ddot{\zeta_1} = 0$, $\vec{R}_K = 0$, $\beta = \beta_{imposed}$

$C_{l_i} \leqslant C_{l_{max}}$, $\delta_i \leqslant \delta_{max_i}$

Given: Flight path parameters

With Respect to: θ, ϕ, ψ , p, q, r, δ_r, δ_e, δ_a, δ_t

The results of a series of trim solution with various sideslip angles imposed are shown in Figure 40. In the Figure 40(a), it can be observed that the condition $\beta = 0°$ does not lead to zero rudder input and lift coefficient on the vertical stabilizer, as expected from an aircraft in a steady turn condition.

In Figure 40(c), a build-up of the trim objective cost function is shown. It can be seen that the total cost is dominated by the rudder deflection for large values of sideslip. The overall minimum of the cost function occurred at approximately the value of $\beta = -2.5°$, which corresponds to an aircraft nose pointing towards the outside of the turn.

The solution to the trim for the single aircraft attached to the ground and the 3 aircraft attached to the suspended mass are shown in Table 7. Additional details about the forces and moments acting on the aircraft for this condition are provided in Appendix E.

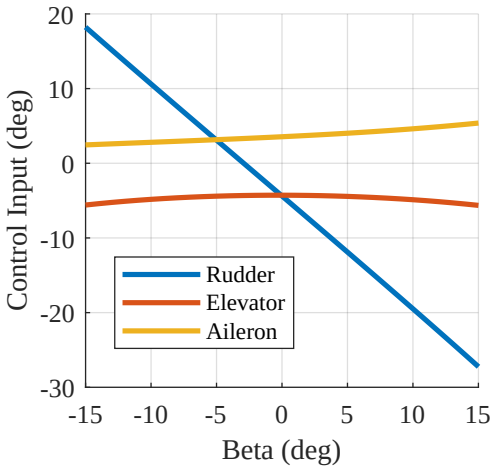

(a) Control input

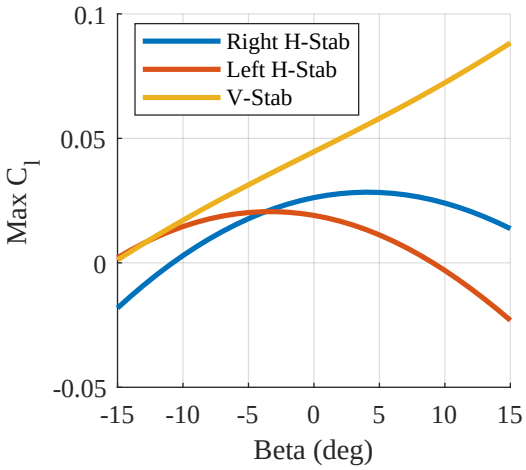

(b) Max lift Coefficient on the stabilizers

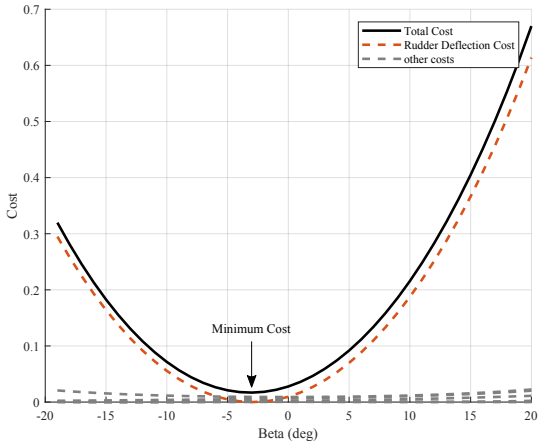

(c) Trim function cost buildup

Figure 40: Salient results of trim exploration when sideslip is imposed

5.2.2 Open-Loop Stability Assessment

The MBC model, as presented in Equations 73 - 74 presents the simplest dynamic model of the multiple tethered aircraft system. Due to the presence of a total of 36 states, the system is expected to have complex motion. A useful tool for the analysis of dynamic motion is the study of the linear dynamics through a modal analysis.

In order to gain the most insight into the system and to leverage to a maximum the available models, the open-loop stability of the three aircraft lifting a shared load model in multi-blade coordinates is presented along with the results analysis of a single aircraft tethered to the ground and a single aircraft in cruise.

5.2.2.1 Single Fixed-Wing Aircraft in Cruise

In this section, the open-loop dynamics of a single fixed-wing aircraft in cruise are presented. Even if this concept has been studied in great details in many textbook, it represents a great platform to gain insight in the more complex tethered aircraft models.

The flight condition is the cruise condition at 34.5 m/s, trimmed for steady-level flight. It is important to note that one third of the 500 kg payload has been added to the aircraft mass, at the locating of the aircraft nominal cg to represent the apparent load lifted by each aircraft.

The state vector is the following:

$$\vec{x} = [u, v, w, \phi, \theta, \psi, p, q, r]^T \tag{91}$$

The modes of the linear approximation of the dynamic model are presented in the Figure 41 and in Table 8.

For the analysis of the eigenvectors, the velocities u, v and w have been normalized as follows:

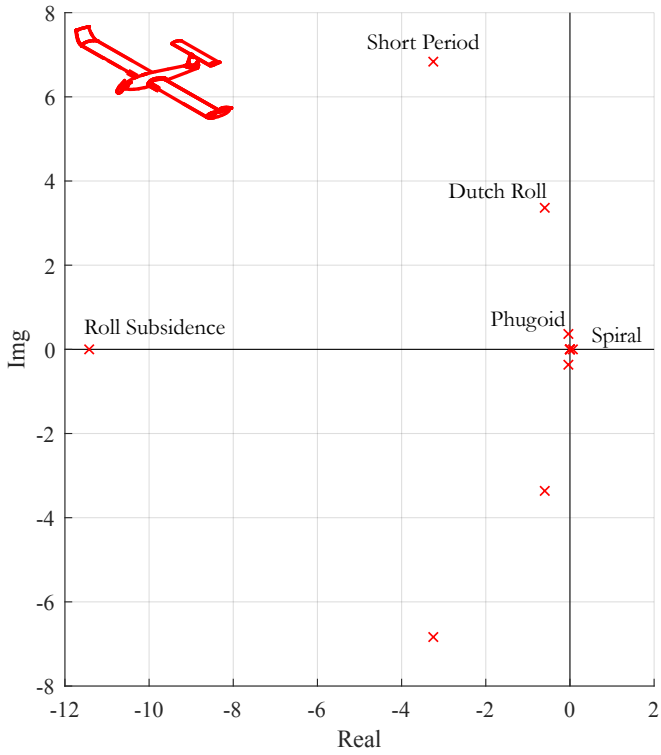

Figure 41: Dynamic modes of a single aircraft in steady level cruise condition

Table 8: Dynamic modes of a single aircraft in cruise

	Roll Subsidence -11.4 + 0i	Short Period -3.2 + 6.8i	Dutch Roll -0.6 + 3.4i
ϕ	0.087 + 0i	0 + 0i	0.05 - 0.07i
θ	0 + 0i	0.12 - 0.036i	0 + 0i
ψ	0.01 + 0i	0 - 0i	0.26 - 0.02i
$\bar{u}$	0 + 0i	-0.01 - 0i	0 - 0i
$\bar{v}$	-0.006 + 0i	0 + 0i	-0.26 + 0i
$\bar{w}$	-0 + 0i	0.14 + 0i	0 + 0i
p	-0.98 + 0i	0.002 + 0.003i	0.21 + 0.16i
q	0.004 + 0i	-0.16 + 0.96i	0.001 + 0i
r	-0.12 + 0i	0 + 0.005i	-0.09 + 0.88i

	Phugoid -0.04 + 0.36i	Spiral 0.07 + 0i	Rigid Body Mode 0+0i
ϕ	0 + 0.01i	-0.24 + 0i	0 + 0i
θ	-0.11 - 0.75i	0 + 0i	0 + 0i
ψ	0.01 - 0i	-0.96 + 0i	1 + 0i
$\bar{u}$	0.59 + 0i	0 + 0i	0 + 0i
$\bar{v}$	0 + 0i	0 + 0i	0 + 0i
$\bar{w}$	0.02 - 0i	0 + 0i	0 + 0i
p	0 + 0i	-0.012 + 0i	0 + 0i
q	0.27 - 0.01i	0 + 0i	0 + 0i
r	0 + 0i	-0.066 + 0i	0 + 0i

$$\bar{u} = \frac{u}{u_0}, \bar{v} = \frac{v}{u_0}, \bar{w} = \frac{w}{u_0}, \tag{92}$$

It can be observed that the typical modes of conventional fixed wing aircraft are observed: the roll subsidence, short period, dutch roll, phugoid and spiral dive. Due to the setup of the problem and the inclusion of the three aircraft body angles, an additional mode, appeared at the origin, and represents a rigid body rotation of the aircraft about the z-axis.

Roll Subsidence The roll subsidence, roll convergence or simply roll mode, is the highest frequency mode, and is well damped, primarily constituted of roll rate p.

Short Period The second highest frequency mode is the short period mode. It is oscillatory, but also well damped. The motion is primarily longitudinal, with a pitch up motion(θ), in phase with an increase of aerodynamic angle of attack $\alpha \approx w/u_0$

Dutch Roll The third highest frequency mode is the dutch roll. It is oscillatory, with little damping. The motion is primarily constituted of yaw angle and aerodynamic sideslip $\beta \approx v/u_0$

Phugoid The fourth highest frequency mode is the phugoid mode. It is oscillatory, with almost no damping. The motion is primarily longitudinal, with an increase in axial velocity u, out-of-phase with the pitching motion of the aircraft, θ. This lead to the typical up-and-down motion of the aircraft, with little change in aerodynamic angle of attack $\alpha \approx w/u_0 \approx 0$.

Spiral The spiral model is a very slow, diverging motion. It represents an increasing roll and yaw angles. Even if this mode is unstable, it is usually deemed acceptable due to the its very slow behavior.

Rigid Body Motion As described in the opening paragraph, there is a rigid body mode about the z-axis, located at the origin of the complex plane. The presence of this mode is supported by the orientation of the aircraft about the z-axis - whether the aircraft was pointing to the north, or to the south - would not change the motion. This mode is a result of the problem formulation, and does not represent a relevant motion for the analysis of the system.

5.2.3 Single Aircraft tethered to the ground

In order to gain the greatest insight in the system's motion, the modal analysis was also performed on the linear approximation of the dynamics of a single aircraft tethered to the ground and a single aircraft in cruise. The eigenvalues are also shown on Figure 42, and the mode shapes are shown in Table 9.

In order to gain more knowledge in the behavior of the non-linear systems, the modes were also simulated using the non-linear dynamic model. The initial conditions for the simulation were the trimmed control input and the trimmed states plus a variation based on the mode shapes. Since the modes shapes are made of complex numbers, any vector representing the modes shapes could be used. For the purpose of this simulation, the real part of the modes shapes multiplied by a scaling factor were used as initial conditions. Consequently, the type of motion of the system is of interest, but not the magnitude of the displacement. The simulation results are shown in Appendix G.

The state vector for the single aircraft tethered to the ground system is the following:

$$\vec{x} = [\zeta, \xi, \phi, \theta, \psi, \dot{\zeta}, \dot{\xi}, p, q, r]^T \tag{93}$$

It is also possible to convert the modeshapes and retrieve the aircraft velocity in the body frame. This is performed by linearizing the Equation 48 about the trim

condition. Note that the equation is simplified by the absence of tether elongation and elongation rate ϵ and $\dot{\epsilon}$, no motion of the fuselage $\dot{x}_p$, $\dot{y}_p$ and $\dot{z}_p$ as well as no contribution of the offset of the attachment point from the aircraft center of gravity.

The conversion becomes:

$$\begin{bmatrix} u \\ v \\ w \end{bmatrix} = \begin{bmatrix} -34.6 & -1.5 & 0 & -2.5 & -1.5 & 1.1 & 38.8 \\ 1.2 & -34.4 & 2.6 & 4.6 & -34.4 & -43.7 & -1.3 \\ -2.7 & 4.5 & 1.1 & 34.3 & 4.5 & -33.3 & 2.9 \end{bmatrix} \begin{bmatrix} \zeta \\ \xi \\ \phi \\ \theta \\ \psi \\ \dot{\zeta} \\ \dot{\xi} \end{bmatrix} \tag{94}$$

Mode G: Roll Subsidence The highest frequency mode is the mode G, which is very close in frequency and in overall motion to the roll subsidence mode of a single aircraft in cruise. The simulated motion of the aircraft in the inertial frame is shown on Figure 43.

Mode F: Short Period Similarly, the second mode, the mode F is very close in frequency and overall motion to the short period longitudinal mode. The motion is shown on Figure 44.

Mode E: Dutch Roll Similarly, the second mode, the mode E is very close in frequency and overall motion to the dutch roll. The motion of the mode is shown on Figure 45. In Table 10, where the motion is expressed with velocities in the body frame, characteristic side-slip of the dutch roll $\bar{v}$ is more apparent.

Mode D: Phugoid The mode D is very close to the phugoid motion of the single aircraft in cruise. It represents a pitch up and pitch down motion of the aircraft θ,

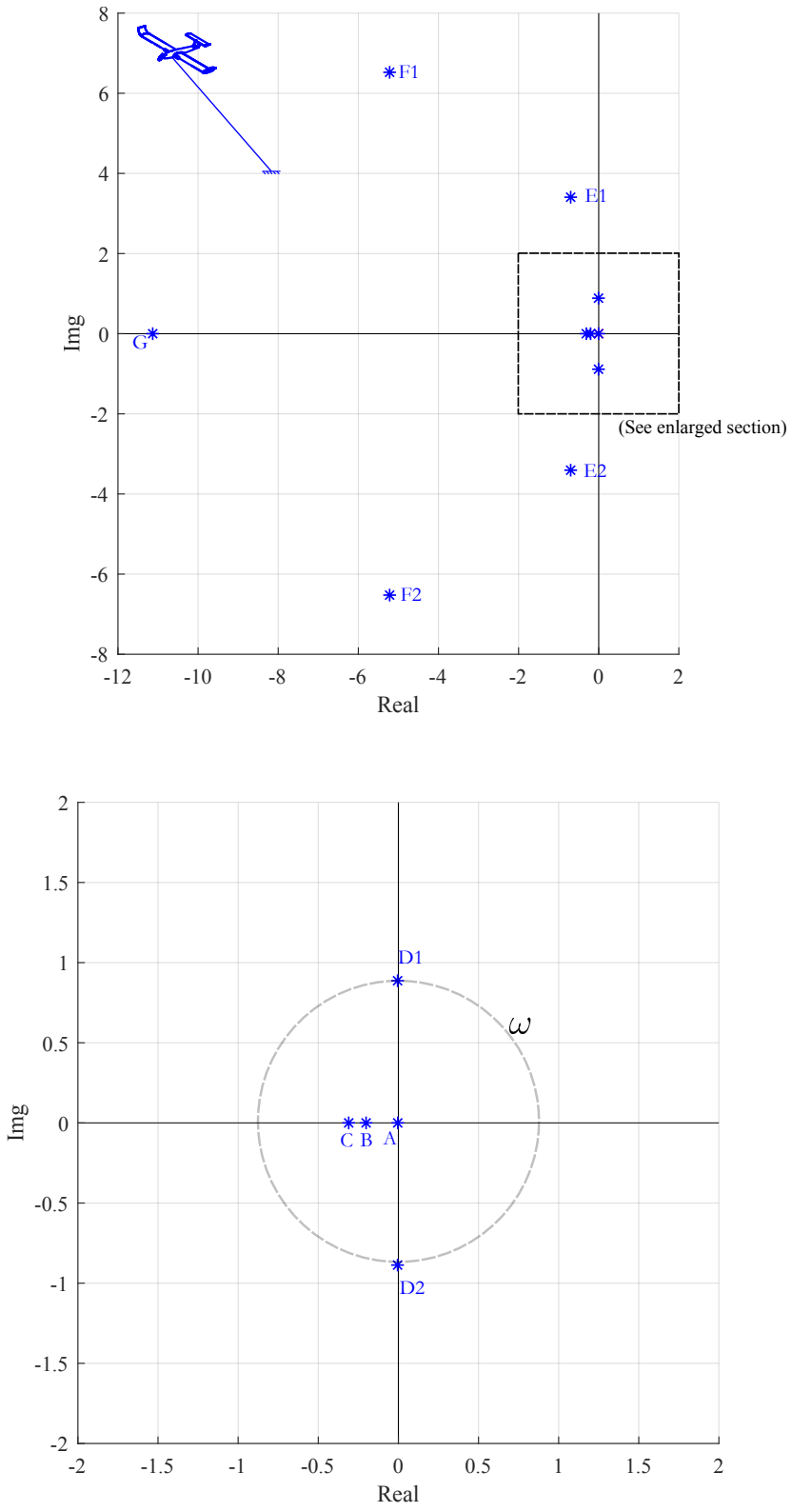

Figure 42: Dynamic modes of a single aircraft tethered to the ground

Table 9: Dynamic modes of a single aircraft tethered to the ground

	Mode G -11.1 + 0i	Mode F1 -5.2 + 6.52i	Mode E1 -0.70 + 3.4i	Mode D1 -0.005 + 0.887i
ζ	-0.001 + 0i	0.008 + 0.003i	-0.004 - 0.009i	-0.45 - 0.021i
ξ	0 + 0i	-0.001 - 0.001i	-0.002 + 0.001i	0.036 + 0.335i
ϕ	-0.085 + 0i	0.005 - 0.033i	-0.066 - 0.04i	0.46 + 0i
θ	-0.028 + 0i	-0.074 - 0.087i	0.028 - 0.03i	0.004 - 0.448i
ψ	-0.005 + 0i	0.016 + 0.02i	-0.057 - 0.252i	-0.032 + 0.101i
$\dot{\zeta}$	0.007 + 0i	-0.06 + 0.04i	0.034 - 0.006i	0.021 - 0.399i
$\dot{\xi}$	-0.001 + 0i	0.008 - 0.001i	-0.003 - 0.006i	-0.298 + 0.03i
p	0.918 + 0i	0.139 + 0.125i	0.145 - 0.223i	0.007 + 0.01i
q	0.372 + 0i	0.968 + 0i	0.019 + 0.155i	-0.001 + 0.013i
r	0.107 + 0i	-0.086 - 0.003i	0.911 + 0i	-0.09 - 0.056i

	Mode C -0.31+0i	Mode B -0.2+0i	Mode A -0.004+0i
ζ	-0.05 + 0i	-0.037 + 0i	-0.001 + 0i
ξ	0.667 + 0i	0.611 + 0i	0.707 + 0i
ϕ	0.045 + 0i	0.363 + 0i	0.001 + 0i
θ	0.02 + 0i	0.027 + 0i	0 + 0i
ψ	-0.678 + 0i	-0.593 + 0i	-0.707 + 0i
$\dot{\zeta}$	0.016 + 0i	0.007 + 0i	0 + 0i
$\dot{\xi}$	-0.207 + 0i	-0.123 + 0i	-0.003 + 0i
p	-0.011 + 0i	-0.058 + 0i	0 + 0i
q	-0.075 + 0i	-0.343 + 0i	-0.001 + 0i
r	0.203 + 0i	0.075 + 0i	0.003 + 0i

Table 10: Dynamic modes of a single aircraft tethered to the ground with aircraft velocity expressed in the body frame

	Mode G -11.1 + 0i	Mode F1 -5.2 + 6.52i	Mode E1 -0.70 + 3.4i	Mode D1 -0.005 + 0.887i
ϕ	-0.085 + 0i	0.005 - 0.033i	-0.066 - 0.04i	0.46 + 0i
θ	-0.028 + 0i	-0.074 - 0.087i	0.028 - 0.03i	0.004 - 0.448i
ψ	-0.005 + 0i	0.016 + 0.02i	-0.057 - 0.252i	-0.032 + 0.101i
$\bar{u}$	0.002 + 0i	0.004 + 0.003i	0.002 + 0.015i	0.117 + 0.055i
$\bar{v}$	-0.031 + 0i	0.051 - 0.083i	0.015 + 0.25i	0.002 + 0.007i
$\bar{w}$	-0.037 + 0i	-0.013 - 0.123i	-0.015 - 0.059i	0.009 + 0.002i
p	0.918 + 0i	0.139 + 0.125i	0.145 - 0.223i	0.007 + 0.01i
q	0.372 + 0i	0.968 + 0i	0.019 + 0.155i	-0.001 + 0.013i
r	0.107 + 0i	-0.086 - 0.003i	0.911 + 0i	-0.09 - 0.056i

	Mode C -0.31+0i	Mode B -0.2+0i	Mode A -0.004+0i
ϕ	0.045 + 0i	0.363 + 0i	0.001 + 0i
θ	0.02 + 0i	0.027 + 0i	0 + 0i
ψ	-0.678 + 0i	-0.593 + 0i	-0.707 + 0i
$\bar{u}$	-0.18 + 0i	-0.1 + 0.003i	-0.003 + 0i
$\bar{v}$	0.003 + 0i	0.008 - 0.083i	0 + 0i
$\bar{w}$	-0.01 + 0i	0.026 - 0.123i	0 + 0i
p	-0.011 + 0i	-0.058 + 0i	0 + 0i
q	-0.075 + 0i	-0.343 + 0i	-0.001 + 0i
r	0.203 + 0i	0.075 + 0i	0.003 + 0i

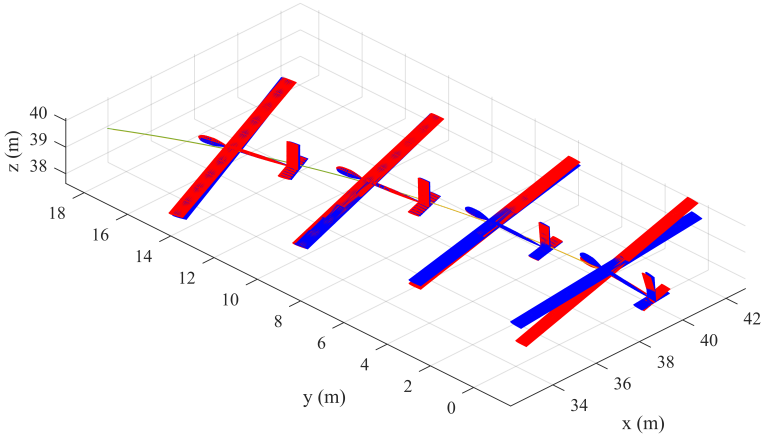

Figure 43: Motion of mode G

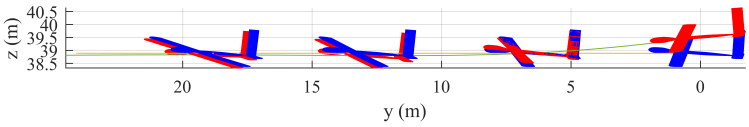

Figure 44: Motion of mode F

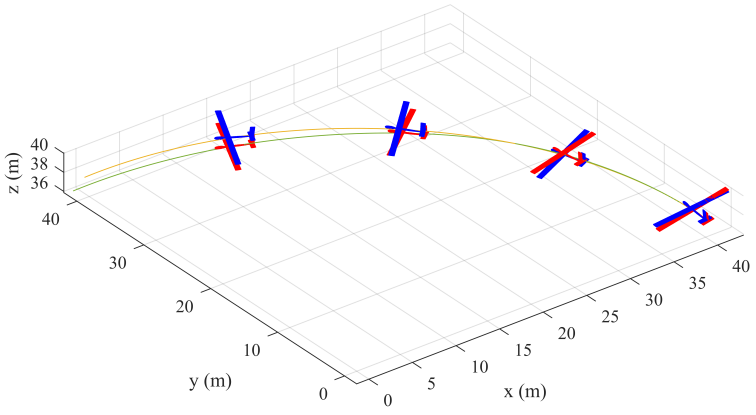

Figure 45: Motion of mode E

that is leading the up and down motion of the aircraft ζ of the aircraft by almost 90°. Similarly to how the aircraft accelerates and decelerates in a classic phugoid motion, the mode D exhibits the acceleration by the $\dot{\xi}$ term. In Table 10, where the motion is expressed with velocities in the body frame, it is apparent that the angle of attack, $\bar{w}$ is very small, but the axial velocity of the aircraft $\bar{u}$, typical to the phugoid mode of a single aircraft is present.

The frequency of this mode is quite different from the phugoid mode of the single aircraft in cruise: for the tethered case, the frequency is the frequency of the aircraft circling about the origin Ω, which means that the aircraft reaches a maximal altitude at the same azimuth location in the inertial frame. The tridimensional motion of the aircraft has been simulated and is shown in Figure 46.

Mode C The modes C is a converging mode located on the real axis. Since the period of the mode is longer than the time it takes to make a revolution about the attachment point, the motion of the mode is hard to visualize when the snapshots

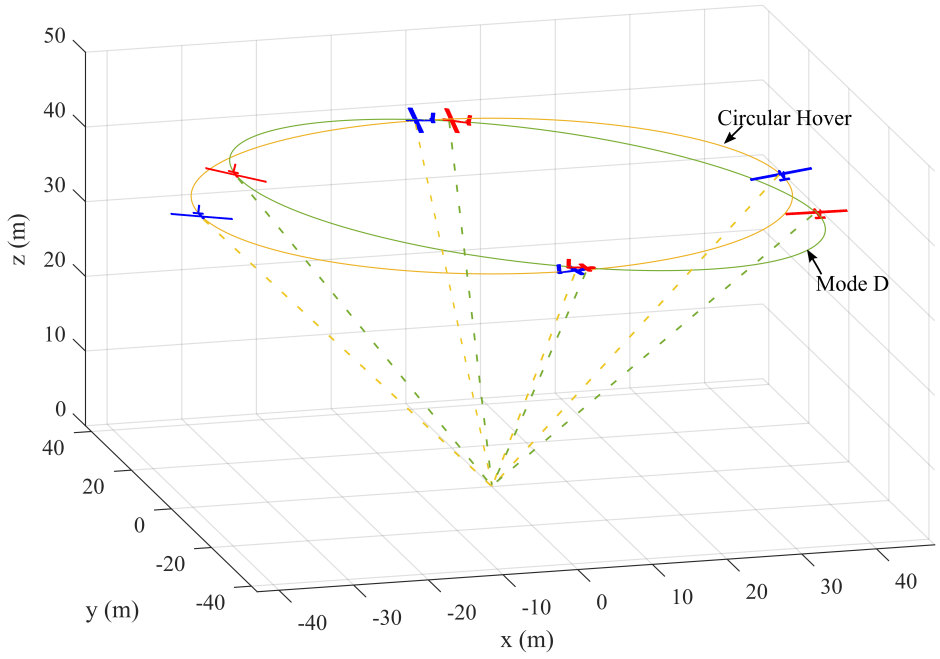

Figure 46: Motion of mode D

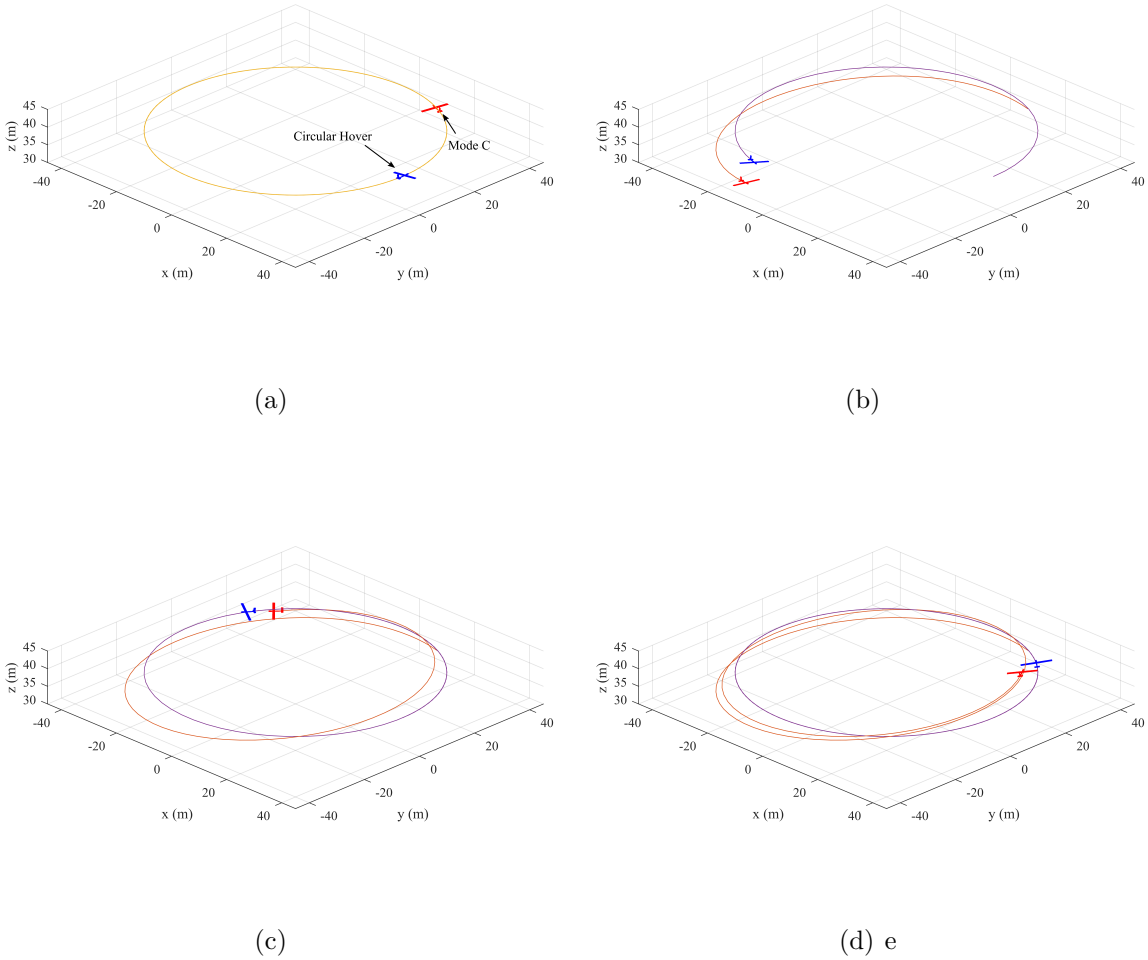

Figure 47: Motion of the mode C compared to circular hover flight path

are superimposed. Consequently, the motion is shown on 4 different snapshots of the simulated mode, shown on Figure 47.

As seen in the motion of the mode, the mode is initially comprised of an advancing position ξ, but a lower velocity $\dot{\xi}$. The advancing position is close to the inverse of the change in angle ψ, denoting a coordinated rotation of the aircraft and its azimuthal position. The expression of the velocity in the body frame effectively shows little to no change in aerodynamic sidelslip angle.

This mode is mainly comprised of a convergence in aircraft speed.

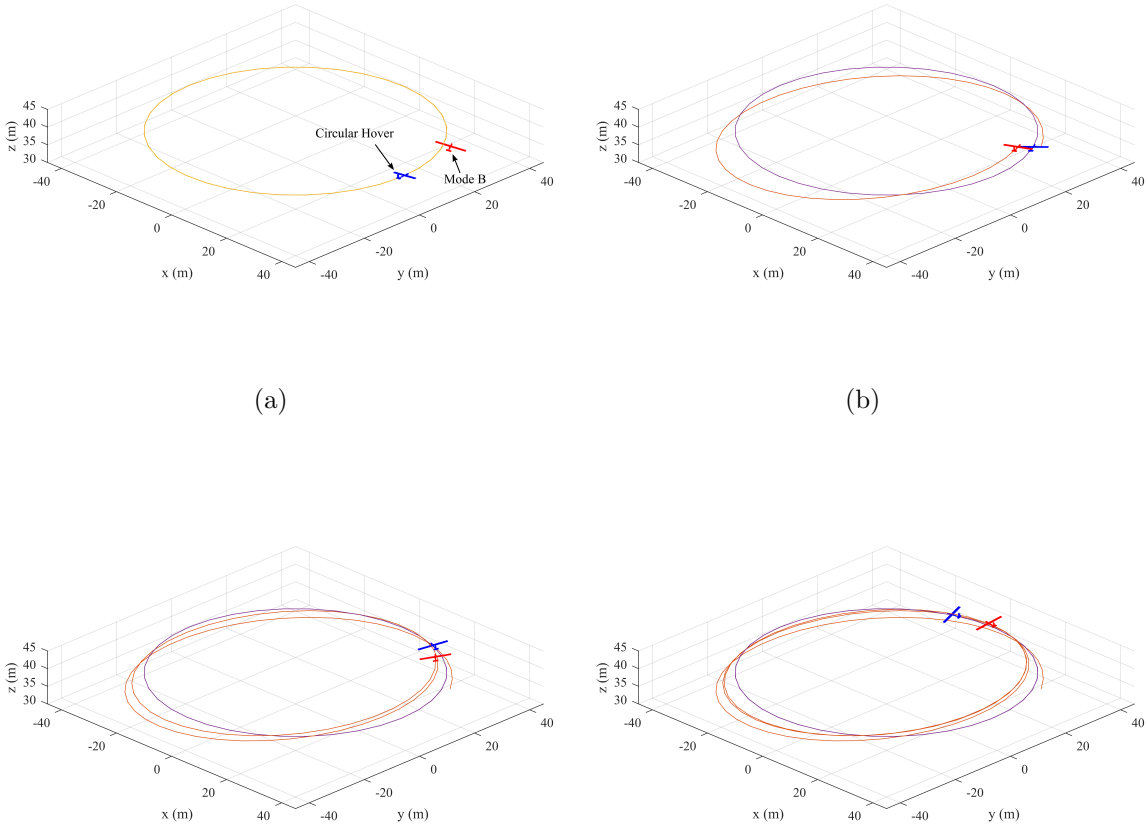

(a) (b)

(c) (d) e

Figure 48: Motion of the mode B compared to circular hover flight path

Mode B The mode B is similar to the mode C, as it is another slow converging mode. The motion is similar to mode B as well, as is there is a portion of the motion that involves a initial slower aircraft $\dot{\xi}$. The motion of mode B is compared to a circular flight path on Figure 48.

Mode A The mode A, located at $(0 + 0i)$ is a pure rigid body mode in rotation of the whole system about the z-axis at the attachment point. This rotation involves an equal rotation of the tether angle ξ and the inverse of the aircraft about the z-axis ψ. Similar to the single aircraft in cruise, this mode is attributable to the problem

setup.

Observations Similar to the canonical problem, there seem to be a spectral separation between modes A, B, C, D (low frequency) and the modes E, F and G (higher frequency). The higher frequency modes present similarities in frequency and motion to the roll subsidence, short period and dutch roll modes of the same aircraft in cruise condition.

The phugoid mode presents the interesting difference that the period of the mode is the same as the time it takes for the aircraft to make a full revolution. Finally, there are two stable spiral modes that present some axial velocity damping characteristics as well.

5.2.3.1 Dynamic Modes of Three Aircraft Tethered to a Shared Load

Details About Analysis in Multi-Blade Coordinates Johnson demonstrated the results of the dynamic analysis for a helicopter blade flapping, which represents a classic application of MBC. The analysis of a single blade is compared to the analysis the same blade, part of a three-bladed rotor system, studied in MBC explained by Johnson [55] :

> The nonrotating eigenvalues for the β_{nc} and β_{ns} degrees of freedom are simply the rotating roots shifted in frequency by n/rev: $s = s_r \pm in$.

A notional representation of how the modes are shifted with multi-blade coordinates is shown on Figure 49.

Johnson also notes [55]:

> When the individual blades of the rotor are not independent, but rather are coupled through the fixed system (such as by the control system or shaft motion), the nonrotating modes are not all influenced in the same manned and the real parts of the roots will not necessarily be identical not

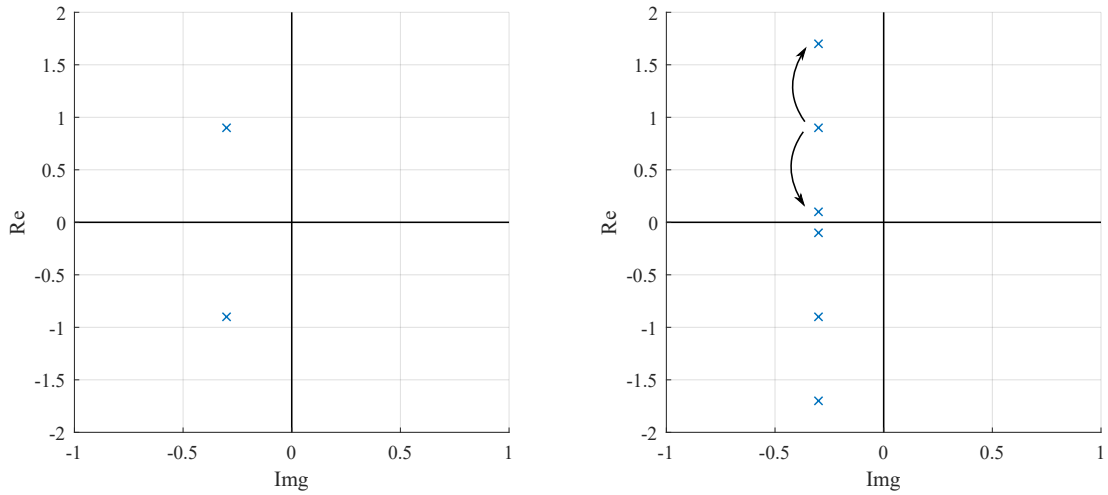

(a) Modes of all blades, in the rotating frame

(b) Modes in the nonrotating frame (MBC)

Figure 49: Notional representation of the flapping modes of a 3-bladed rotor system in the rotating frame and in the nonrotating frame

> will the frequencies be separated by exactly n/rev. The basic character [...] still dominates the roots in the nonrotating frame however.

For tethered aircraft, it is clear that the aircraft are not independent, due to the coupling of the motion thought the payload motion. However, some modes might exhibit similar trends when compared from the IBC to MBC.

Analysis of the Dynamic Modes An eigenvalue analysis of the matrix A_{NR} was performed. In order to avoid including the rigid body modes, the column and rows associated with the payload states x, y and z were removed. The analysis led to 18 modes, and their eigenvalues are shown on Figure 50.

Similar to the analysis of the modeshapes of a single aircraft tethered to the ground, the illustration of the aircraft velocity in the body frame can be relevant to the analysis.

The conversion of the velocity for the first aircraft becomes:

$$\begin{bmatrix} u \\ v \\ w \end{bmatrix} = \begin{bmatrix} -35 & -1.5 & 0 & -2.5 & -1.5 & 1.1 & 38.8 & 0 & 1 & 0.1 \\ 1.2 & -34 & 2.6 & 4.6 & -34 & -44 & -1.3 & 1 & 0 & -0.1 \\ -2.7 & 4.5 & 1.1 & 34 & 4.5 & -33 & 2.9 & -0.1 & 0.1 & -1 \end{bmatrix} \begin{bmatrix} \zeta \\ \xi \\ \phi \\ \theta \\ \psi \\ \dot{\zeta} \\ \dot{\xi} \\ \dot{x}_p \\ \dot{y}_p \\ \dot{z}_p \end{bmatrix} \quad (95)$$

The controllability of the different modes is also investigated. In order to do so, the Popov-Belevitch-Hautus (PBH) controllability [26, 76] test is performed on the system. The PBH test consists of identifying whether the left eigenvectors $\mathtt{w}$ of the matrix $\mathbf{A}_{nr}$, which represent the dynamic modes of the linear system, are orthogonal to the columns of the input matrix $\mathbf{B}_{nr}$. An uncontrollable mode will lead to:

$$\mathtt{w_i}^T \mathbf{B}_{nr} = 0 \quad (96)$$

The results of this test also inform of the contribution of the components of the control vector to control the mode $\mathtt{w_i}$.

It can be observed that some of the roots exhibit the conventional MBC representation results: the MBC roots are similar to the IBC, with some shift of the imaginary part. This is the case of the mode E in IBC and modes 11, 12 and 13 in MBC, the mode F in IBC and modes 14, 15 and 16 in MBC and the mode G in IBC and modes 17 and 18 in MBC. For each of those sets, the mode shapes are compared in Tables 11, 13 and 16. Because of the large number of states for the three aircraft system, the five to six most relevant states for each mode are outlined.

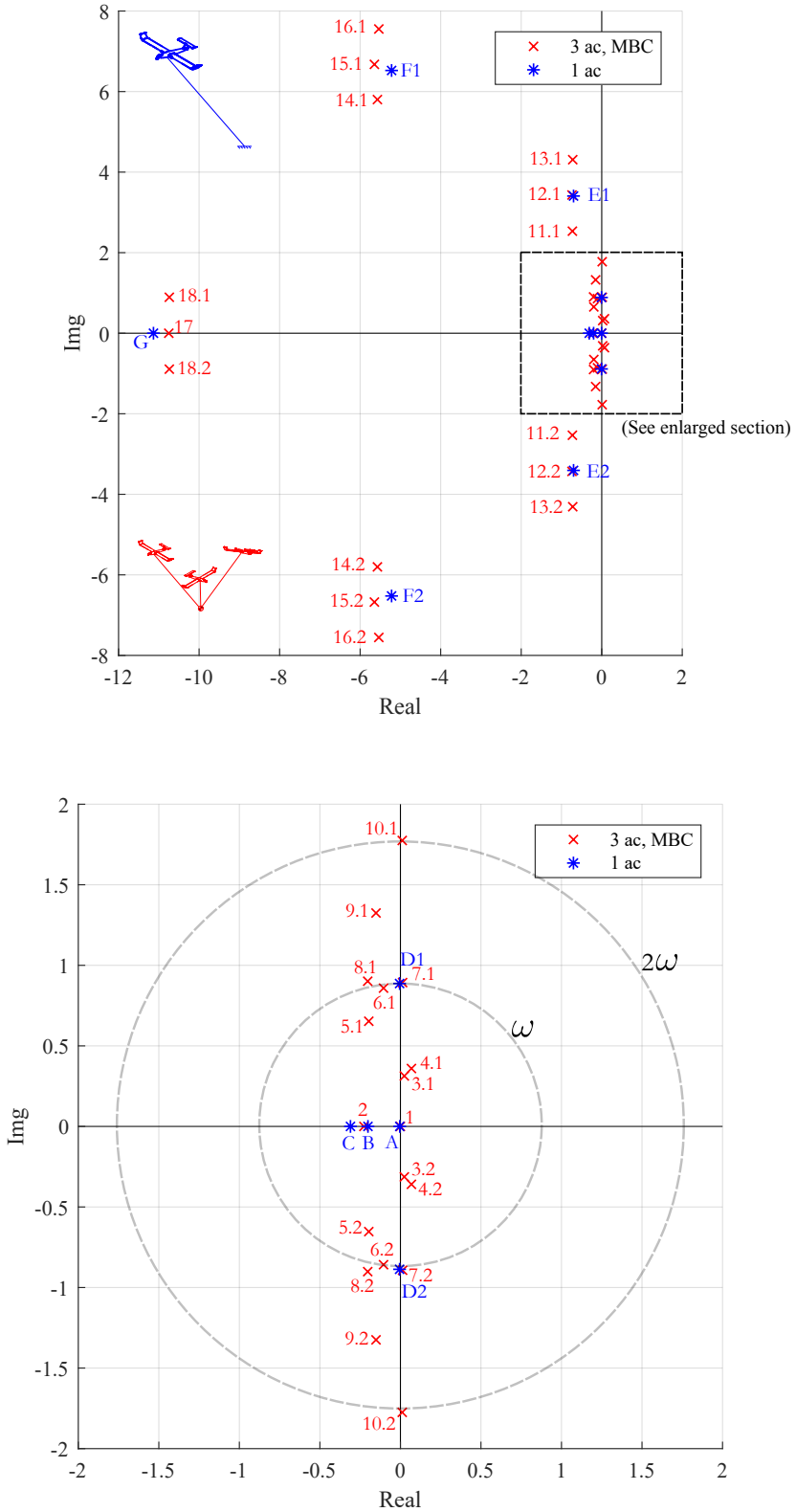

Figure 50: Dynamic modes of a single aircraft tethered to the ground compared to the modes of a system of 3 aircraft, in MBC

The other modes of the three aircraft system do not necessarily follow the IBC to MBC trend and are characterized by a lower frequency. The associated mode-shapes are shown in Table 19 to 27.

It is observed that the modes have either only only collective degrees of motion, or cyclic ones. The collective degrees of freedom are z_p, $\dot{z}_p$, ζ_0, $\dot{\zeta}_0$, ξ_0, $\dot{\xi}_0$, as well as the collective aircraft body angles and angular rates ϕ_0, θ_0, ψ_0, p_0, q_0, r_0. In counterparts, the cyclic degrees of freedom are x_p, $\dot{x}_p$, y_p, $\dot{y}_p$, ζ_c, $\dot{\zeta}_c$, ξ_s, $\dot{\xi}_s$, ϕ_c, ϕ_s, θ_c, θ_s, ϕ_c, ϕ_s, p_c, p_s, q_c, q_s, r_c, r_s. The modes will be referred to as either *collective modes* or *cyclic modes* based on which set of degrees of freedom are present.

Modes 17 and 18 v.s. Mode G: Roll Subsidence Mode 17 (-10.75+0i) and mode 18 (-10.7 - 0.89i) are very close to the mode G of the single tethered aircraft system, and their associated eigenvectors are shown in Table 11. The product $\mathtt{w_i}^T\mathbf{B}_{nr}$ is expressed in Table 12.

As per the mode G, mode 17 is primarily a motion of the aircraft in roll p, slightly in pitch q, and is critically damped. The mode 17 represented a synchronized motion of the airplanes, which also introduces a slight up-and-down motion of the fuselage w, a component not expressed by the single aircraft tethered to the ground system. The control input that have authority on this mode are mainly the synchronized elevator and aileron deflection, as shown in Table 12.

It is possible to convert easily the modeshape of mode 17 and retrieve the variations of aircraft velocity in the body frame $\bar{u}$, $\bar{v}$ and $\bar{w}$, as the motion is collective to the aircraft. However, for the proposed representation of the modeshapes, the change in aircraft body velocities are very small.

The mode 18 is the cyclic variation of roll and pitch motion of the aircraft. This mode has a periodic component, but is still highly damped. This mode introduces no motion to the fuselage, possibly due to the high frequency of the mode. The

Table 11: Comparison of modal analysis of a single aircraft tethered to the ground and three aircraft in MBC: Mode G, 17 and 18

1 AC			
Mode G			
-11.1 + 0i			
ζ	-0.001	+	0i
ξ	0	+	0i
ϕ	-0.085	+	0i
θ	-0.028	+	0i
ψ	-0.005	+	0i
$\dot{\zeta}$	0.007	+	0i
$\dot{\xi}$	-0.001	+	0i
p	0.918	+	0i
q	0.372	+	0i
r	0.107	+	0i

3AC, MBC							
Mode 17				Mode 18.1			
-10.75+0i				-10.7 - 0.89i			
p_0	0.934	+	0i	p_s	0.666	+	0i
q_0	0.297	+	0i	p_c	0	-	0.666i
$\dot{z}_p$	0.16	+	0i	q_s	0.215	+	0.001i
ϕ_o	-0.087	+	0i	q_c	0.001	-	0.215i
r_0	0.069	+	0i	ϕ_s	-0.062	+	0.005i
				ϕ_c	-0.005	+	0.062i

sine component of the motion leads the cosine component in phase by 90°, which means that the motion is receding in the nonrotating frame: The aircraft fly in the counterclockwise direction above the fuselage, and the mode rotates in the clockwise direction.

As expected, the control input that have authority on this mode are the cyclic variation of elevator and aileron deflection, as shown in Table 12.

Modes 14, 15 and 16 v.s. Mode F: Short Period The modes 14, 15 and 15 are very close in frequency and motion of the Mode F from the single aircraft tethered to the ground model, which represented a mode similar to the longitudinal Short Period

Table 12: Product of the left eigenvectors and the input matrix for modes 17 and 18

$\mathtt{w_{17}}^T\mathbf{B}_{nr}$				$\mathtt{w_{18}}^T\mathbf{B}_{nr}$			
δ_{a0}	-46.4	+	0i	δ_{as}	33.2	+	0i
δ_{e0}	11.7	+	0i	δ_{ac}	0	+	33.2i
δ_{r0}	0.89	+	0i	δ_{es}	-8.7	+	0i
δ_{t0}	-0.0092	+	0i	δ_{ec}	-0.036	-	8.66i
				δ_{rs}	0.011	-	0.47i
				δ_{rc}	0.47	-	0.011i

mode.

All three modes have a very similar real part of their eigenvector, as highligthed in Table 13.

The mode 15 represents the synchronized motion of the three aircraft, where only the collective part of the motion are present, as per typical MBC analysis. When compared to the mode F, there is an additional up-and-down motion of the fuselage present w. The conversion of the motion expressed in the aircraft body frame is shown in Table 14. It shows the increase of angle of attack typical to short period modes.

For the mode 14, the sine part of the motion leads the cosine part of the motion in phase by 90°, which means that it represents a receding motion in the nonrotating frame. The motion of the fuselage, described by u and v, is also counterclockwise.

In comparison, for the higher frequency mode 16, the cosine part of the motion leads the sine part of the motion in phase by 90°, which means that the mode is advancing in the nonrotating frame.

For all three modes, the control input that have authority on the motion are mainly the elevator and the aileron.

The mode 15 and 16 represent well the trend expected in the conversion of the modes from the rotating frame to the nonrotating frame, as shown in Figure 51. The simulation results of the aircraft angle θ are similar in trend and timing for modes

Table 13: Comparison of modal analysis of a single aircraft tethered to the ground and three aircraft in MBC: Mode F, 14, 15 and 16

1 AC			
Mode F1 -5.2 + 6.52i			
ζ	0.008	+	0.003i
ξ	-0.001	-	0.001i
ϕ	0.005	-	0.033i
θ	-0.074	-	0.087i
ψ	0.016	+	0.02i
$\dot{\zeta}$	-0.06	+	0.04i
$\dot{\xi}$	0.008	-	0.001i
p	0.139	+	0.125i
q	0.968	+	0i
r	-0.086	-	0.003i

3AC, MBC											
Mode 14.1 -5.57 +5.8i				Mode 15.1 -5.65 + 6.68i				Mode 16.1 -5.54 + 7.55i			
q_c	0.611	+	0i	q_0	0.79	+	0i	q_c	-0.631	+	0i
q_s	-0.008	+	0.611i	$\dot{z}_p$	-0.44	-	0.301i	q_s	0.006	+	0.63i
$\dot{y}_p$	-0.177	-	0.195i	p_0	0.224	-	0.097i	$\dot{y}_p$	-0.103	-	0.178i
$\dot{x}_p$	-0.191	+	0.177i	r_0	-0.146	-	0.004i	$\dot{x}_p$	0.177	-	0.099i
p_c	0.171	+	0.078i	θ_0	-0.058	+	0.069i	p_c	-0.177	-	0.083i
p_s	-0.08	+	0.170					p_s	-0.083	-	0.177

15 and F. Note that the range of values are not the same due to the scaling factor on the modeshape. Similarly, due to the fact that this mode is collective mode, the value of $\theta_0 = \theta_{ac_1} = \theta_{ac_3} = \theta_{ac_3}$. Moreover, the value of values of $\theta_s = \theta_c = 0$. The mode 16, in counterparts, is a cyclic mode. For this mode, the value of $\theta_0 = 0$. In counter parts, θ_s and θ_c take about the same time to reach a steady state value than θ_0 of mode 15.

.

Modes 11, 12 and 13 v.s. Mode E: Dutch Roll The modes 11, 12 and 13 are the three modes that are approximated as representing the mode E, or Dutch Roll of

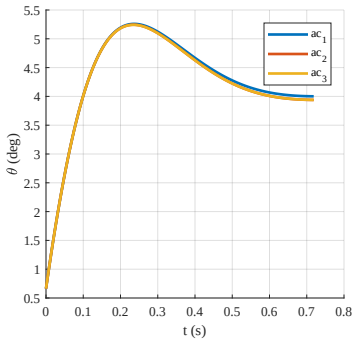

(a) Individual aircraft angle θ t during simulation of mode 15

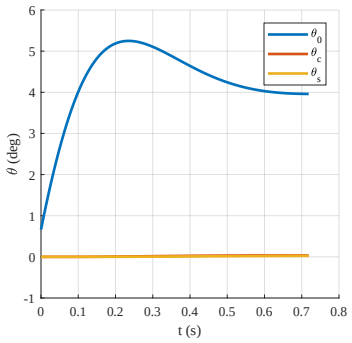

(b) Angle θ in the nonrotating frame during simulation of mode 15

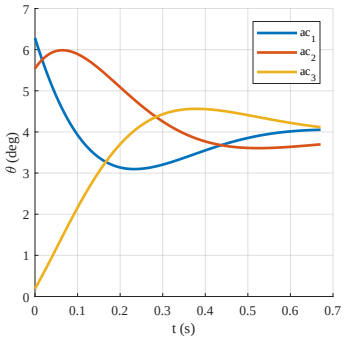

(c) Individual aircraft angle θ during simulation of mode 16

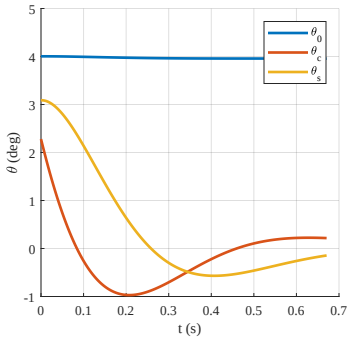

(d) Angle θ in the nonrotating frame during simulation of mode 16

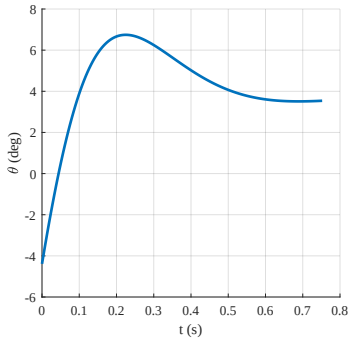

(e) Angle θ of the single aircraft attached to the ground during simulation of mode F

Figure 51: Comparison of aircraft pitch angle θ time signature for mode 15 and 16

the single aircraft tethered to the ground. As per the mode E, the modes 11, 12 and 13 are mainly yaw and roll motion. All three modes have a similar real part, and are lightly damped.

The mode 12, is the synchronized motion of the aircraft about the collective

Mode 15 -5.65 + 6.68i			
q_0	0.79	+	0i
$\dot{z}_p$	-0.44	-	0.301i
p_0	0.224	-	0.097i
r_0	-0.146	-	0.004i
$\bar{w}$	-0.006	-	0.101i
θ_0	-0.058	+	0.069i
$\bar{v}$	0.033	-	0.057i

Table 14: Mode 15 with velocity expressed in aircraft body frame

Table 15: Product of the left eigenvectors and the input matrix for modes 14, 15 and 16

$\mathtt{w_{14}}^T\mathbf{B}_{nr}$				$\mathtt{w_{15}}^T\mathbf{B}_{nr}$				$\mathtt{w_{16}}^T\mathbf{B}_{nr}$			
δ_{es}	0.16	+	27.12i	δ_{e0}	-35.53	-	0.58i	δ_{es}	0.41	-	27.97i
δ_{ec}	-27.11	-	0.20i	δ_{a0}	12.42	-	4.53i	δ_{ec}	-27.96	-	0.14i
δ_{ac}	9.29	-	3.77i	δ_{r0}	0.21	+	0.72i	δ_{ac}	9.60	-	4.07i
δ_{as}	-3.94	-	9.21i	δ_{t0}	-0.023	-	0.016i	δ_{as}	4.01	+	9.62i
δ_{rc}	0.31	+	0.34i					δ_{rc}	-0.21	-	0.40i
δ_{rs}	0.34	+	0.3i					δ_{rs}	0.40	-	0.21i

degrees of freedom, which also introduces a up-and-down motion of the fuselage w.

The lower frequency mode 11 the cosine part of the motion leads the sine part in phase by 90°, which makes this mode an advancing mode, while for the higher frequency mode 13, the sine part of the motion leads the cosine part in phase by 90°, which makes this mode an receding mode.

For all three modes, the control input that have authority on the motion are the aileron and rudder input.

Modes 10: Cyclic altitude variation of the aircraft The mode 10 is a cyclic mode characterized by a cyclic variation of the altitude of the aircraft, with its pulsation located at about this the angular velocity of the aircraft Ω. This mode can be compared to the mode D of the single aircraft tethered to the ground, in which the

Table 16: Comparison of modal analysis of a single aircraft tethered to the ground and three aircraft in MBC: Mode E, 11, 12 and 13

1 AC			
Mode E1 -0.70 + 3.4i			
ζ	-0.004	-	0.009i
ξ	-0.002	+	0.001i
ϕ	-0.066	-	0.04i
θ	0.028	-	0.03i
ψ	-0.057	-	0.252i
$\dot{\zeta}$	0.034	-	0.006i
$\dot{\xi}$	-0.003	-	0.006i
p	0.145	-	0.223i
q	0.019	+	0.155i
r	0.911	+	0i

3AC, MBC											
Mode 11.1 -0.729 + 2.53i				Mode 12.1 -0.738 + 3.43i				Mode 13.1 -0.72 + 4.31i			
r_s	-0.613	+	0i	r_0	0.875	+	0i	r_s	0.65	+	0i
r_c	0.001	-	0.613i	$\dot{z}_p$	-0.163	-	0.223i	r_c	0.001	-	0.65i
ψ_s	0.064	-	0.224i	p_0	0.192	+	0.188i	p_s	0.143	+	0.137i
ψ_c	0.223	+	0.064i	ψ_o	-0.052	+	0.244i	p_c	0.137	-	0.143i
p_s	-0.134	-	0.131i					ψ_s	-0.025	+	0.147i
p_c	0.131	+	0.135i					ψ_c	0.147	-	0.025i

Mode 12 -0.738 + 3.43i			
r_0	0.875	+	0i
$\dot{z}_p$	-0.163	-	0.223i
p_0	0.192	+	0.188i
ψ_o	-0.052	+	0.244i
$\bar{v}$	0.01	+	0.243i
$\bar{w}$	-0.014	-	0.058i

Table 17: Mode 12 with velocity expressed in aircraft body frame

Table 18: Product of the left eigenvectors and the input matrix for modes 11, 12 and 13

$\mathtt{w}_{11}{}^T\mathbf{B}_{nr}$				$\mathtt{w}_{12}{}^T\mathbf{B}_{nr}$				$\mathtt{w}_{13}{}^T\mathbf{B}_{nr}$			
δ_{as}	6.67	+	6.47i	δ_{a0}	9.66	+	9.38i	δ_{as}	-7.11	-	6.74i
δ_{ac}	-6.44	+	6.65i	δ_{r0}	6.68	+	0.08i	δ_{ac}	-6.73	+	7.10i
δ_{rc}	4.52	-	0.12i	δ_{e0}	1.93	+	4.02i	δ_{rs}	0.21	+	4.76i
δ_{rs}	0.11	+	4.51i	δ_{t0}	-0.01	-	0.0113i	δ_{rc}	-4.76	+	0.22i
δ_{ec}	-3.03	+	1.47i					δ_{ec}	-3.27	+	1.45i
δ_{es}	-1.48	-	3i					δ_{es}	1.47	+	3.25i

motion of the aircraft is out of phase, creating a higher-frequency mode in the nonrotating frame. On Figure 52, the blue circle illustrates the the instantaneous plane on which the three aircraft are located: The motion of this plane is complete after a full period of the mode. In comparison, Figure 53 shows that the up and down motion, represented by the tether angle ζ is a bout halfway through its cycle. Additional states and their conversion to the nonrotating frame are found in the appendix.

During the simulation of mode 10 the fuselage also sees a circular motion, but it is small in amplitude when compared to the aircraft change of altitude.

Analogously to how mode D had little to no damping, the mode is slightly unstable, and its time to double amplitude is multiple factors of the aircraft period about the fuselage. While the mode is unstable, it is still stabilizable : the main control input that have authority on this mode are the aileron and elevator.

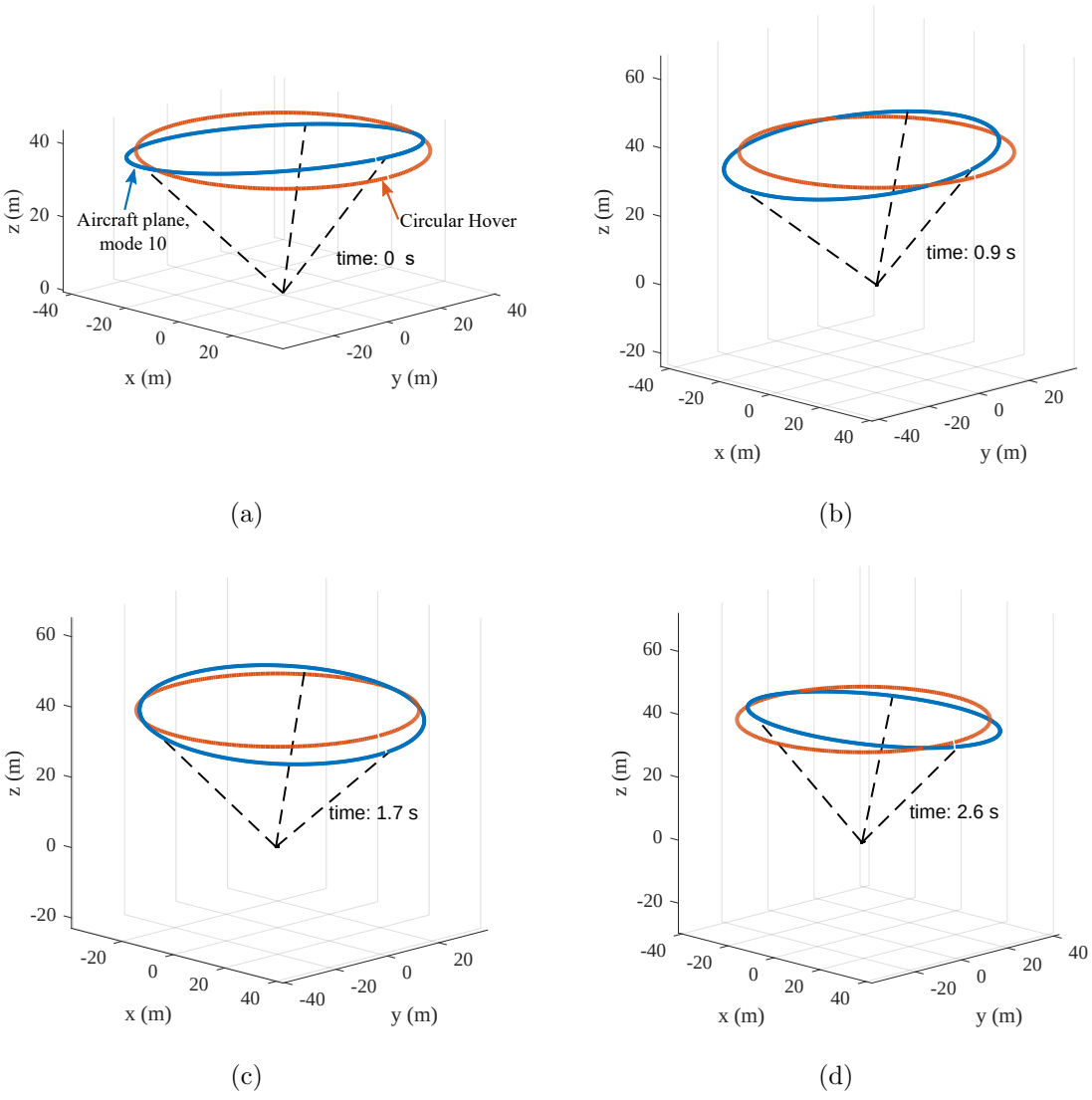

Figure 52: Snapshots of the instantaneous circular flight plane for mode 10

Mode 10.1 0.011 + 1.78i			
$\dot{y}_p$	0.55	+	0i
$\dot{x}_p$	0	-	0.54i
p_s	-0.20	-	0.09i
p_c	-0.09	+	0.20i
q_c	-0.20	-	0.08i
q_s	0.08	+	0.19i

$\mathtt{w}_{10}{}^T\mathbf{B}_{nr}$			
δ_{as}	-10.21	-	4.78i
δ_{ac}	-4.81	+	10.14i
δ_{ec}	8.84	+	2.76i
δ_{es}	-2.74	+	8.78i
δ_{rc}	-0.22	+	0.50i
δ_{rs}	0.49	+	0.18i

Table 19: Mode 10

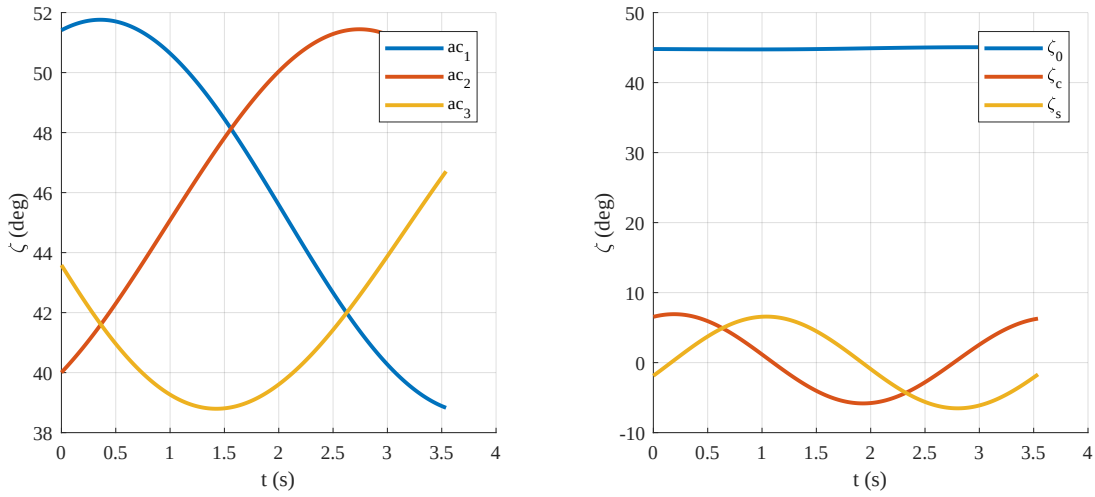

(a) Individual aircraft tether angle

(b) Tether angle in the nonrotating frame

Figure 53: Tether angle ζ during the simulation of mode 10

Modes 8 and 9: cyclic acceleration of the aircraft Mode 8 and 9 show similar characteristics. Their motion are primarily a cyclic acceleration of the aircraft velocity, coupled to a small, anti-clockwise motion of the fuselage. Both modes are stable.

A main difference lies in how the control have authority on the motion: for mode 9, most cyclic control input have authority on the motion, while for mode 8, the cyclic aileron input has the majority of the impact, as shown Table 21.

Modes 7: Scissor mode The mode 7 is a collective mode, dominated the fuselage vertical velocity and tether angle ζ_0. The altitude of the fuselage and of one of the aircraft is shown in 55: The vertical position of the fuselage is out of phase with

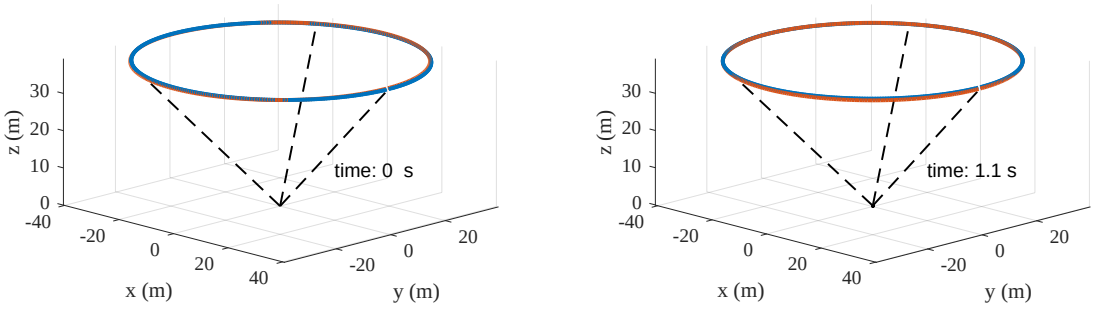

(a) (b)

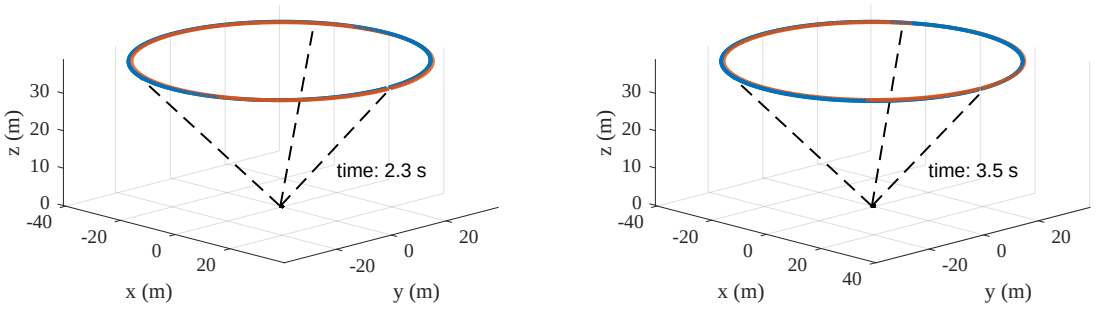

(c) (d)

Figure 54: Snapshots of the instantaneous circular flight plane for mode 9

Mode 9.1 -0.15 + 1.32i			
$\dot{y}_p$	0.6681	+	0i
$\dot{x}_p$	-0.0002	+	0.67i
$\dot{\xi}_s$	-0.0125	+	0.14i
$\dot{\xi}_c$	-0.14	-	0.012i
r_c	0.12	+	0.005i
r_s	0.005	-	0.12i

$\mathtt{w_9}^T\mathbf{B}_{nr}$			
δ_{rs}	0.89	+	0.705i
δ_{rc}	-0.70	+	0.89i
δ_{es}	0.44	+	0.618i
δ_{ec}	0.62	-	0.428i
δ_{as}	-0.15	-	0.057i
δ_{ac}	-0.06	+	0.14i

Table 20: Mode 9

Mode 8.1 -0.20 - 0.90i			
$\dot{y}_p$	-0.4	+	0i
$\dot{x}_p$	0	-	0.4i
ξ_s	-0.15	+	0.23i
ξ_c	-0.23	-	0.15i
ψ_s	0.15	-	0.22i
ψ_c	0.22	+	0.15i

$\mathtt{w_8}^T\mathbf{B}_{nr}$			
δ_{ac}	-5.15	+	7.07i
δ_{as}	-7.07	-	5.16i
δ_{rs}	-1.18	-	1.92i
δ_{rc}	1.92	-	1.18i
δ_{ec}	-0.86	-	1.03i
δ_{es}	1.023	-	0.87i

Table 21: Mode 8

the vertical position of the aircraft. In three dimensions, the motion leads to an increase of the radius of the aircraft circular path when the fuselage is up, hence the comparison to the motion of a "scissor mode", as shown in Figure 56.

The frequency of the mode is very close to the aircraft angular velocity about the fuselage. While this mode is unstable, it is controllable, mainly by the collective action of the aircraft elevator, aileron and rudder.

Mode 7.1 0.013 + 0.89i			
$\dot{z}_p$	0.876	+	0i
ζ_0	0.056	-	0.18i
ϕ_o	-0.08	+	0.16i
θ_0	-0.16	-	0.06i
$\dot{\zeta}_0$	-0.17	-	0.05i

Mode 7.1 0.013 + 0.89i			
$\dot{z}_p$	0.876	+	0i
ζ_0	0.056	-	0.18i
ϕ_o	-0.08	+	0.16i
θ_0	-0.16	-	0.06i
$\bar{u}$	-0.004	-	0.035i

$\mathtt{w_7}^T\mathbf{B}_{nr}$			
δ_{e0}	4.29	+	6.34i
δ_{a0}	6.39	-	3.81i
δ_{r0}	-1.94	+	0.14i

Table 22: Mode 7

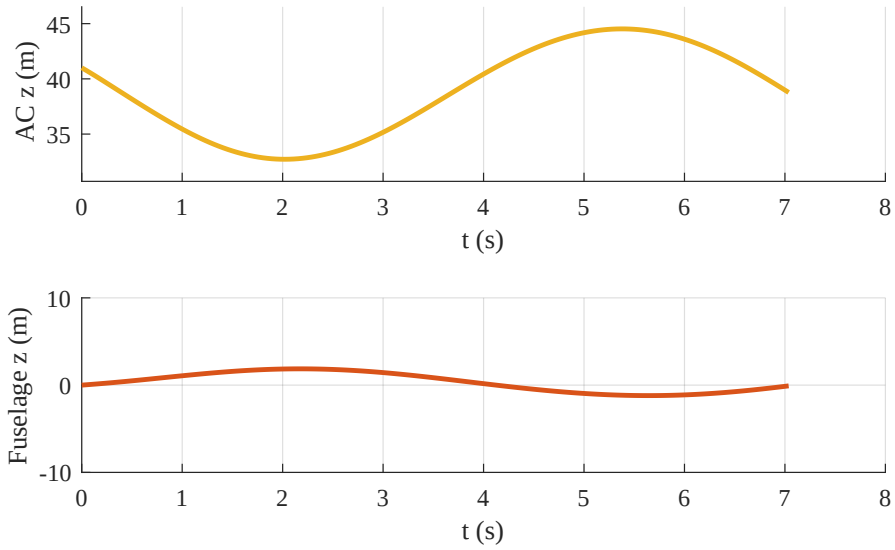

Figure 55: Mode 7: Change of aircraft altitude compared to change of fuselage altitude

Modes 6: Phugoid-type mode The mode 6 is a collective mode, characterized by a up-and-down motion of the suspended mass. Since there is little contribution of the tether angle ζ, the aircraft move up-and-down simultaneously, as shown in Figure 57.

It is interesting to note that the frequency of the mode is very close to the aircraft angular velocity about the fuselage. Similar to mode 7, the mode has very little damping, it is controllable, mainly by the collective action of the aircraft elevator, aileron and rudder.

Modes 5: Cyclic acceleration of the aircraft Mode 5 is a cyclic mode that is similar to modes 8 and 9: is it constituted of a cyclic acceleration of the aircraft axial velocity, and a counter-clockwise motion of the payload. The real-part of the eigenvalue for this root is also the same as for modes 8 and 9.

Modes 3 and mode 4: Fuselage Whirl The modes 3 and 4 are the two cyclic modes with a frequency lower than the the aircraft angular velocity Ω. Both modes are unstable, both with a very large time to double, but they are stabilizable, with

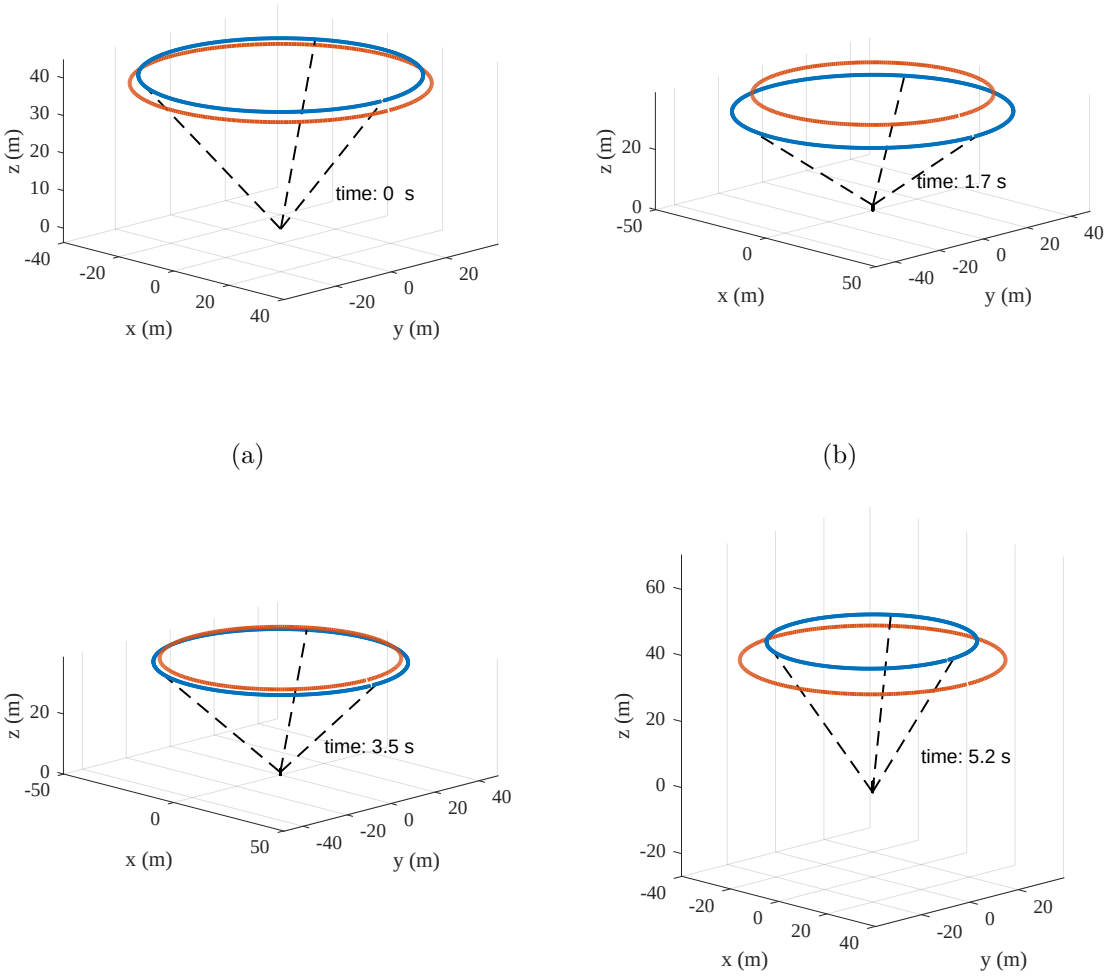

Figure 56: Snapshots of the aircraft circular flight plane for mode 7

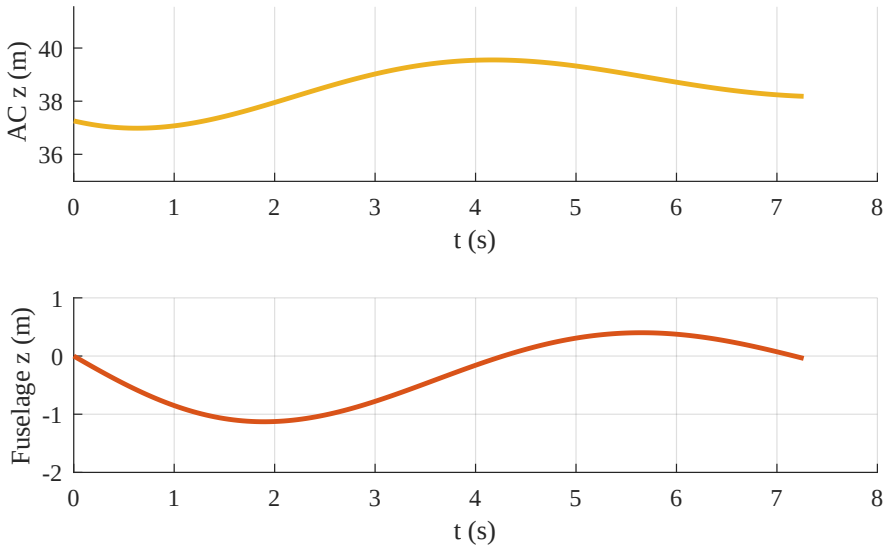

Figure 57: Mode 6: Change of aircraft altitude compared to change of fuselage altitude

Mode 6.1 -0.18 + 0.86i			
$\dot{z}_p$	-0.992	+	0i
ϕ_o	0.038	+	0.038i
θ_0	-0.026	+	0.041i
p_0	0.029	-	0.036i
q_0	0.038	+	0.018i

Mode 6.1 -0.18 + 0.86i			
$\dot{z}_p$	-0.992	+	0i
ϕ_o	0.038	+	0.038i
θ_0	-0.026	+	0.041i
p_0	0.029	-	0.036i
q_0	0.038	+	0.018i
$\bar{u}$	0.021	-	0.026i

$\mathtt{w}_6{}^T\mathbf{B}_{nr}$			
δ_{e0}	-3.42	-	0.88i
δ_{a0}	2.34	-	1.77i
δ_{r0}	1.89	-	0.05i

Table 23: Mode 6

Mode 5.1 -0.20 + 0.65i			
$\dot{y}_p$	0.655	+	0i
$\dot{x}_p$	-0.003	+	0.65i
ξ_s	0.163	+	0.03i
ξ_c	-0.029	+	0.163i
ψ_s	-0.14	-	0.033i
ψ_c	0.034	-	0.139i

$\mathtt{w}_5{}^T\mathbf{B}_{nr}$			
δ_{as}	-1.18	-	0.93i
δ_{ac}	-0.93	+	1.17i
δ_{es}	1.15	+	0.36i
δ_{ec}	0.36	-	1.14i
δ_{rs}	0.67	+	0.33i
δ_{rc}	-0.33	+	0.66i

Table 24: Mode 5

similar contributions from rudder, elevator and aileron input.

One of the main differences between the modes are the fact that the fuselage rotates in a counter-clockwise direction (same as the aircraft) for the mode 4, and in a clockwise direction for the mode 3.

Mode 4.1 0.077 + 0.36i			
$\dot{y}_p$	0.72	+	0i
$\dot{x}_p$	0.027	+	0.69i
ξ_c	0.02	+	0.03i
ξ_s	0.03	-	0.02i
ψ_s	0.006	+	0.03i
ψ_c	-0.026	+	0.006i

$\mathtt{w_4}^T\mathbf{B}_{nr}$			
δ_{rc}	-0.844	-	0.019i
δ_{rs}	-0.046	+	0.819i
δ_{as}	-0.736	-	0.252i
δ_{ac}	-0.267	+	0.696i
δ_{es}	0.679	-	0.251i
δ_{ec}	-0.246	-	0.631i

Table 25: Mode 4

Mode 3.1 0.024 + 0.31i			
$\dot{y}_p$	0.7208	+	0i
$\dot{x}_p$	0.0085	-	0.69i
θ_c	-0.0014	-	0.029i
θ_s	0.0288	-	0.001i
ϕ_s	0.01	+	0.02i
ϕ_c	0.02	-	0.01i

$\mathtt{w_3}^T\mathbf{B}_{nr}$			
δ_{rc}	-0.765	-	0.03i
δ_{es}	0.653	+	0.365i
δ_{rs}	0.018	-	0.737i
δ_{ec}	-0.362	+	0.61i
δ_{as}	-0.655	-	0.194i
δ_{ac}	0.185	-	0.63i

Table 26: Mode 3

Modes 2 Mode 2 is slow collective mode located on the real axis. The frequency and motion of the mode 2 is akin to the one of the modes C and B of the single aircraft tethered to the ground: the main elements driving the motion are the lag of the aircraft with respect to its nominal position and it's axial velocity $\bar{u}$.

This mode is stable and slow, and the control input that have authority is mainly the collective aileron deflection.

Mode 1: Rigid body motion Similar to the single aircraft system, the mode 1, located as $0 + 0i$ is a rigid body mode, comprised of an equal rotation of the aircraft and the tether about the z-axis.

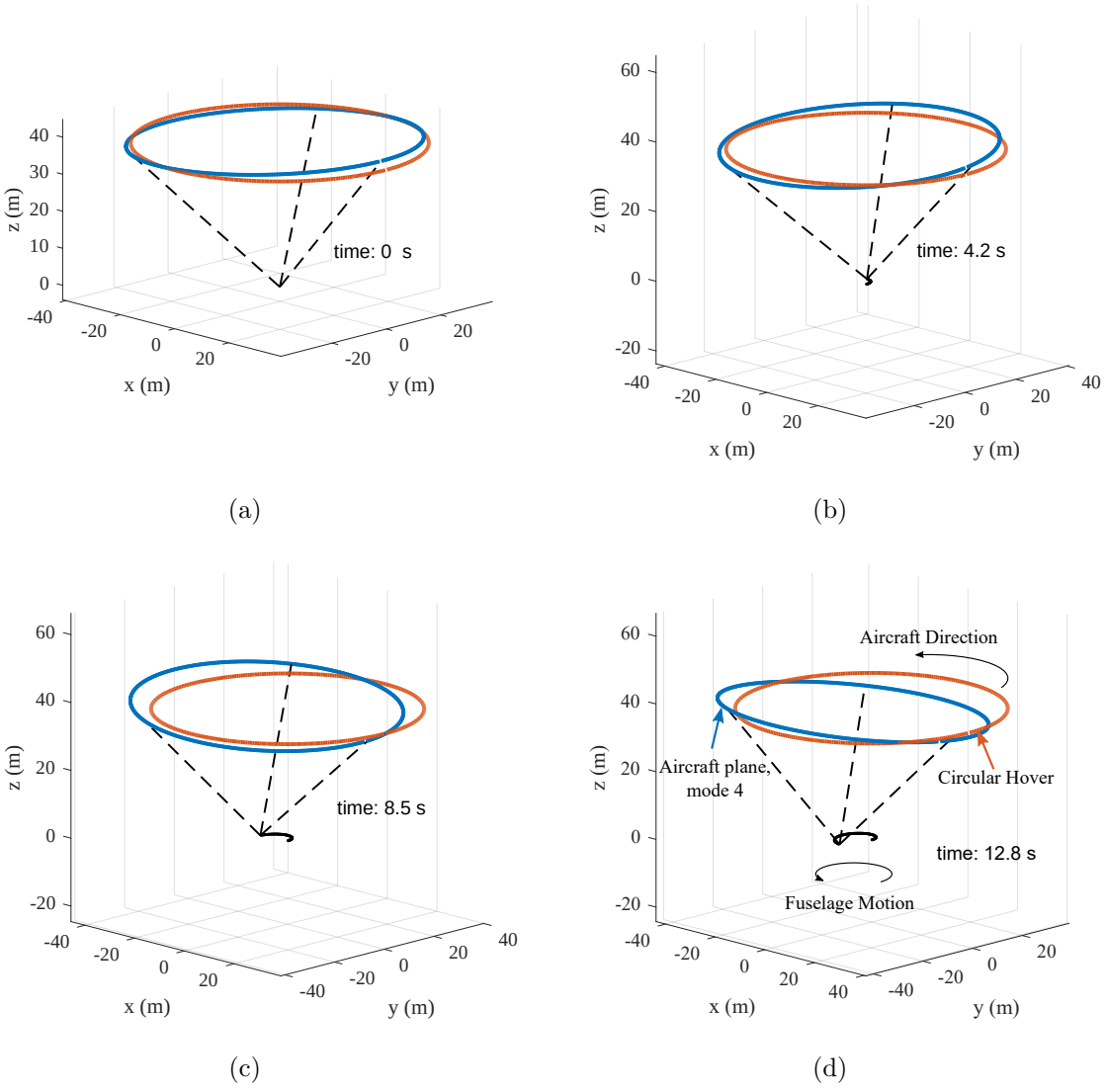

Figure 58: Snapshots of the instantaneous circular flight plane for mode 4

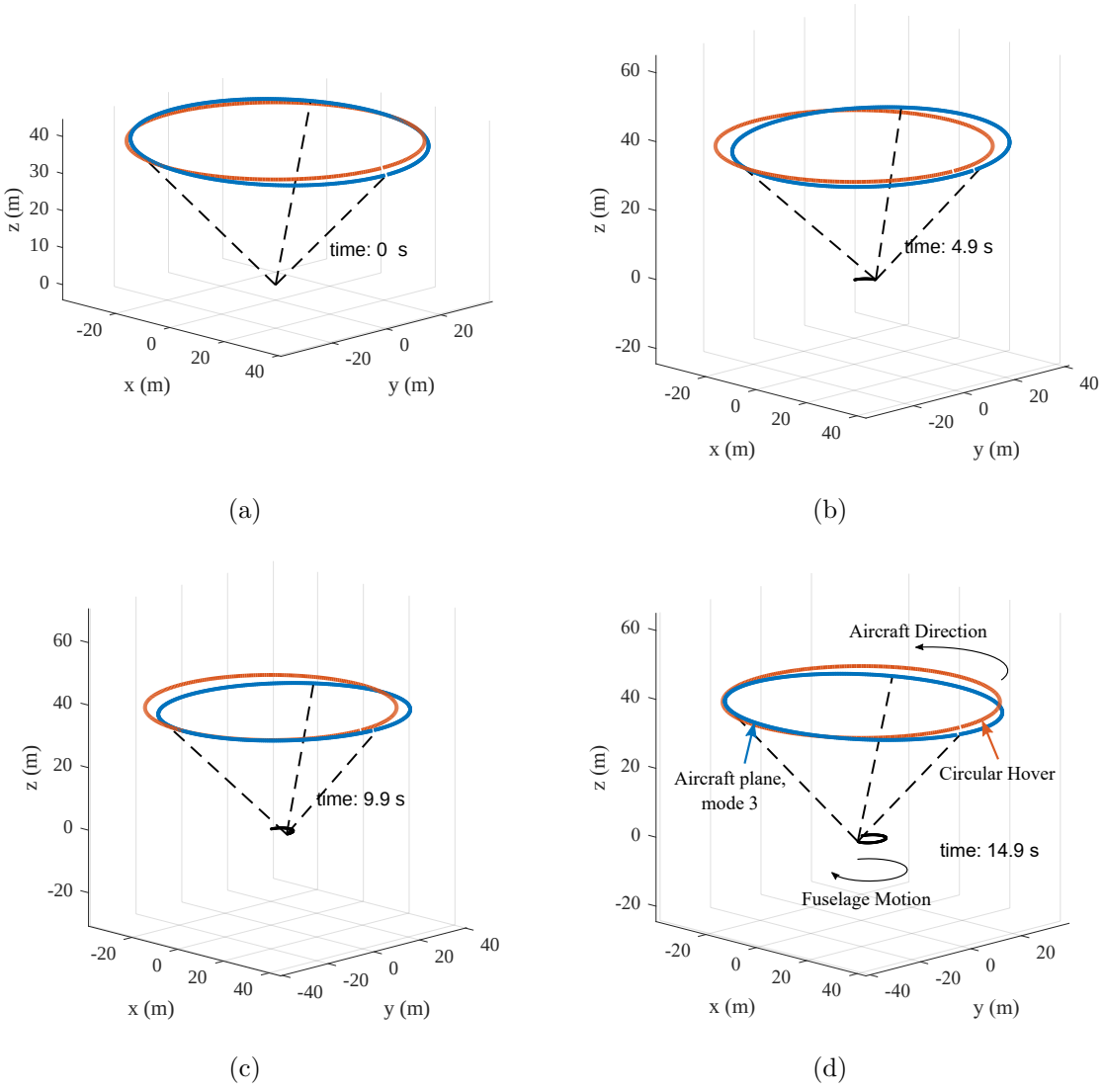

Figure 59: Snapshots of the instantaneous circular flight plane for mode 3

Mode 2.1 -0.23 + 0i			
ξ_0	-0.658	+	0i
ψ_o	0.645	+	0i
ϕ_o	-0.305	+	0i
$\dot{\xi}_0$	0.149	+	0i
r_0	-0.146	+	0i

Mode 2.1 -0.23 + 0i			
ξ_0	-0.658	+	0i
ψ_o	0.645	+	0i
ϕ_o	-0.305	+	0i
r_0	-0.146	+	0i
$\bar{u}$	0.128	+	0i
$\bar{w}$	-0.0227	+	0i
$\bar{v}$	-0.0071	+	0i

$\mathtt{w_2}^T\mathbf{B}_{nr}$			
δ_{a0}	3.519	+	0i
δ_{e0}	-1.288	+	0i
δ_{r0}	-1.03	+	0i

Table 27: Mode 2

5.2.4 Observations on the dynamic modes

5.2.4.1 Observations on the modes of the single aircraft tethered to ground

The use of the conventional aircraft in cruise model is useful to compare the dynamic modes of the single aircraft tethered to the ground. It is observed that the higher frequency modes: roll subsidence, short period and dutch roll kept a similar root. However, the phugoid mode for the tethered aircraft shifted frequency and is now on the imaginary axis, at a frequency of Ω, the angular velocity of the aircraft about the fixed point. Two new spiral types of modes were also observed, both stable.

5.2.4.2 Comparison of the Modes With Different Levels of Complexity

The dynamic modes of the single aircraft tethered to the ground system were compared to the dynamics of the three aircraft tethered to the shared payload in MBC. Even if they represent different characteristics, each models present interesting features. While the three aircraft system presents the full dynamics and has all the modes, the single aircraft system is simpler to analyze and allows to gain more insight in the aircraft motion. Mainly, the single aircraft tethered to the ground model was appropriate to evaluate the higher frequency modes of the system: the coupling

of the motion through the fuselage degrees of freedom did not affect the overall motion of the roll subsidence, short period and dutch roll modes. The transformation to MBC created a trio of modes separated on the imaginary axis by about Ω, as expected from this type of transformation.

5.2.4.3 Dynamic modes of the three aircraft system in multi-blade coordinates

The use of the multi-blade coordinates allowed to successfully analyze the linear, dynamic modes of the three aircraft lifting a shared load, and lead to the following observations.

First, the system exhibits 18 dynamic modes, including a rigid body mode. Seven modes were observed to be derived from the aircraft-dominated modes of roll roll subsidence, short period and dutch roll.

The other, lower frequency modes can be separated in collective and cyclic modes. The collective modes were a series of phugoid mode, a scissor mode as well as a spiral type of motion of the aircraft. The collective characteristic of the mode indicates that all aircraft see a coordinate motion, the suspended fuselage sees a up-and-down motion only, and only the collective control input have authority on the motion.

The series of cyclic modes included a cyclic up-and-down motion of the aircraft, three cyclic acceleration of the aircraft modes as well as two fuselage whirl modes.

Multiple modes were located on the real axis, and some were unstable, but the rate at which the amplitude of the motion increases is in the order of the rate of increase for the spiral dive of the single aircraft in cruise condition. Finally, it was observed that all of the modes were controllable based on the PBH controllability test.

5.2.5 Comparison to discretized tether model

One of the assumptions used in the development if this model was the use of a massless, rigid tether. In order to gain some insight on how these assumptions affect

the dynamic assessment, a discretized, tether model based on the equations used in Rancourt [79] was created. The model assumptions are the following:

- The tether is discretized in five spring-like elements.
- Lift and drag forces are calculated on each elements.
- The mass of each tether element is concentrated at a point which has the associated position and velocity states.

The assumptions for the tether parameters are the following: the tether has a linear mass of 0.1 kg/m and an outside diameter of 6.4 mm, inspired by the data available for the Makani system [2]. The final parameter is the axial rigidity which is harder to evaluate from literature. Among published results, Williams [104] presented the stiffness properties for multiple tether components. Among them, the *Spectra*, with Young modulus of 120 GPa is presented as a material of choice. Assuming that the cable's stiffness property is represented by this value of Young's modulus, a cross-section of 8.3 mm^2 would be required to have the a stiffness of 10^6. This represents a tether which would include a structural component with a diameter of 3.3 mm. This seems appropriate given the data published on the external diameter (6.4 mm). Consequently, an axial stiffness of 1000 kN/ϵ is selected, where ϵ represent the axial deformation, with the units of deformation per unit length ($\Delta L/L$).

In the previous section, it was identified that the single aircraft tethered to the ground model presented interesting dynamic modes and presented simpler analysis requirements, namely by having fewer states and no need to transform in multi-blade coordinates. Consequently, a comparison of the dynamic modes of the single aircraft tethered to the ground with and without tether flexibility is investigated.

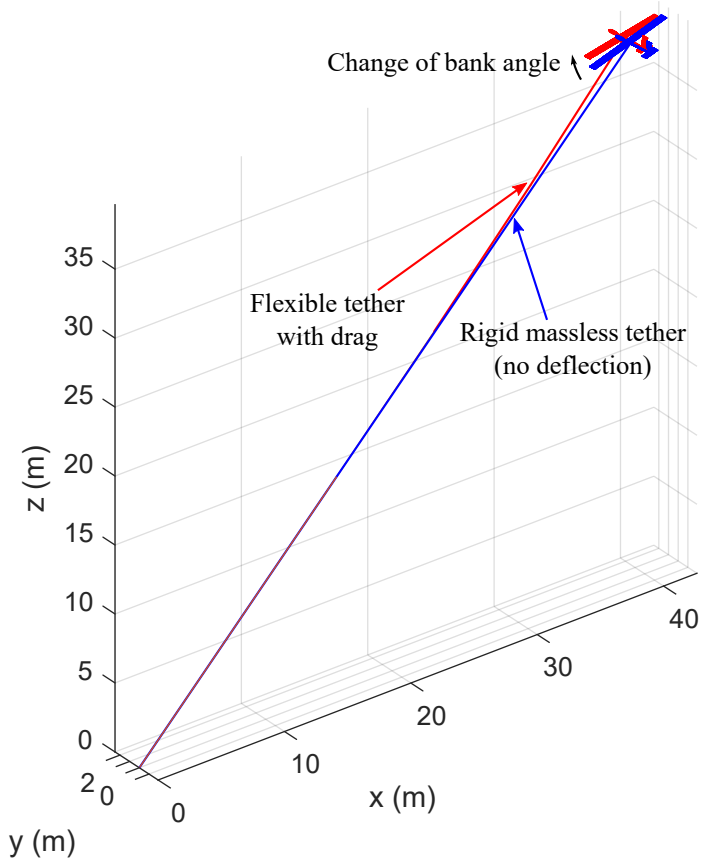

Figure 60: Trim solution for a single aircraft tethered to the ground with a rigid tether (blue) and with a flexible tether (red).

5.2.5.1 Trim Results

First, the trim analysis is presented in Figure 60. In both models, the force vector at the attachment point and the aircraft velocity are imposed. It can be observed that there is a small change in aircraft attitude, mainly the bank angle. This is due to the fact that tether mass creates additional centrifugal load that for which the aircraft has to compensate. Also, it can be observed that the tether deflection is noticeable, but small. For example, the deflection in the y-axis is 1.4 m, which is relatively small compared to the tether length (55 m). Moreover, it is a lot smaller than the deflection seen in the analysis from Williams detailed in the literature.

5.2.5.2 Dynamic Modes

The second analysis of interest in the comparison of the dynamic modes, as seen in Figure 61. The first observation that can be made is that the model with flexible tether has many high frequency modes, going up to almost two orders of magnitude when compared to the mode G. These high frequency modes are related to the tether motion, with little to no damping, which is coherent with the spring-like tether model.

The aircraft dominated modes (E,G and F) do not see a great impact from the choice of the tether models. The mode D, which was the phugoid-type mode, has two equivalent modes for the model with a flexible tether. One of them has greater damping, coherent with the presence of additional drag on the tether, and the other one is a lower frequency mode presenting similar characteristics as mode D. Finally, the spiral-type modes remain similar regardless of the choice of tether model.

5.2.5.3 Observations

The comparison of the the system with rigid or a flexible tether allowed to identify interesting characteristics. First, the contribution of the tether drag, weight and centrifugal loading does not impose a radical change on the steady-state condition, or trim. While these effects might be important for power requirements and performance evaluation, the dynamic implications of the difference of trim conditions are relatively limited.

Second, the model also allowed a comparison of the linear dynamic modal analysis. The presence of flexibility in the tether created a high number of very high frequency modes, mainly dominated by tether motion. This would have an impact on the accuracy of the prediction of the tether force, for example. In counterparts, the presence of those modes would impart a higher computational cost for the simulation, and would represent a challenge for the state conversion to multi-blade coordinates.

While this experiment allowed to highlight some of the limitations of the dynamic

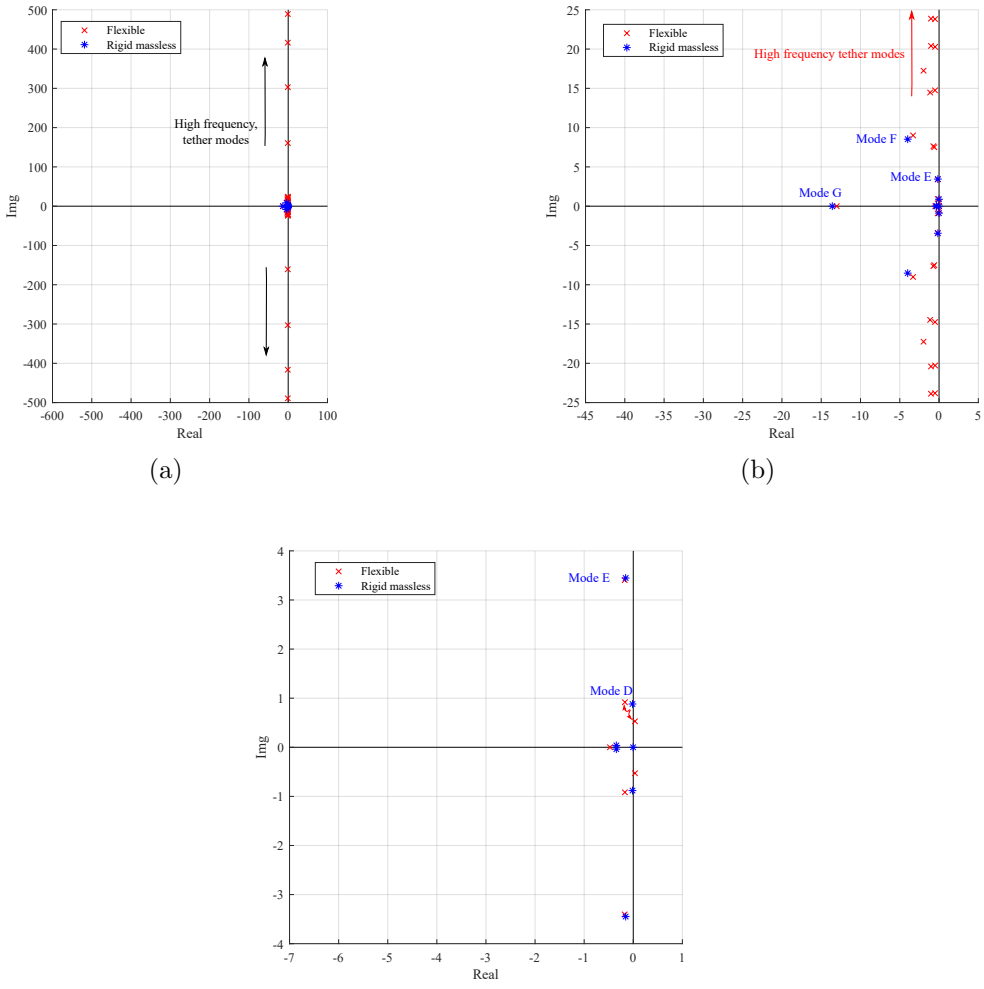

Figure 61: Comparison of the dynamic modes for a single aircraft tethered to the ground with: with and without tether flexibility

model, the aircraft-dominated modes remain close to unchanged. Given the advantages and characteristics of the rigid massless tether model, it is kept for the remaining steps of the analysis.

5.3 Assessment of Tether Attachment Location

For an aircraft with a given aerodynamic layout, the location of the center of gravity represents a variable that can be tuned in order to meet some dynamic criteria. On the case of a tethered aircraft, the location of the attachment point of the tether represents an additional degree of freedom. The present section will present the method to assess the possible location of the tether attachment point.

The overall method presented is a step-like approach. It involves: finding the attachment volume in which trim feasible, finding the subset that leads to a stable aircraft, and finally, rank the feasible cases based on their ability to operate in a steady wind condition.

5.3.1 Trim Constrained Attachment Volume

The first constraint on the tether attachment location is whether it is possible to trim the aircraft in circular hover flight. The related constraints include the maximum aerodynamic coefficients on the lifting surfaces, maximum control deflections, etc.

The limits of the attachment point in the x-y plane are shown in Figure 62. The area is loosely centered around the center of gravity, extends forwards, backwards as well as both in the positive and negative y direction. The first observation from this result is that it would not be possible to attach the aircraft at by the wingtip for this flight condition.

Different constraints are active on the attachment point boundary. Figure 63 illustrates which element constraints the attachment point on the boundary: maximum lift coefficient, maximum control deflections or sideslip angle.

In order to gain insight in the results illustrated in Figure 63, especially for the

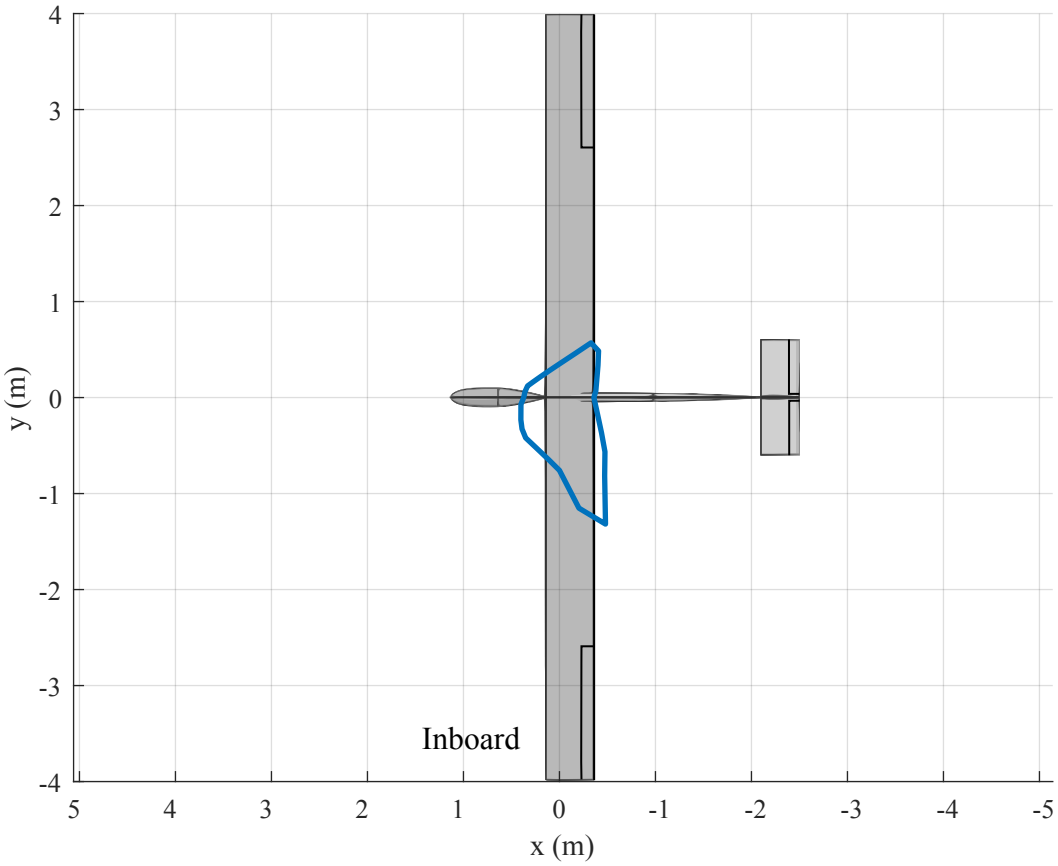

Figure 62: Tether attachment point constrained by trim limits

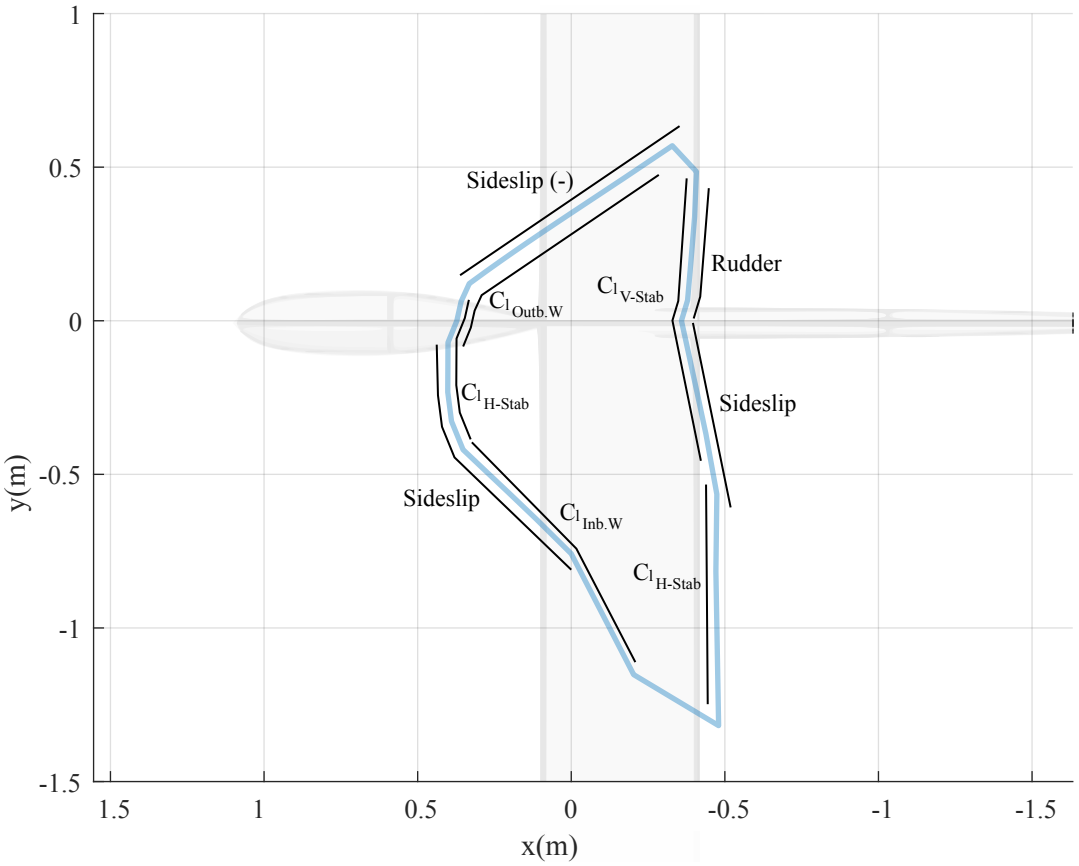

Figure 63: Active constraints on the attachment limit

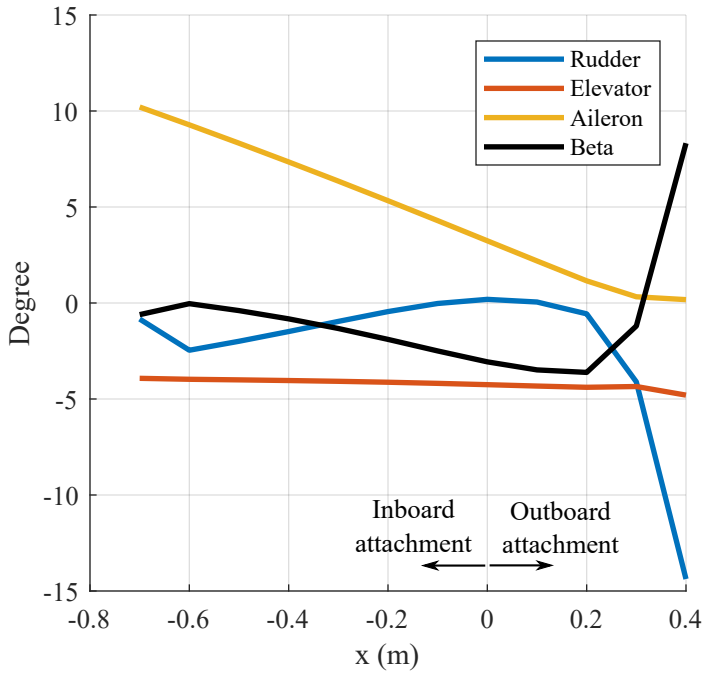

Figure 64: Control deflection as a function of the spanwise tether attachment point.

region inside the feasible domain, a sweep of attachment location along the spanwise axis has been analyzed and the results are illustrates in Figure 64. It can be observed that for this sweep,the aileron deflection (positive with the inboard section aileron down) is monotonically decreasing as the attachment point moves outward. The sideslip angle and the rudder deflection become important limiting factors as the attachment moves to the extremes. Consequently, multiple factors must be considered for possible actuation margins and their selection is not trivial.

5.3.2 Open-Loop Constraints

In the previous subsection, the limit of the tether attachment locations based on the capability to trim were presented. The next step is to identify the attachment point region that leads to desirable open-loop-characteristics.

5.3.2.1 Change with Longitudinal Tether Attachment Location

In order to gain insight on the impact of the tether attachment location on the open-loop characteristics, a sweep of different longitudinal attachment points on the aircraft were analyzed: $x = -0.25, -0.12, 0, 0.125, 0.25\ m$.The roots of the linear approximation of the dynamics are shown in Figure 65. It can be seen that the for the range of tether attachment locations, all the modes remain stable except for two: mode D and mode B.

Mode D The mode D is the tilt of the flight path plane, at the frequency corresponding to the aircraft angular velocity. It is observed that when the attachment point is at -0.125 m, this mode becomes slightly unstable. The real part of the root is less than 2 %. It is understood that the method used to obtain these roots might have numerical errors, and this observation might be the consequence of the limitations of the models.

Mode B The mode B is the spiral-type of motion. It is observed that when the tether attachment point is in front of the center of gravity, the spiral mode becomes unstable. While spiral mode is very slow, it is deemed appropriate that this configuration would be discarded.

In light of these observations, the open-loop requirements were adjusted, following Figure 66. First, the requirement on the single aircraft tethered to the ground system has been shifted by a small value ϵ to include possible numerical errors. For the three aircraft system expressed in MBC, the requirement to have the modes slower than the aircraft angular velocity Ω has been shifted by a value $f > 1$, to account for possible errors on the numerical analysis. Finally, instead of having a constraint to have all the modes stables, the constraint is shifted by a damping ratio of -0.25.

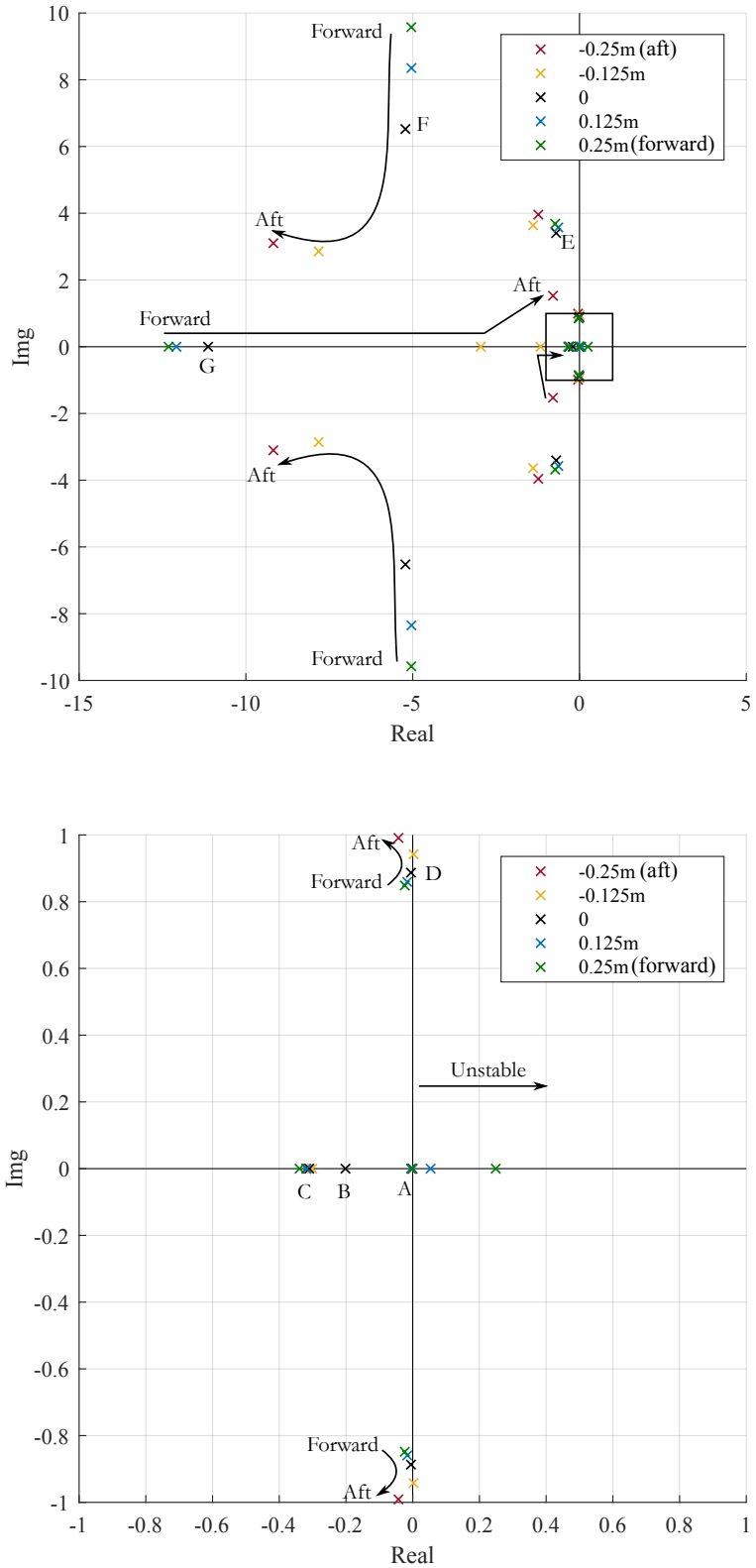

Figure 65: Dynamic modes of a single aircraft tethered to the ground, for varying longitudinal attachment point

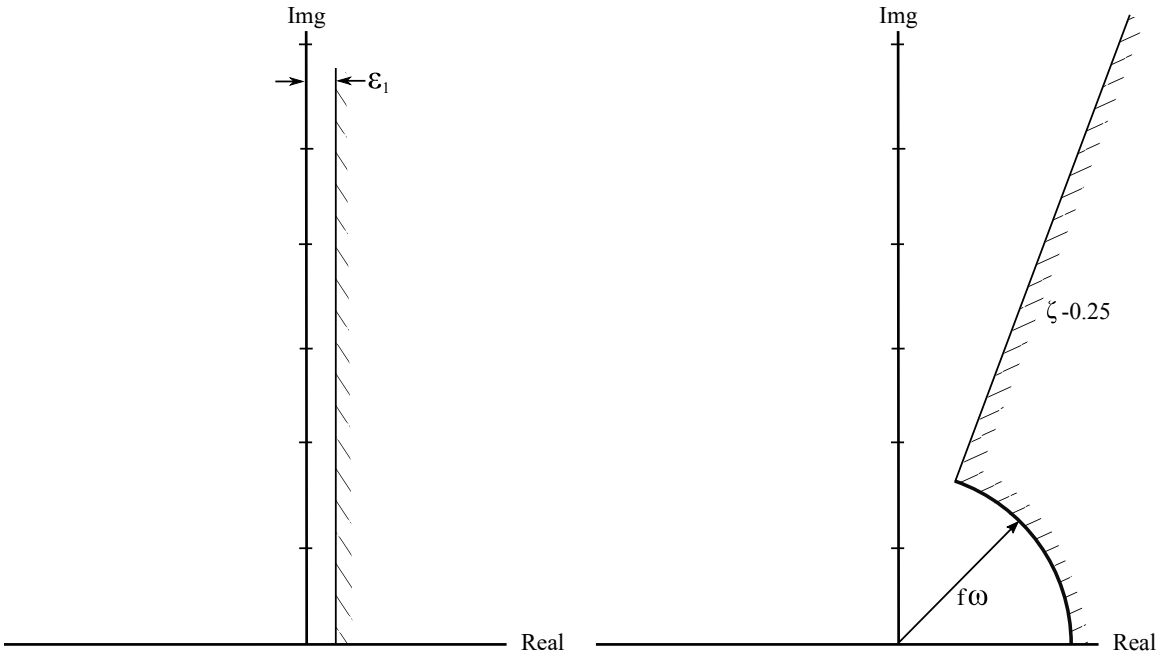

Figure 66: Open loop characteristics required for a single aircraft attached to the ground and for the three aircraft system

The results of the new open-loop constrained attachment region for the nominal flight path are illustrated in Figure 67. The feasible attachment region remains relatively large, and extends to about 0.7 m on the inboard portion of the wing.

5.3.3 Trimmed in Steady Wind Constraint

The analysis of the feasibility to operate under a steady-wind condition while still maintaining positive actuation and lift coefficient margins was performed over the attachment region defined in Figure 67.

First, it was observed that most of the previously defined region leads to feasible results, except a few cases located on the edge of the feasible space described in Figure 67. Some of the cases were able to operate with no margin, which led to a very high cost functions Φ. These cases were discarded from the analysis, but it was noted that attachment points located on the edge of the feasibility space should be treated with care.

The result of the cost function to operate in a steady wind is displayed in Figure

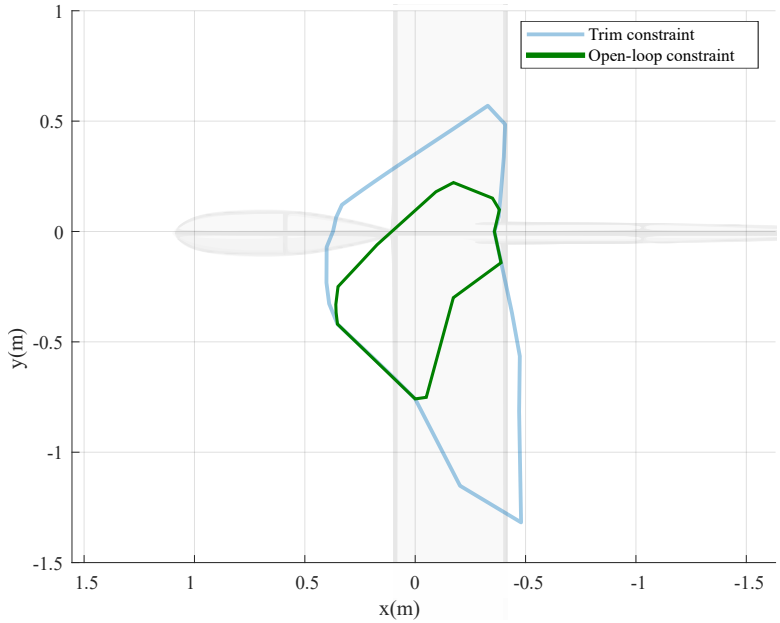

Figure 67: Attachment location constrained by the desirable open loop characteristics

68. Contour lines of cost are displayed on the Figure, and the contours of maximum and minimum values are identified. It can be observed that the minimal cost function is located aft of the center of gravity, very close to the neutral point and extends to both +y and -y directions. Most of the contour lines are parallel to the x-axis, which leads to no differentiation along the span-wise direction.

The process was also applied to the trim results of the steady-state, circular hover cases. The results of the cost function Φ_{hover} are shown in Figure 69. Similar results from the steady-wind conditions are obtained: small variation of the cost along the span, and the optimal solution located slightly aft of the center of gravity. In light of those results, the best tether attachment location for this flight path is rear of the center of gravity, at about x=-0.1 m, y=0 m.

The decomposition of the components that contribute to the cost-to-trim in the no wind condition are illustrated in Figure 70: the maximum lift coefficient seen on the wings, the rudder, elevator and aileron deflection. The trends are relatively homogeneous, but some of the objectives are conflicting. The maximum allowed local

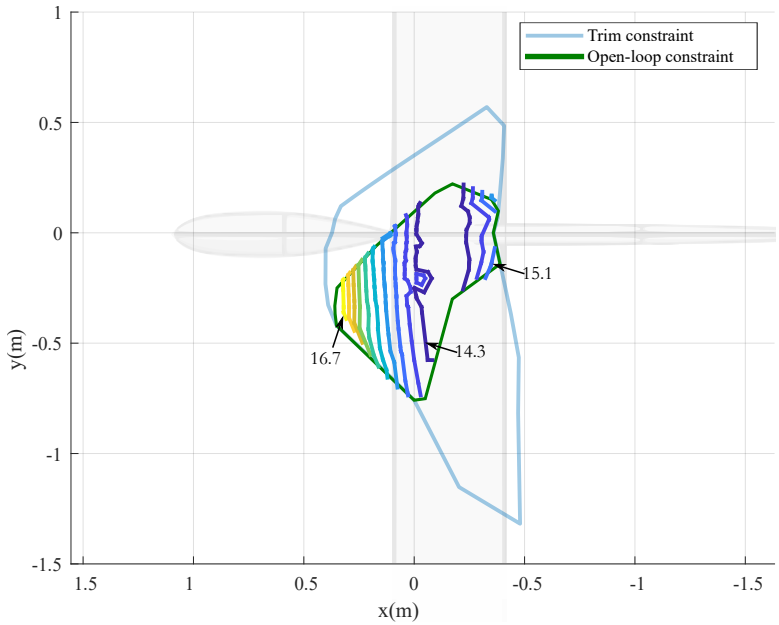

Figure 68: Cost function Φ_{wind} to operate under a steady-wind

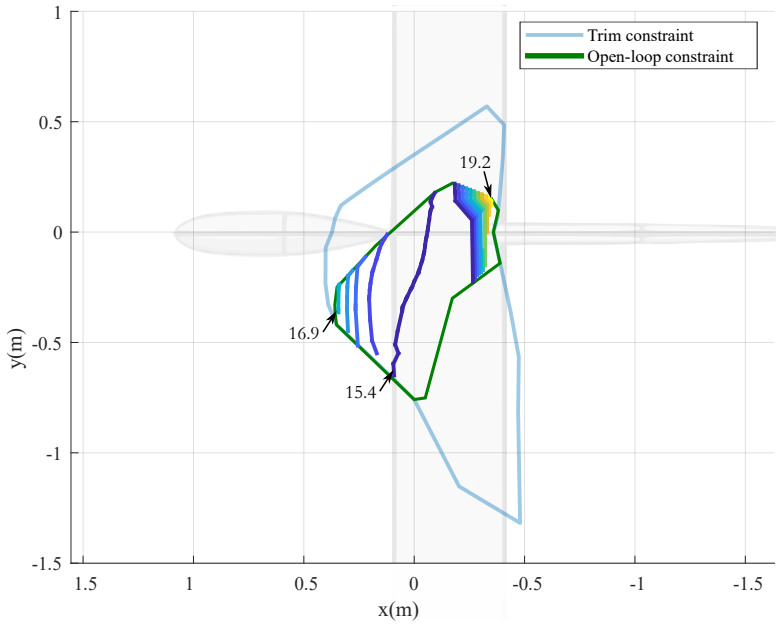

Figure 69: Cost function to operate in trimmed, circular hover Φ_{hover}

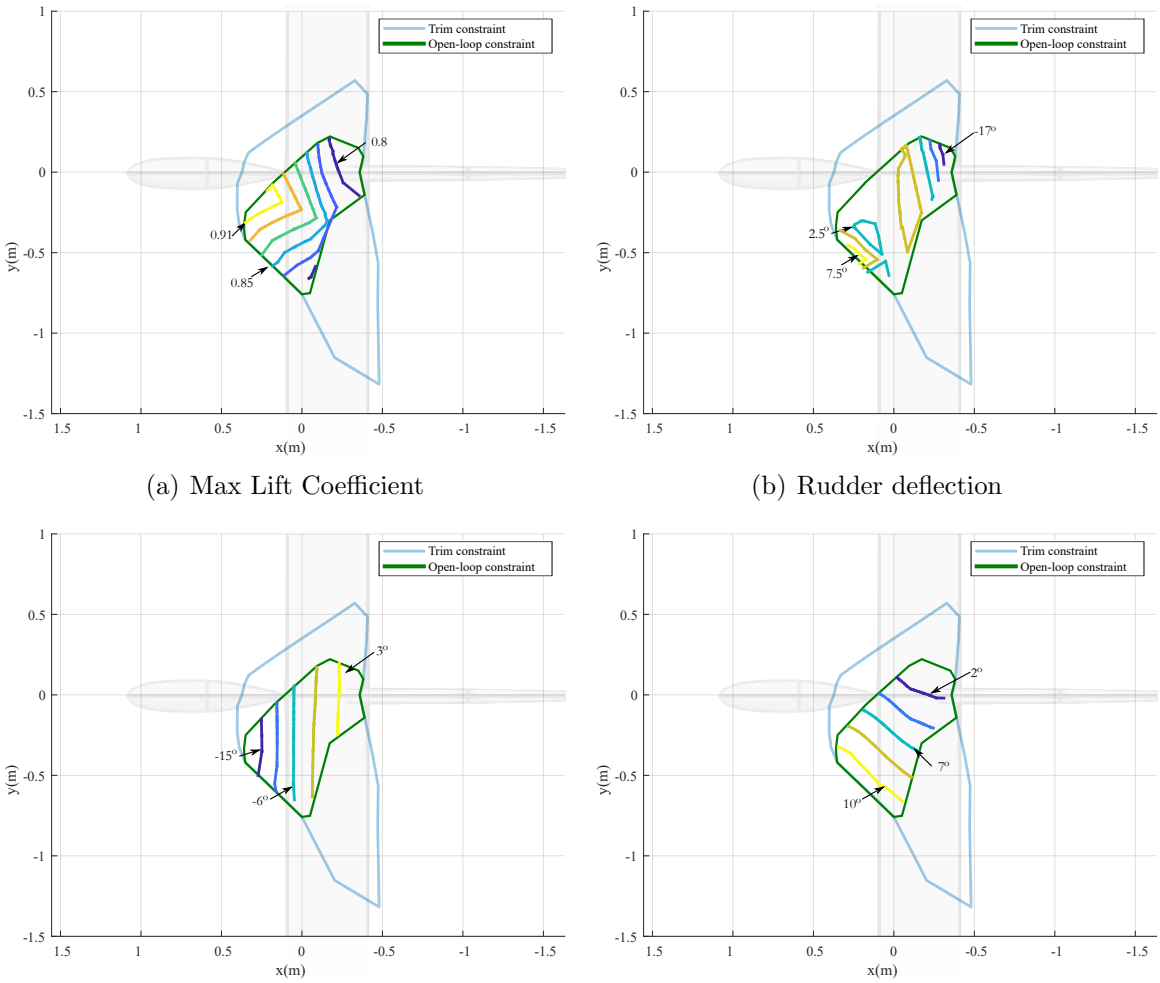

(a) Max Lift Coefficient

(b) Rudder deflection

(c) Elevator deflection

(d) Aileron deflection

Figure 70: Components of the cost-to-trim as a function of the tether attachment point

lift coefficient is 1, and the maximum control deflection is 45°, which shows that the lift coefficient margin is sometimes relatively small, while the actuation margin in hover is always greater than 25°. Consequently, the lift coefficient mainly drives the cost function showed on Figure 69. Finally, from the results of Figure 70, it can be observed that indeed, the point x=-0.1 m, y=0 m is an appropriate tradeoff between the various elements contributing to the cost-to-trim.

5.4 Assessment of Different Flight Paths

The previous section evaluated the nominal flight path, defined by a tether angle of $\zeta = 45°$. The variations around the nominal flight path presented in Chapter 3 are presented in the section.

5.4.1 Results: Comparison of the Off-Design Configurations

The process described for the nominal flight path was repeated for the two off-design conditions. The result of the combined cost to trim in hover and cost to trim with a steady wind condition, Φ_{config}, are illustrated in Figure 71. For all three configurations, the attachment point that minimizes the combined cost to hover and operate in a steady wind condition is aft of the cg. The optimal costs are similar, and do not clearly differentiate between the configurations themselves. The power required could be an additional differentiating factor, for example. Among these three configurations, the configuration with the minimal power required was the nominal flight path with $\zeta = 40°$. The fact that this condition has minimal power is an artifact of the problem setup: the tether both the tether length and the tether angles were imposed.

5.5 Assessment of the Vehicle Performance Through Varying Suspended Mass

As outlined in the first chapter, one application of the tethered aircraft is long endurance flight. The analysis presented in this section tries to find an attachment point that would be applicable to different values of suspended mass.

Three values of suspended mass are studied: 200 kg, 350 kg and the nominal case of 500 kg. The minimal value of 200 kg represents the end of a mission, where all the fuel has been depleted. The results of their individual analyses are illustrated in Figure 72.

The results were combined in an aggregated cost functions over the union of

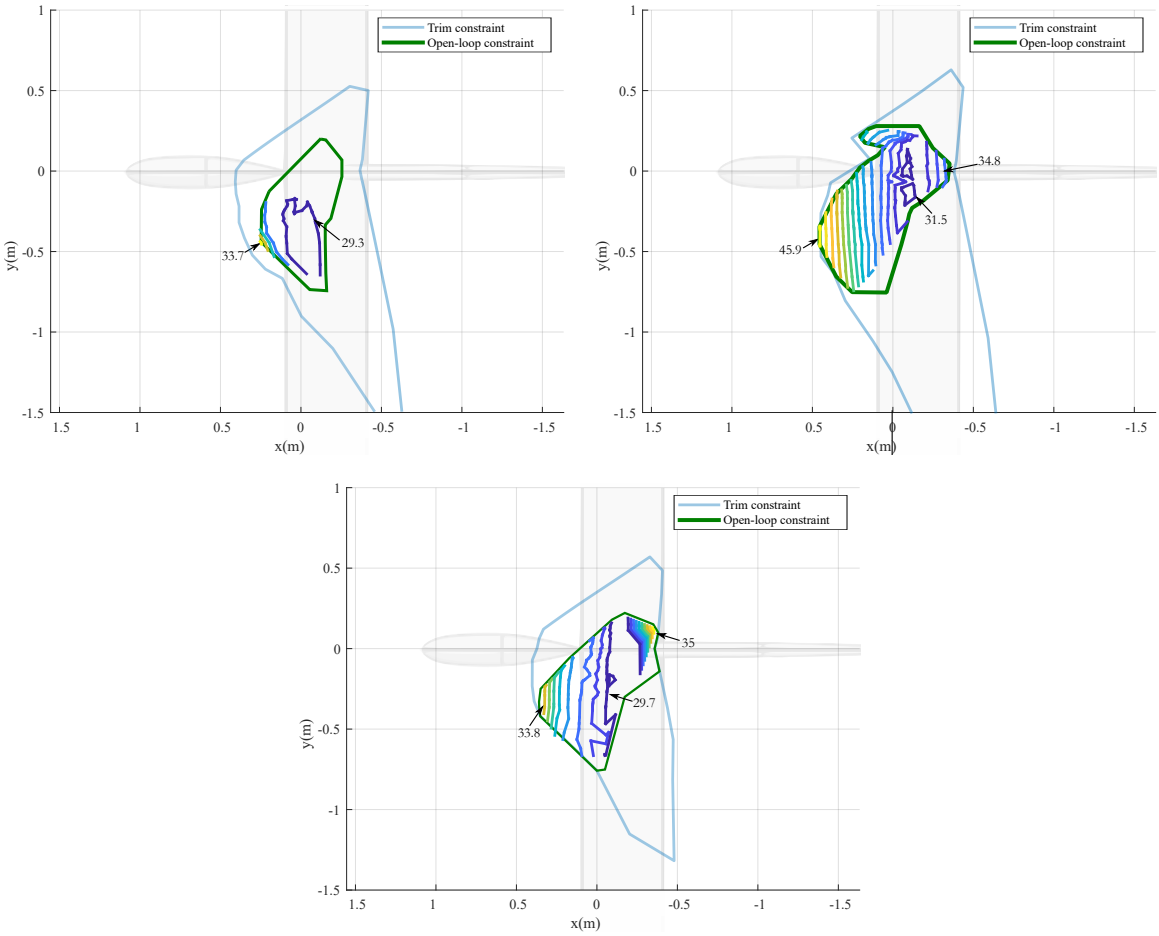

Figure 71: Combined cost function to operate in trimmed, circular hover and with a steady wind for three flight paths Φ_{config}: $\zeta = 40°$ left, $\zeta = 50°$ right and nominal flight path $\zeta = 45°$ at the bottom

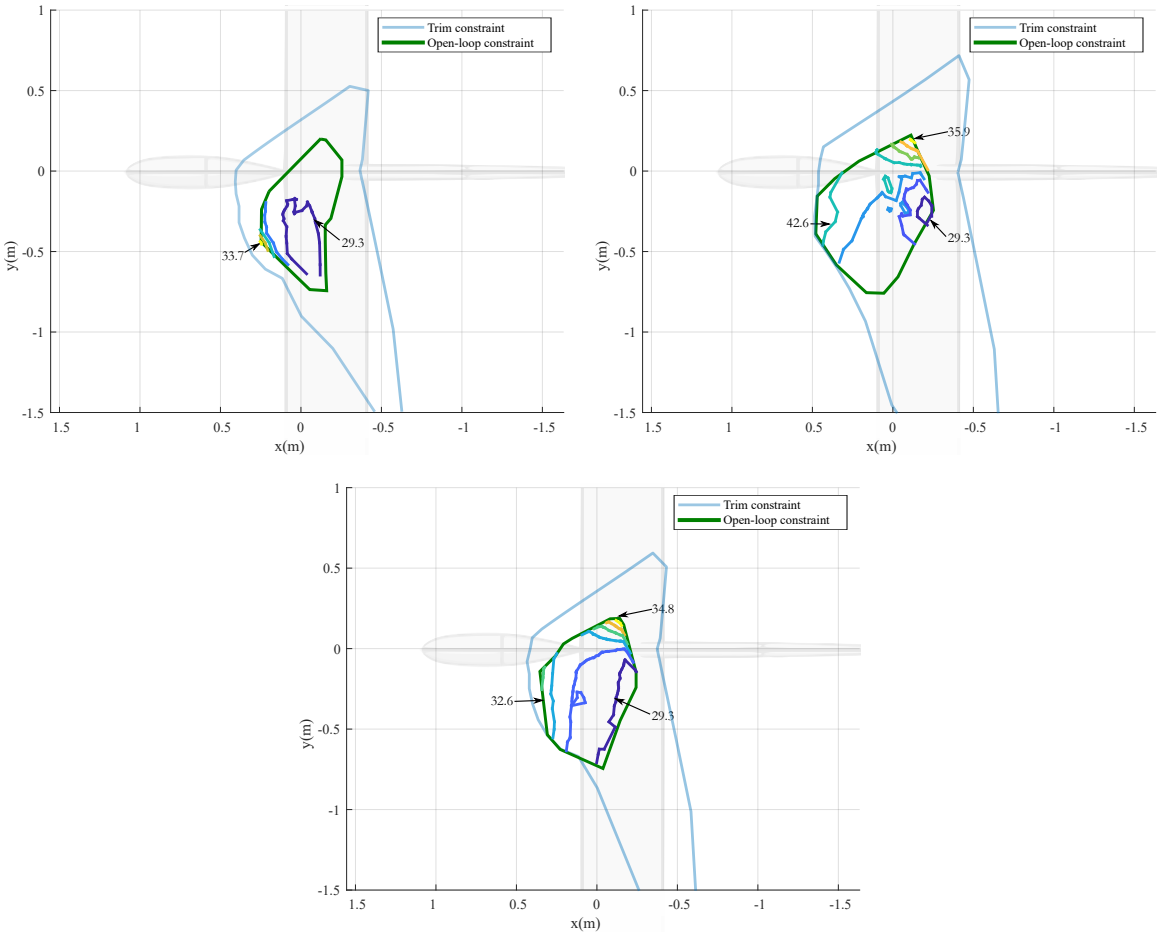

Figure 72: Combined cost function to operate in trimmed, circular hover and with a steady wind for a system with variable suspended mass Φ_{config}: 200 kg left, 350 kg right and the nominal case of 500 kg, bottom.

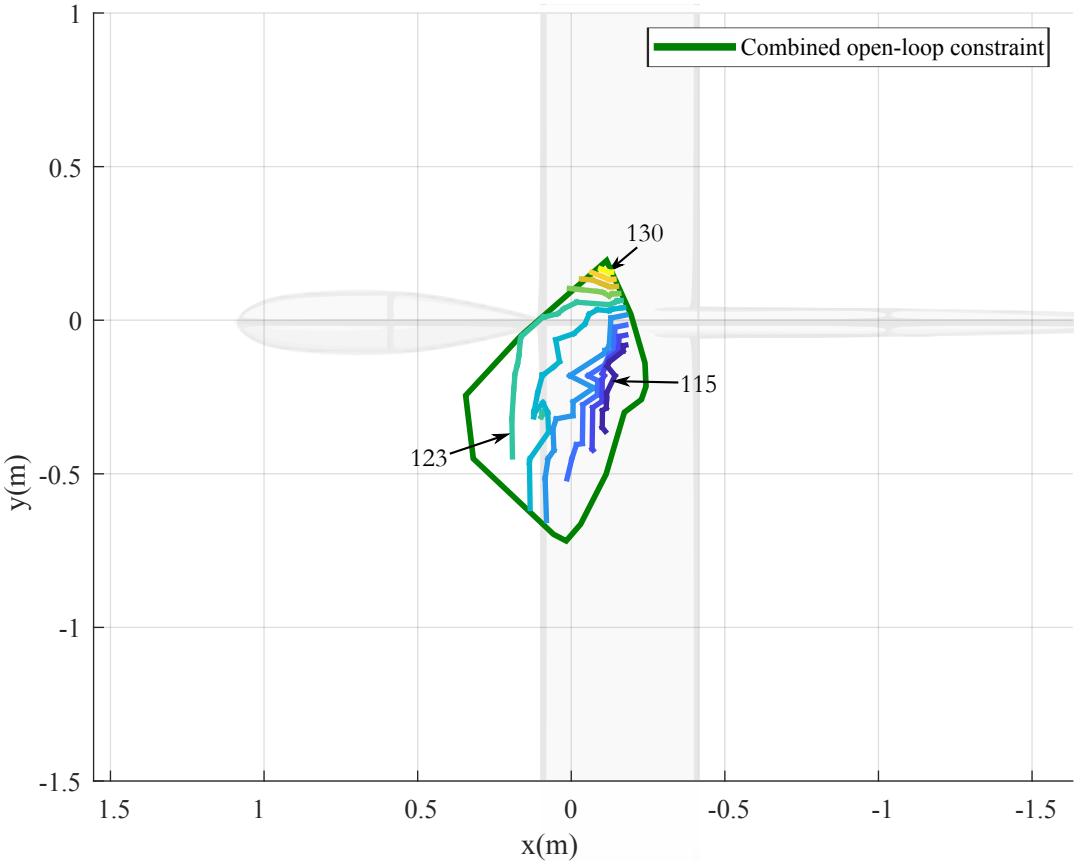

Figure 73: Combined cost function Φ_{total} for the attachment location across the cases defined my a suspended mass of 200 kg, 350 kg and 500 kg.

the open-loop constrained region of the three suspended mass cases. the results are presented in Figure 73. The longitudinal position of the minimal cost function is similar to the other results: slightly aft of the center of gravity. However, along the y-axis, the optimal attachment point is 0.25 m toward the inboard wing.

This result is not trivial to predict. However, it can be noted however that an attachment point defined previously of x=-0.1 m, y=0 m be an other feasible, yet sub-optimal alternative.

5.6 Closed-loop Simulation

The previous sections detailed the selection of different design and operational parameters. The current section will utilize the results, and leverage the dynamic models

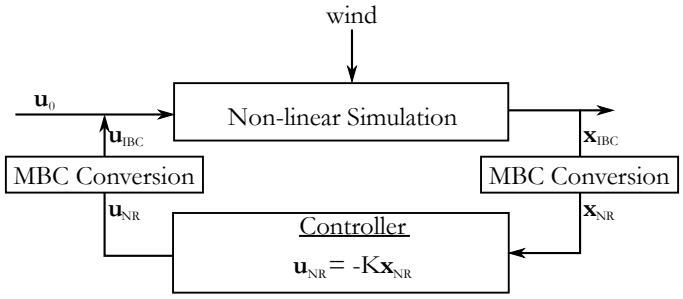

Figure 74: The linear controller in the nonrotating frame requires conversion of the states from IBC to MBC and conversion of the control input from MBC to IBC

in an attempt to include a simple controller on the system and simulate a constant wind step input.

For this case, the tether attachment location was at one of the optimal attachment point identified in the previous section, which is x=-0.1 m, y=0 m.

The model in the multi-blade coordinates allows to generate a simple controller in the nonrotating frame. The controller is linear in the rotating frame, but requires transformations of the states and of the control input back to the nonrotating so that they can be used in the non-linear simulation, as shown in Figure 74.

Many techniques exist for the control of multi-input, multi-output systems. The technique selected for this demonstration is the linear quadratic regulator (LQR), as it allows to give weights to the states and control input based on intuition and engineering judgment, without the need to study each axis individually.

A series of weights were attributed to the various control inputs and states, all in the nonrotating frame. The weight matrices for the controller are detailed in Appendix D. The full-state feedback gain matrix was generated and implemented in the simulation, as per Figure 74. The time marching solution of the states and control input are shown in Figure 75 and 76, and additional results can be found in Appendix F.

The wind profile specified in the Sikorsky 24 hour hover challenge was not specified in the RFP. In counterparts, ADS-33 provides multiples wind profiles, including a step

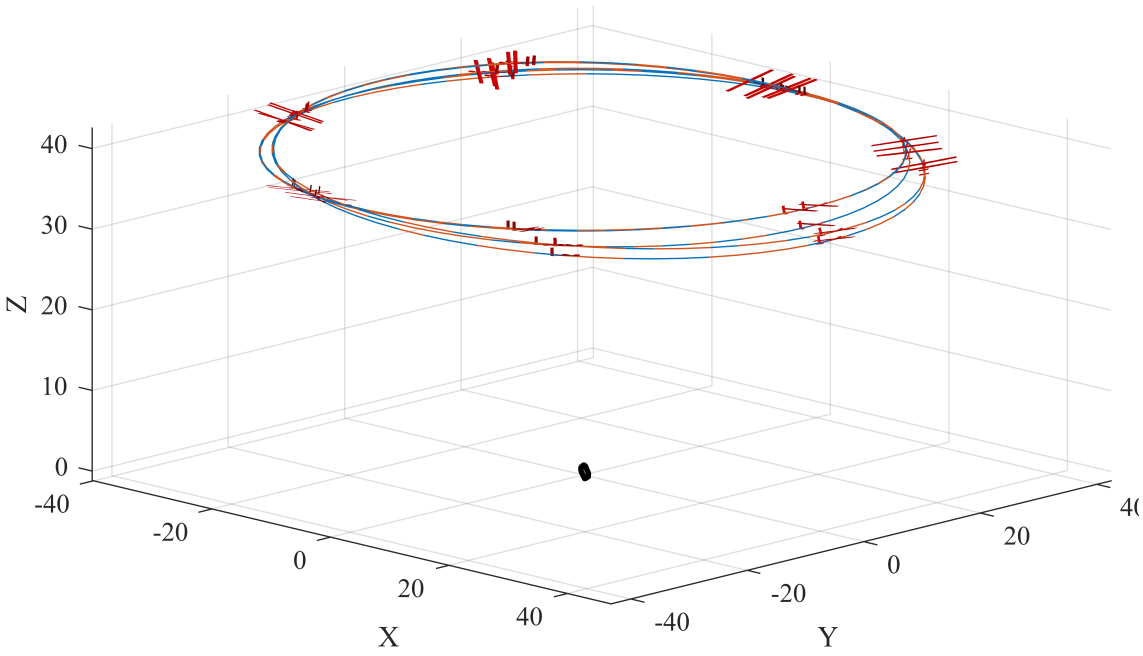

Figure 75: Flight path and snapshot of the orientation of one aircraft during the wind step input

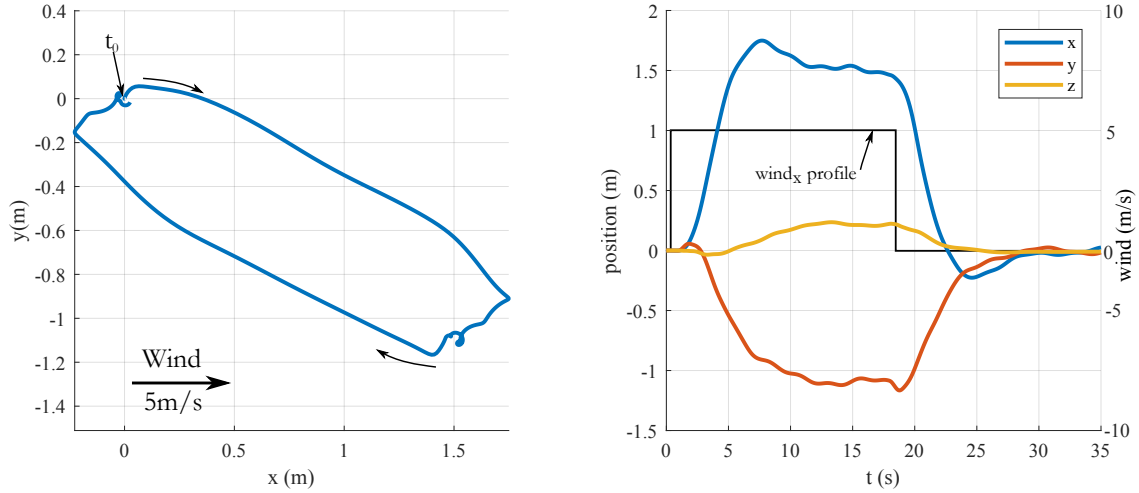

Figure 76: Payload position in space during the wind step input, as well as time marching position expressed in the Cartesian coordinates

input. For this demonstration, a step input was selected as a worse case scenario, and was included as an external disturbance not detected by the system. The wind profile is shown in Figure 76: it is a 5 m/s wind in the x direction from 1 s-18 s. The 17 seconds duration of the profile was based on the system angular velocity: if an aircraft takes in the order of 8 seconds to fly over a full circle, having the wind profile lasting for 17 seconds guarantees at least 2 revolutions during the wind portion of the analysis.

It can be seen that the system is successful at controlling the suspended mass during the maneuver, as it stays well inside a 20 m diameter sphere: the maximal payload excursion is in the order of 2 m. Since the system does not have integrator gain, the suspended mass stays at the disturbed location $x \approx 1.5\ m$, $y \approx -1\ m$ during the windy portion of the maneuver then comes back to the origin once the wind dies down.

The actuation and lift coefficient margins are respected during the flight, including during the transient response, which has not been taken into account in the models so far. It can be observed that the flight path plane described in the nonrotating frame by $\zeta_0, \zeta_c, \zeta_s$ sees a tilt of about -4° in ζ_c, which represents a tilt *towards* the wind.

5.6.1 Quasi-Steady State Approximation

The construction of a full-state feedback system allows evaluate the stationary point of the system under a steady wind condition. The approximation of the dynamics of the system is shown in Equation 97 and 98, where the control input is given by $u_{NR} = -Kx_{nr}$.

$$\dot{x}_{nr} = (A_{nr} - B_{nr}K)x_{nr} + B_{dnr}w \tag{97}$$

$$y_{nr} = C_{nr}x_{nr} + D_{nr}u_{nr} + D_{dnr}w \tag{98}$$

This formulation allows to find an approximation of the states, control input and

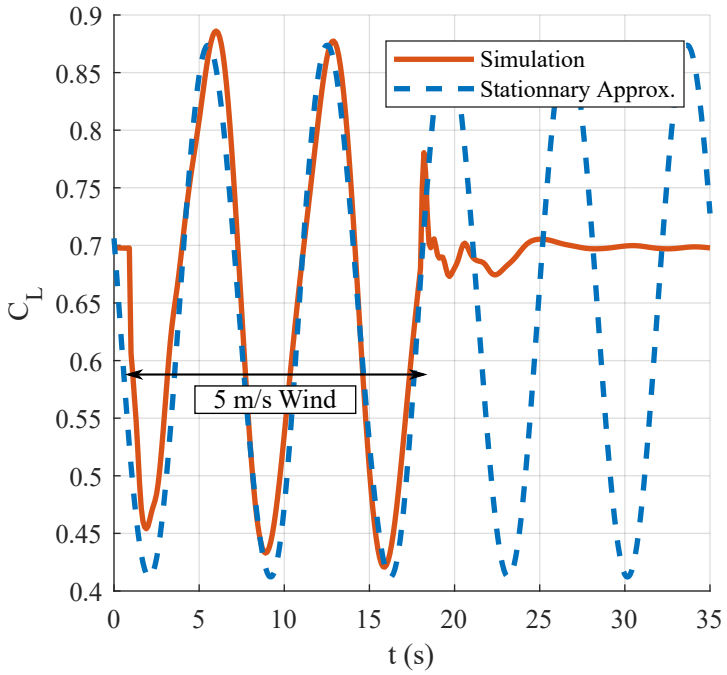

Figure 77: Lift coefficient of aircraft number one as a function of time compared to the approximation of the stationary point

output in the nonrotating frame that lead to quasi-static equilibrium, characterized by $\ddot{q}_{NR} = 0$.

The time signature of the lift coefficient of aircraft number one as it operates under a the 5 m/s wind condition is shown on Figure 77. The simulation results are compared to the approximation derived from the nonrotating results, shown with a dashed line. The approximation of the lift coefficient agrees adequately to the simulation results during the segment of flight where the wind is blowing, and the peak values are deemed acceptable to evaluate the margins required in the methodology described in the previous section.

It is important to note the dynamic model in MBC was generated for a no wind condition. Apparent winds generate periodic actions on the system which limits the applicability of the approximations. The results presented in this section are in agreement to the non-linear simulation results, but caution should be exercised when analysing non-hover conditions.

These results illustrated a successful implementation of a simple linear controller in the rotating frame to control the motion of the tethered aircraft system to a step increase in the wind profile.

CHAPTER VI

CONCLUSION AND CONTRIBUTIONS

Vertical Takeoff and Landing aircraft play an important role in our society by accomplishing a wide range of missions. While some VTOL concepts aim at increasing speed capability, there is an interest to increase the endurance capabilities as well.

The concept of interest is a novel system that uses unmanned electric fixed wing aircraft to lift tethered load. Preliminary studies have suggested that this concept is expected to provide long endurance capabilities. Some advanced flight paths have also been proposed to increase the load lifting capabilities and forward flight speed. However, limited analysis of the system's dynamics has been presented.

This gap in understanding of the system led to the development of the research objective:

Research Objective:

Provide a framework to analyze the dynamics-driven design decisions of a system comprised of multiple aircraft tethered to a shared load during hovering, circular flight.

To meet this research objective, it is hypothesized that three parameters were of great importance in the design: The attachment location of the tether on the aircraft, the nominal flight path parameters and the variation of the payload mass through the mission. In order to answer questions related to those parameters, a dynamic modeling and analysis framework was created.

First, a lower-complexity performance evaluation module was implemented as a means to rapidly differentiate between the various flight path combinations. This

module was based on quasi-steady formulation with only the wing used as lifting surface. It allowed to generate the nominal flight path parameters of interest.

Second a dynamic simulation environment of the three aircraft lifting a shared load was developed. The model is a multi body dynamic model that uses singular perturbation method to represent a rigid tether connection between the aircraft and the suspended load. The aircraft are assumed as rigid body with a sum of aerodynamic forces and moments derived from regression models based on aerodynamic angles, aircraft body rates and control input. The fuselage is assumed as a point mass with only a drag component acting at its center.

The rigid massless tether assumption was compared to the use of a discretized tether model which included elasticity, distributed mass and aerodynamic forces. It was found that the difference in steady state solution as well as in the dynamic modes of the linearized systems was small enough in comparison to the gain in complexity and reduction in computational requirements justified the use of a rigid tether.

The relatively small flight path radius introduced a new challenge for the trim problem, during which the sideslip angle can have an important on the performance. Consequently, the trim was posed as an optimization problem that aimed at maximizing actuation margin.

In order to analyze the full systems dynamics, a linear dynamic representation of the system in multi-blade coordinates was generated. This model allowed to study the dynamics modes, assess the stability and controllability of the linear representation of the system. In order to gain understanding of the system, the newly found dynamic modes were compared to the dynamic modes of a single aircraft in steady-level flight as well as to the dynamic modes of a single aircraft attached to the ground. It was observed that roll subsidence, the short period longitudinal mode and the dutch roll modes were similar for the three configurations.

Finally, an assessment of the systems ability to operated under a steady-wind condition based on the linear approximation in multi-blade coordinates was performed, during which the actuation and lift coefficient margins are evaluated. In order to verify those results, a time marching simulation with a controller in the nonrotating frame was developed, and supported the margin calculations for the case of interest.

The developed framework allowed to answer the research questions related to design parameters specific to the tethered aircraft system. The first research question arouse from the observation that the tether attachment represent a new design degree variable. While the center of gravity of the aircraft represents a possible attachment point, the selection of the tether attachment point presents unique characteristics, which opened to the first research question:

Research Question 1:

What are the benefits of placing the tether attachment point off the center of gravity?

The hypothesis for the research question 1 is the following: **Allowing the tether attachment point to be a design variable can increase the actuation margin during the circular hover flight phase.**

A series of possible attachment points in the plane of the wing were compared. For each point, the ability to trim in circular hover, and trim in a steady wind condition was assessed. Moreover, a open-loop stability criteria was generated based on the observations of the dynamic modes of the system: the dynamic modes of the system must either have a damping ratio greater than -0.25 or have a natural frequency slower than the angular velocity of the system ω.

For each feasible attachment point, an evaluation criteria based on the wing lift coefficient and the actuation margin was used to inform the decision for the most

desirable tether attachment point. Based on this criteria, which was mainly dominated by the wing lift coefficient, the most desirable attachment point is located at about 25% behind the aircraft center of gravity, or very close to the aircraft neutral point. The aircraft center of gravity remains a feasible tether attachment point, with marginal change in the evaluation criteria when compared to the location of the generated optimal point (neutral point).

The power evaluation module allowed to find the flight path parameters that lead to the lowest power requirement in circular, hover flight. It also allowed to observe that there was a relatively small change in power required with change of flight path radius. This observation represents an opportunity to explore off-optimal flight paths that could potentially allow interesting characteristics without imposing a large power penalty on the operation.

This observation lead to the second research question:

Research Question 2:

What are the benefits of selecting a circular flight path radius and velocity different than the one defining the minimum power required?

Due to the presence of tether forces on the aircraft and relatively tight turn radius, the selection of a flight path radius, namely with the coupling from the bank angle presents non-trivial trim characteristics. Consequently, the hypothesis was fir the second research question was formulated as follows:

Selecting a set of nominal flight path parameter that differ from the power-optimal point can increase the actuation margin during the circular hover flight phase.

The exploration of three different flight paths was used to assess the trends in the ability to perform steady level flight. The feasible attachment point region differed

from one nominal flight path to another, but the optimal attachment point based on actuation margin and lift coefficient remained similar to the previously defined attachment point, i.e. located at the neutral point.

Finally, the operation of the system for long endurance hover missions can leads to a large change of suspended load between the takeoff to the landing. This change in the suspended mass can affect the forces acting on the aircraft, analogous to the study of research question 2. This lead to the third and final research question:

Research Question 3:

How does the operation over a varying suspended mass influence the selection of the tether attachment point?

Since the tether attachment point is not modified once the aircraft is in flight, the hypothesis was made that the variation of suspended mass impacted the selection of the attachment point:

The selection of the tether attachment point must take into account the actuation margin and open-loop response constraints imposed by the varying suspended mass.

In order to answer this question, a sweep of suspended mass was performed, and the flight path that lead to the minimum power to operate was found with the use of the power evaluation module. For each configuration, the feasible attachment point region was generated, and the union of those region was created, as a means to represent region that would be usable throughout the mission. Within this region, an aggregate cost function was generated to assess the performance of each feasible point throughout the mission. The most desirable location remain at a similar position, which was about at the location of the aircraft neutral point.

The completion of the research questions and the creation of the modeling and

analysis environment fulfilled the research objective.

6.1 Contributions

Throughout the development of environment used to fulfill the research questions, various methods and tools were created that can be identified as contributions.

Development of a framework to inform design-driven decision The first contribution of this thesis is the development of a framework with the ability to provide information about some of the design-driven decisions for this novel concept. Because the system has multiple design and operational parameters, traditional aircraft design tools cannot be applied directly.

The ability to represent the coupling between the elements is crucial to the this analysis. Consequently, the framework includes performance considerations at the system level, steady-state trim constraints, open-loop characteristics and control margins during steady state wind operations. This framework can be implemented on one configuration, or can be use to find appropriate trade-off when the the system has to face variation in its parameters.

Dynamic modeling environment for multiple tethered aircraft The dynamic simulation environment differs from existing environment due to its flexible characteristic. The use of the singular perturbation method to remove tether elastic degree of freedom can be leveraged and additional components can be added such as additional aircraft, multiple tethered bodies, suspended mass rotational degrees of freedom, etc.

Also, a trim procedure for this environment was proposed with no explicit requirement on side-slip. The trim procedure was also modified to assess the attachment point limits based on steady level circular flight constraints.

Dynamic assessment in the multi-blade coordinates To the knowledge of the author, this is the first instance of an analysis of multiple tethered fixed-wing aircraft done in the multi-blade coordinates. The use of multi-blade coordinates provided multiple advantages.

First, it allowed to study the coupled motion of the aircraft that are flying on a circular flight path and the stationary mass by converting the aircraft's motion to the nonrotating frame. Capturing accurately the coupling the aircraft and the suspended mass is crucial to a good representation of the system.

Second, the use of MBC provided a greater physical insight into the model. Because the aircraft are always in motion, their individual degrees of freedom become hard to analyze. Representing the whole system in the rotating frame allowed the represent the whole period with a single snapshot.

Finally, the representation of the system in the nonrotating frame allowed to include a simple linear controller. While the states and the input may require to be transformed from the rotating frame to the nonrotating frame or vice-versa, the control law's complexity was akin to the one implemented on a multi-input multi-output, linear-time invariant system.

6.2 Future Work

The analysis framework created for this work was selected as being the simplest model that can fulfill the analysis requirements. While this strategy allows a clearer understanding of the dynamic behavior and the dynamic related constraints, it also opens to additional work. Moreover, many aspects of this novel concept still present many unknown characteristics.

Exploration of additional parameters First, the analyses were carried out for a limited number of parameters for the system. Some of these parameters can be

modified and analyses directly with the environment as it is presented in this document. Among them, there are the number of aircraft, different suspended mass, tether length and general flight path parameters. Similarly, additional considerations could be given to the aircraft geometric and aerodynamic parameters.

Integration of Advanced Flight Path The analyses presented in this thesis were focused on the circular hover phase, with some consideration to control power during a steady wind operation. However, Rancourt presented some advanced flight path in hover that can lead to a reduction in induced power. Similar to how the nominal flight path parameters for the circular hover were generated with an external module, advanced flight paths could be generated by an advanced aerodynamic environment's, similar to Rancourt's.

Control Law The control law implemented on the dynamic simulation environment was developed with the objective of having the lowest level of complexity possible. However, developments in on-board computational power for control and autonomy shows promises that many advanced controllers could be used for the control of multiple aircraft tethered to a shared load.

Flight Test Finally, the development of a physical prototype and some flight test of the system represents one of the most interesting future work for the system. Many technical challenges need to be overcome in order to make a successful prototype. It is hoped that the work from this thesis can be used to inform the design of such system and provide analysis tool for its understanding.

APPENDIX A

CANONICAL PROBLEM

A linearization of the equations of motion of the canonical example system was performed around the trimmed condition. The system is characterized by the following equation, expressed in the form $\dot{X} = AX + Bu$:

$$
\begin{bmatrix} \dot{\beta}_1 \\ \dot{\theta}_1 \\ \dot{\beta}_2 \\ \dot{\theta}_2 \\ \dot{x} \\ \dot{z} \\ \ddot{\beta}_1 \\ \ddot{\theta}_1 \\ \ddot{\beta}_2 \\ \ddot{\theta}_2 \\ \ddot{x} \\ \ddot{z} \end{bmatrix} = \begin{bmatrix} 0 & 0 & 0 & 0 & 0 & 0 & 1 & 0 & 0 & 0 & 0 & 0 \\ 0 & 0 & 0 & 0 & 0 & 0 & 0 & 1 & 0 & 0 & 0 & 0 \\ 0 & 0 & 0 & 0 & 0 & 0 & 0 & 0 & 1 & 0 & 0 & 0 \\ 0 & 0 & 0 & 0 & 0 & 0 & 0 & 0 & 0 & 1 & 0 & 0 \\ 0 & 0 & 0 & 0 & 0 & 0 & 0 & 0 & 0 & 0 & 1 & 0 \\ 0 & 0 & 0 & 0 & 0 & 0 & 0 & 0 & 0 & 0 & 0 & 1 \\ -2.2 & 8.85 & -0.53 & -5.8 & 0 & 0 & -1.7 & 0.15 & -0.6 & -0.1 & -0.07 & 0.025 \\ -1.6 & -394 & -1.36 & 83.9 & 0 & 0 & 50.5 & -15 & 6.7 & 1.46 & -0.11 & -15.9 \\ -0.7 & 4.9 & -1.74 & -10.6 & 0 & 0 & -0.7 & 0.1 & -2.2 & -0.23 & -0.03 & -0.39 \\ 1.1 & 86 & 2.78 & -401 & 0 & 0 & -14 & 1.9 & -51.6 & -25 & -0.47 & -15.5 \\ 101 & -47 & 8.23 & 64 & 0 & 0 & 6 & -1 & 7 & 1.18 & -0.04 & 0.8 \\ -0.2 & -177 & 1.2 & -176 & 0 & 0 & 29 & -4 & -14.5 & -3 & 0.99 & -17 \end{bmatrix} \begin{bmatrix} \beta_1 \\ \theta_1 \\ \beta_2 \\ \theta_2 \\ x \\ z \\ \dot{\beta}_1 \\ \dot{\theta}_1 \\ \dot{\beta}_2 \\ \dot{\theta}_2 \\ \dot{x} \\ \dot{z} \end{bmatrix}
$$

$$
+ \begin{bmatrix} 0 & 0 & 0 & 0 \\ 0 & 0 & 0 & 0 \\ 0 & 0 & 0 & 0 \\ 0 & 0 & 0 & 0 \\ 0 & 0 & 0 & 0 \\ 0 & 0 & 0 & 0 \\ 0.78 & -0.23 & -1.3 & 0.014 \\ -87.5 & 1.1 & -0.51 & -0.07 \\ 0.195 & 0.06 & 0.03 & -0.7 \\ 1 & -87.8 & 0.18 & 0.23 \\ -1.9 & 2. & -0.31 & -0.14 \\ -6.04 & -6.6 & -0.92 & 0.43; \end{bmatrix} \begin{bmatrix} \delta_{e1} \\ RPM_1 \\ \delta_{e2} \\ RPM_2 \end{bmatrix} \quad (99)
$$

APPENDIX B

PROPELLER GEOMETRY

Radius (m)	Chord (m)	Pitch (deg)
0.058	0.056	66.6
0.076	0.070	59.8
0.093	0.080	54
0.11	0.086	49
0.12	0.089	44.8
0.14	0.090	41.1
0.16	0.090	38
0.18	0.088	35.3
0.19	0.086	32.9
0.21	0.083	30.8
0.23	0.080	29
0.25	0.077	27.4
0.26	0.073	25.9
0.28	0.069	24.6
0.30	0.065	23.4
0.32	0.060	22.3
0.33	0.054	21.3
0.35	0.046	20.4
0.37	0.037	19.5
0.39	0.022	18.7
0.40	0.012	18.3

APPENDIX C

KINEMATIC CONVERSION

This section will present additional details on the kinematic conversion.

C.1 Aircraft velocity in the body frame

The first step, Equation (49) described the aircraft velocity in the body frame. The term $\frac{d}{dt}(T_{C\to B}T_{B\to H})$ is derived here:

$$\frac{d}{dt}(T_{C\to B}T_{B\to H}) = \begin{bmatrix} a_{11} & a_{12} & a_{13} \\ a_{21} & a_{22} & a_{23} \\ a_{31} & a_{32} & a_{33} \end{bmatrix} \tag{100}$$

with:

$$\begin{aligned}
a_{11} &= c_\theta s_\psi \dot{\psi} + c_\psi s_\theta \dot{\theta} \\
a_{12} &= -s_\phi s_\psi \dot{\phi} - c_\phi c_\psi s_\theta \dot{\phi} + c_\phi c_\psi \dot{\psi} + s_\phi s_\psi s_\theta \dot{\psi} - c_\psi c_\theta s_\phi \dot{\theta} \\
a_{13} &= -c_\phi s_\psi \dot{\phi} + c_\psi s_\phi s_\theta \dot{\phi} - c_\psi s_\phi \dot{\psi} + c_\phi s_\psi s_\theta \dot{\psi} - c_\phi c_\psi c_\theta \dot{\theta} \\
a_{21} &= c_\psi c_\theta \dot{\psi} - s_\psi s_\theta \dot{\theta} \\
a_{22} &= -c_\psi s_\phi \dot{\phi} + c_\phi s_\psi s_\theta \dot{\phi} - c_\phi s_\psi \dot{\psi} + c_\psi s_\phi s_\theta \dot{\psi} + c_\theta s_\phi s_\psi \dot{\theta} \\
a_{23} &= -c_\phi c_\psi \dot{\phi} - s_\phi s_\psi s_\theta \dot{\phi} + s_\phi s_\psi \dot{\psi} + c_\phi c_\psi s_\theta \dot{\psi} + c_\phi c_\theta s_\psi \dot{\theta} \\
a_{31} &= c_\theta \dot{\theta} \\
a_{32} &= -c_\phi c_\theta \dot{\phi} + s_\phi s_\theta \dot{\theta} \\
a_{33} &= c_\theta s_\phi \dot{\phi} + c_\phi s_\theta \dot{\theta}
\end{aligned}$$

C.2 Aircraft state derivatives conversion to the spherical-like coordinates

In the Equation 50, the expression for the time derivative of a matrices is the following:

$$\frac{d}{dt}\begin{bmatrix} Lc_\xi c_\zeta & -L(1+\epsilon)s_\xi c_\zeta & -L(1+\epsilon)c_\xi s\zeta \\ Ls_\xi c_\zeta & L(1+\epsilon)c_\xi c_\zeta & -L(1+\epsilon)s_\xi s_\zeta \\ Ls_\zeta & 0 & L(1+\epsilon)c_\zeta \end{bmatrix} = L\begin{bmatrix} b_{11} & b_{12} & b_{13} \\ b_{21} & b_{22} & b_{23} \\ b_{31} & b_{32} & b_{33} \end{bmatrix} \tag{101}$$

with:

$$\begin{aligned}
b_{11} &= -c_\zeta s_\xi \dot{\xi} - c_\xi s_\zeta \dot{\zeta} \\
b_{12} &= -c_\zeta s_\xi \dot{\epsilon} - c_\xi c_\zeta (1+\epsilon)\dot{\xi} + (1+\epsilon)s_\xi s_\zeta \dot{\zeta} \\
b_{13} &= -c_\xi s_\zeta \dot{\epsilon} + (1+\epsilon)s_\xi s_\zeta \dot{\xi} - c_\xi c_\zeta (1+\epsilon)\dot{\zeta} \\
b_{21} &= c_\xi c_\zeta \dot{\xi} - s_\xi s_\zeta \dot{\zeta} \\
b_{22} &= c_\xi c_\zeta \dot{\epsilon} - c_\zeta (1+\epsilon)s_\xi \dot{\xi} - c_\xi (1+\epsilon)s_\zeta \dot{\zeta} \\
b_{23} &= -s_\xi s_\zeta \dot{\epsilon} - c_\xi (1+\epsilon)s_\zeta \dot{\xi} - c_\zeta (1+\epsilon)s_\xi \dot{\zeta} \\
b_{31} &= c_\zeta \dot{\zeta} \\
b_{32} &= 0 \\
b_{33} &= c_\zeta \dot{\epsilon} - (1+\epsilon)s_\zeta \dot{\zeta}
\end{aligned}$$

Similarly, still in Equation 50, the expression for the second time derivative of the rotation matrix $\frac{d^2}{dt^2}(T_{C\to B}T_{B\to H})$ is the following:

$$\frac{d^2}{dt^2}(T_{C\to B}T_{B\to H}) = \begin{bmatrix} c_{11} & c_{12} & c_{13} \\ c_{21} & c_{22} & c_{23} \\ c_{31} & c_{32} & c_{33} \end{bmatrix} \tag{102}$$

with:

$$
\begin{aligned}
c_{11} =& c_\psi c_\theta \dot{\psi}^2 - 2 s_\psi s_\theta \dot{\psi}\dot{\theta} + c_\psi c_\theta \dot{\theta}^2 + c_\theta s_\psi \ddot{\psi} + c_\psi s_\theta \ddot{\theta} \\
c_{12} =& - c_\phi s_\psi \dot{\phi}^2 + c_\psi s_\phi s_\theta \dot{\phi}^2 - 2 c_\psi s_\phi \dot{\phi}\dot{\psi} + 2 c_\phi s_\psi s_\theta \dot{\phi}\dot{\psi} - c_\phi s_\psi \dot{\psi}^2 + c_\psi s_\phi s_\theta \dot{\psi}^2 \\
& - 2 c_\phi c_\psi c_\theta \dot{\phi}\dot{\theta} + 2 c_\theta s_\phi s_\psi \dot{\psi}\dot{\theta} + c_\psi s_\phi s_\theta \dot{\theta}^2 - s_\phi s_\psi \ddot{\phi} - c_\phi c_\psi s_\theta \ddot{\phi} + c_\phi c_\psi \ddot{\psi} + s_\phi s_\psi s_\theta \ddot{\psi} - c_\psi c_\theta s_\phi \ddot{\theta} \\
c_{13} =& s_\phi s_\psi \dot{\phi}^2 + c_\phi c_\psi s_\theta \dot{\phi}^2 - 2 c_\phi c_\psi \dot{\phi}\dot{\psi} - 2 s_\phi s_\psi s_\theta \dot{\phi}\dot{\psi} + s_\phi s_\psi \dot{\psi}^2 + c_\phi c_\psi s_\theta \dot{\psi}^2 + \\
& 2 c_\psi c_\theta s_\phi \dot{\phi}\dot{\theta} + 2 c_\phi c_\theta s_\psi \dot{\psi}\dot{\theta} + c_\phi c_\psi s_\theta \dot{\theta}^2 - c_\phi s_\psi \ddot{\phi} + c_\psi s_\phi s_\theta \ddot{\phi} - c_\psi s_\phi \ddot{\psi} + c_\phi s_\psi s_\theta \ddot{\psi} - c_\phi c_\psi c_\theta \ddot{\theta} \\
c_{21} =& - c_\theta s_\psi \dot{\psi}^2 - 2 c_\psi s_\theta \dot{\psi}\dot{\theta} - c_\theta s_\psi \dot{\theta}^2 + c_\psi c_\theta \ddot{\psi} - s_\psi s_\theta \ddot{\theta} \\
c_{22} =& c_\phi c_\psi \dot{\phi}^2 - s_\phi s_\psi s_\theta \dot{\phi}^2 - 2 s_\phi s_\psi \dot{\phi}\dot{\psi} + 2 c_\phi c_\psi s_\theta \dot{\phi}\dot{\psi} + c_\phi c_\psi \dot{\psi}^2 - s_\phi s_\psi s_\theta \dot{\psi}^2 + 2 c_\phi c_\theta s_\psi \dot{\phi}\dot{\theta} + \\
& 2 c_\psi c_\theta s_\phi \dot{\psi}\dot{\theta} - s_\phi s_\psi s_\theta \dot{\theta}^2 + c_\psi s_\phi \ddot{\phi} + c_\phi s_\psi s_\theta \ddot{\phi} + c_\phi s_\psi \ddot{\psi} + c_\psi s_\phi s_\theta \ddot{\psi} + c_\theta s_\phi s_\psi \ddot{\theta} \\
c_{23} =& c_\psi s_\phi \dot{\phi}^2 - c_\phi s_\psi s_\theta \dot{\phi}^2 + 2 c_\phi s_\psi \dot{\phi}\dot{\psi} - 2 c_\psi s_\phi s_\theta \dot{\phi}\dot{\psi} + c_\psi s_\phi \dot{\psi}^2 - c_\phi s_\psi s_\theta \dot{\psi}^2 - 2 c_\theta s_\phi s_\psi \dot{\phi}\dot{\theta} + \\
& 2 c_\phi c_\psi c_\theta \dot{\psi}\dot{\theta} - c_\phi s_\psi s_\theta \dot{\theta}^2 - c_\phi c_\psi \ddot{\phi} - s_\phi s_\psi s_\theta \ddot{\phi} + s_\phi s_\psi \ddot{\psi} + c_\phi c_\psi s_\theta \ddot{\psi} + c_\phi c_\theta s_\psi \ddot{\theta} \\
c_{31} =& - s_\theta \dot{\theta}^2 + c_\theta \ddot{\theta} \\
c_{32} =& c_\theta s_\phi \dot{\phi}^2 + 2 c_\phi s_\theta \dot{\phi}\dot{\theta} + c_\theta s_\phi \dot{\theta}^2 - c_\phi c_\theta \ddot{\phi} + s_\phi s_\theta \ddot{\theta} \\
c_{33} =& c_\phi c_\theta \dot{\phi}^2 - 2 s_\phi s_\theta \dot{\phi}\dot{\theta} + c_\phi c_\theta \dot{\theta}^2 + c_\theta s_\phi \ddot{\phi} + c_\phi s_\theta \ddot{\theta}
\end{aligned}
$$

APPENDIX D

CONTROL LAW DEVELOPMENT

As detailed in the Chapter 5, a controller was implemented in the system to demonstrate the results of a simulation subjected to a varying wind profile.

The weight matrices include diagonal terms only. The weight were generated from engineering judgment, based on the principle that the weight associated with each state or control input should be in the order of the inverse of the maximal allowed variation squared. While some of the states do not have an explicit requirement on the maximum, a value was associated anyway.

The weights for the states are expressed as follows:

$$Q_x = Q_y = Q_z = \frac{1}{5m^2} \tag{103}$$

$$Q_u = Q_v = Q_w = \frac{1}{5m/s^2} \tag{104}$$

$$Q_\zeta = Q_\xi = Q_\phi = Q_\theta = Q_\psi = \frac{1}{20^{o2}} \tag{105}$$

$$\tag{106}$$

And the weights for the control input are the following:

$$R_{\delta_e} = R_{\delta_r} = R_{\delta_a} = \frac{1}{45^{o2}} \tag{107}$$

$$R_{\delta_T} = \frac{1}{2kRPM^2} \tag{108}$$

APPENDIX E

DECOMPOSITION OF THE FORCES AND MOMENTS

This section aims at decomposing the different forces and moments acting on the aircraft during the trimmed, steady-level flight.

E.1 Tether attached at the Center of Gravity

The first case studied is the case where the tether is attached at the aircraft center of gravity. The solution of the trim analysis for a shared fuselage of 500 kg, and a tether length of 55 m can be summarized in the Table 28

	Trim states
ζ	45^o
ξ	0^0
ϕ	7.7^o
θ	4.1^o
ψ	92.5^o
$\dot{\zeta}$	$0\ ^o/s$
$\dot{\xi}$	$51.2\ ^o/s$
p	$3.65\ ^o/s$
q	$6.9\ ^o/s$
r	$-50.7\ ^o/s$

	Trim control input
δ_r	0.2^o
δ_e	-4.2^0
δ_a	3.23^o
δ_P	$3.53\ kRPM$

Table 28: Nominal flight path trim results

To study the conditions of interest, the forces and moments will be decomposed and summed along various reference frames. The sum of forces will be realized in the hub reference frame $\boldsymbol{H}$, and the moments will be summed in the aircraft body frame $\boldsymbol{C}$.

The aerodynamic forces in the body frame $\boldsymbol{C}$ are expressed as follows:

$$\vec{F^C}_{aero} = \begin{bmatrix} 31.7 \\ -10.2 \\ -2211 \end{bmatrix} \tag{109}$$

The propeller thrust also introduce a force on the aircraft:

$$\vec{F^C}_{prop} = \begin{bmatrix} 135.7 \\ 0 \\ 0 \end{bmatrix} \tag{110}$$

These are transformed to the inertial frame $\boldsymbol{H}$ as follows:

$$\vec{F^H}_{prop} = \boldsymbol{T}_{C\to B}\boldsymbol{T}_{B\to H}(\vec{F^C}_{prop}) \tag{111}$$

$$\vec{F^H}_{aero} = \boldsymbol{T}_{C\to B}\boldsymbol{T}_{B\to H}(\vec{F^C}_{aero}) \tag{112}$$

The tether

Finally, the gravity is acting on the aircraft as follows:

$$\vec{F}_{grav} = \begin{bmatrix} 0 \\ 0 \\ -m_{ac}g \end{bmatrix} \tag{113}$$

For the position of azimuth angle $\xi = 0$, there should be no acceleration along the y and z axes, and a centrifugal acceleration in the -x axis only.

$$\vec{a} \begin{bmatrix} -\frac{v^2}{r} \\ 0 \\ 0 \end{bmatrix} \tag{114}$$

with r, the flight radius, of $55\cos(45^o)$ m, which is 38.9m.

The sum of forces in the inertial frame becomes:

$$\vec{F^H}_{aero} + \vec{F^H}_{prop} + \vec{F^H}_{grav} + \vec{F^H}_{tension} = m\vec{a^H} \tag{115}$$

$$\begin{bmatrix} -167 \\ -10 \\ 2212 \end{bmatrix} + \begin{bmatrix} -167 \\ -10 \\ 2212 \end{bmatrix} + \begin{bmatrix} 0 \\ 0 \\ -588.6 \end{bmatrix} + \begin{bmatrix} -1635 \\ 0 \\ -1635 \end{bmatrix} = \begin{bmatrix} -1868 \\ 0 \\ 0 \end{bmatrix} \tag{116}$$

The residual is the following:

$$\begin{bmatrix} 65 \\ -10 \\ -11 \end{bmatrix} \tag{117}$$

Note that the discrepancy can come from the conversion between the different frames, including the removal of the flexibility in the cable, which is performed through singular unit perturbation. This model included a linearization of the dynamic model around a no elongation case and conversion of the state derivatives about the state vector of interest, which can introduce some variation. The residual is considered acceptable given that when compared to the absolute value of the maximal force $\frac{residual}{F_{max}}$ is less than 3%.

E.1.1 Sum of Moments

The sum of moments is, in counterparts, detailed in the body frame $\boldsymbol{H}$. For the case with the tether attached at the CG, only the aerodynamic moments are acting in the aircraft.

$$\begin{bmatrix} L_{aero} \\ M_{aero} \\ N_{aero} \end{bmatrix} = \begin{bmatrix} -15.2 \\ 2.5 \\ -0.32 \end{bmatrix} \tag{118}$$

The verification is performed as follows:

$$I_{xx}\dot{p} = L + (I_{yy} - I_{zz})qr \tag{119}$$

$$I_{yy}\dot{q} = M + (I_{zz} - I_{xx})rp \tag{120}$$

$$I_{zz}\dot{r} = N + (I_{xx} - I_{yy})pq \tag{121}$$

The residual angular accelerations $\dot{p}$, $\dot{q}$ and $\dot{r}$ are the following:

$$\begin{bmatrix} -0.013 \\ -0.002 \\ -0.002 \end{bmatrix} \tag{122}$$

Which are deemed appropriate withing engineering analysis.

E.2 Tether attached inboard

The second analysis is the case of a tether attached on the inboard section of the wing, at 0.5 m. The position of the attachment point in the reference frame $\boldsymbol{C}$ is:

$$\vec{r}^{C}_{D\to A} = \begin{bmatrix} 0 \\ -0.5 \\ 0 \end{bmatrix} \tag{123}$$

The trim solution is expressed in tables 29.

The sum of forces is performed in the same way as before, with the main exception lying in the fact that the flight path radius is now slightly larger, which affect the centrifugal acceleration. Moreover, the velocity condition imposed during the trimmed is with respect to the tether tip. Consequently, both the aircraft center of gravity and the flight path radius are affected. The radius is 39.4 m, and the velocity of the aircraft center of gravity is 35.2 m/s.

	Trim states
ζ	45^o
ξ	0^0
ϕ	-5.9^o
θ	4.1^o
ψ	89.8^o
$\dot{\zeta}$	$0\ ^o/s$
$\dot{\xi}$	$51.2\ ^o/s$
p	$3.73\ ^o/s$
q	$5.3\ ^o/s$
r	$-50.85\ ^o/s$

	Trim control input
δ_r	-2^o
δ_e	-4.5^0
δ_a	9.35^o
δ_P	$3.5\ kRPM$

Table 29: Trim results for tether attached on the inboard wing

The aerodynamic forces at the center of gravity:

$$\vec{F^C}_{aero} = \begin{bmatrix} 19.8 \\ -35.6 \\ -2215 \end{bmatrix} \tag{124}$$

The propeller thrust is the following:

$$\vec{F^C}_{prop} = \begin{bmatrix} 145 \\ 0 \\ 0 \end{bmatrix} \tag{125}$$

$$\vec{F^H}_{aero} + \vec{F^H}_{prop} \qquad + \vec{F^H}_{grav} + \vec{F^H}_{tension} \qquad = m\vec{a^H} \tag{126}$$

$$\begin{bmatrix} -262 \\ -142 \\ 2195 \end{bmatrix} + \begin{bmatrix} -0.5 \\ 144.5 \\ 10.5 \end{bmatrix} \quad + \begin{bmatrix} 0 \\ 0 \\ -588.6 \end{bmatrix} + \begin{bmatrix} -1635 \\ 0 \\ -1635 \end{bmatrix} \quad = \begin{bmatrix} -1892 \\ 0 \\ 0 \end{bmatrix} \tag{127}$$

The residual is the following:

$$\begin{bmatrix} -5 \\ 3 \\ -17 \end{bmatrix} \tag{128}$$

E.2.1 Sum of Moments

The trimmed aerodynamic moments about the center of gravity are the following:

$$\begin{bmatrix} L_{aero} \\ M_{aero} \\ N_{aero} \end{bmatrix} = \begin{bmatrix} 705 \\ 2.3 \\ 55 \end{bmatrix} \tag{129}$$

It can be seen that there is a significant moment about the the x-axis $\vec{i}_c$, supported by a 6^0 increased in aileron deflection when compared to the case with the tether attached at the center of gravity, where a positive aileron deflection refers to the aileron on the inboard section going down, and the outboard aileron going up.

For the analysis of the moments, the tether tension now has to be considered in the analysis.

$$\vec{M}^C_{Tension} = \vec{r}^C_{D\to A} \times \vec{Tension}^C \tag{130}$$

Where $\vec{Tension}^C$, is the tether tension expressed in the body frame.

$$\begin{bmatrix} L_{Tension} \\ M_{Tension} \\ N_{Tension} \end{bmatrix} = \begin{bmatrix} -726 \\ 0 \\ -56 \end{bmatrix} \tag{131}$$

It can be seen that the moment introduced by the offset of the tether tension is in the same order of magnitude of the change of aerodynamic moments, which leads to residual angular accelerations similar to the case where the tether is attached at the center of gravity $\dot{p}$, $\dot{q}$ and $\dot{r}$:

$$\begin{bmatrix} -0.05 \\ -0.002 \\ -0.001 \end{bmatrix} \tag{132}$$

APPENDIX F

CLOSED-LOOP SIMULATION

The closed loop simulation was presented in section 5.6. Additional results are presented in the following figures.

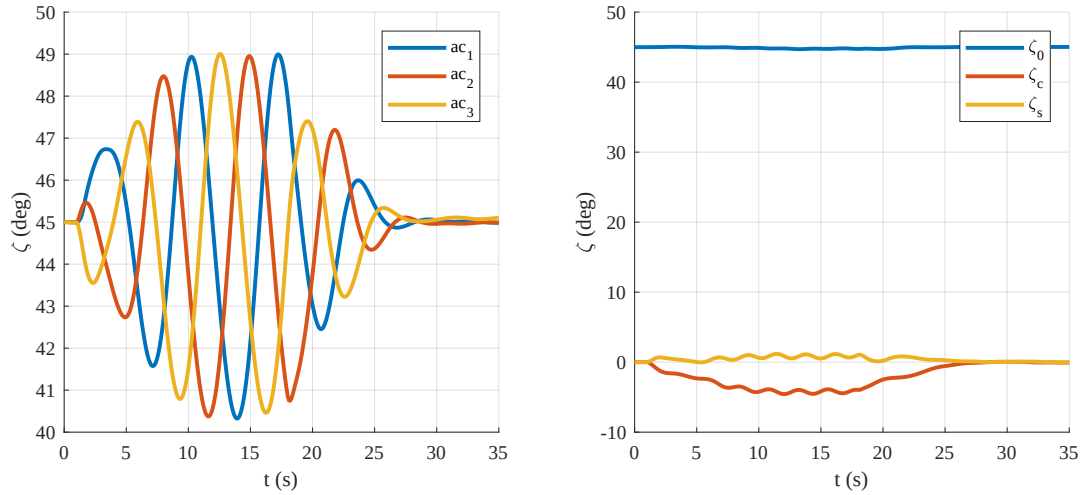

Figure 78: Tether angle ζ

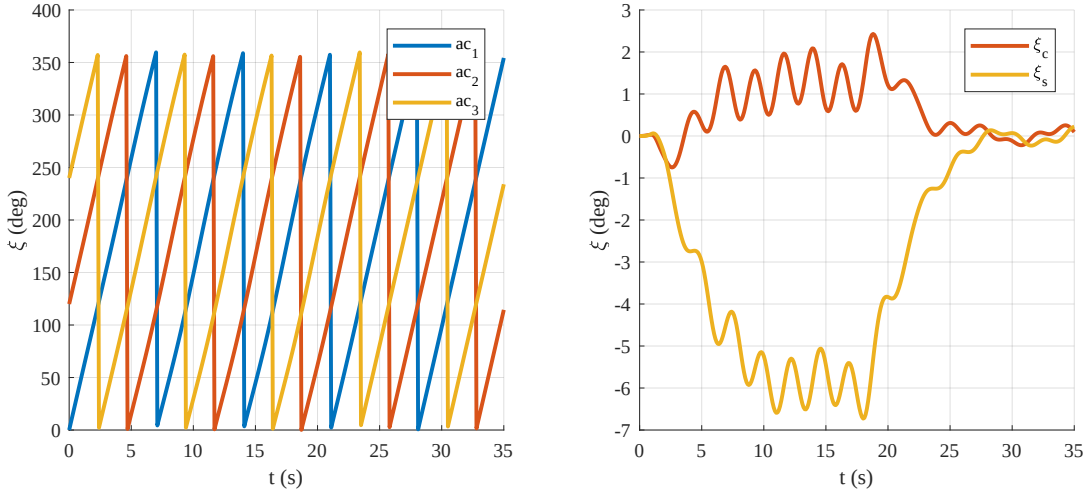

Figure 79: Tether angle ξ

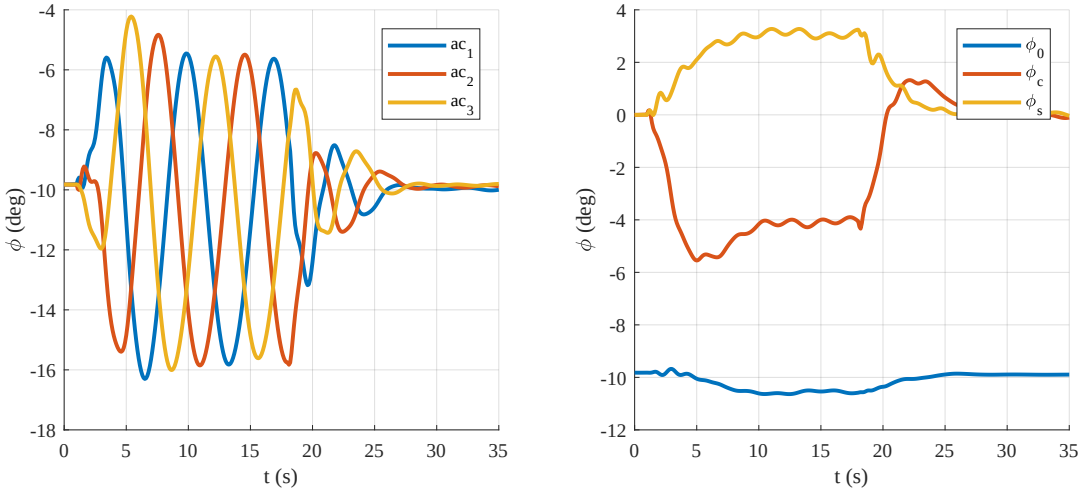

Figure 80: Tether angle ϕ

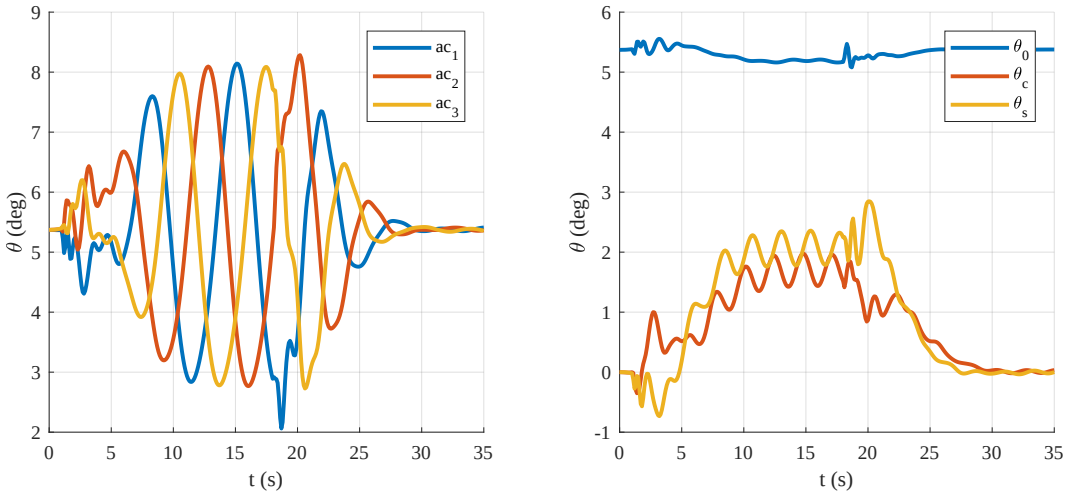

Figure 81: Tether angle θ

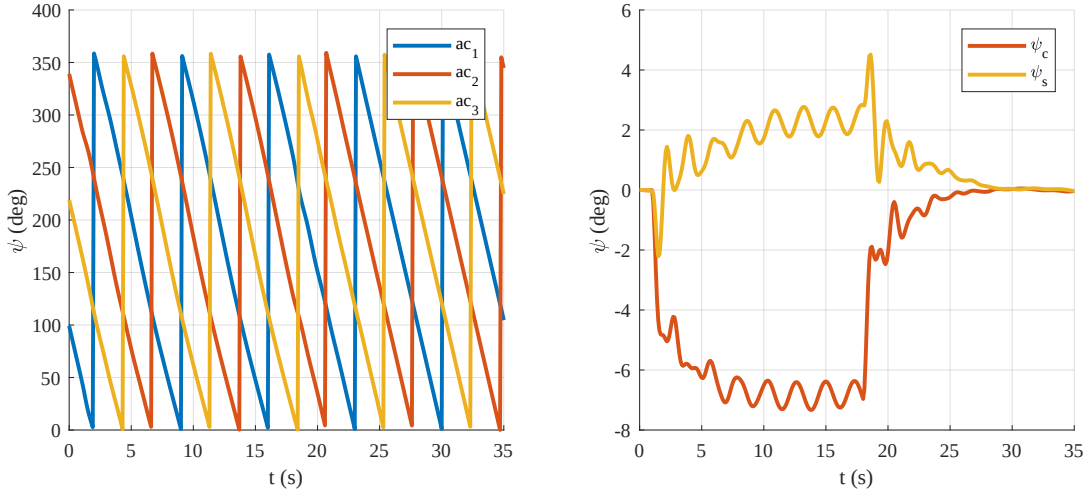

Figure 82: Tether angle ψ

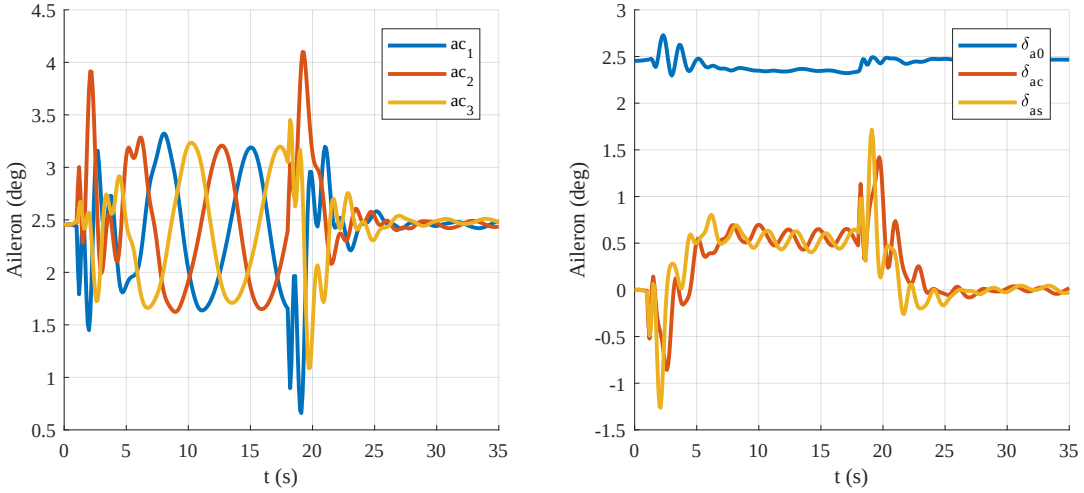

Figure 83: Control input: Aileron

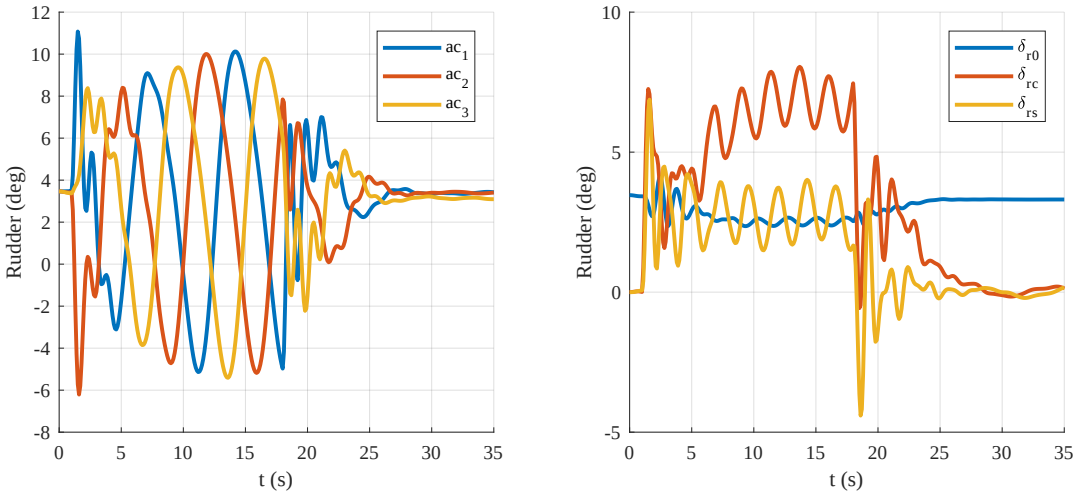

Figure 84: Control input: Rudder

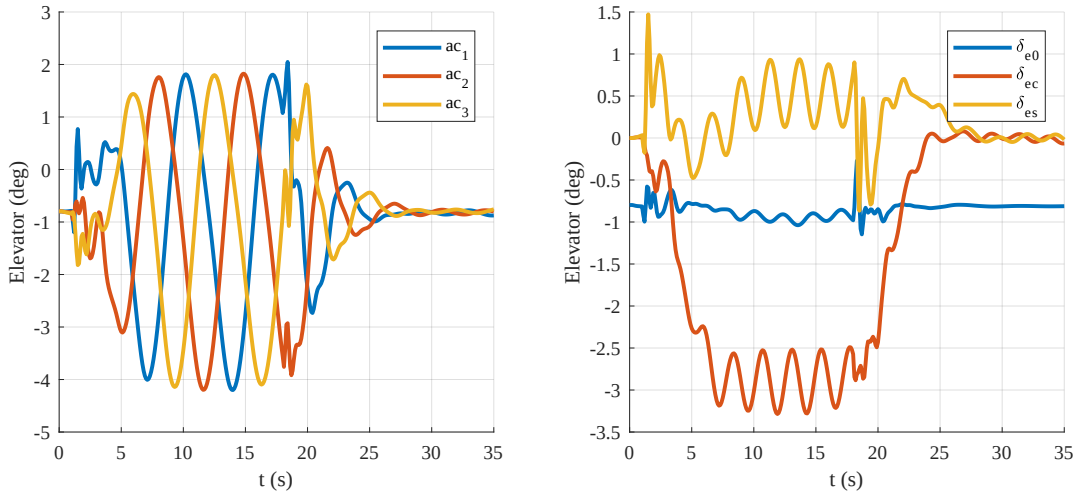

Figure 85: Control input: Elevator

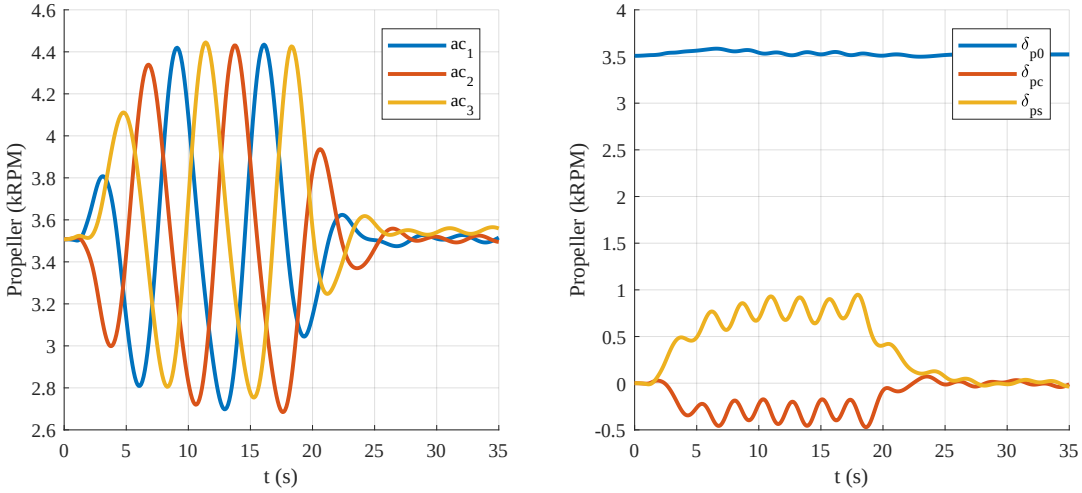

Figure 86: Control input: Propeller angular velocity

APPENDIX G

DYNAMIC MODES OF THE LINEARIZED MODEL

G.1 Simulated motion

The simulated motion of the modes were simulated in the nonlinear simulation environment. The modes 2-10 of the 3 aircraft system were simulated, and the modes B to G of the single aircraft tethered to the ground were simulated as well.

G.1.1 Mode 2

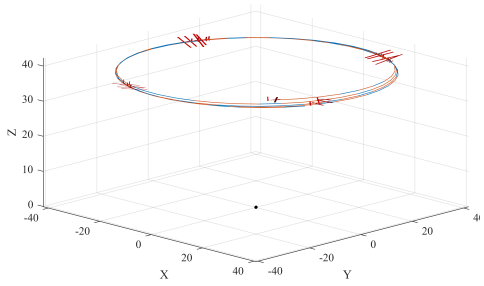

Figure 87: Overall motion of a single aircraft through one period of mode 2

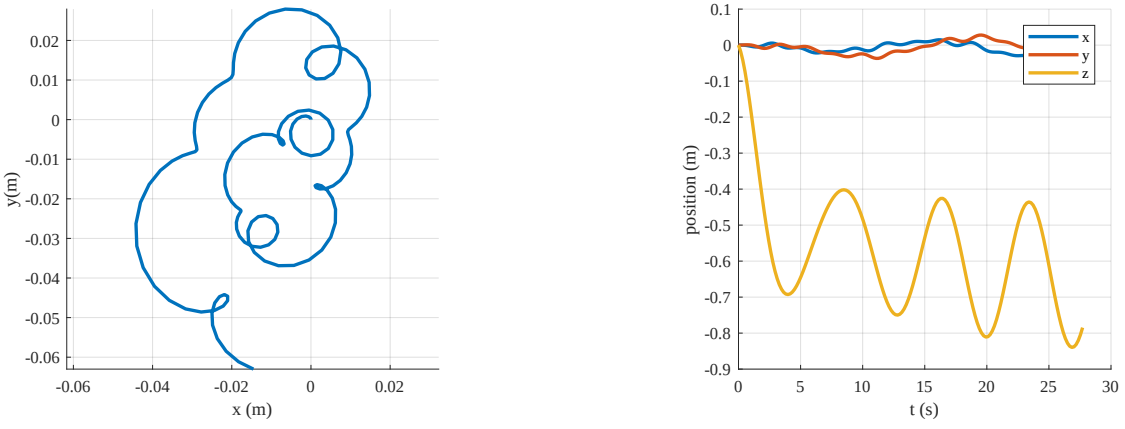

Figure 88: Suspended mass position

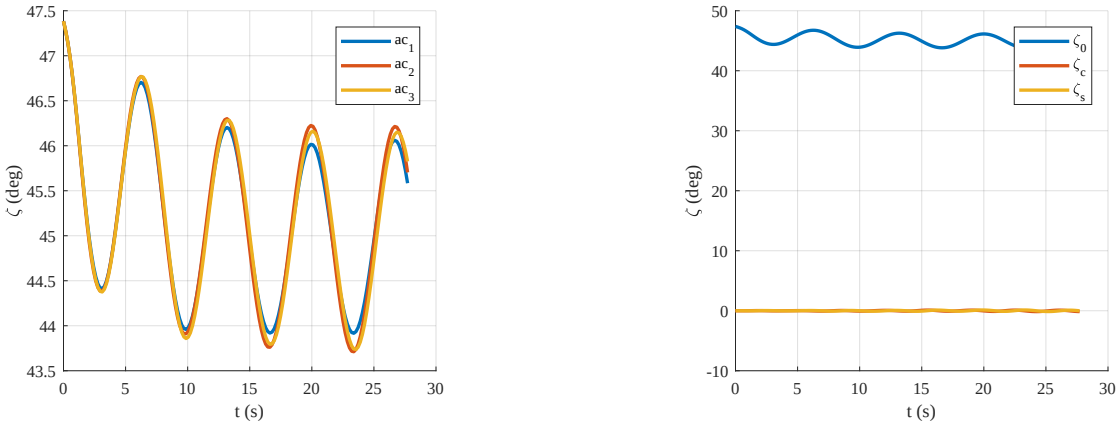

Figure 89: Tether angle ζ

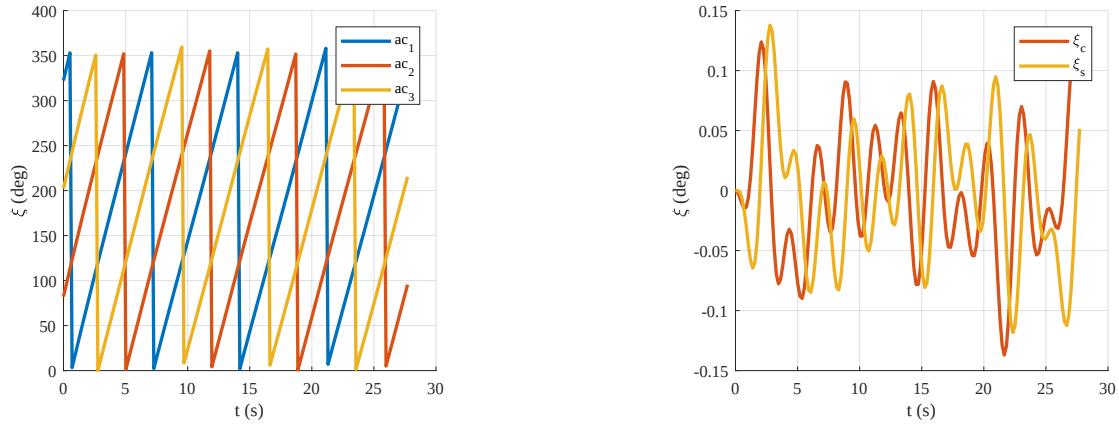

Figure 90: Tether angle ξ

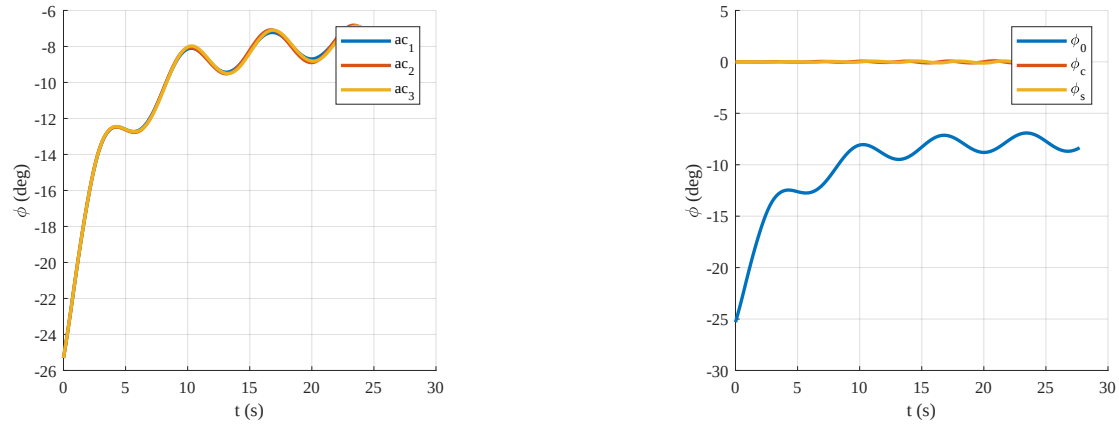

Figure 91: Aircraft angle ϕ

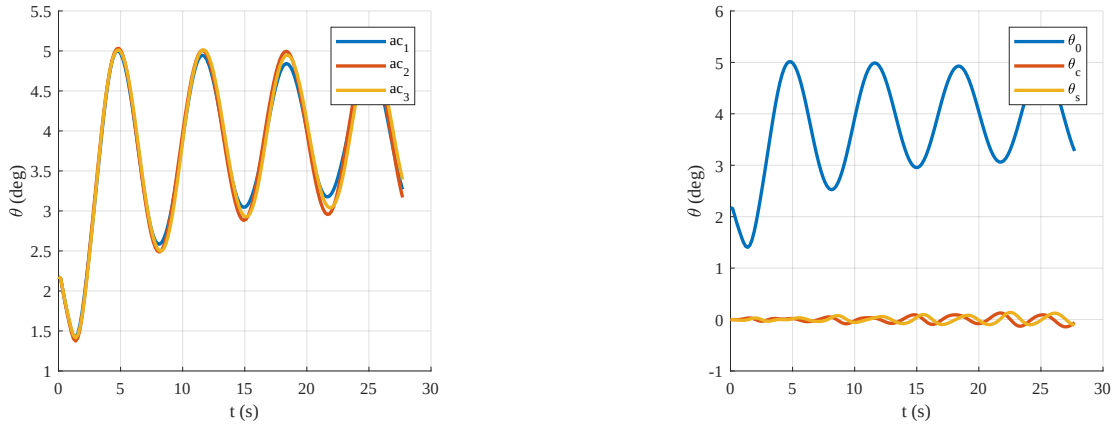

Figure 92: Aircraft angle θ

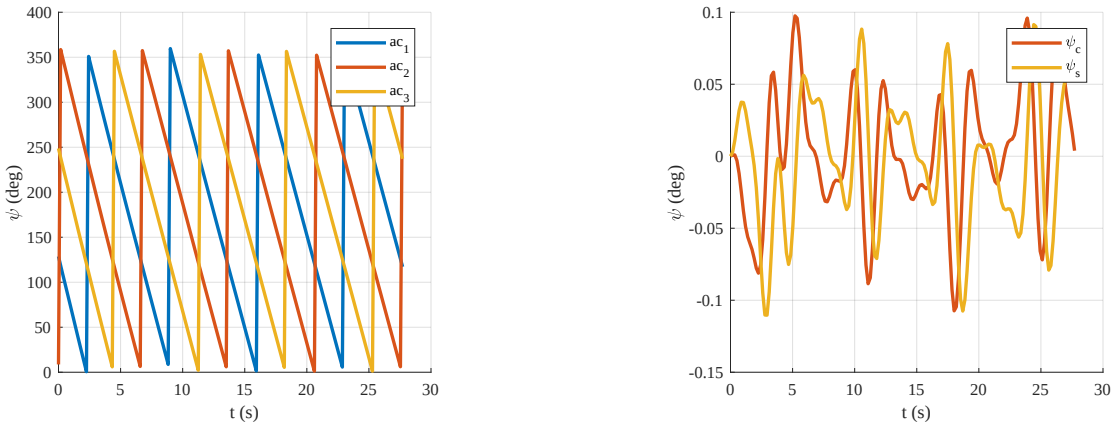

Figure 93: Aircraft angle ψ

G.1.2 Mode 3

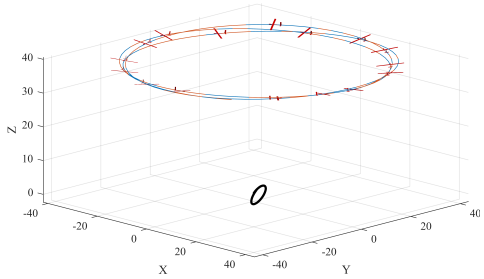

Figure 94: Overall motion of a single aircraft through one period of mode 3

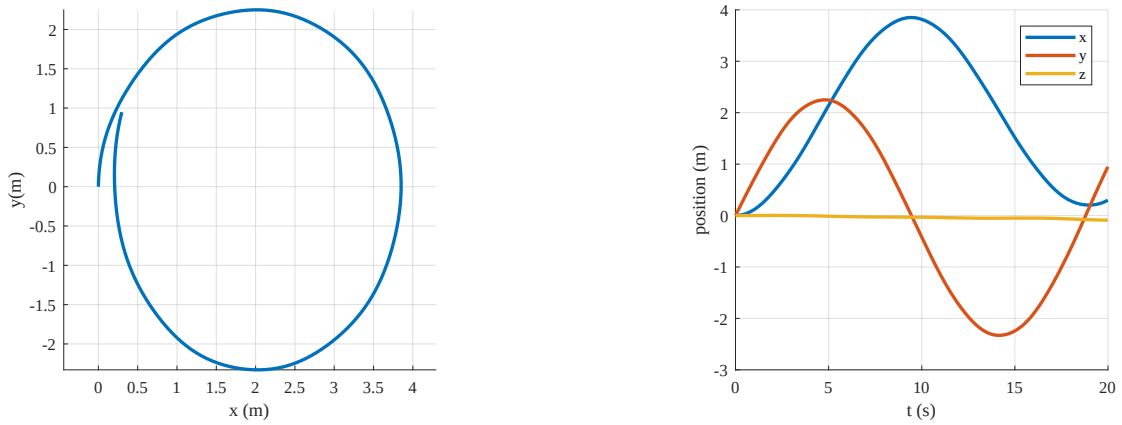

Figure 95: Suspended mass position

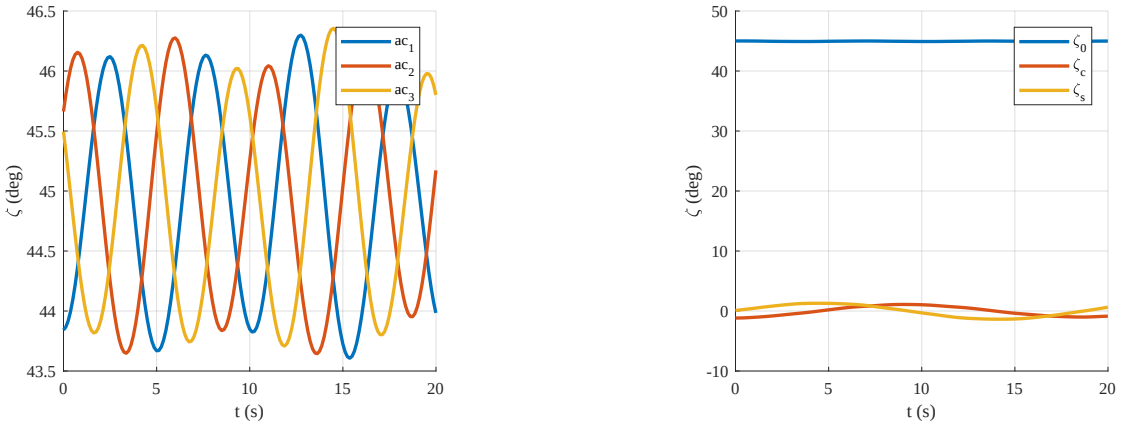

Figure 96: Tether angle ζ

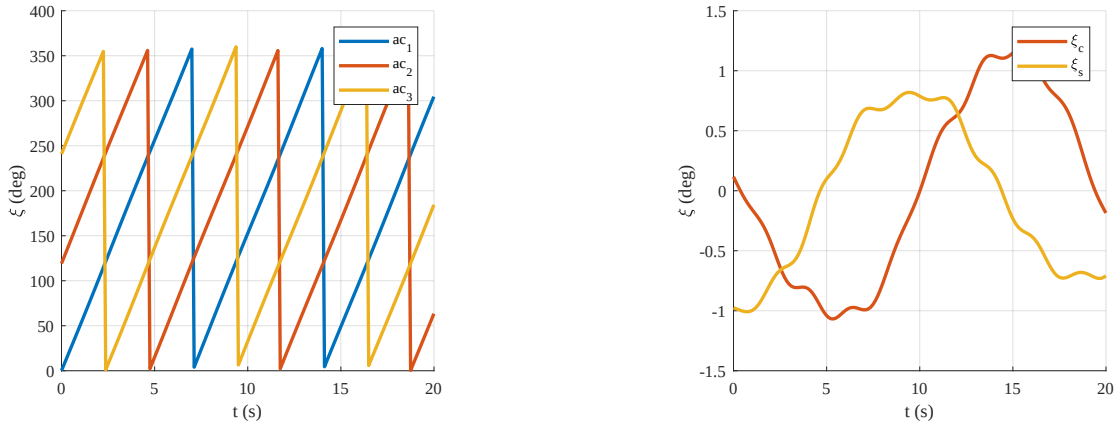

Figure 97: Tether angle ξ

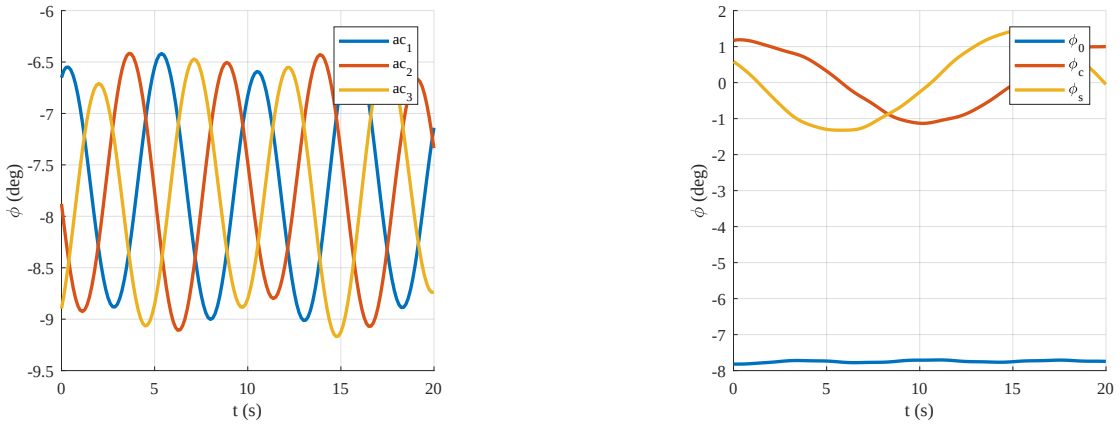

Figure 98: Aircraft angle ϕ

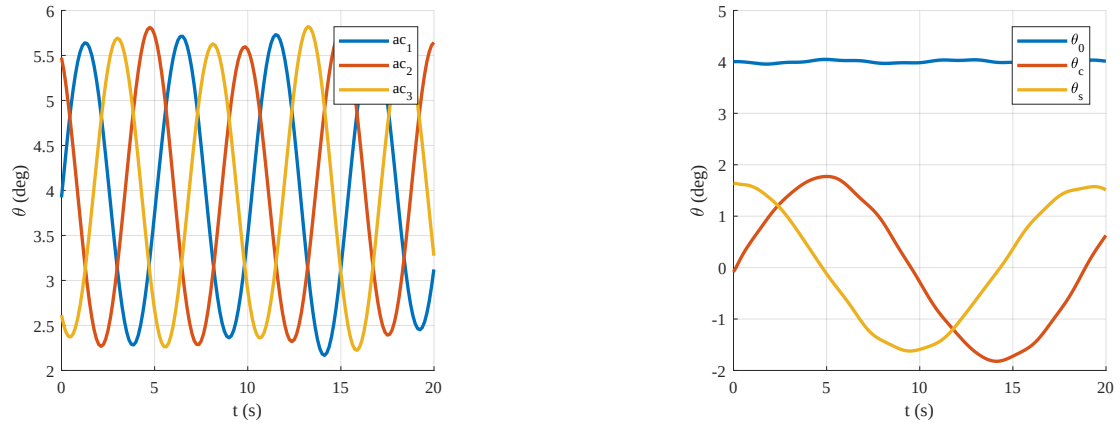

Figure 99: Aircraft angle θ

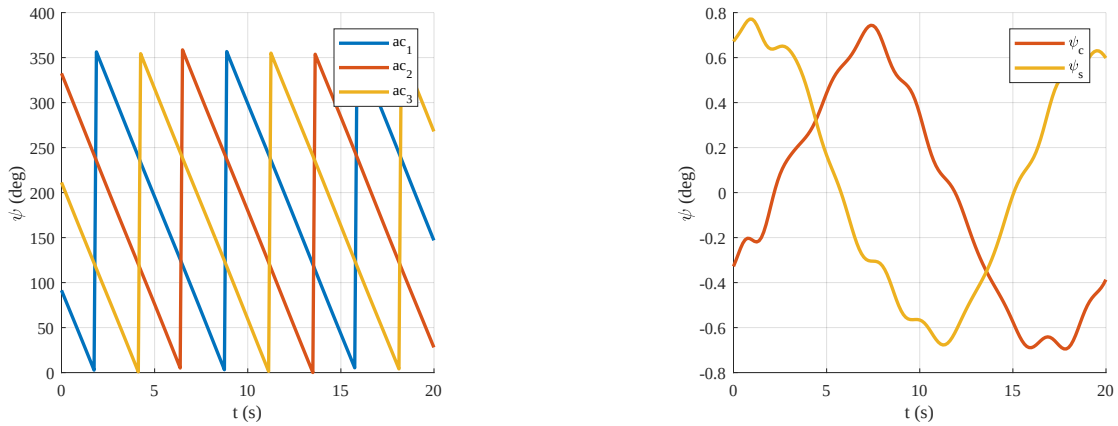

Figure 100: Aircraft angle ψ

G.1.3 Mode 4

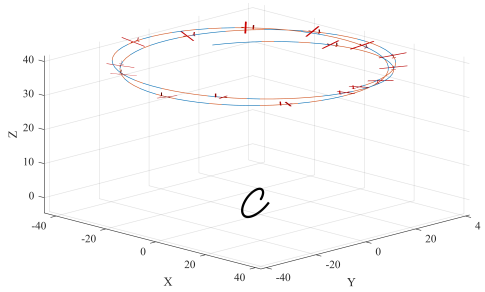

Figure 101: Overall motion of a single aircraft through one period of mode 4

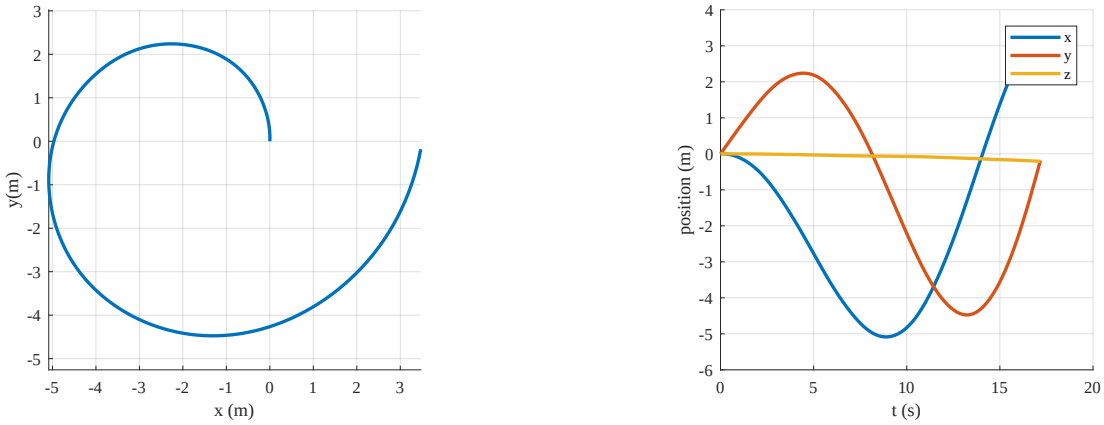

Figure 102: Suspended mass position

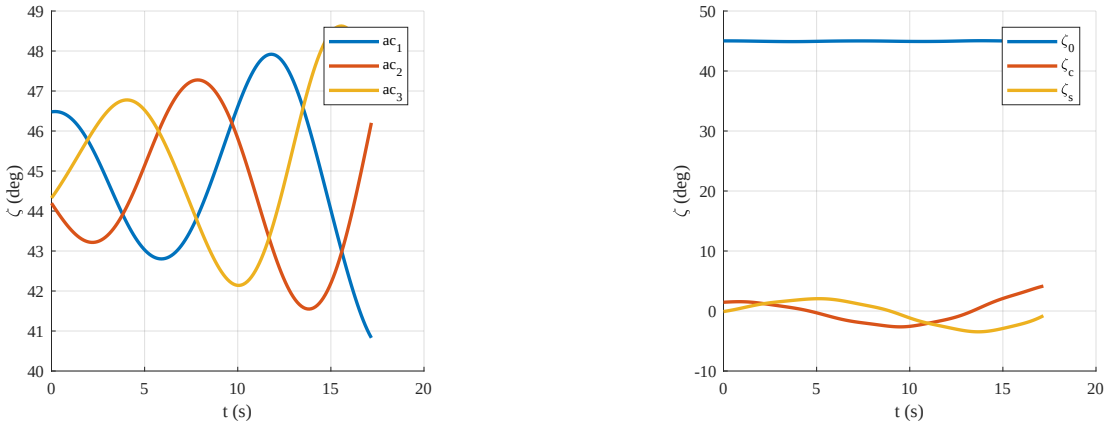

Figure 103: Tether angle ζ

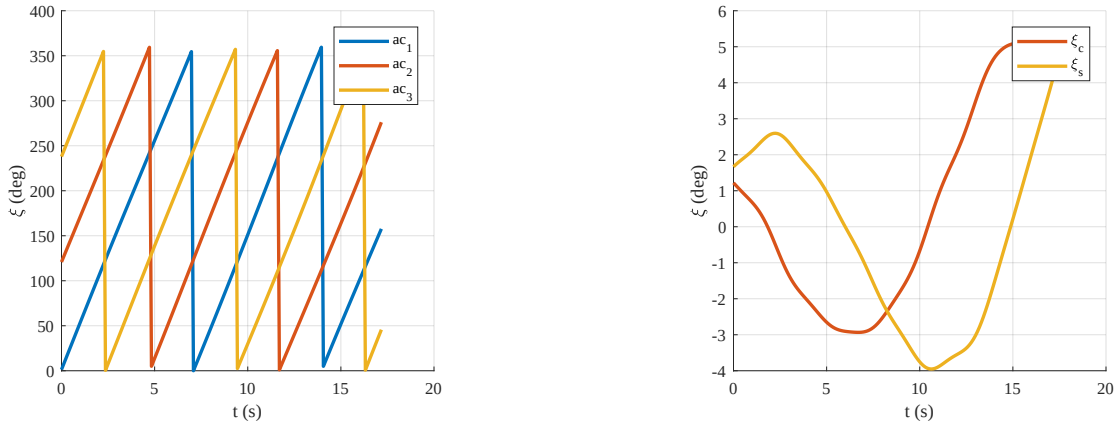

Figure 104: Tether angle ξ

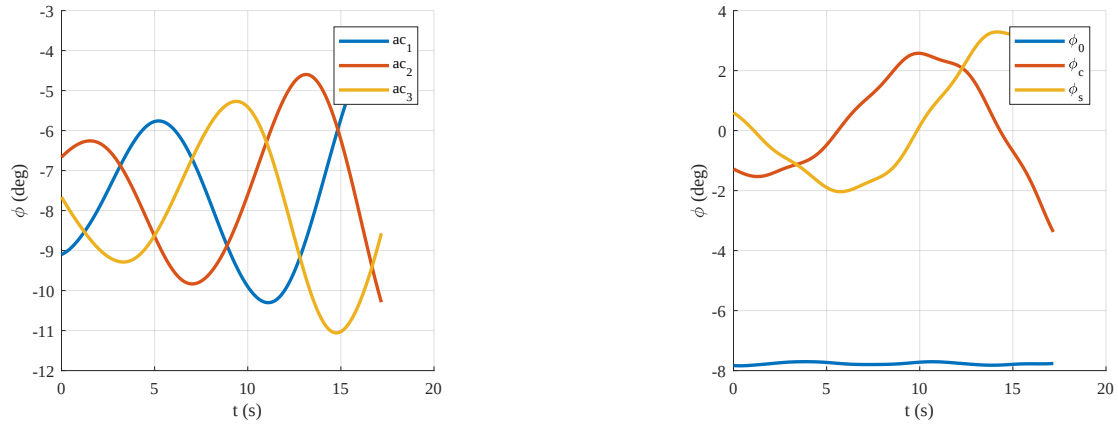

Figure 105: Aircraft angle ϕ

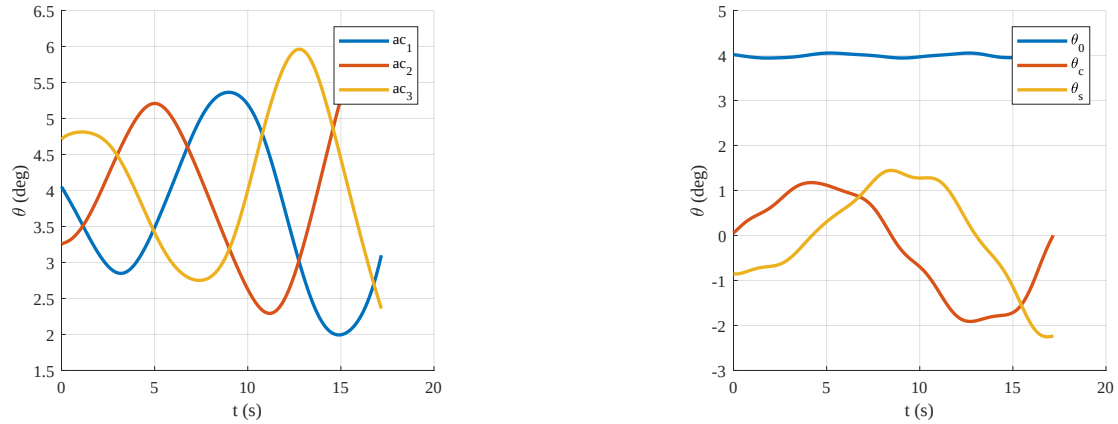

Figure 106: Aircraft angle θ

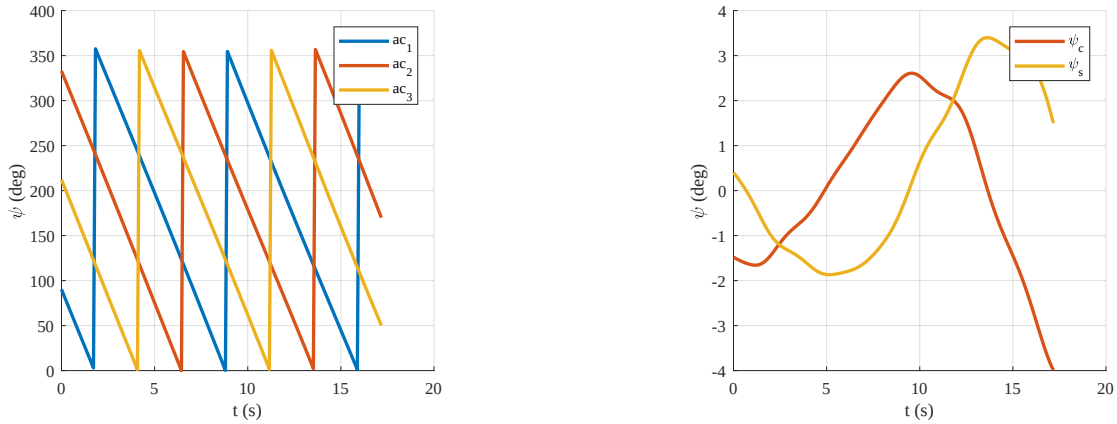

Figure 107: Aircraft angle ψ

G.1.4 Mode 5

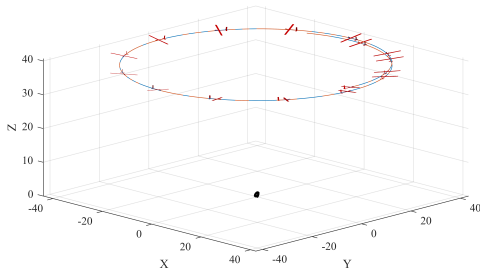

Figure 108: Overall motion of a single aircraft through one period of mode 5

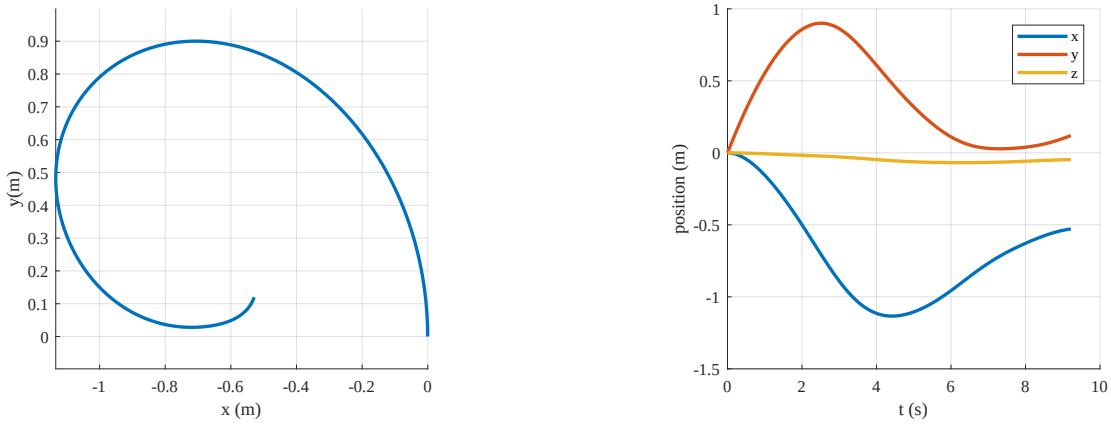

Figure 109: Suspended mass position

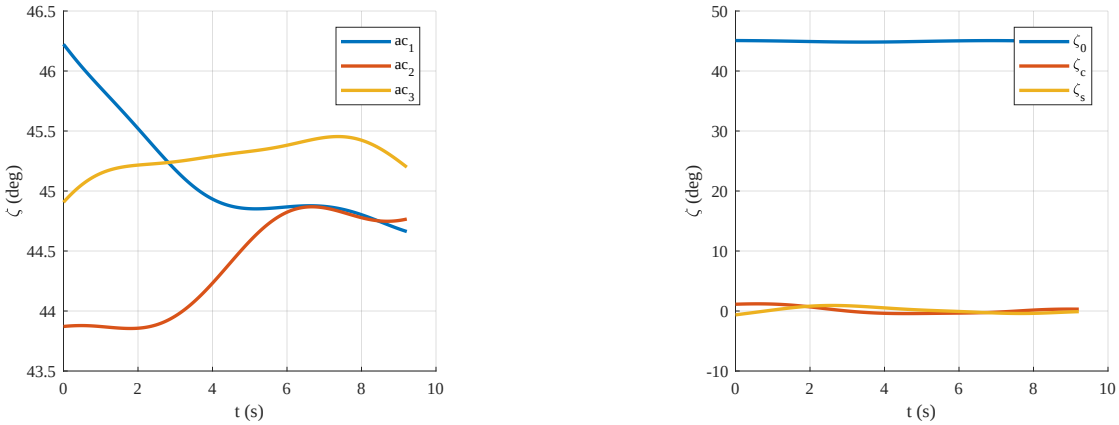

Figure 110: Tether angle ζ

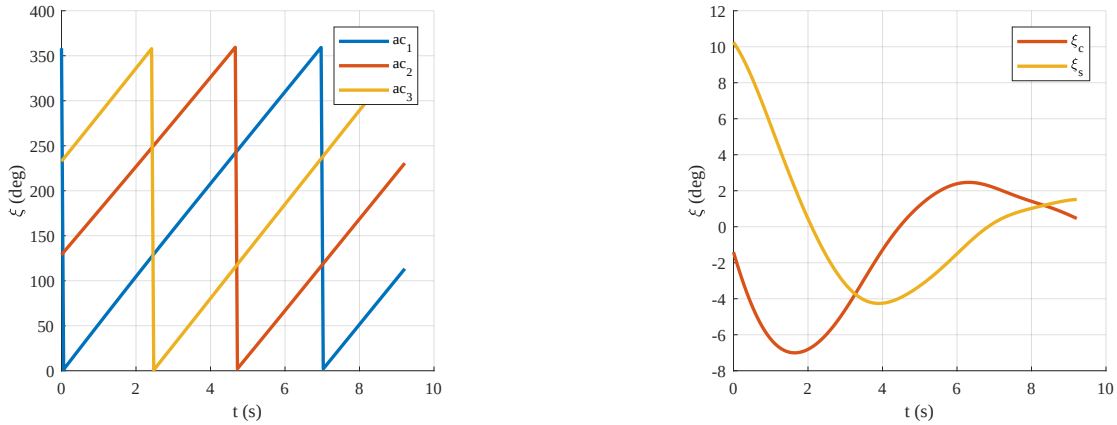

Figure 111: Tether angle ξ

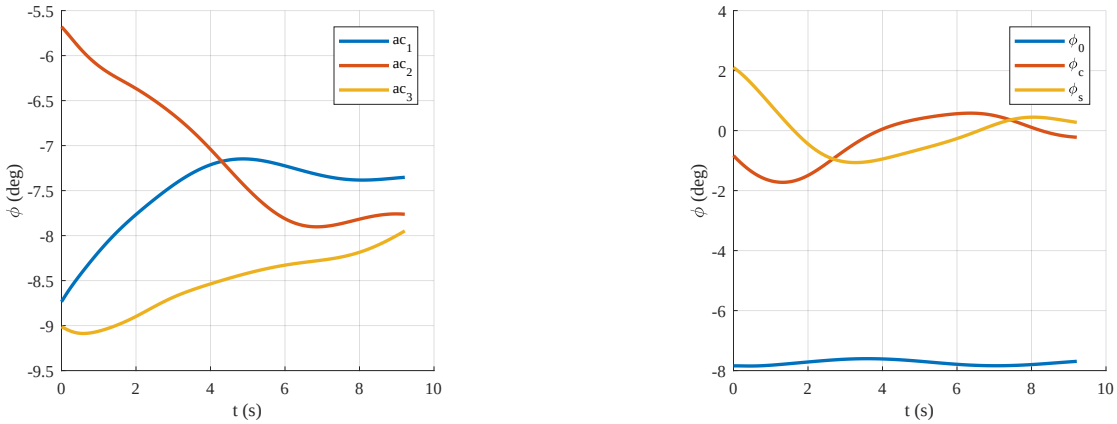

Figure 112: Aircraft angle ϕ

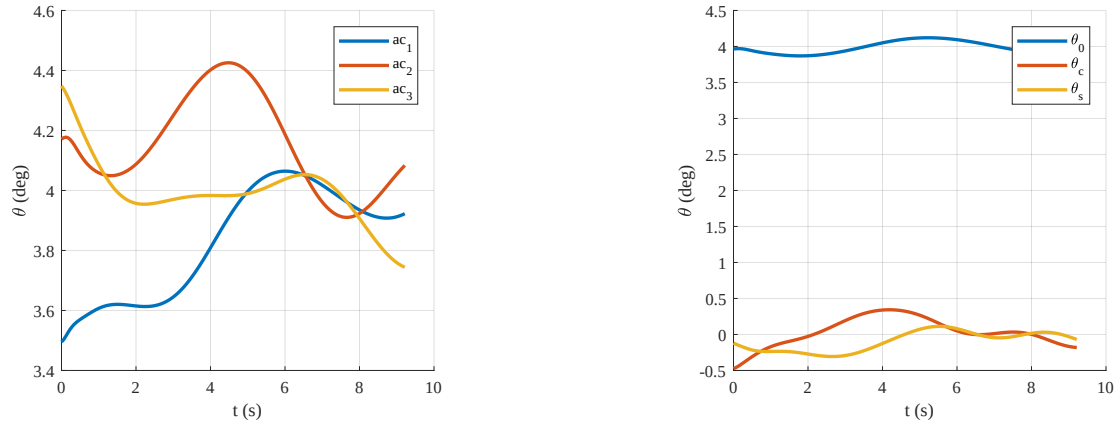

Figure 113: Aircraft angle θ

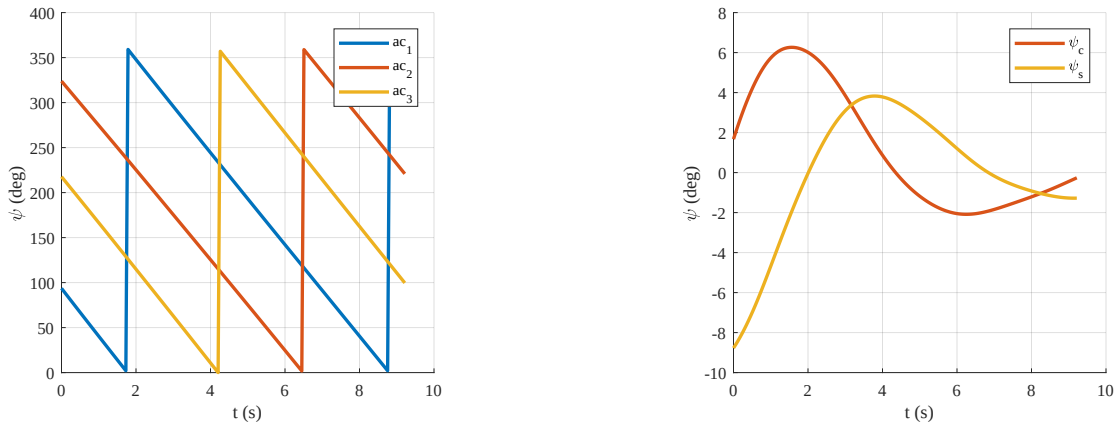

Figure 114: Aircraft angle ψ

G.1.5 Mode 6

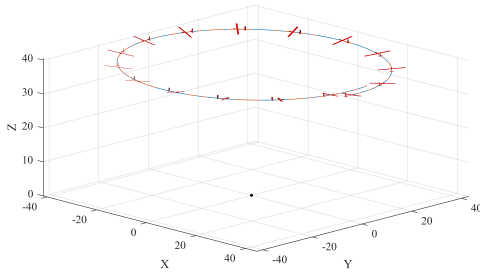

Figure 115: Overall motion of a single aircraft through one period of mode 6

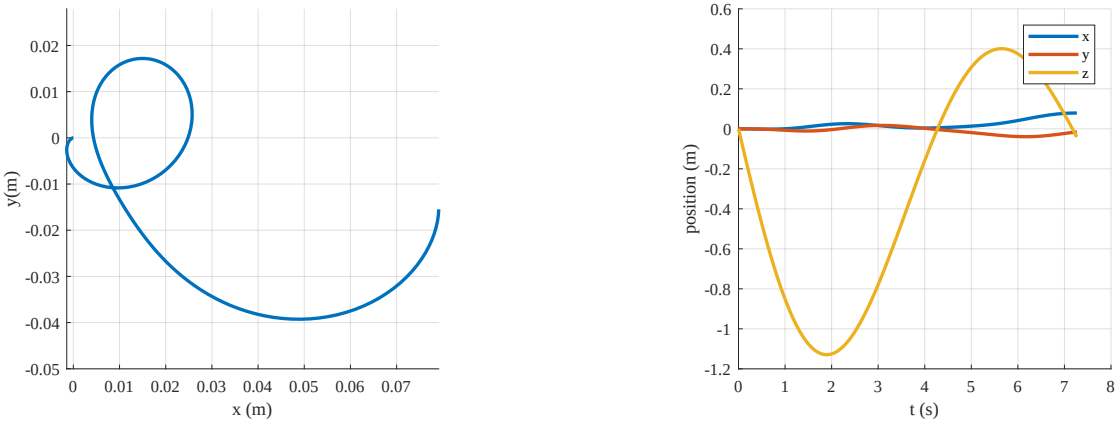

Figure 116: Suspended mass position

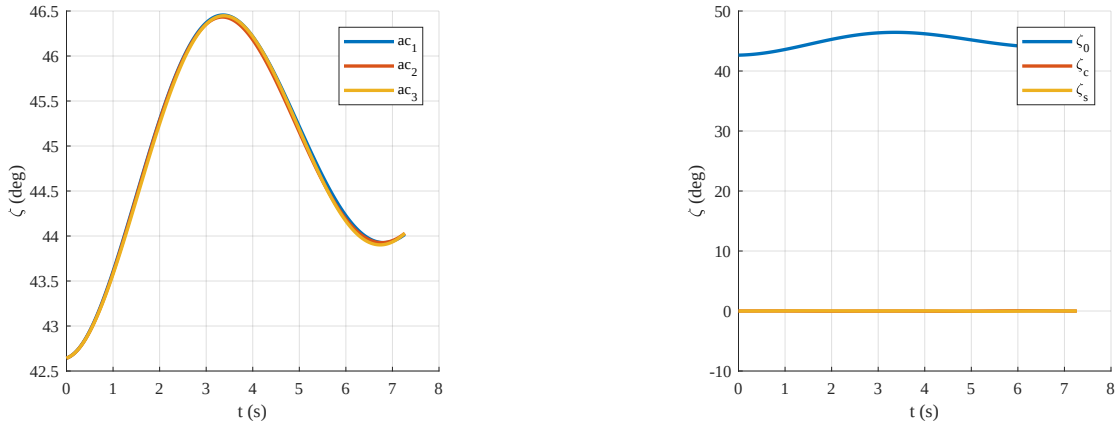

Figure 117: Tether angle ζ

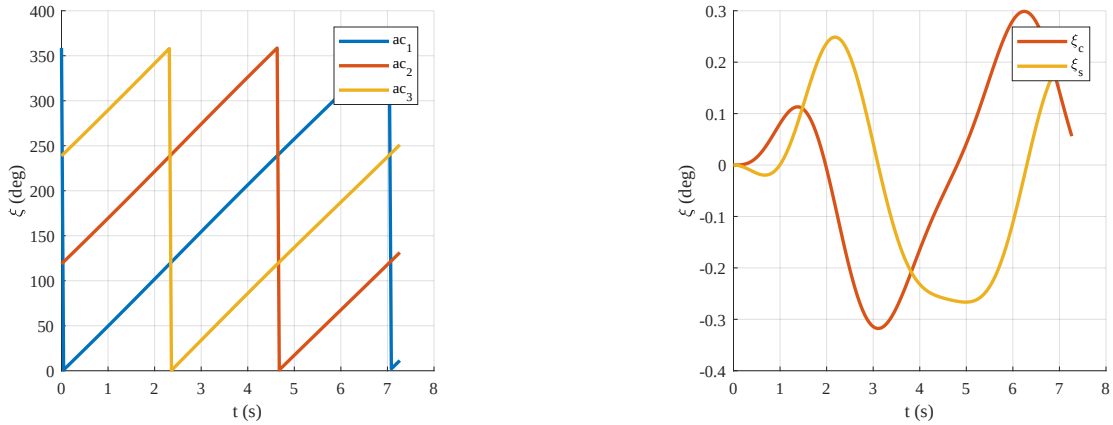

Figure 118: Tether angle ξ

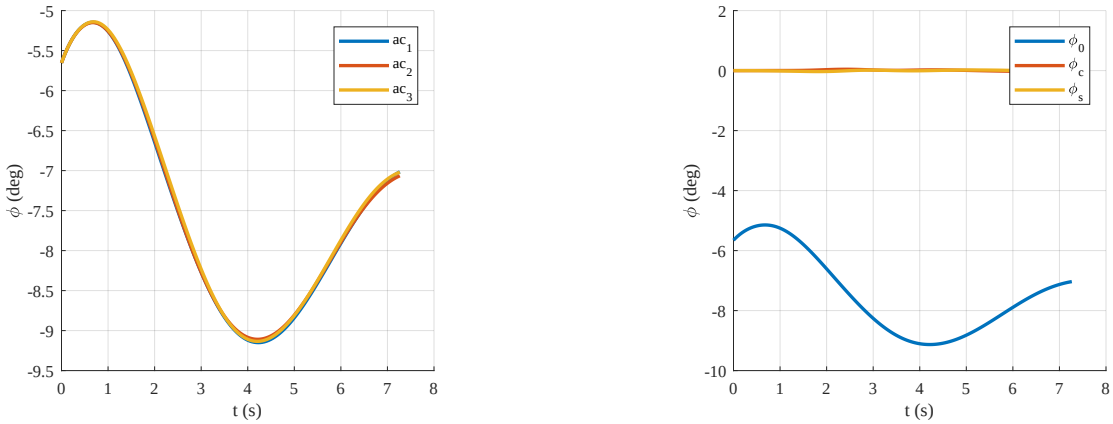

Figure 119: Aircraft angle ϕ

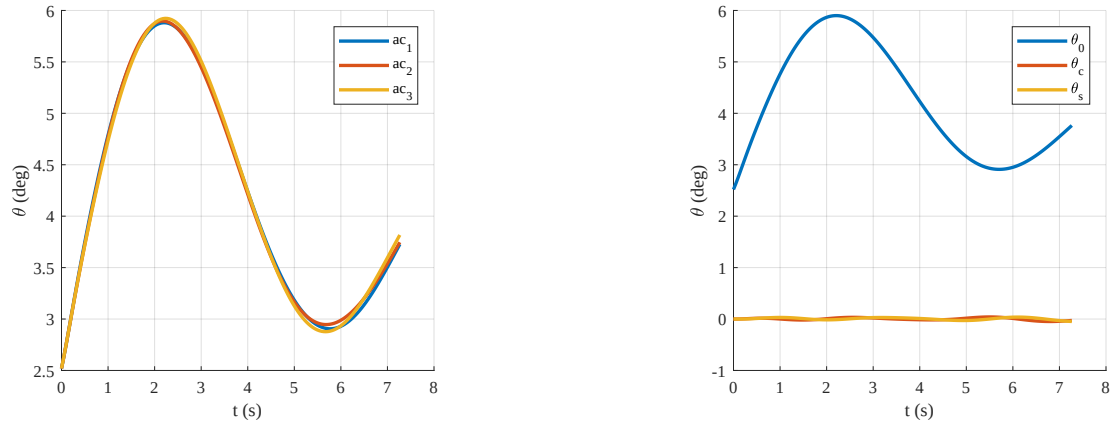

Figure 120: Aircraft angle θ

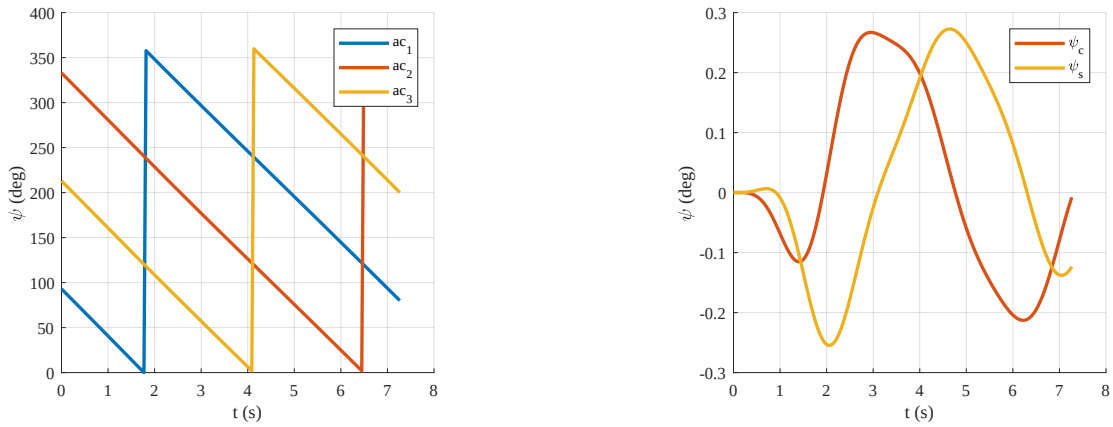

Figure 121: Aircraft angle ψ

G.1.6 Mode 7

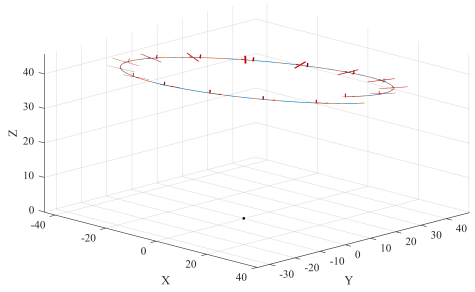

Figure 122: Overall motion of a single aircraft through one period of mode 7

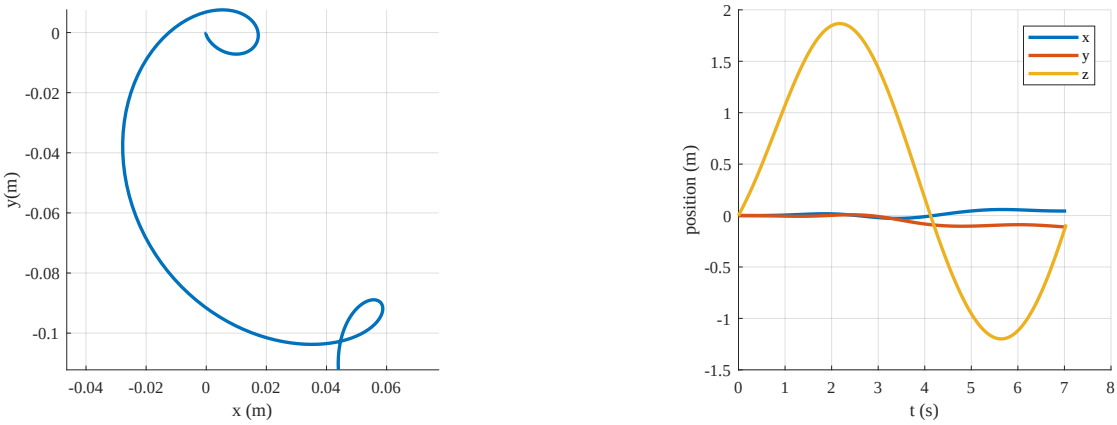

Figure 123: Suspended mass position

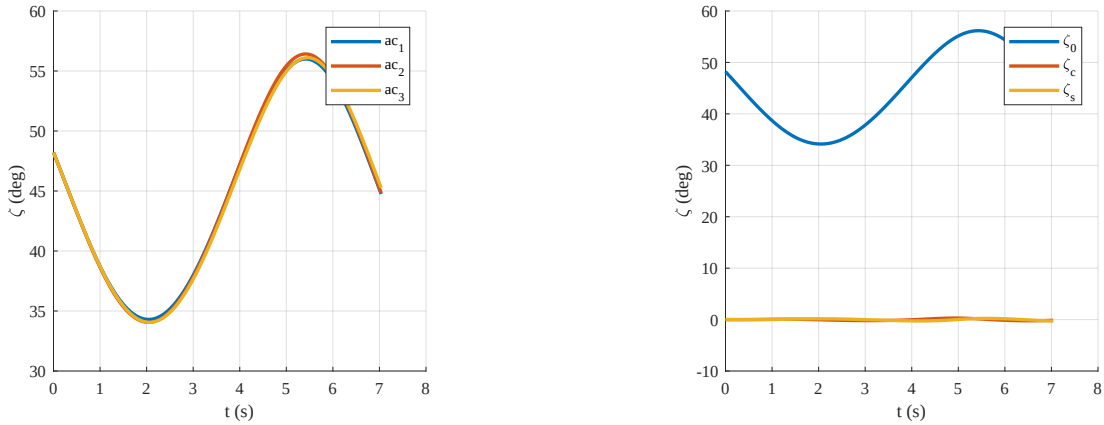

Figure 124: Tether angle ζ

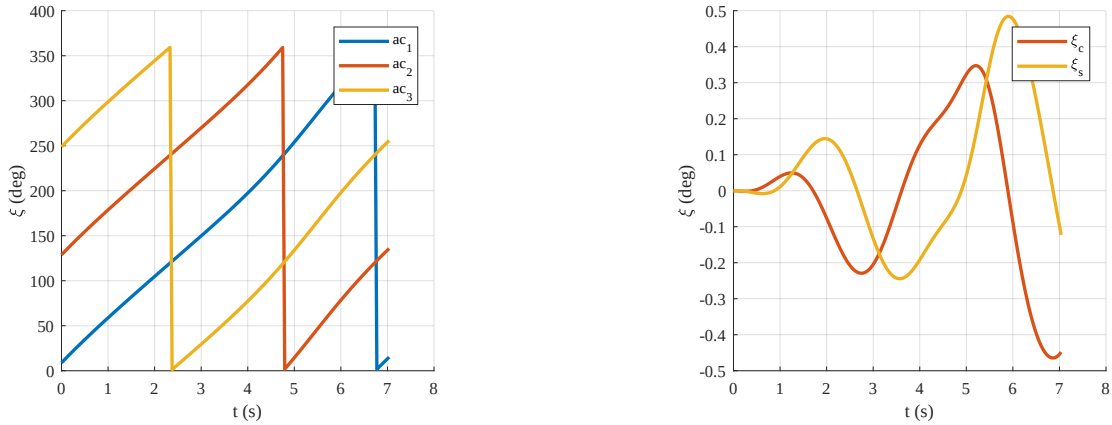

Figure 125: Tether angle ξ

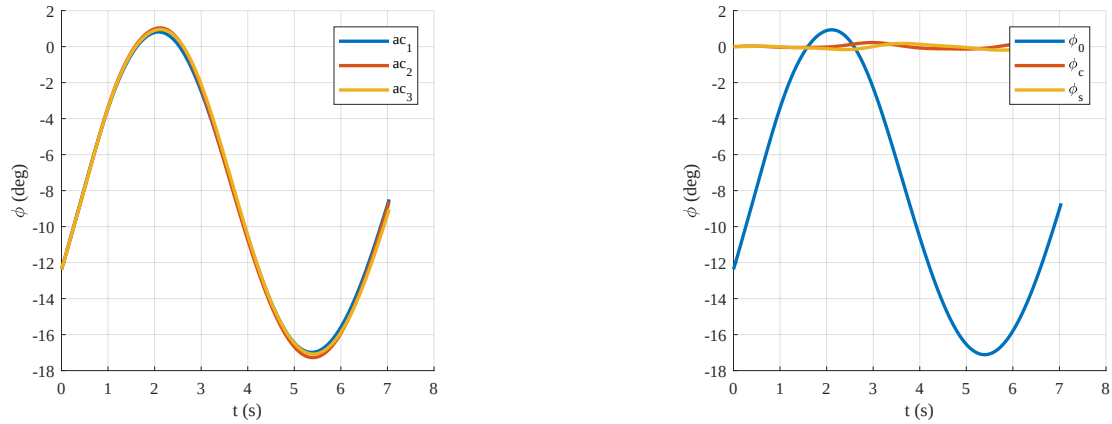

Figure 126: Aircraft angle ϕ

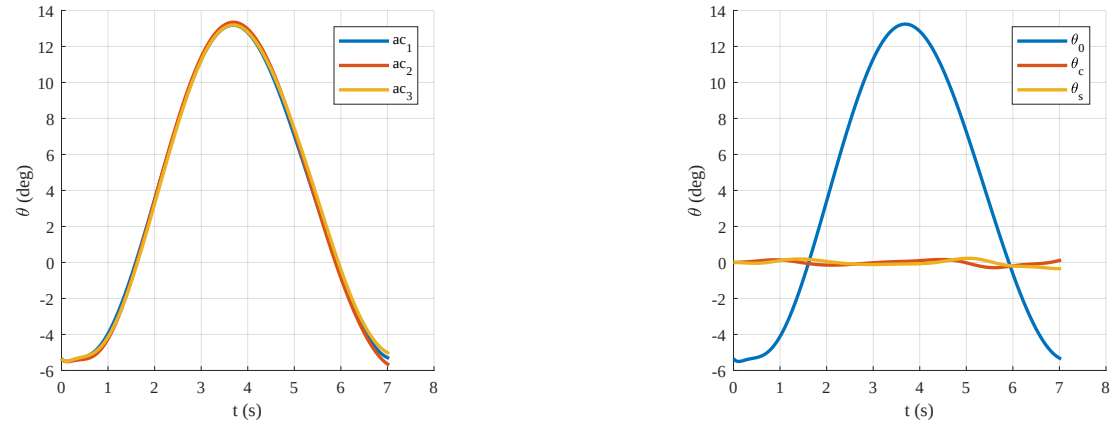

Figure 127: Aircraft angle θ

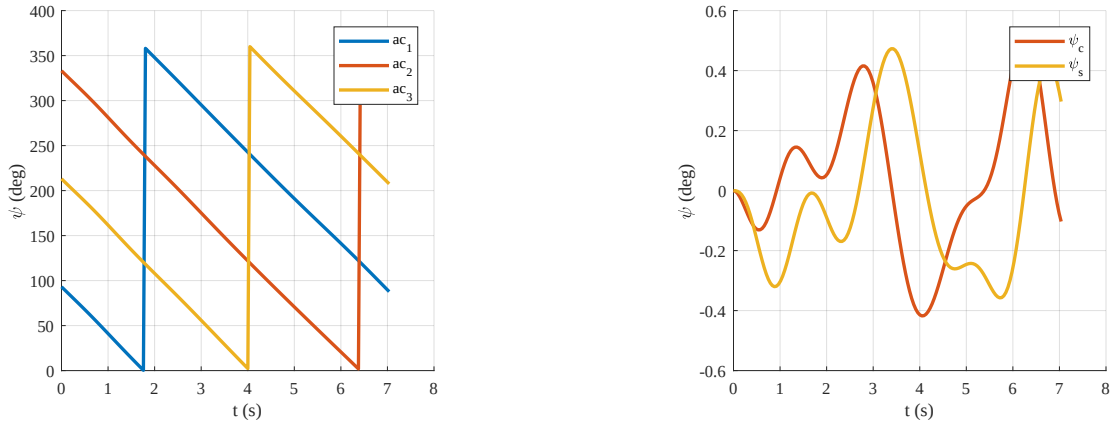

Figure 128: Aircraft angle ψ

G.1.7 Mode 8

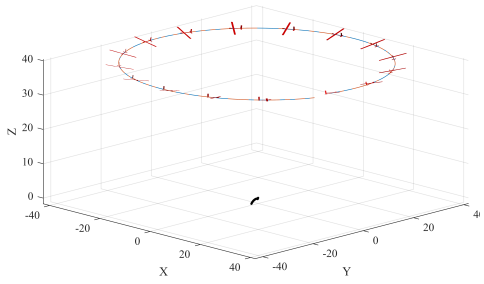

Figure 129: Overall motion of a single aircraft through one period of mode 8

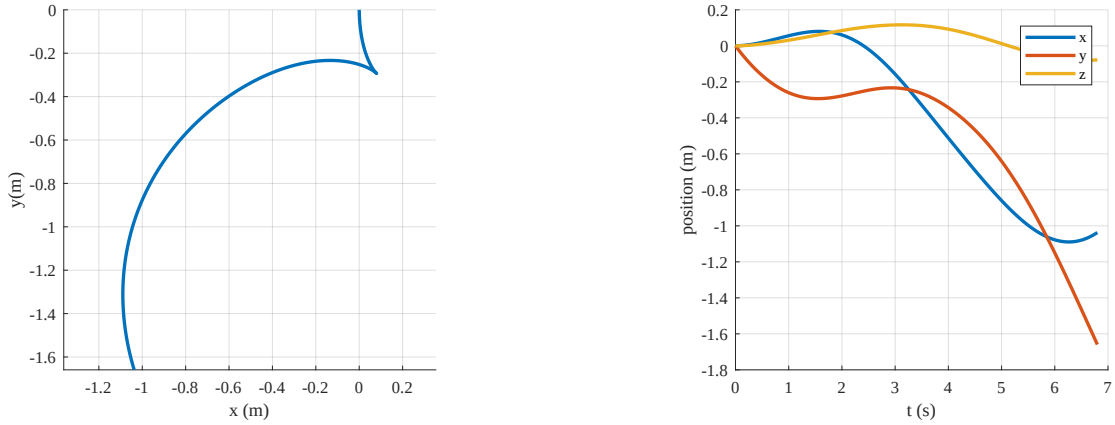

Figure 130: Suspended mass position

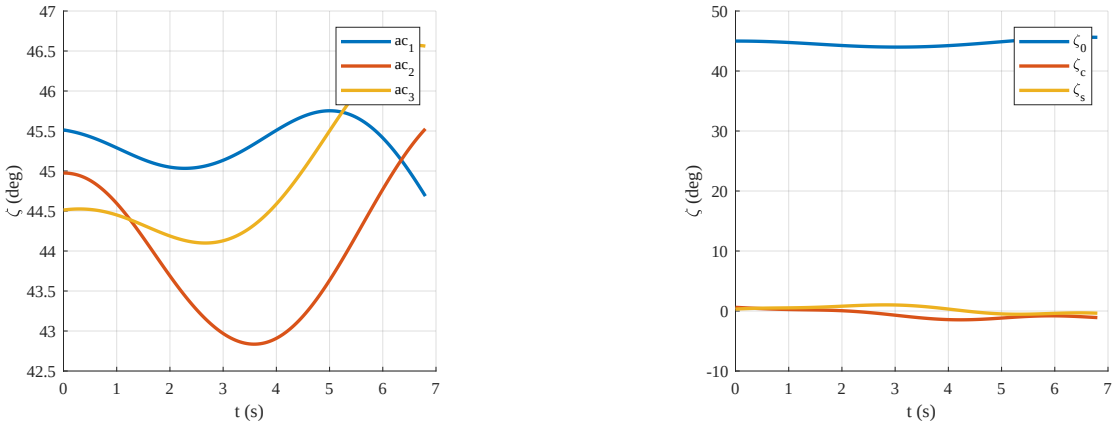

Figure 131: Tether angle ζ

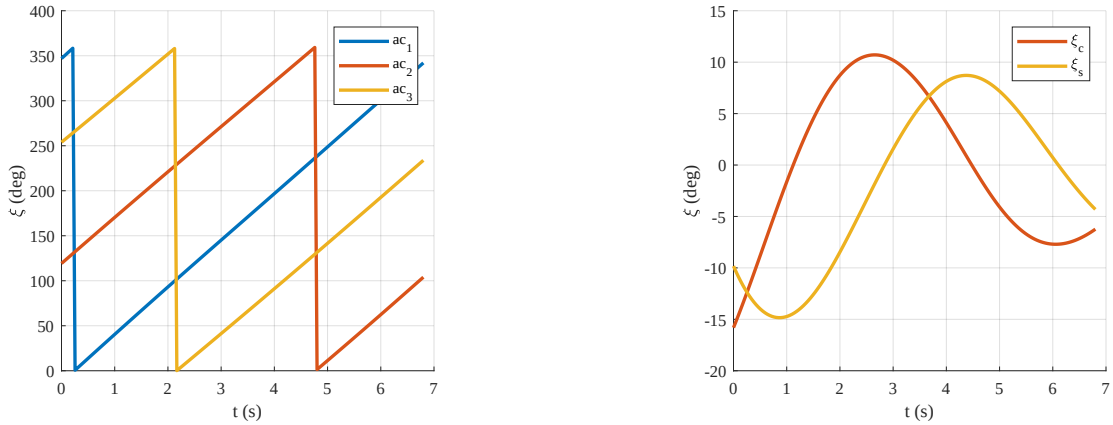

Figure 132: Tether angle ξ

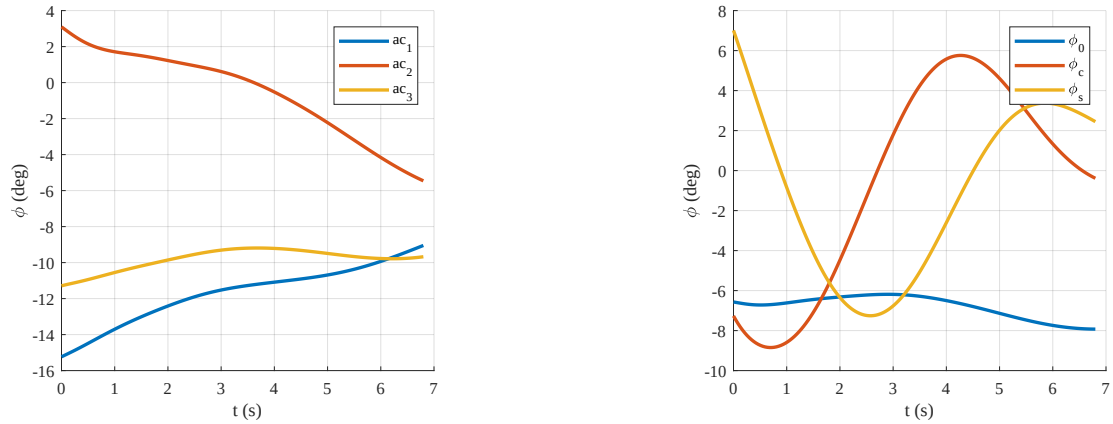

Figure 133: Aircraft angle ϕ

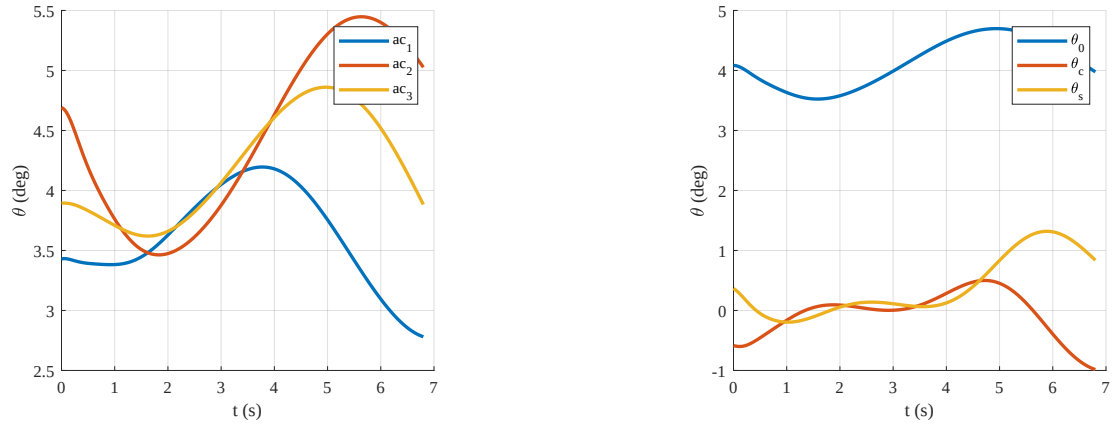

Figure 134: Aircraft angle θ

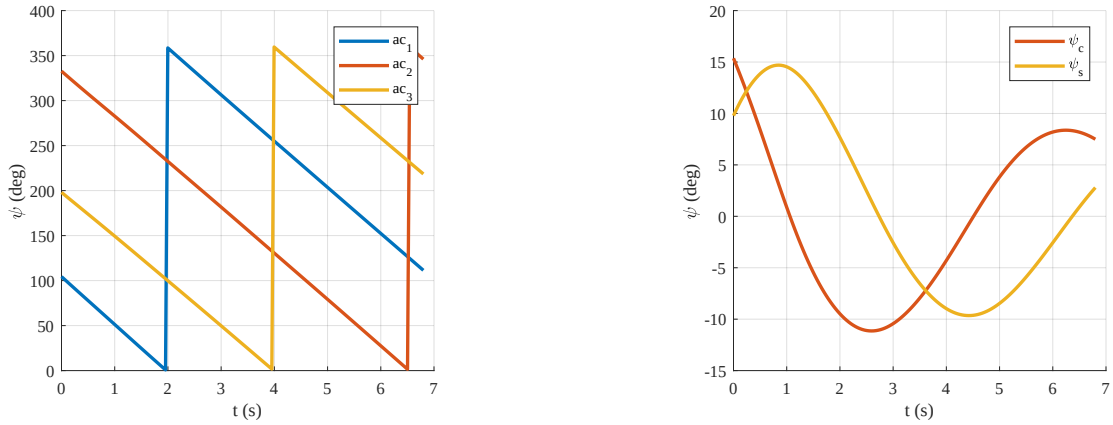

Figure 135: Aircraft angle ψ

G.1.8 Mode 9

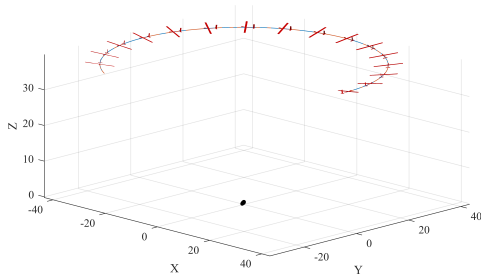

Figure 136: Overall motion of a single aircraft through one period of mode 9

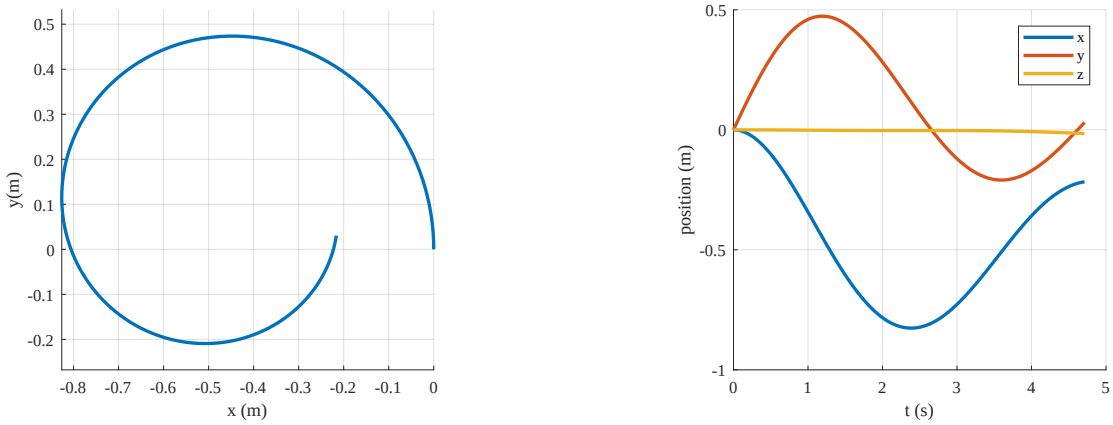

Figure 137: Suspended mass position

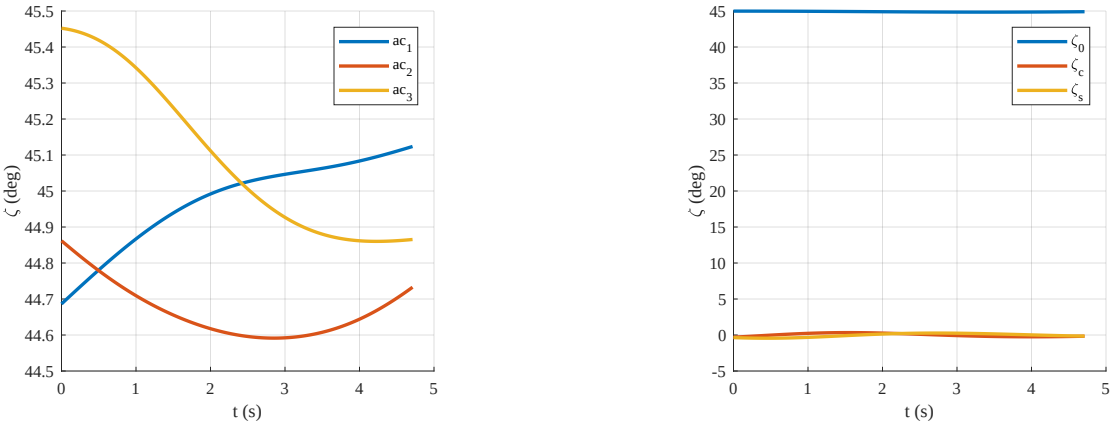

Figure 138: Tether angle ζ

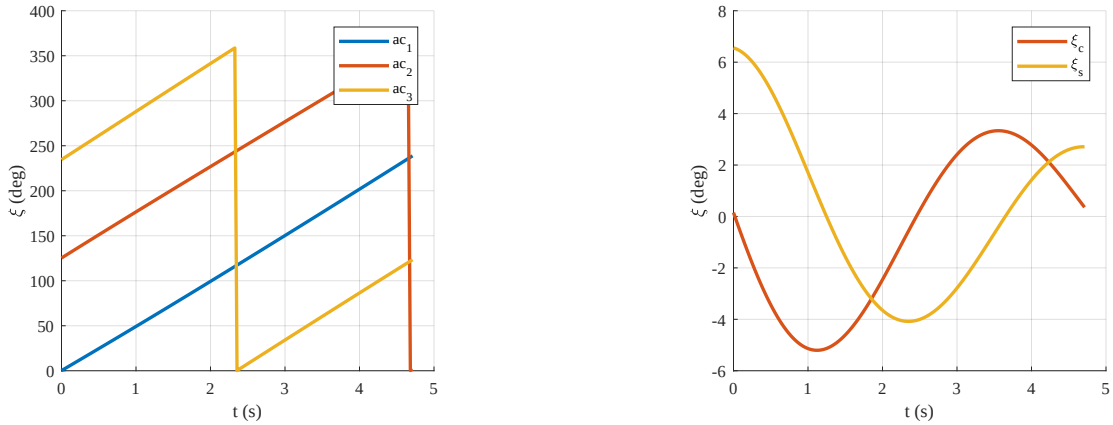

Figure 139: Tether angle ξ

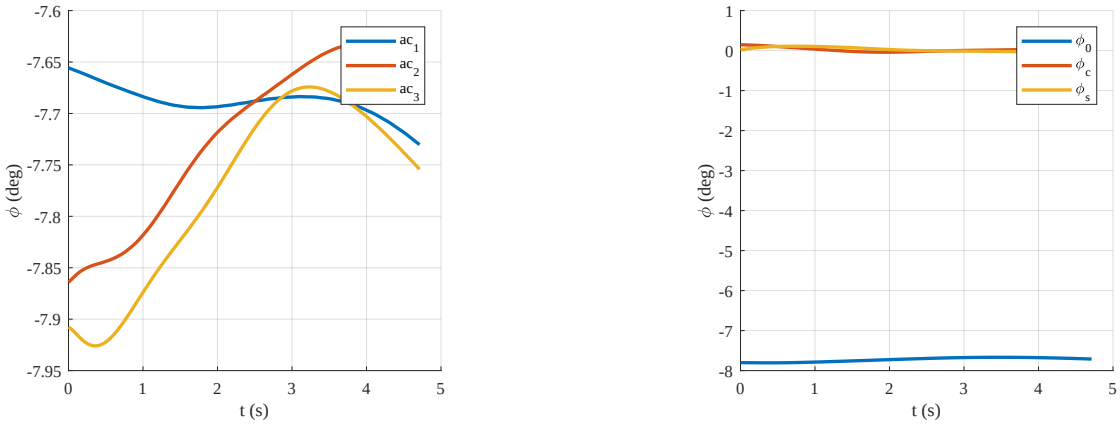

Figure 140: Aircraft angle ϕ

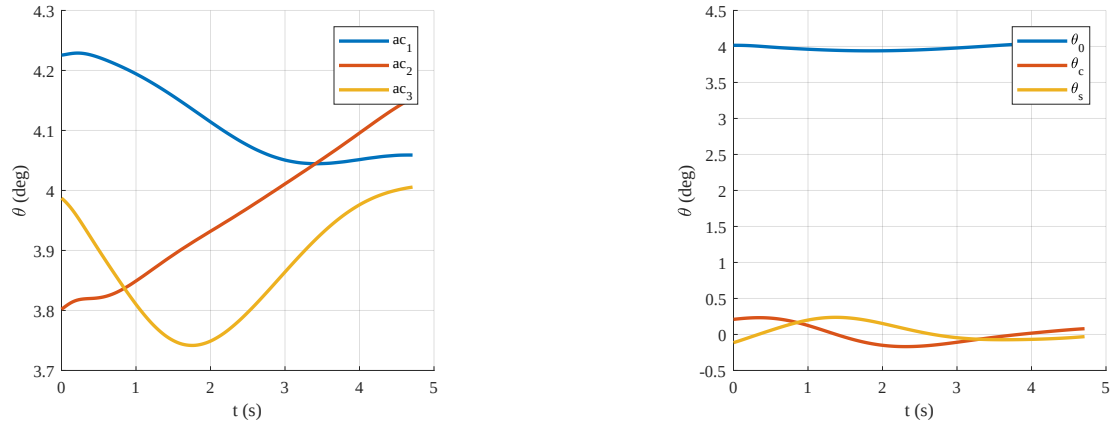

Figure 141: Aircraft angle θ

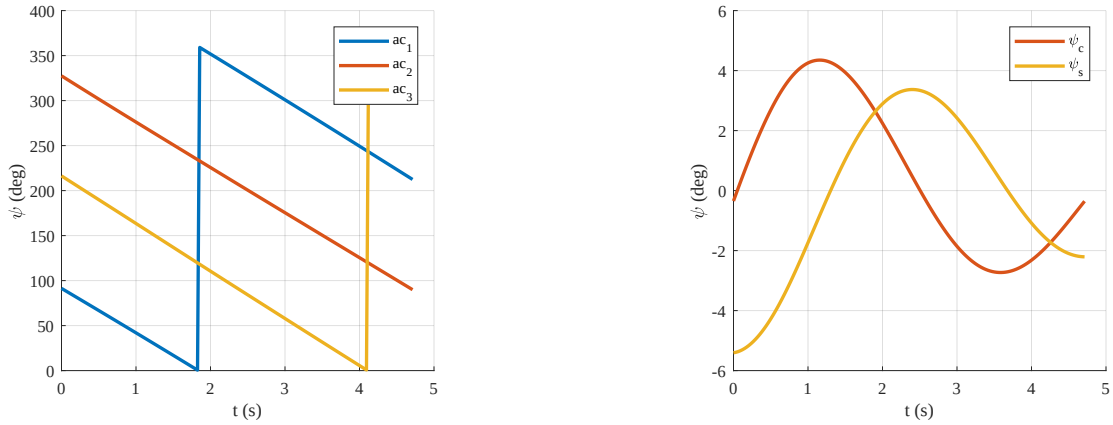

Figure 142: Aircraft angle ψ

G.1.9 Mode 10

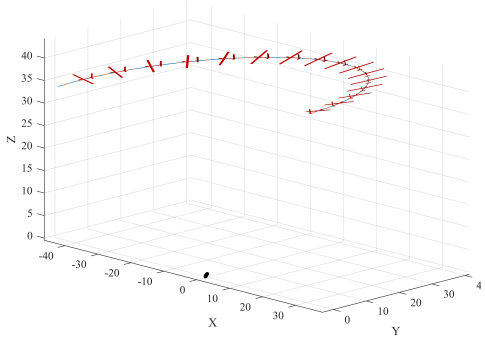

Figure 143: Overall motion of a single aircraft through one period of mode 10

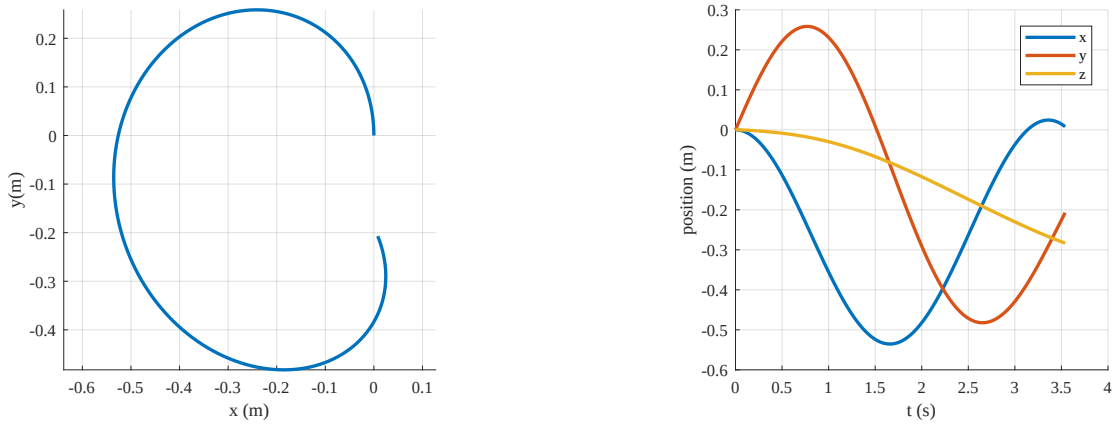

Figure 144: Suspended mass position

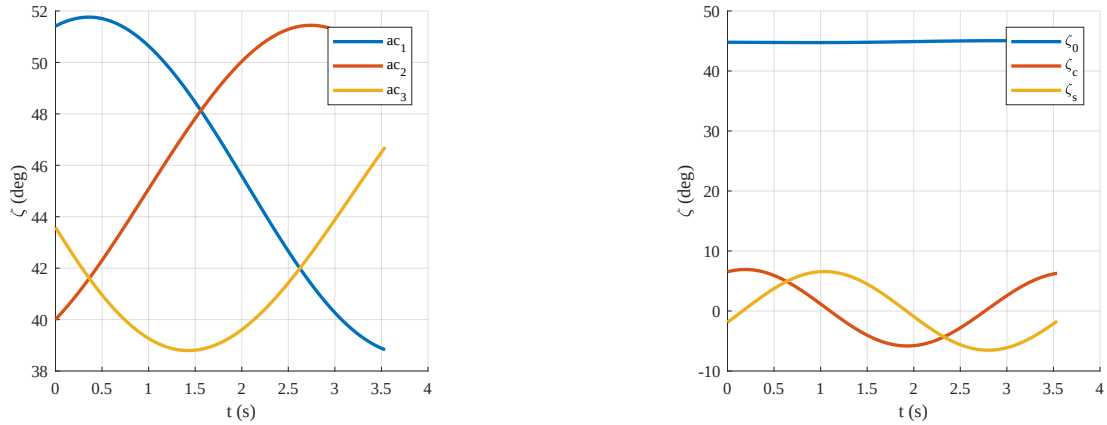

Figure 145: Tether angle ζ

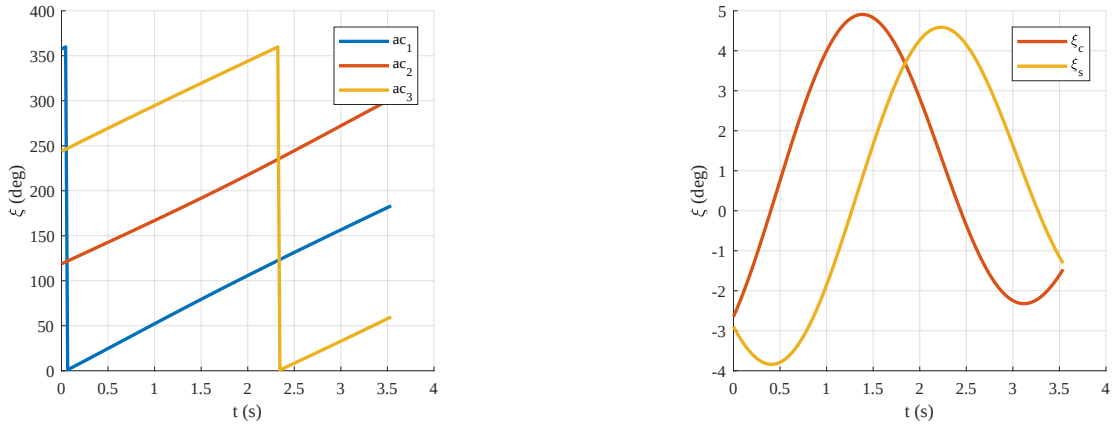

Figure 146: Tether angle ξ

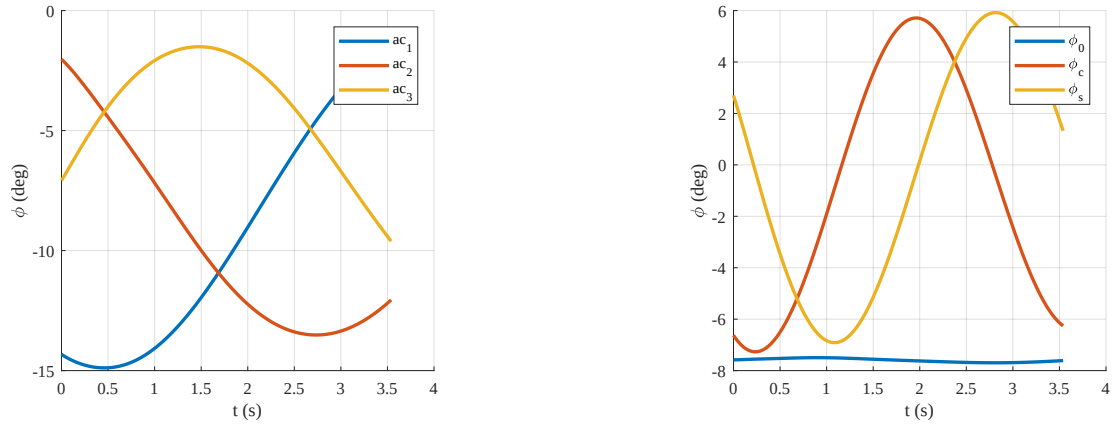

Figure 147: Aircraft angle ϕ

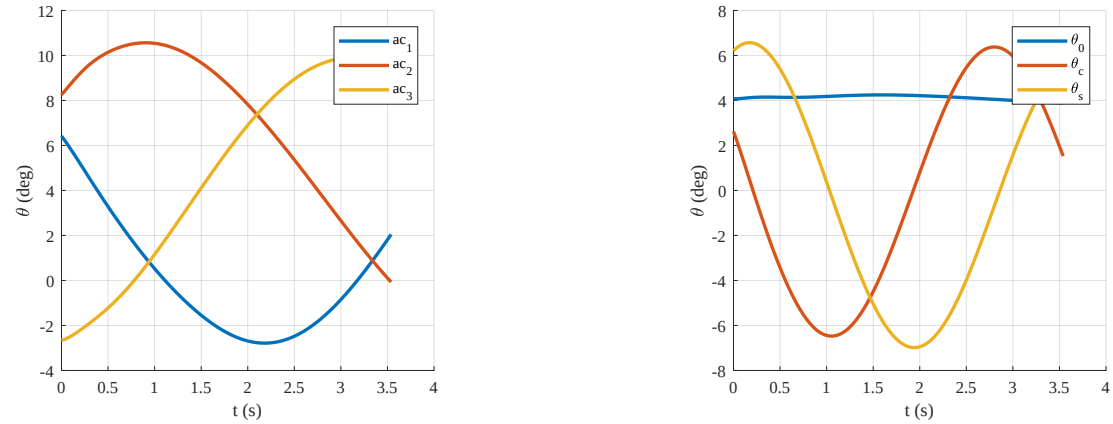

Figure 148: Aircraft angle θ

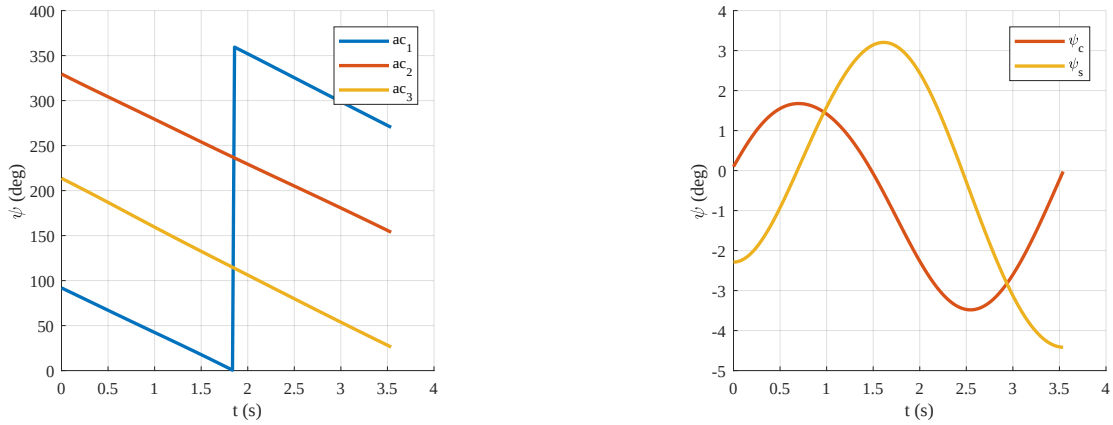

Figure 149: Aircraft angle ψ

G.1.10 Mode 11

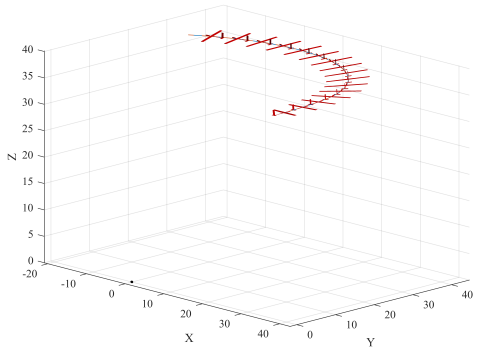

Figure 150: Overall motion of a single aircraft through one period of mode 11

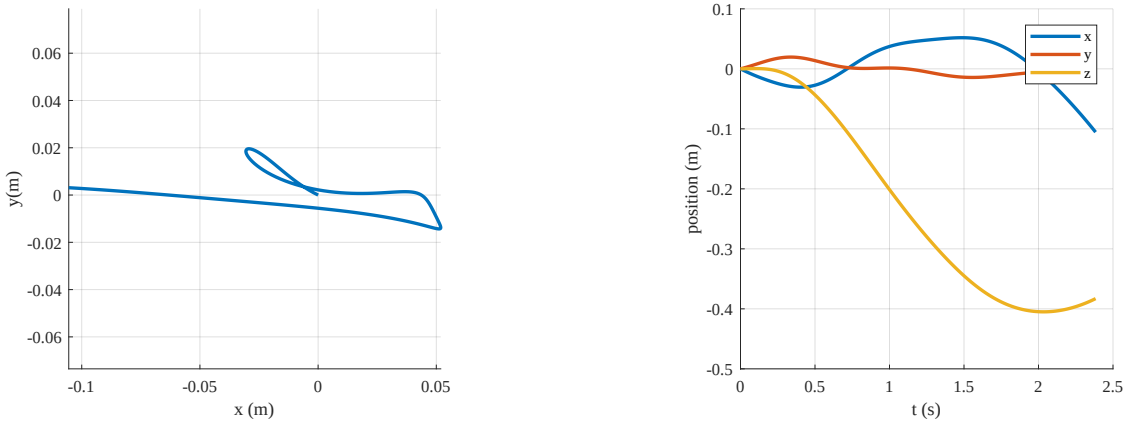

Figure 151: Suspended mass position

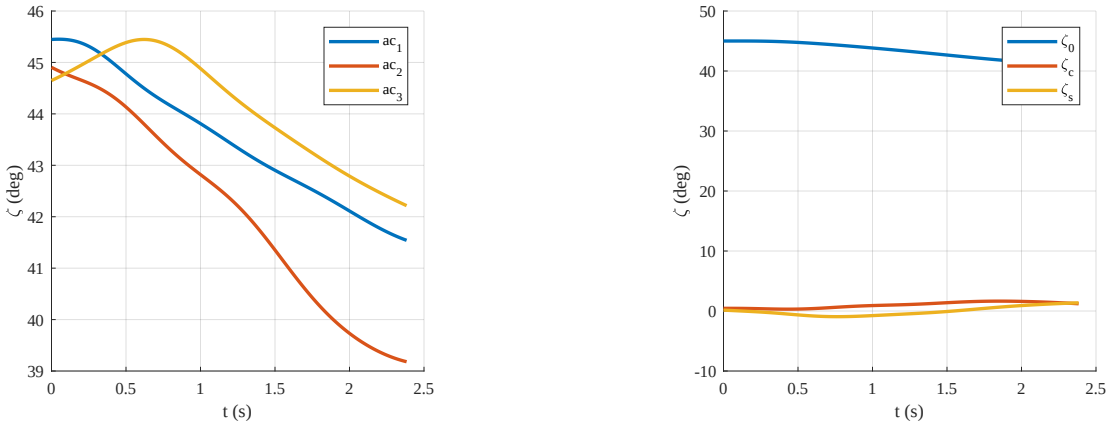

Figure 152: Tether angle ζ

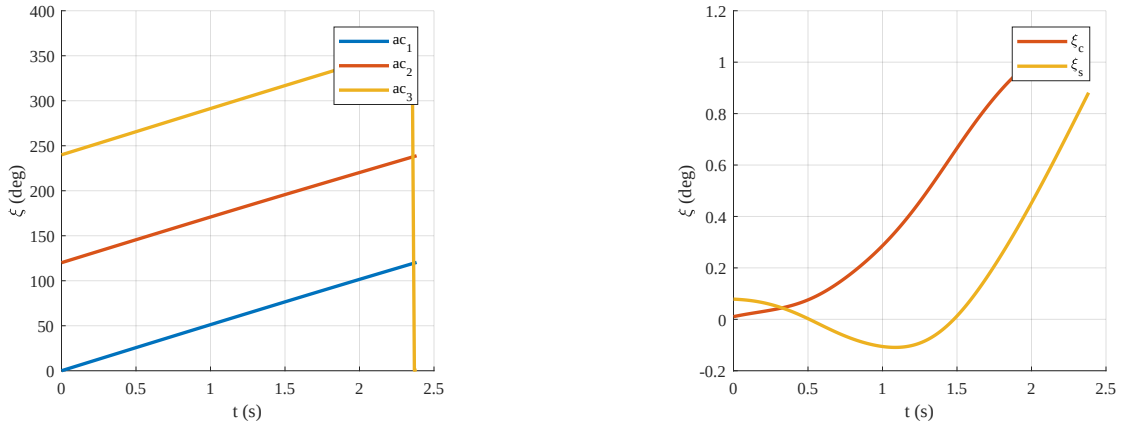

Figure 153: Tether angle ξ

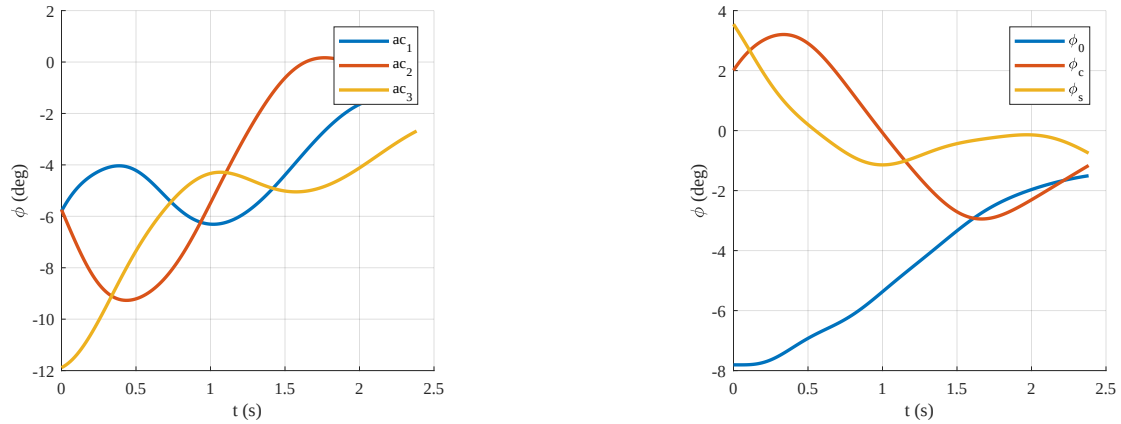

Figure 154: Aircraft angle ϕ

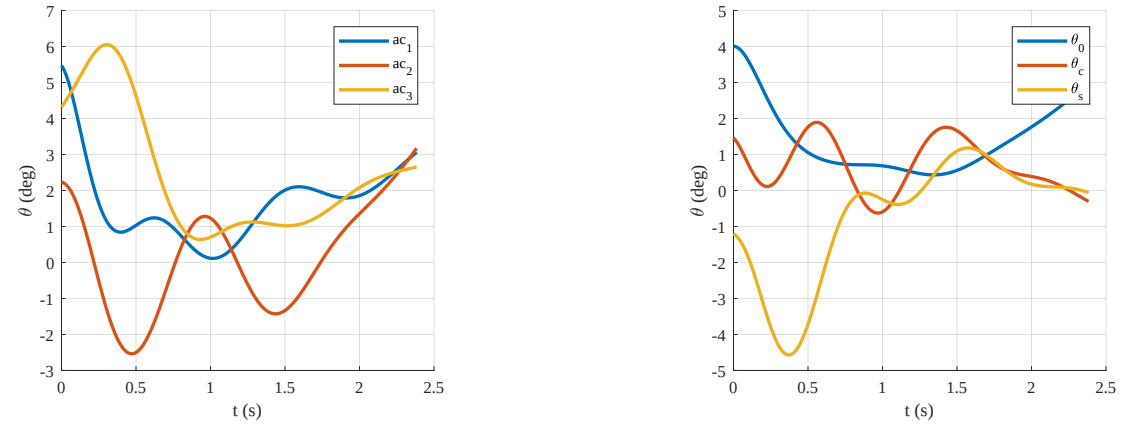

Figure 155: Aircraft angle θ

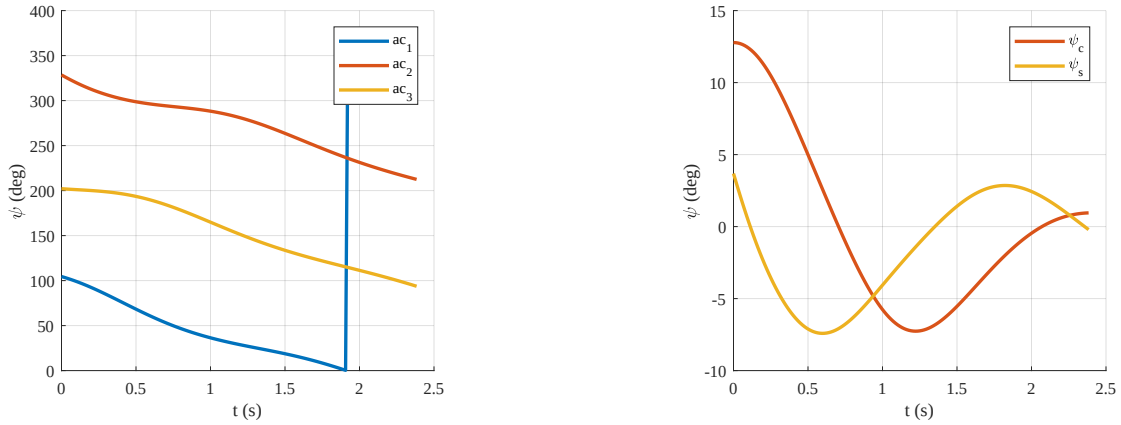

Figure 156: Aircraft angle ψ

G.1.11 Mode 12

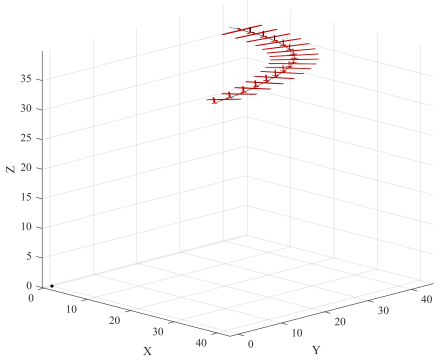

Figure 157: Overall motion of a single aircraft through one period of mode 12

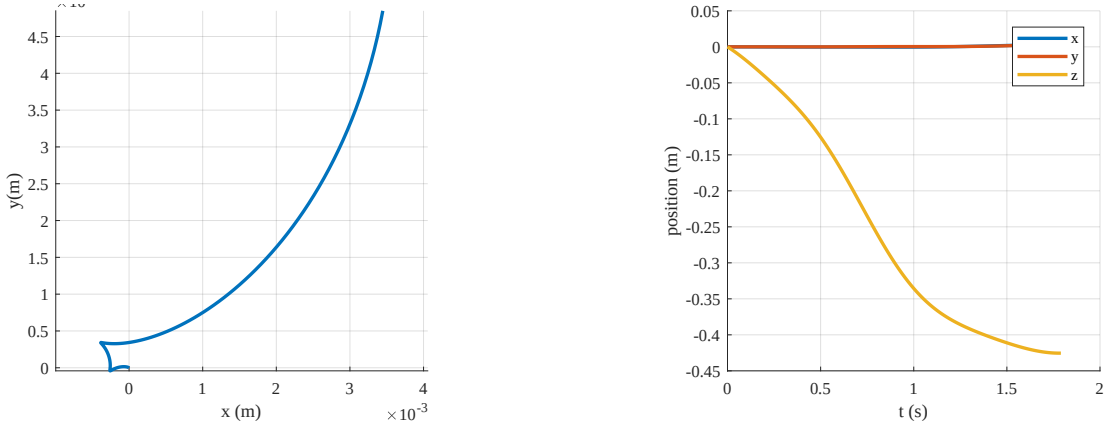

Figure 158: Suspended mass position

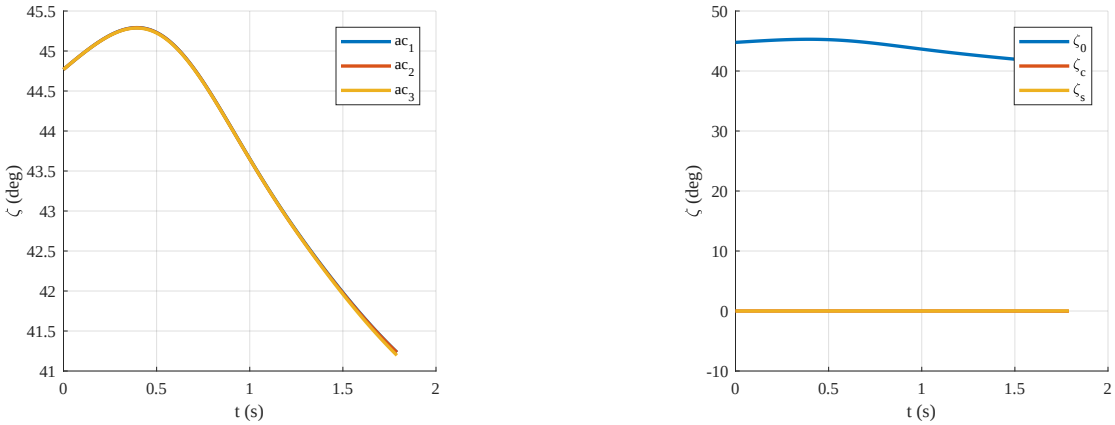

Figure 159: Tether angle ζ

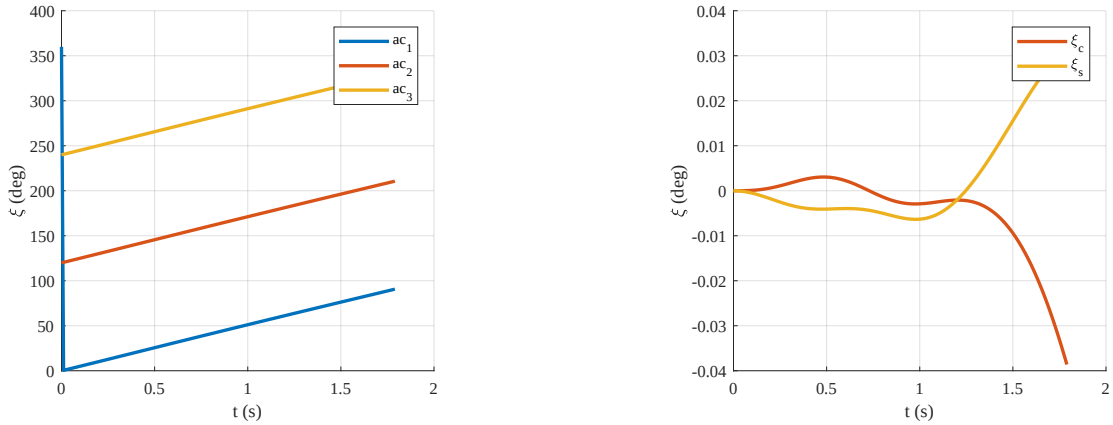

Figure 160: Tether angle ξ

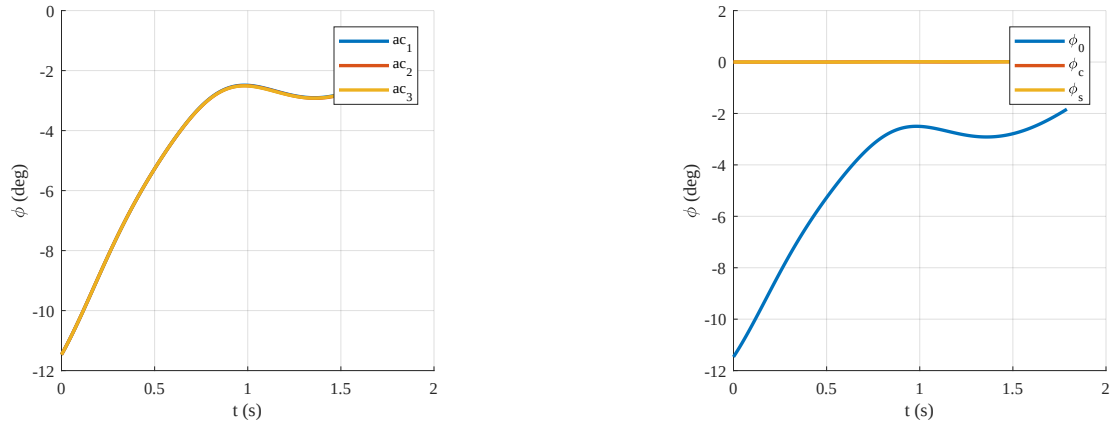

Figure 161: Aircraft angle ϕ

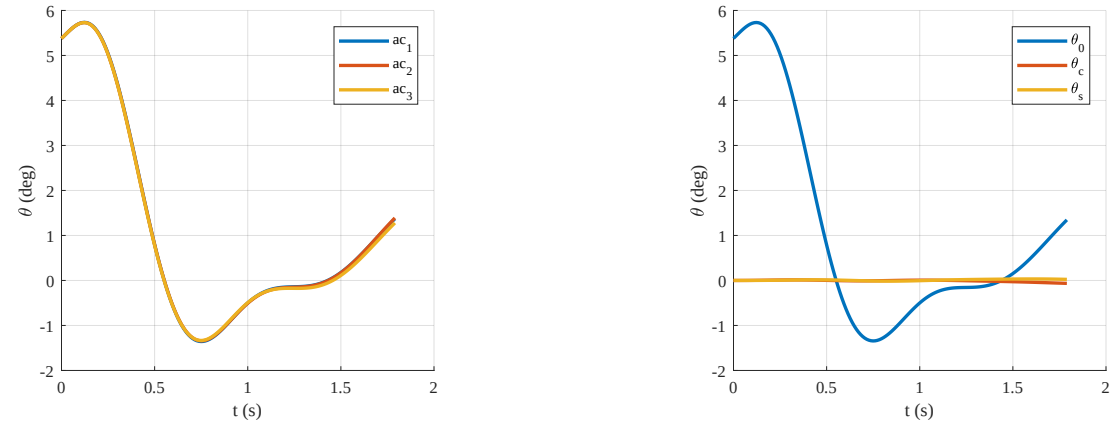

Figure 162: Aircraft angle θ

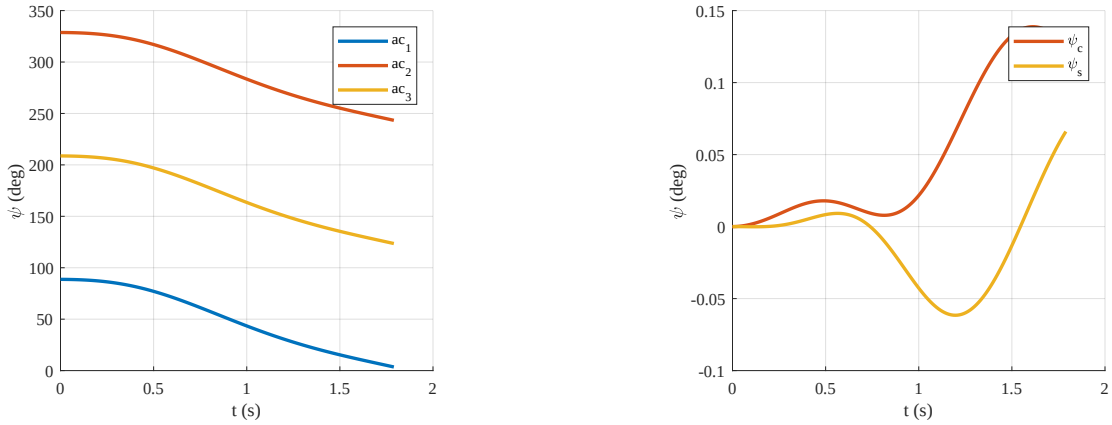

Figure 163: Aircraft angle ψ

G.1.12 Mode 13

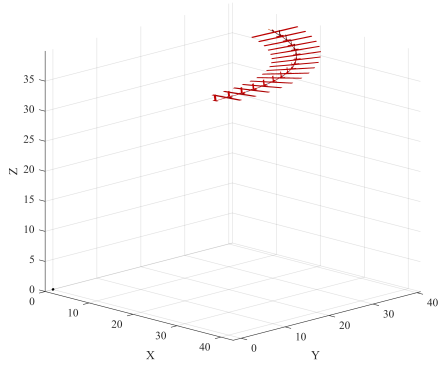

Figure 164: Overall motion of a single aircraft through one period of mode 13

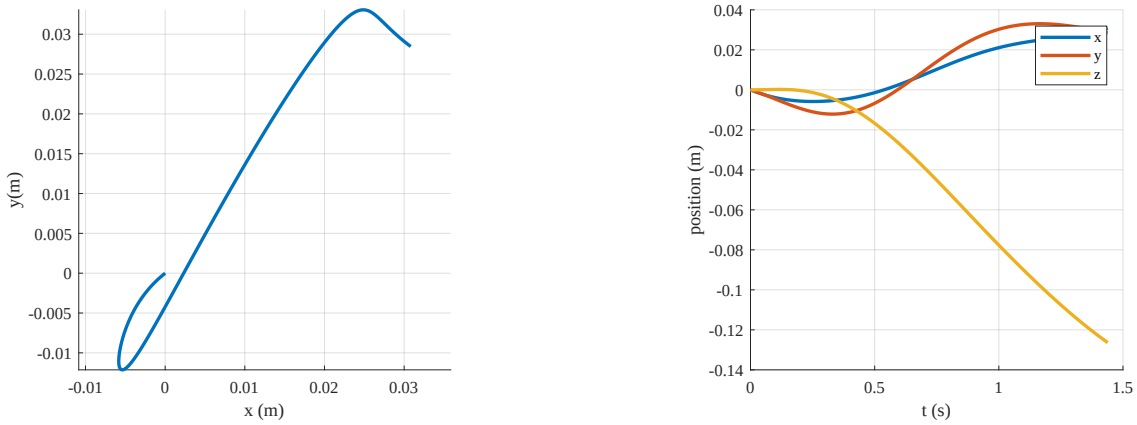

Figure 165: Suspended mass position

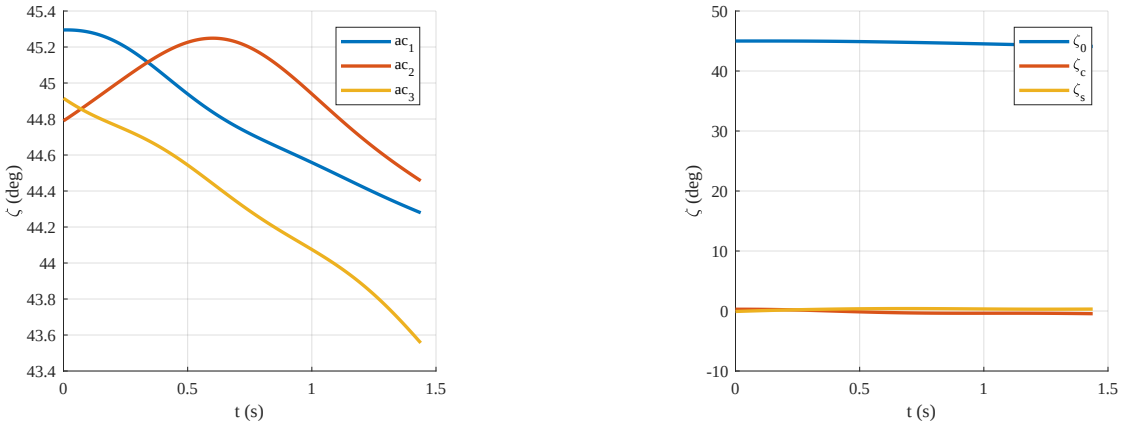

Figure 166: Tether angle ζ

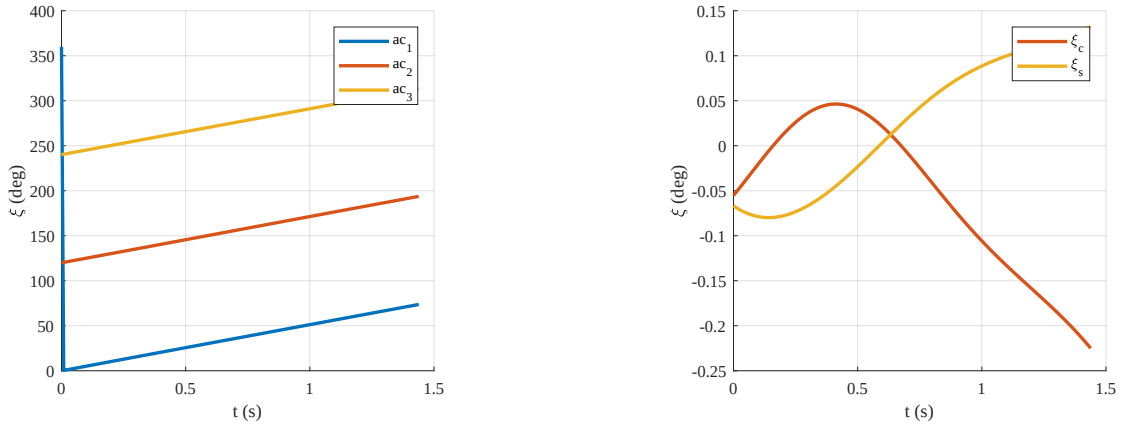

Figure 167: Tether angle ξ

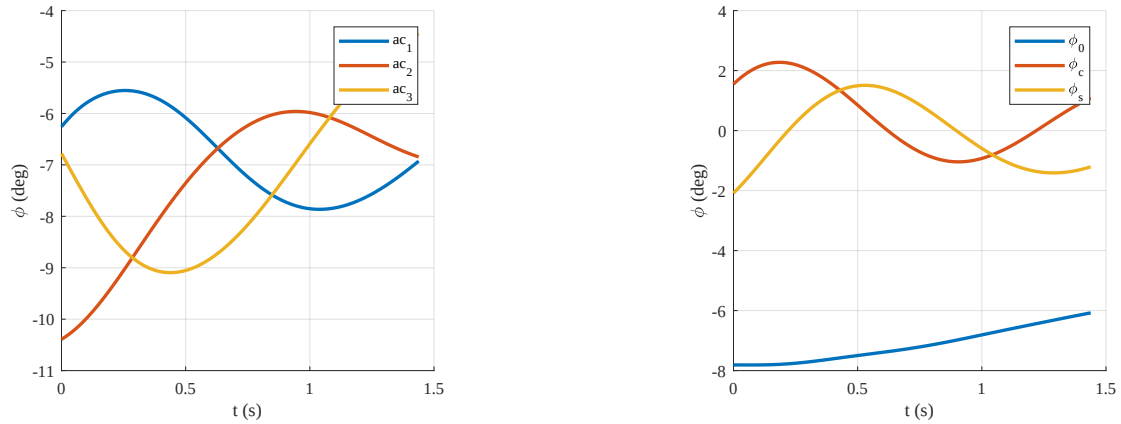

Figure 168: Aircraft angle ϕ

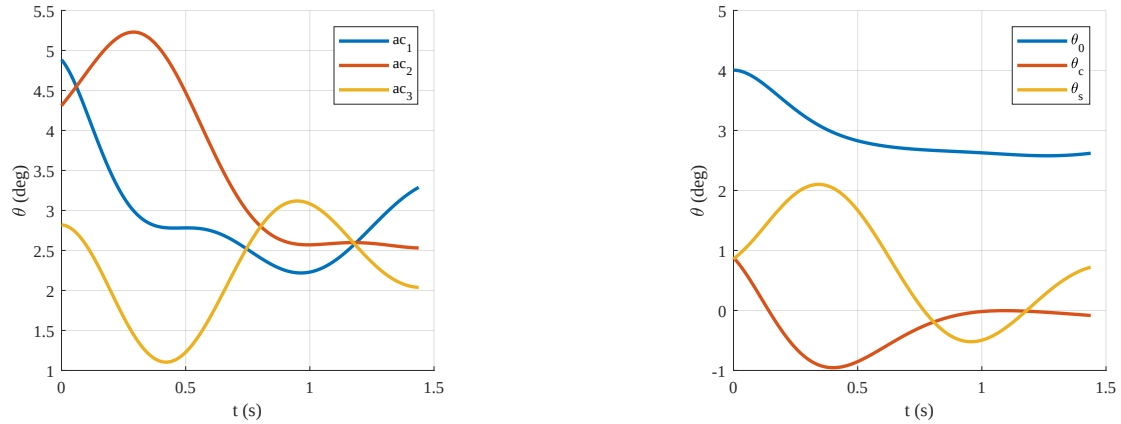

Figure 169: Aircraft angle θ

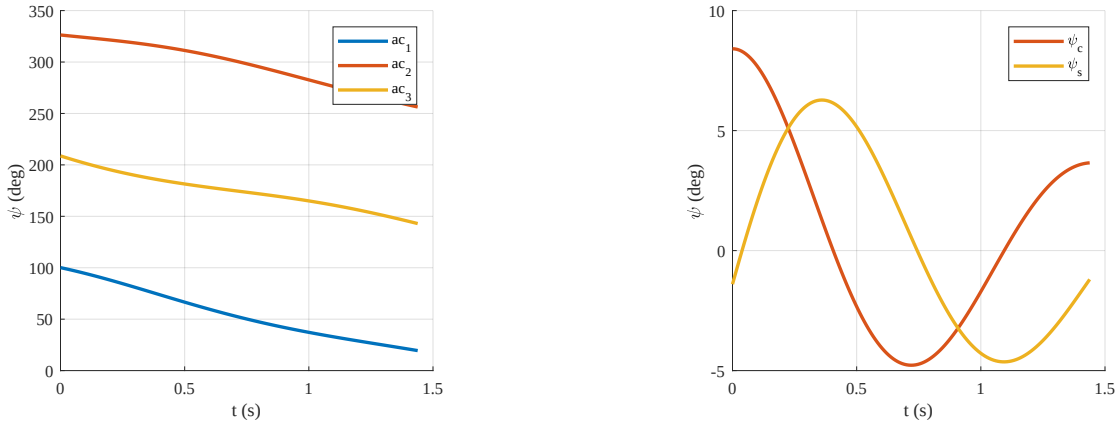

Figure 170: Aircraft angle ψ

G.1.13 Mode 14

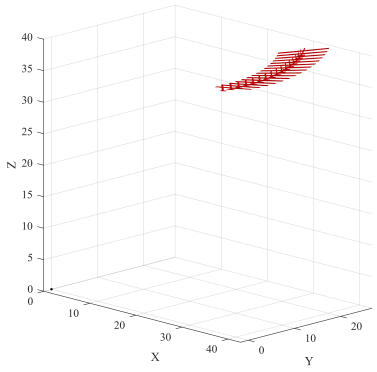

Figure 171: Overall motion of a single aircraft through one period of mode 14

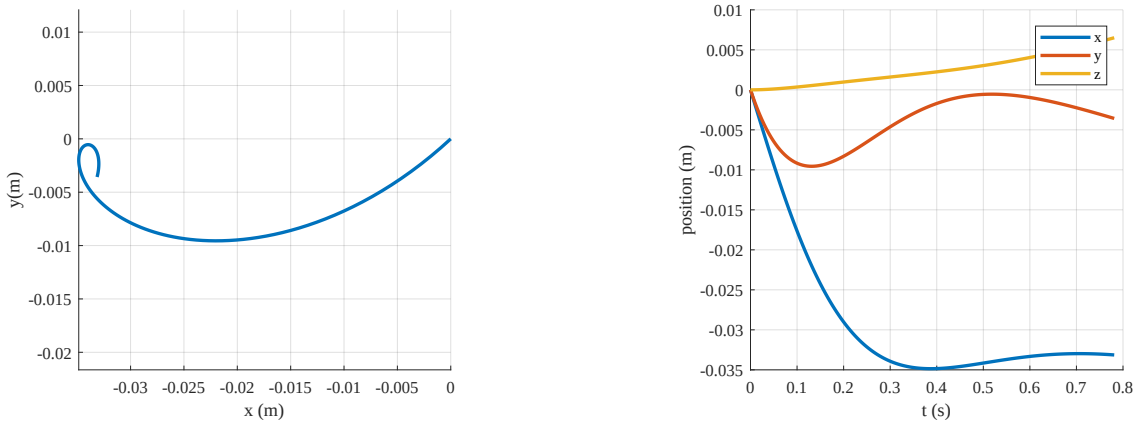

Figure 172: Suspended mass position

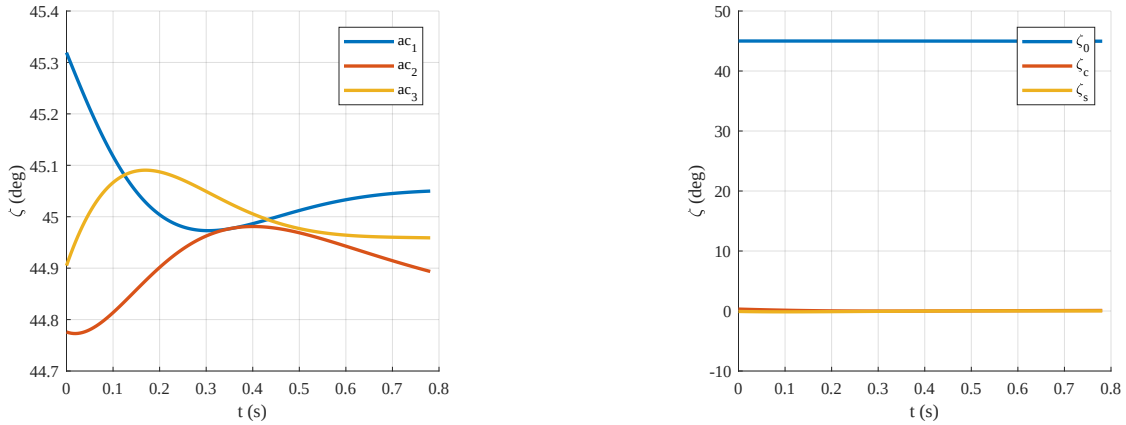

Figure 173: Tether angle ζ

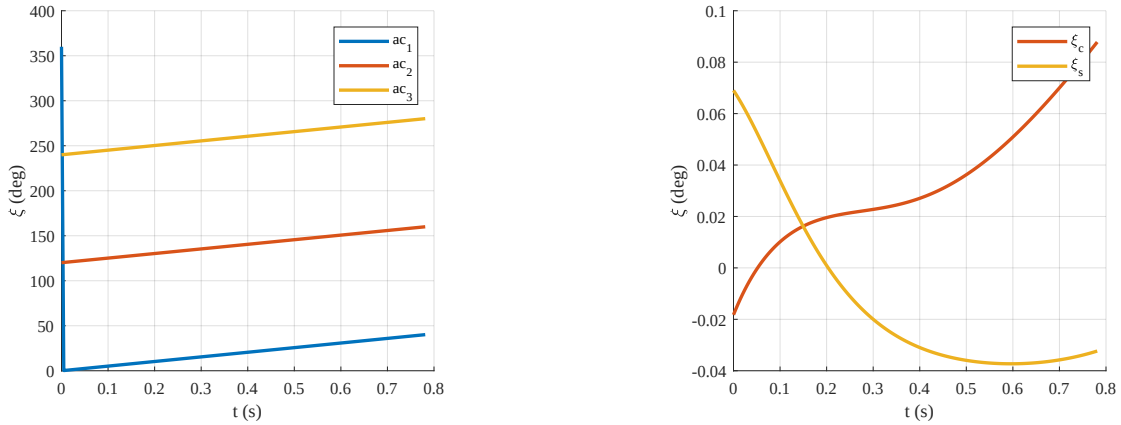

Figure 174: Tether angle ξ

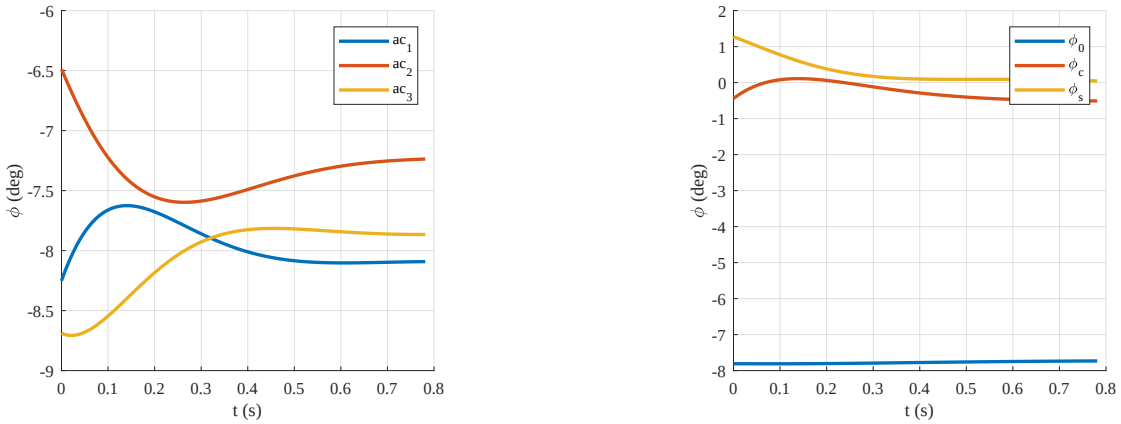

Figure 175: Aircraft angle ϕ

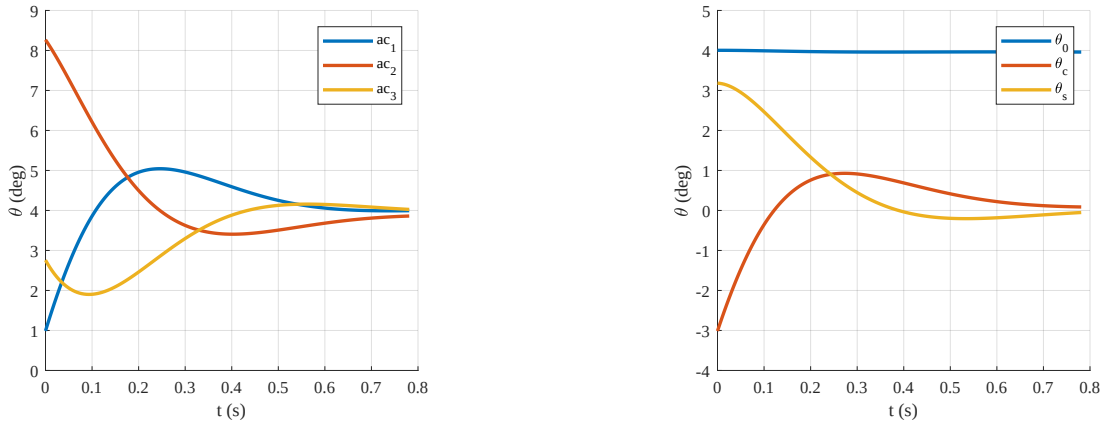

Figure 176: Aircraft angle θ

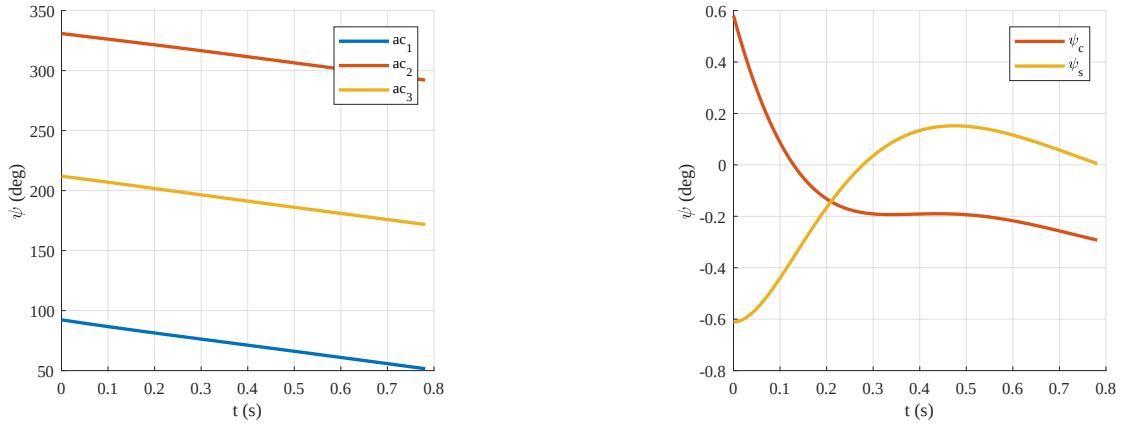

Figure 177: Aircraft angle ψ

G.1.14 Mode 15

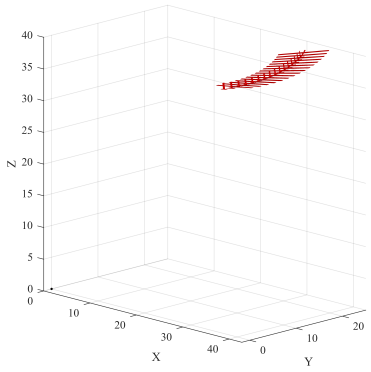

Figure 178: Overall motion of a single aircraft through one period of mode 15

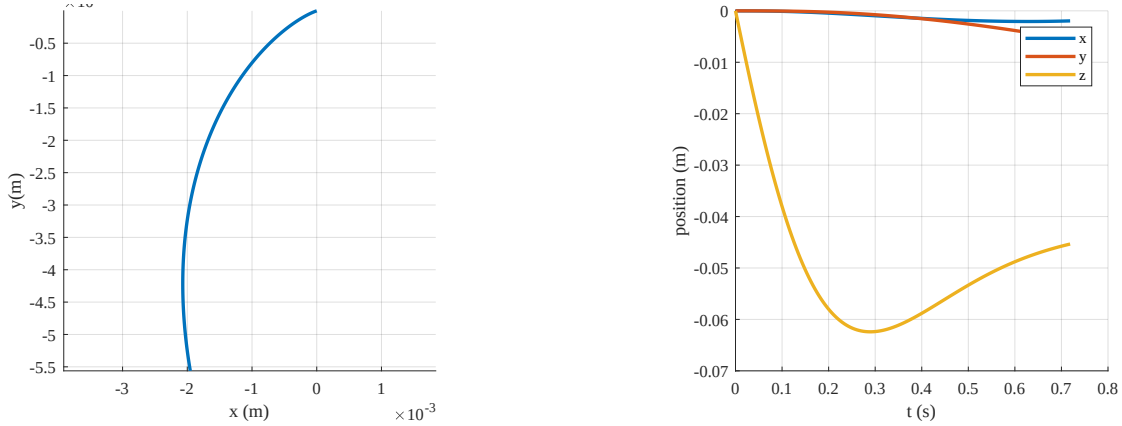

Figure 179: Suspended mass position

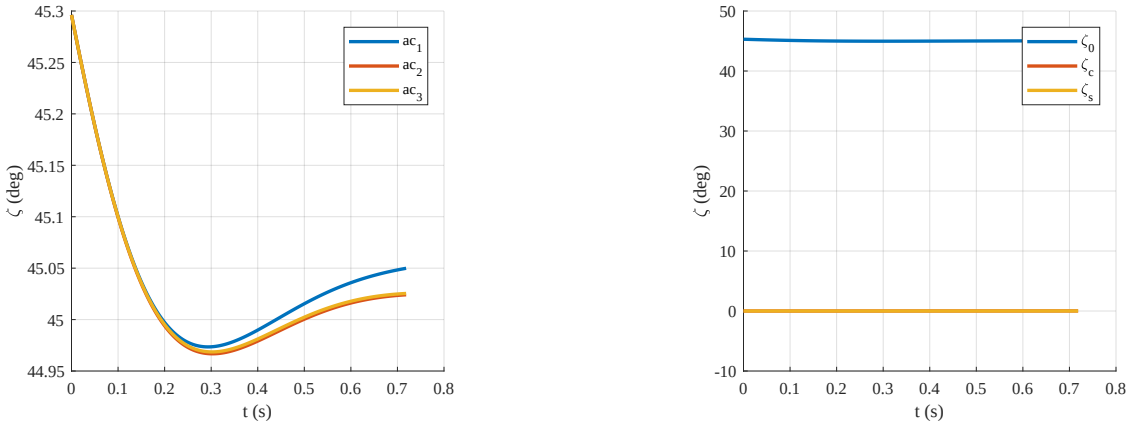

Figure 180: Tether angle ζ

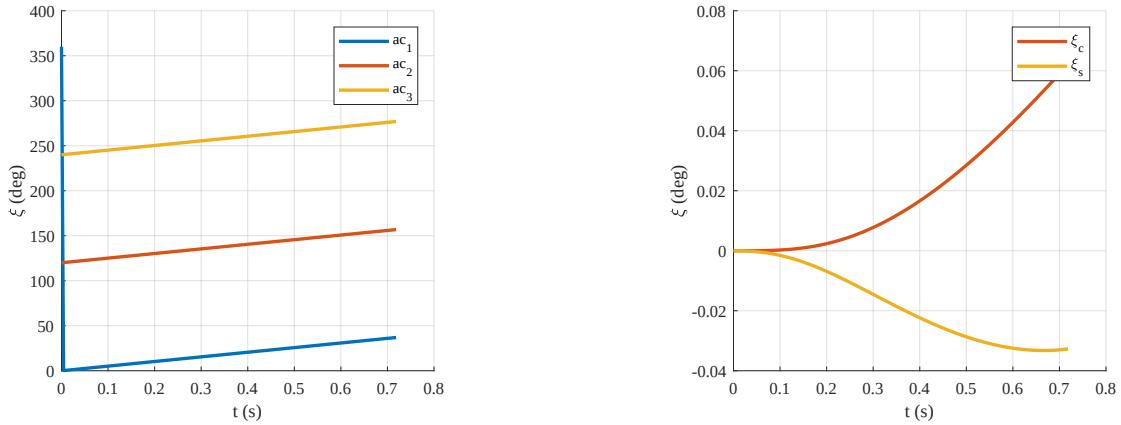

Figure 181: Tether angle ξ

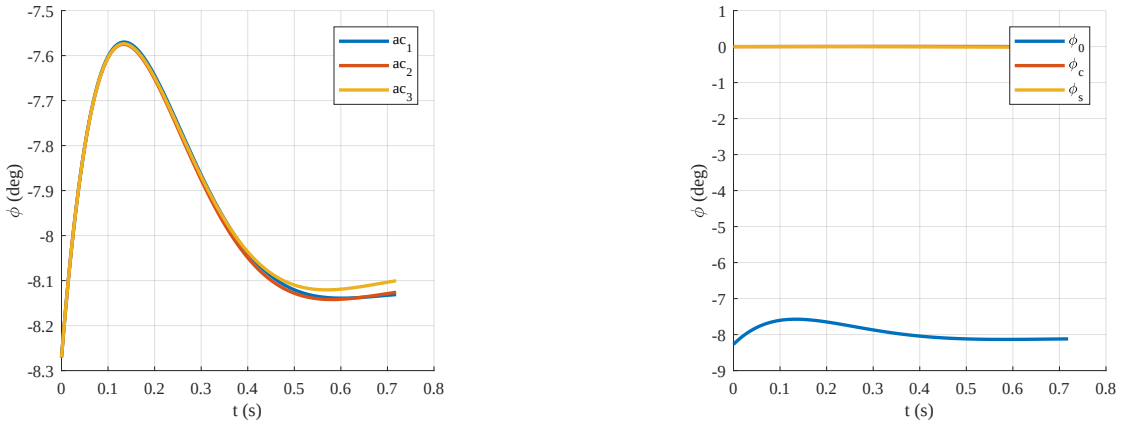

Figure 182: Aircraft angle ϕ

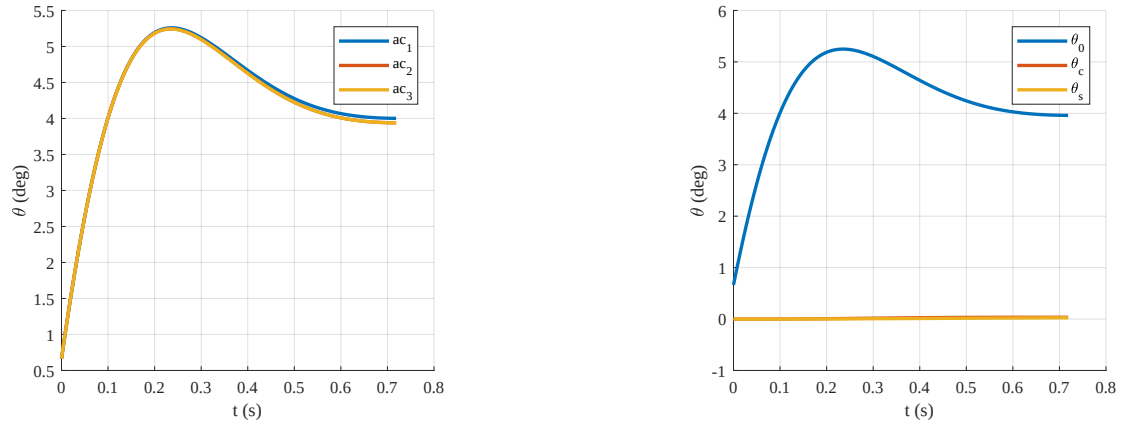

Figure 183: Aircraft angle θ

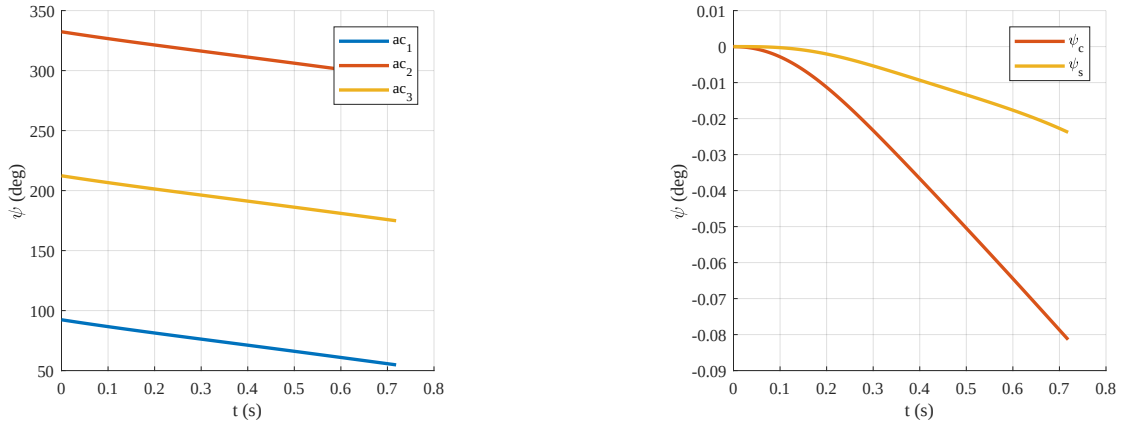

Figure 184: Aircraft angle ψ

G.1.15 Mode 16

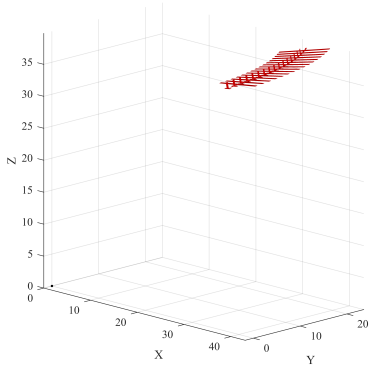

Figure 185: Overall motion of a single aircraft through one period of mode 16

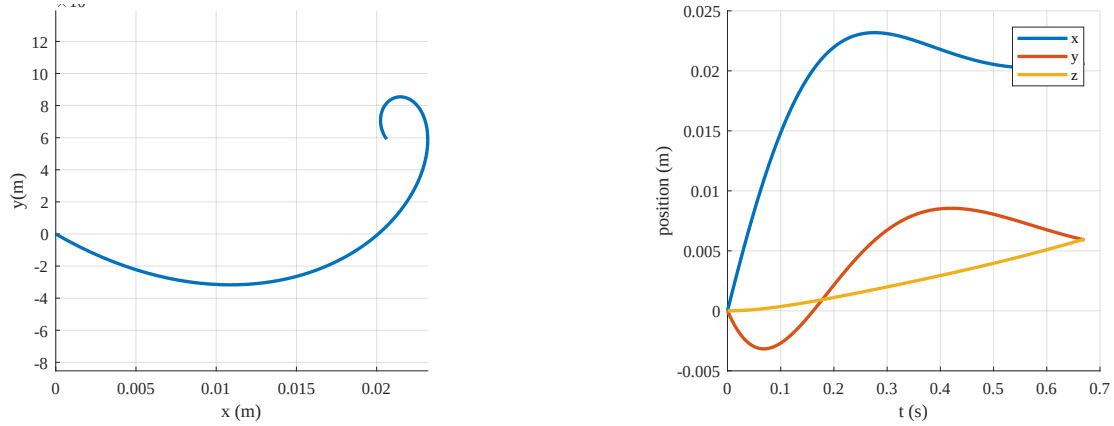

Figure 186: Suspended mass position

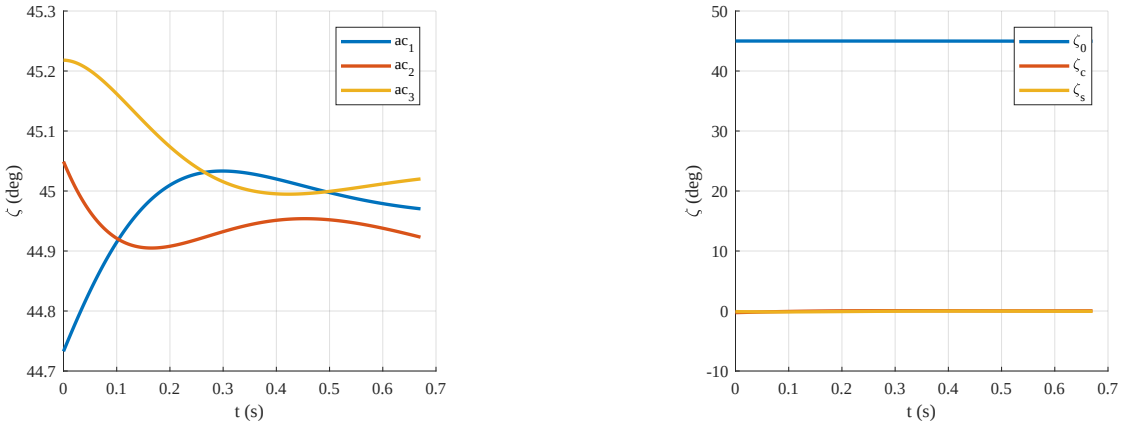

Figure 187: Tether angle ζ

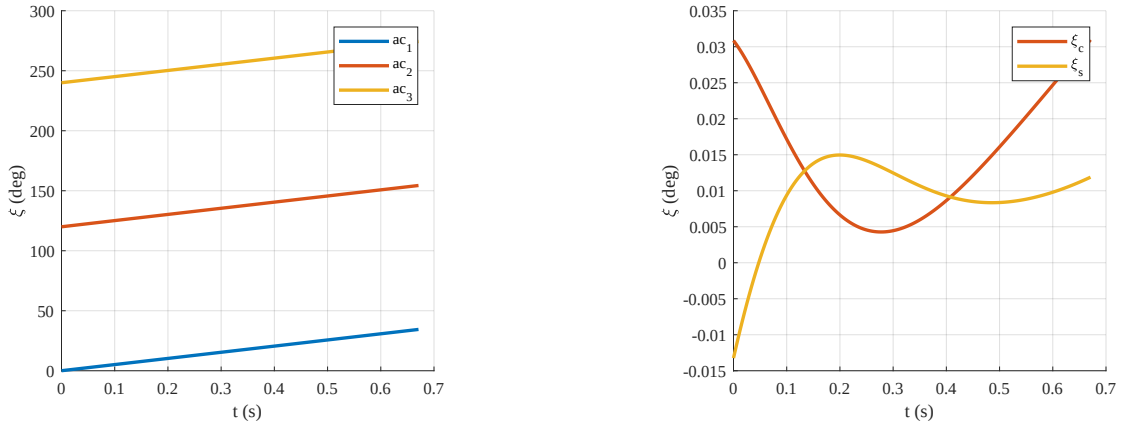

Figure 188: Tether angle ξ

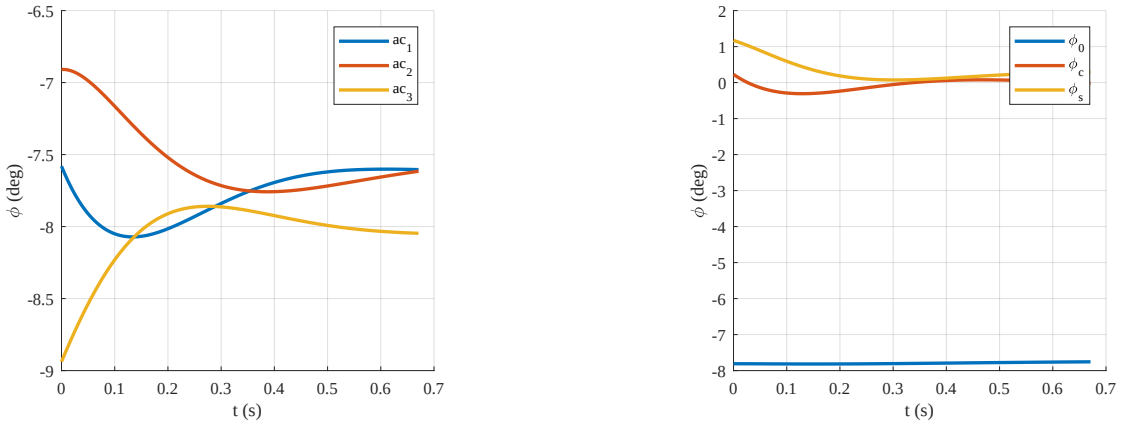

Figure 189: Aircraft angle ϕ

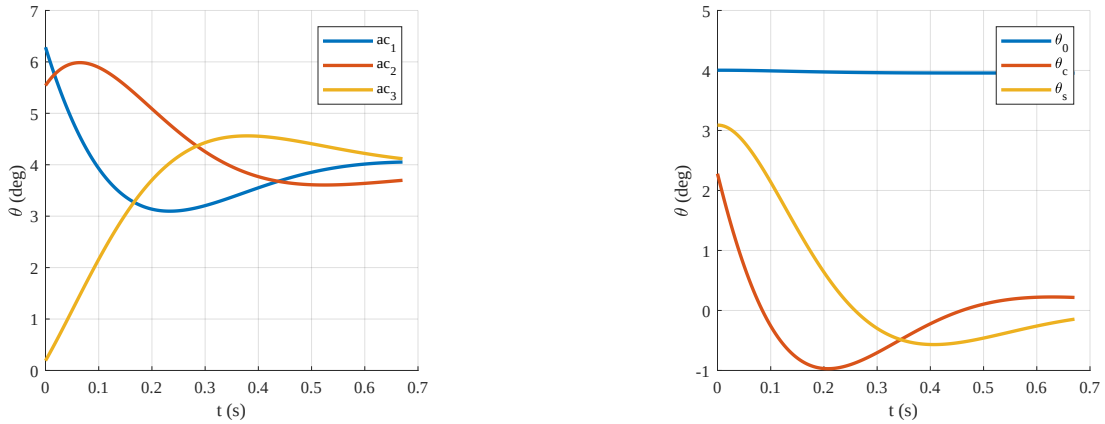

Figure 190: Aircraft angle θ

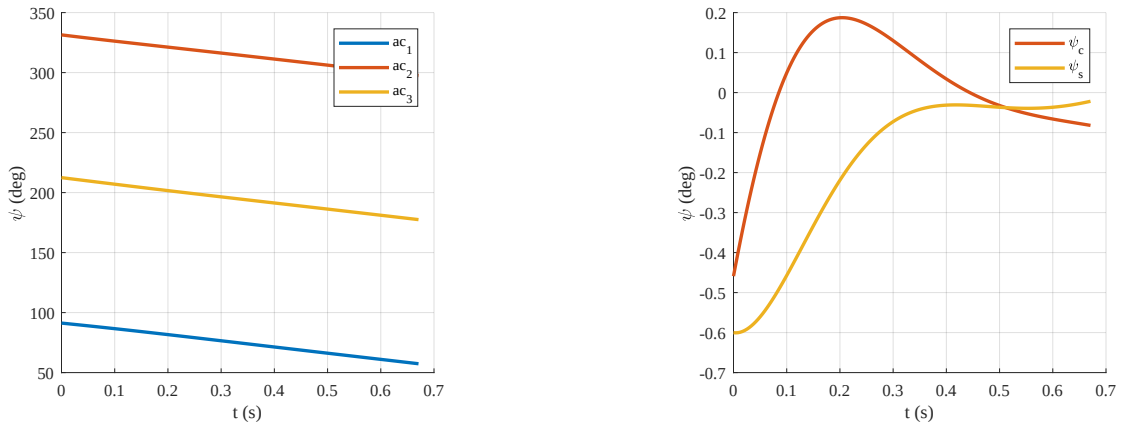

Figure 191: Aircraft angle ψ

G.1.16 Mode 17

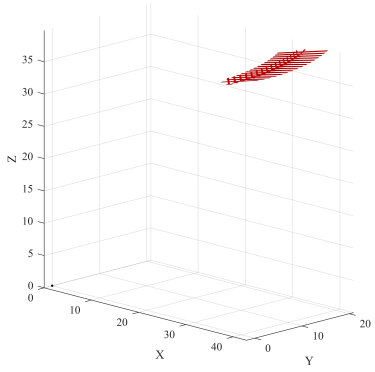

Figure 192: Overall motion of a single aircraft through one period of mode 17

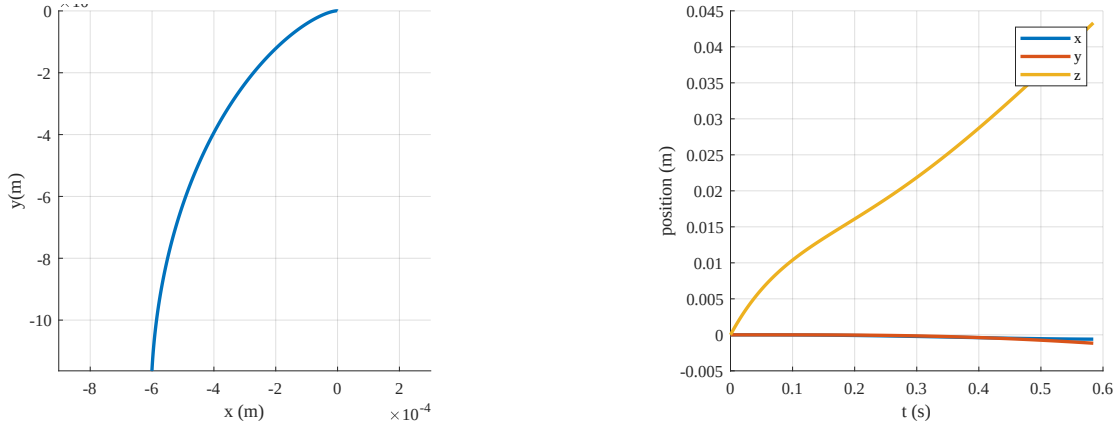

Figure 193: Suspended mass position

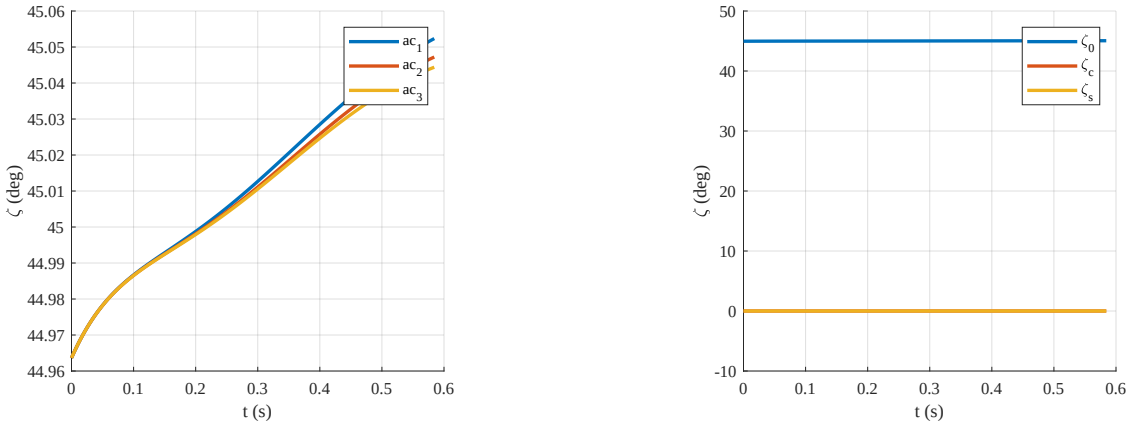

Figure 194: Tether angle ζ

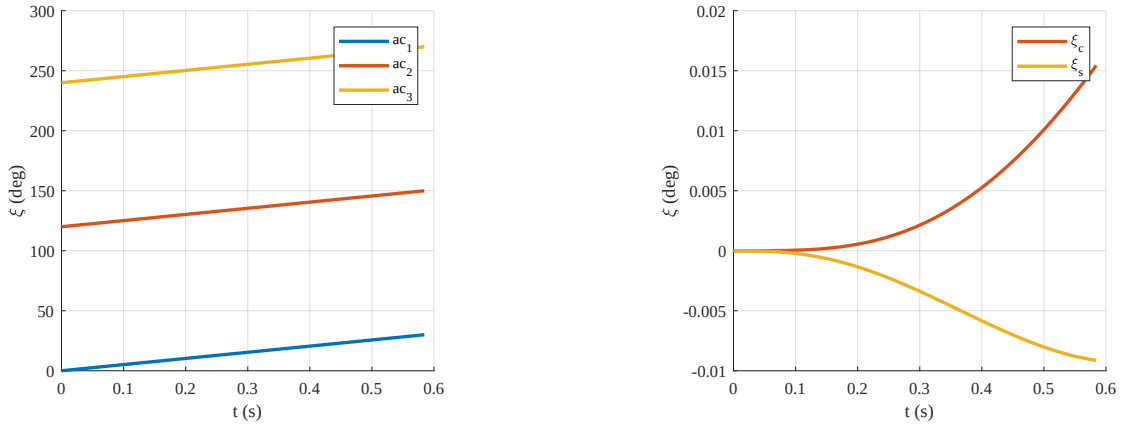

Figure 195: Tether angle ξ

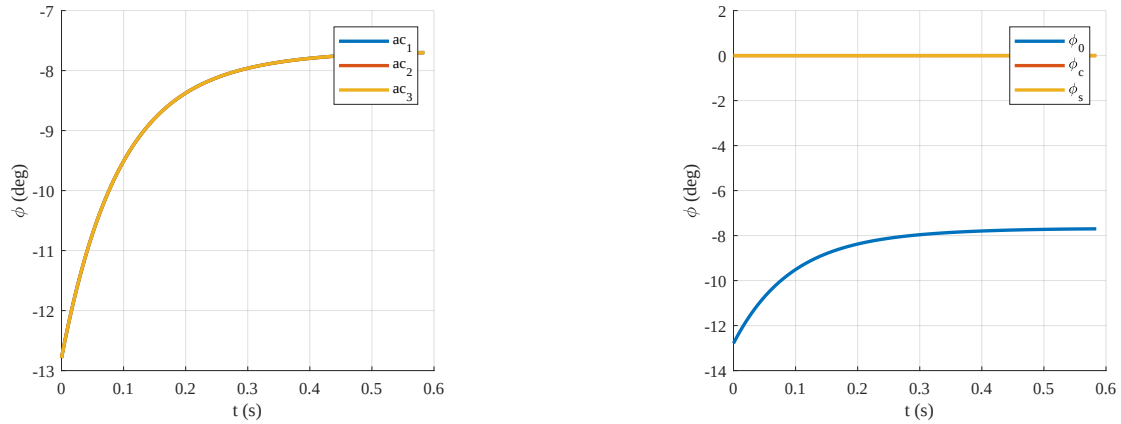

Figure 196: Aircraft angle ϕ

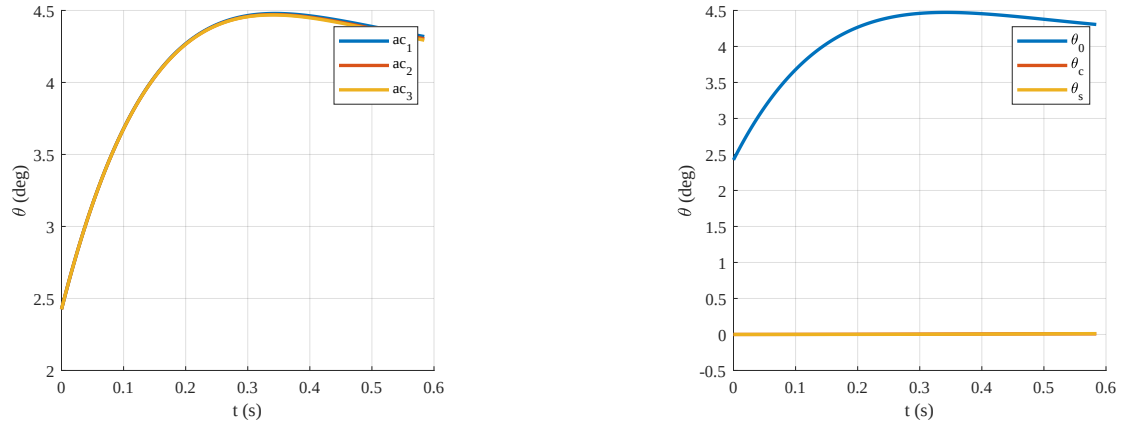

Figure 197: Aircraft angle θ

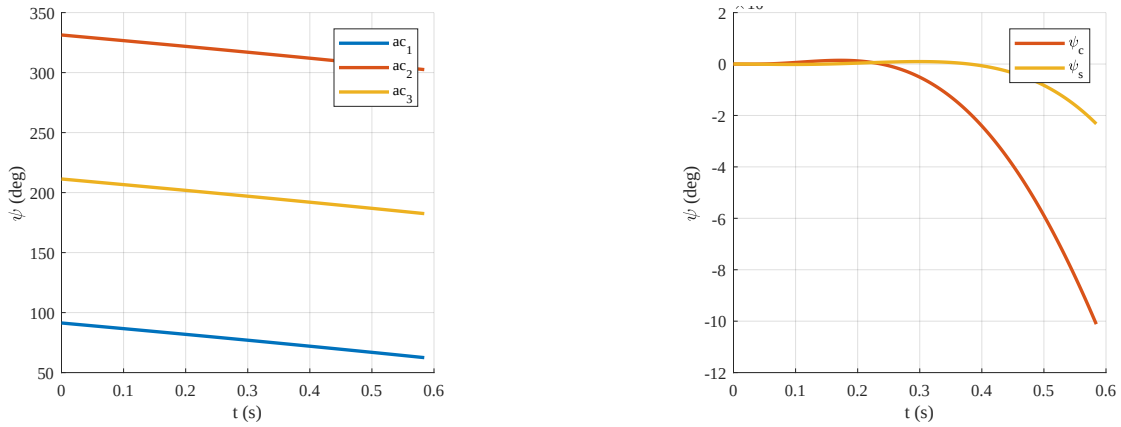

Figure 198: Aircraft angle ψ

G.1.17 Mode 18

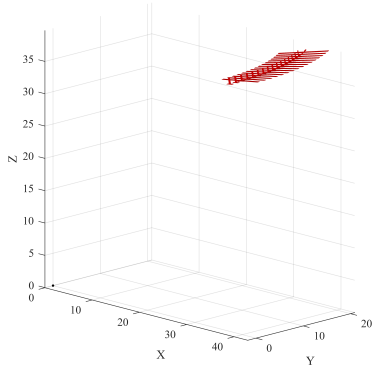

Figure 199: Overall motion of a single aircraft through one period of mode 18

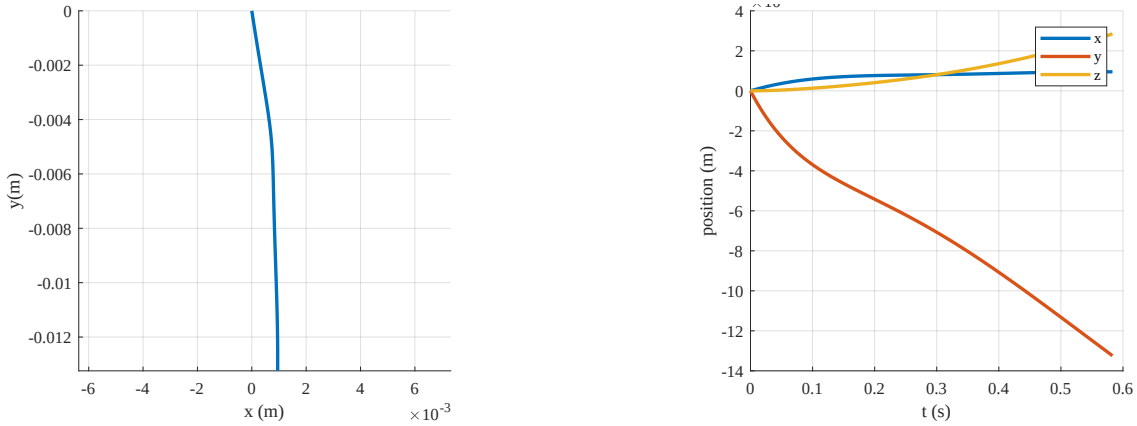

Figure 200: Suspended mass position

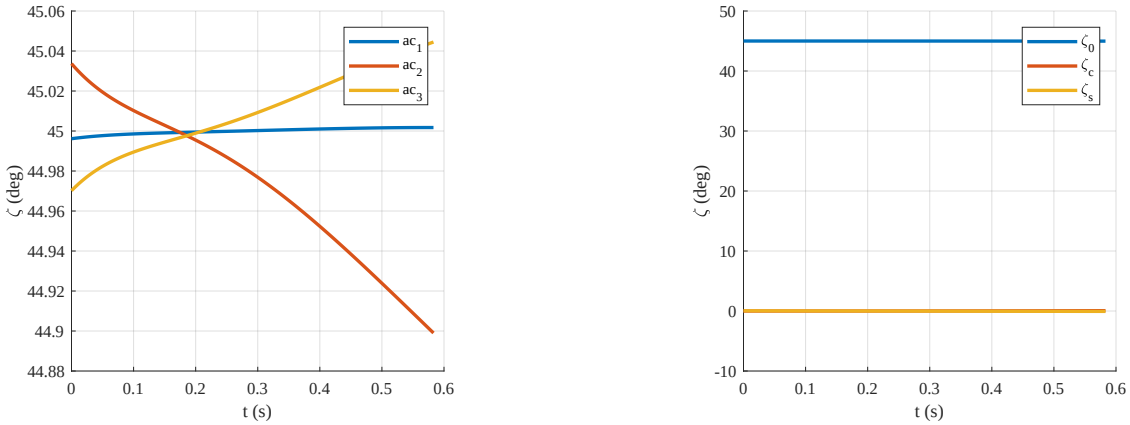

Figure 201: Tether angle ζ

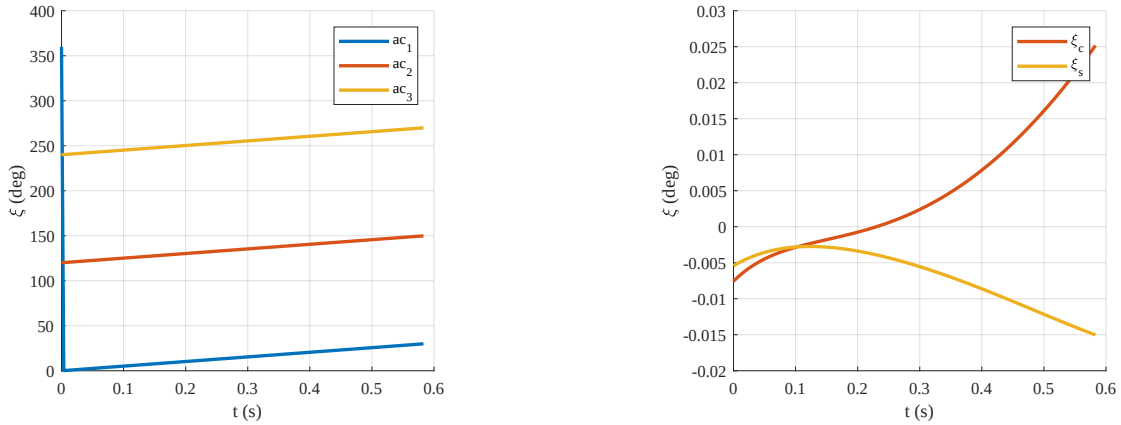

Figure 202: Tether angle ξ

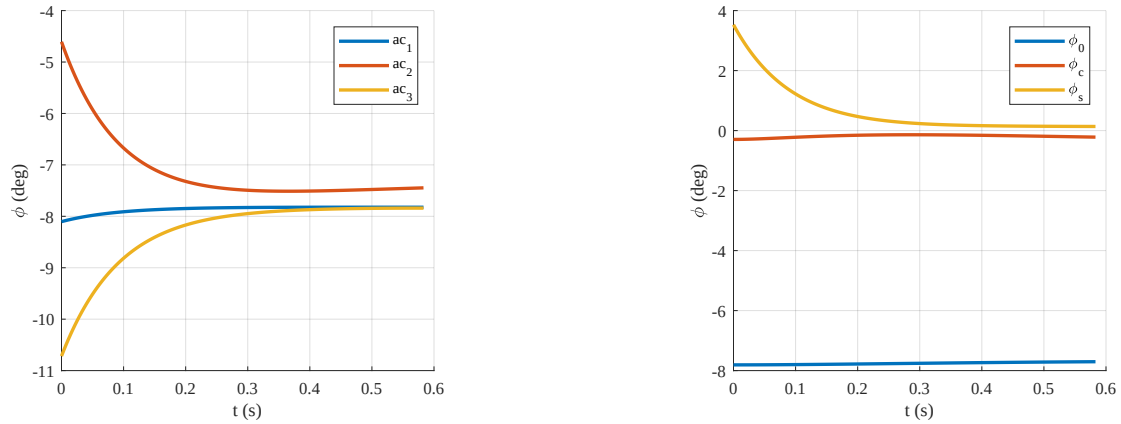

Figure 203: Aircraft angle ϕ

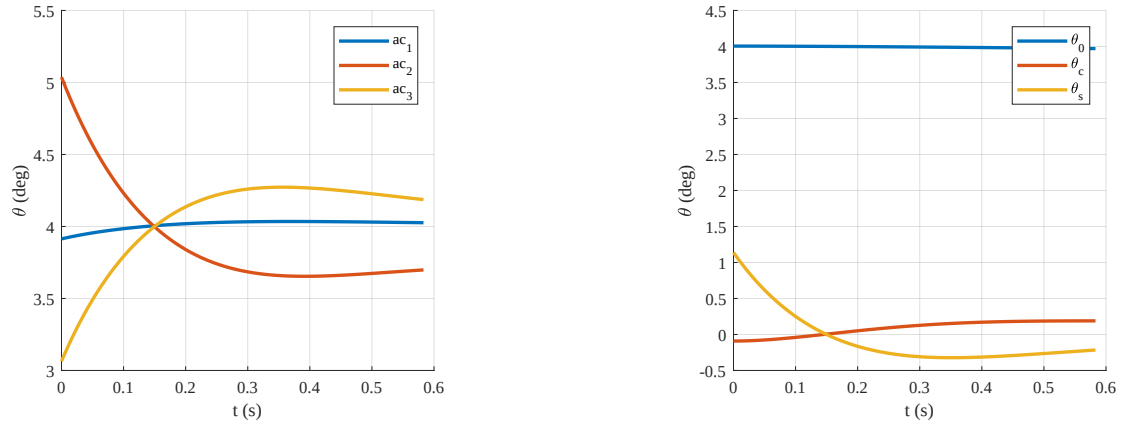

Figure 204: Aircraft angle θ

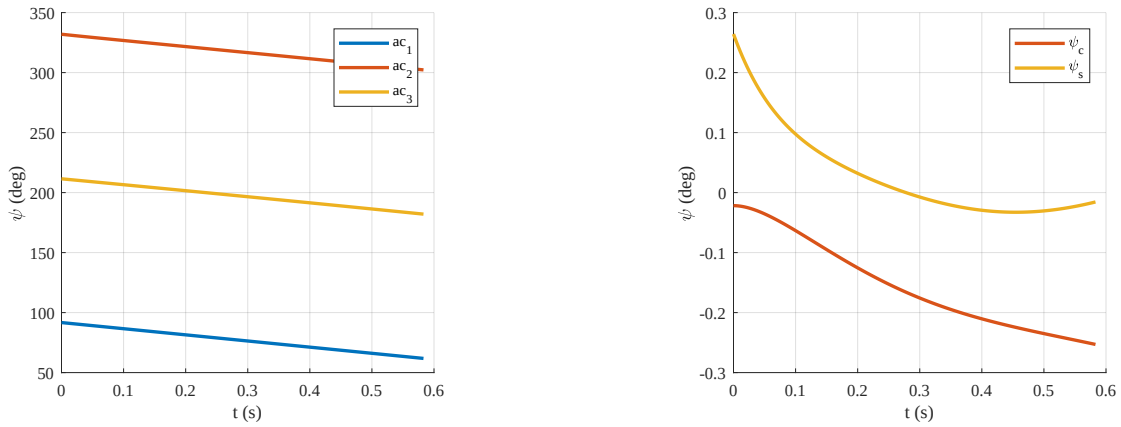

Figure 205: Aircraft angle ψ

G.1.18 Mode B

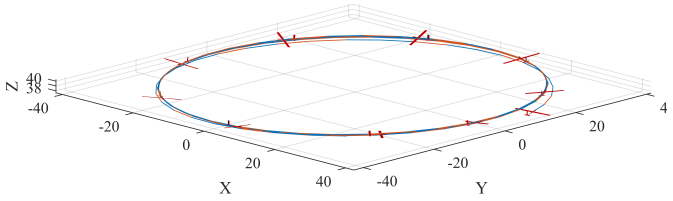

Figure 206: Overall motion of a single aircraft through two periods of mode B

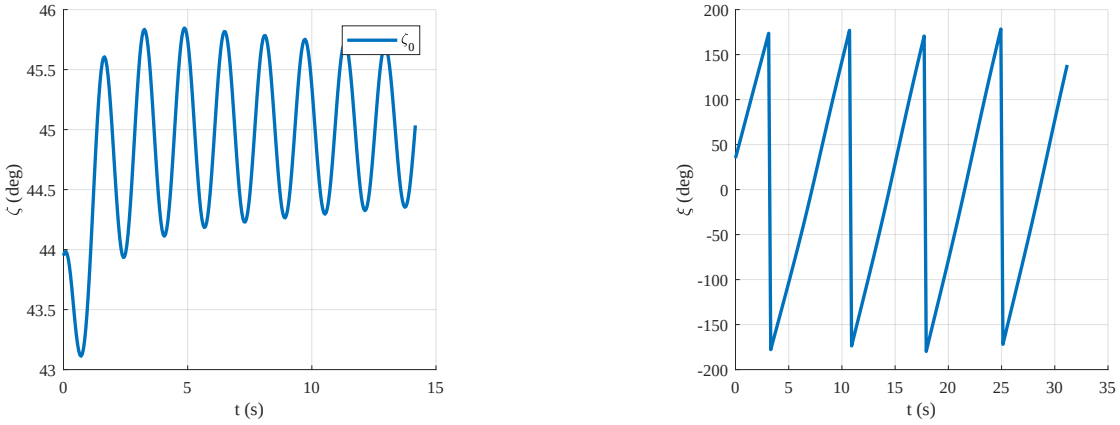

Figure 207: Tether angles ζ and ξ

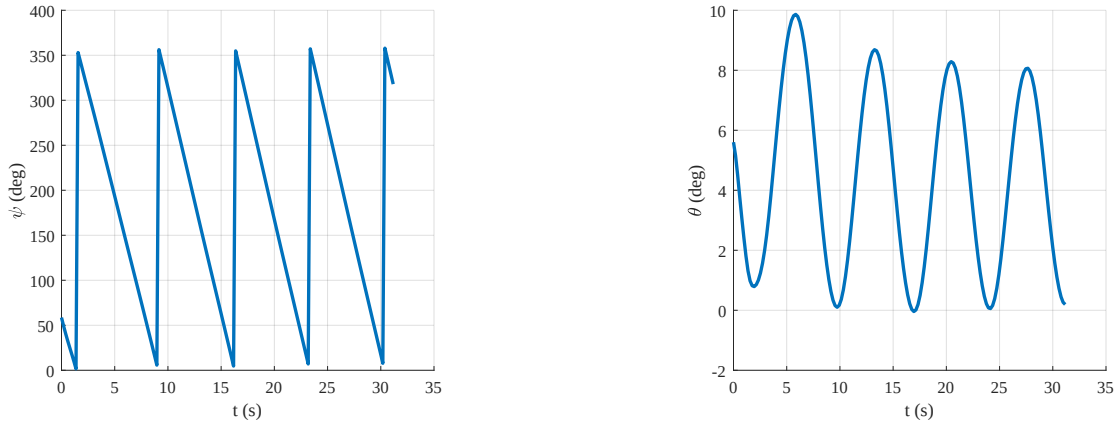

Figure 208: Aircraft angles ψ and θ

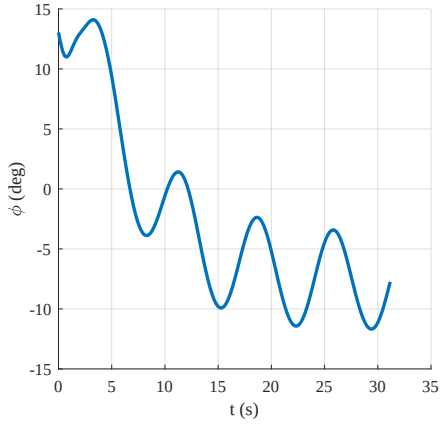

Figure 209: Aircraft angles ϕ

G.1.19 Mode C

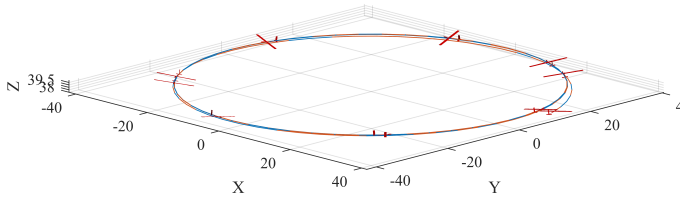

Figure 210: Overall motion of a single aircraft through two periods of mode C

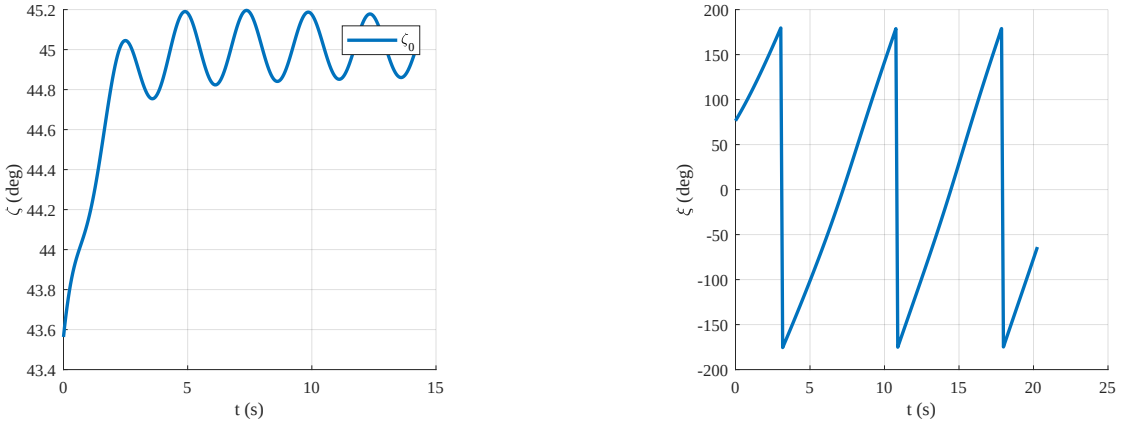

Figure 211: Tether angles ζ and ξ

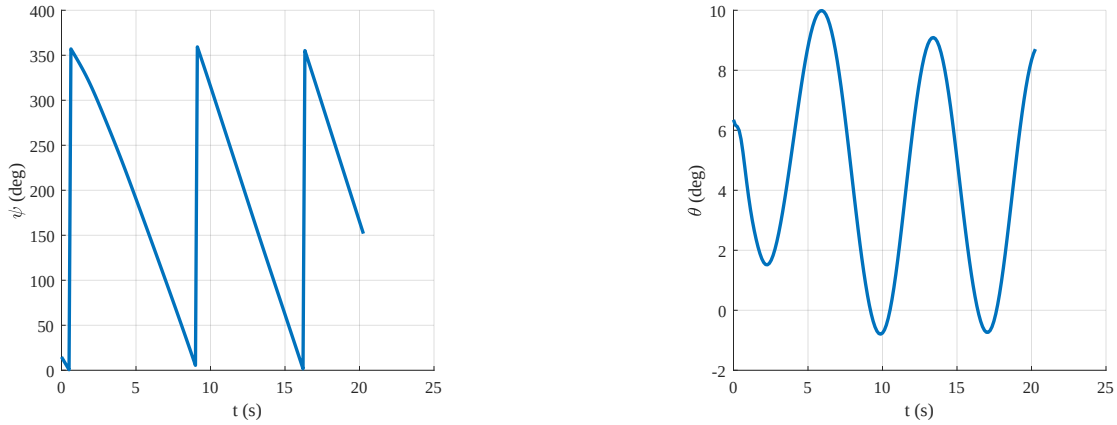

Figure 212: Aircraft angles ψ and θ

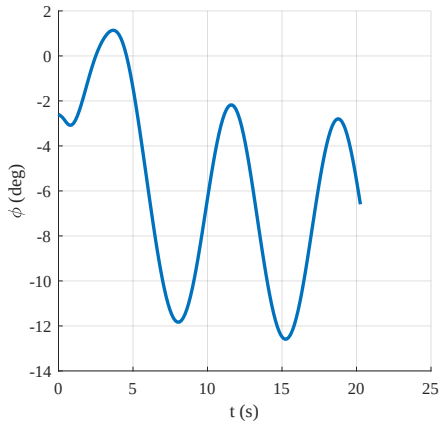

Figure 213: Aircraft angles ϕ

G.1.20 Mode D

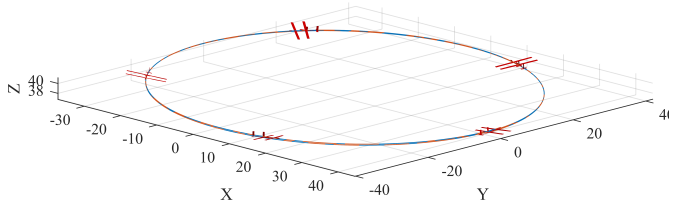

Figure 214: Overall motion of a single aircraft through two periods of mode D

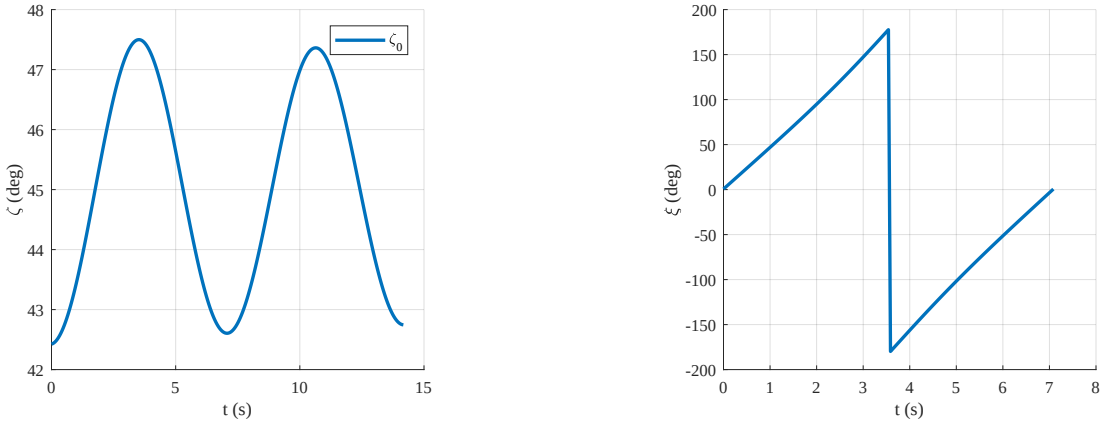

Figure 215: Tether angles ζ and ξ

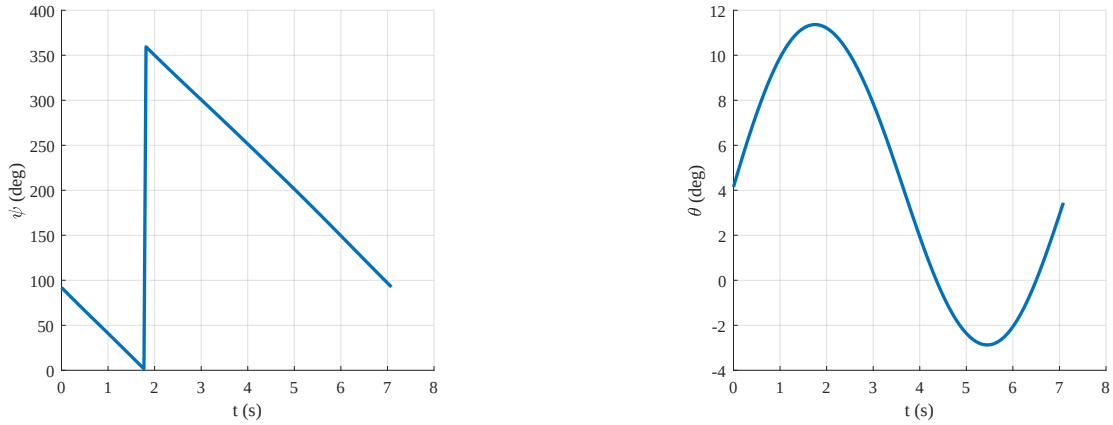

Figure 216: Aircraft angles ψ and θ

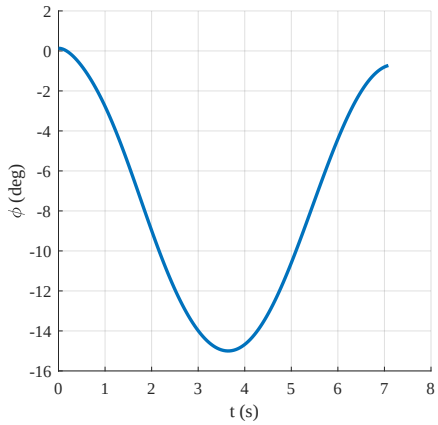

Figure 217: Aircraft angles ϕ

G.1.21 Mode E

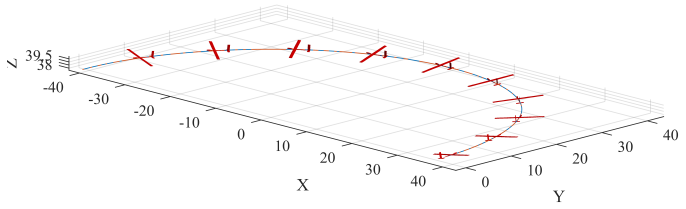

Figure 218: Overall motion of a single aircraft through two periods of mode E

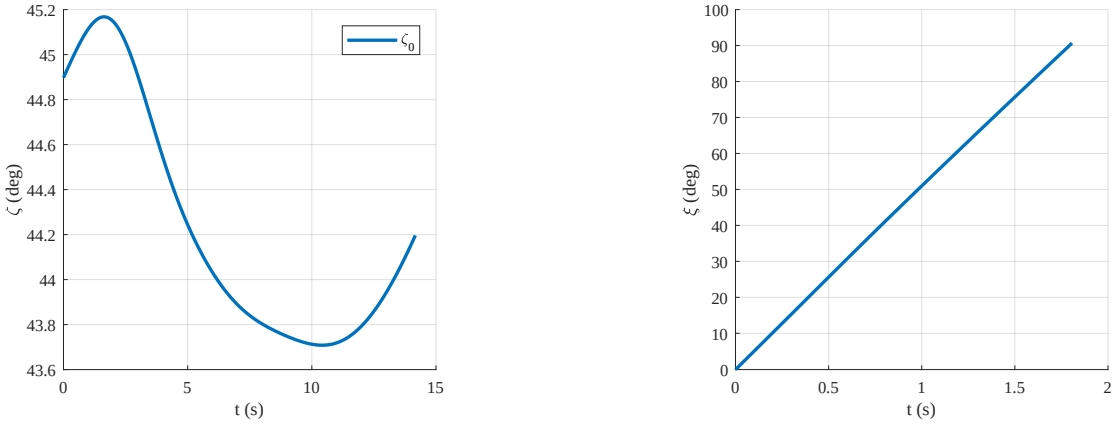

Figure 219: Tether angles ζ and ξ

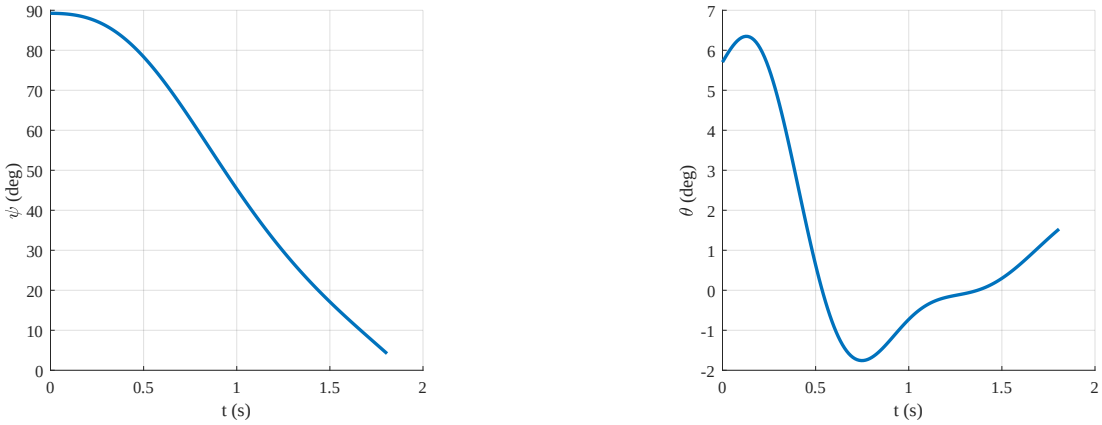

Figure 220: Aircraft angles ψ and θ

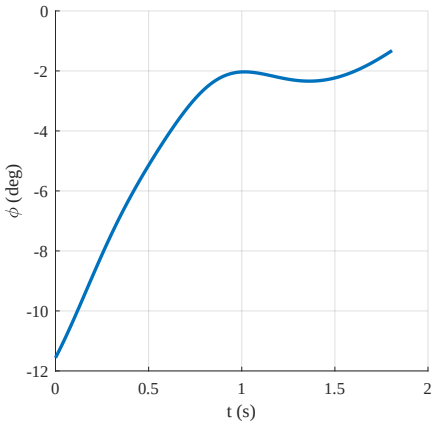

Figure 221: Aircraft angles ϕ

G.1.22 Mode F

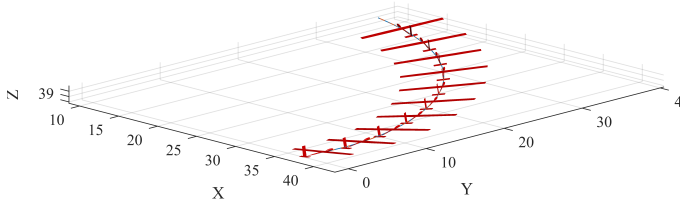

Figure 222: Overall motion of a single aircraft through two periods of mode F

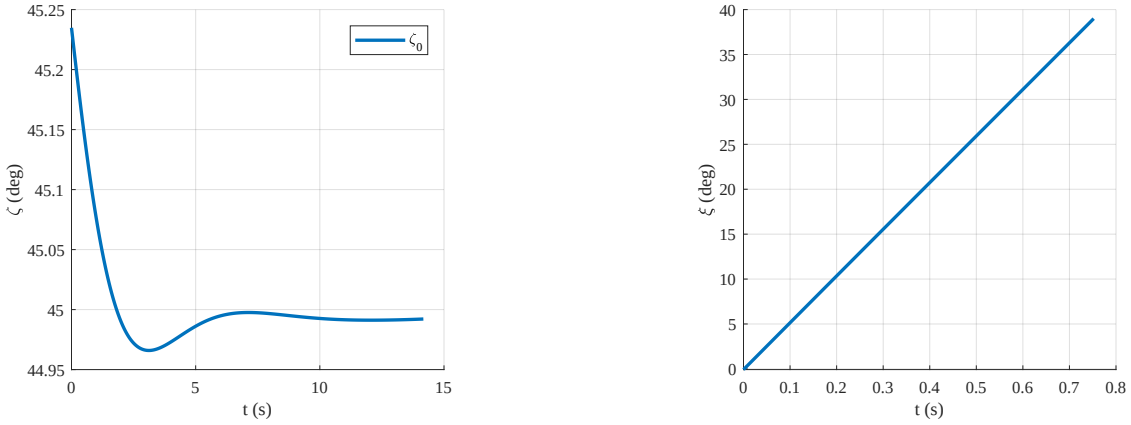

Figure 223: Tether angles ζ and ξ

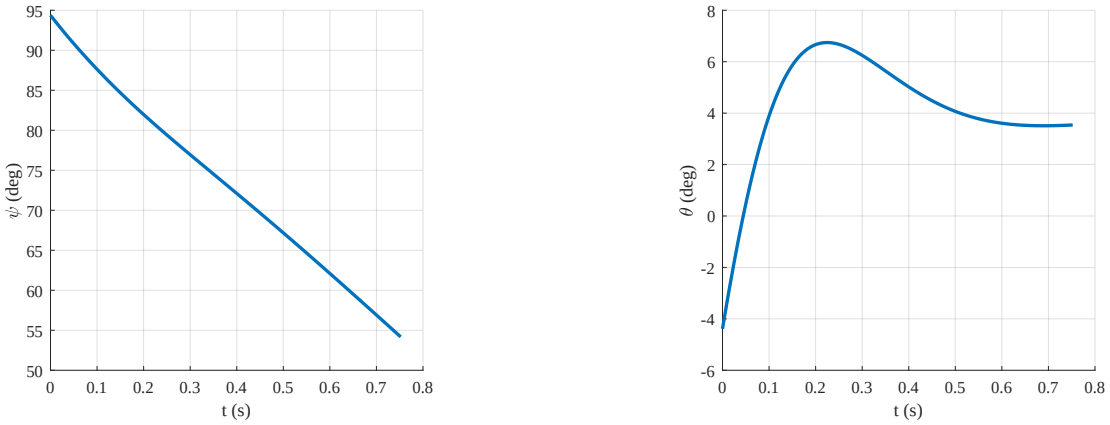

Figure 224: Aircraft angles ψ and θ

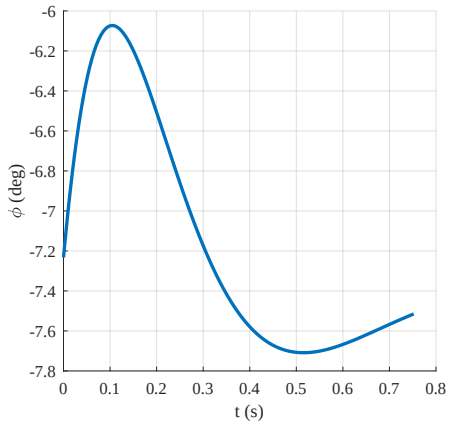

Figure 225: Aircraft angles ϕ

G.1.23 Mode G

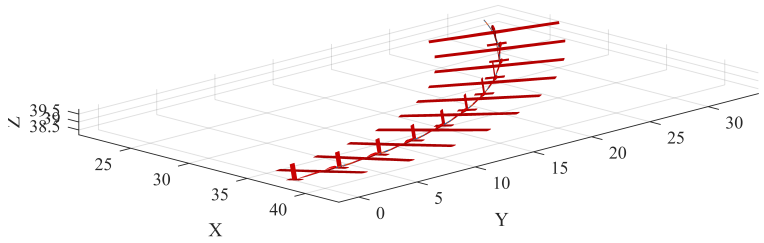

Figure 226: Overall motion of a single aircraft through two periods of mode G

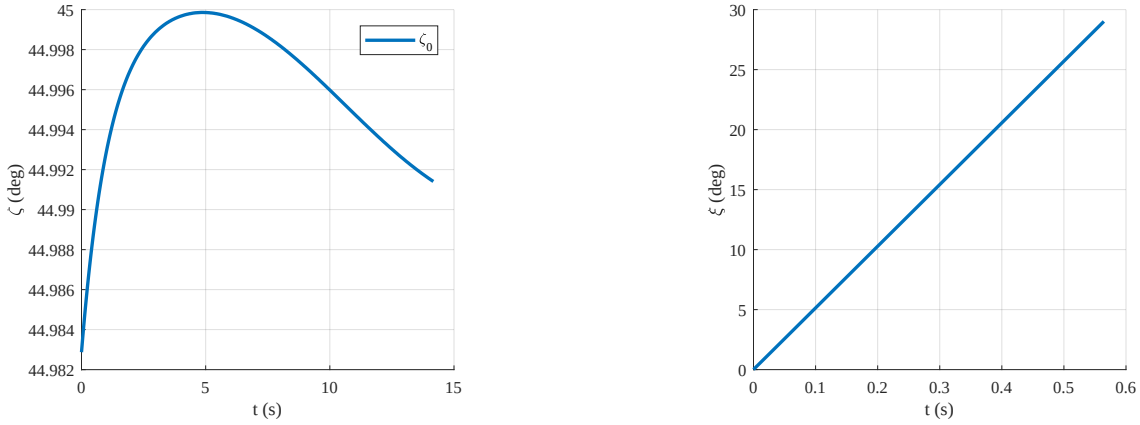

Figure 227: Tether angles ζ and ξ

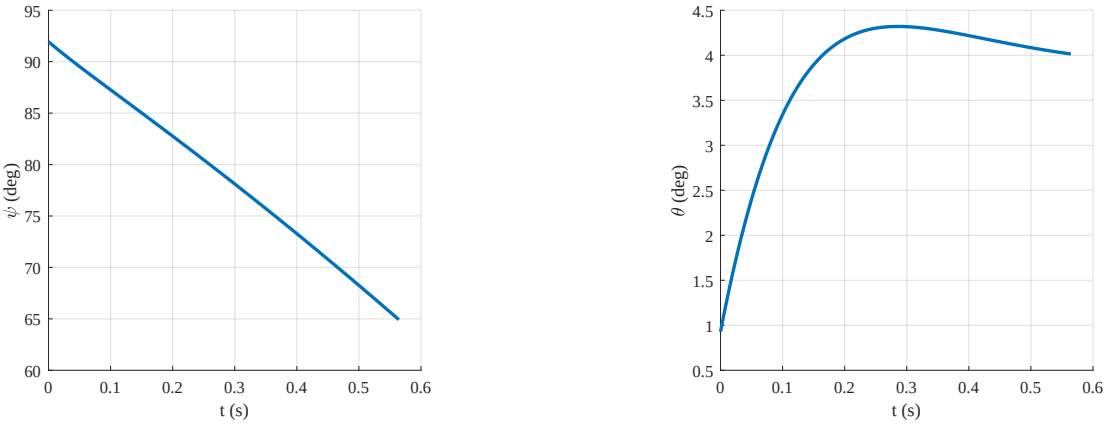

Figure 228: Aircraft angles ψ and θ

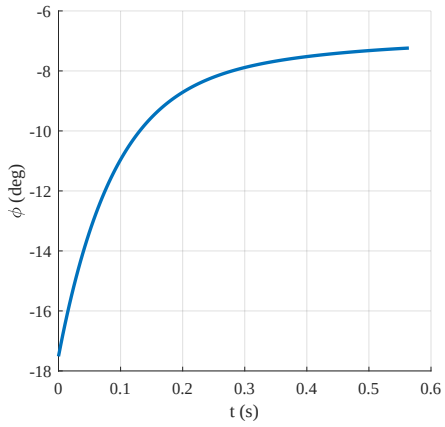

Figure 229: Aircraft angles ϕ

REFERENCES

[1] "Military Specification Flying Quality of Piloted Airplanes MIL-F-8785C," tech. rep., 1980.

[2] Ahrens, U. and Schmehl, R., *Airborne Wind Energy 2011*. Springer, 2011.

[3] AHS, "The AHS International Igor I. Sikorsky 24 Hour Hover Challenge," tech. rep., Vertical Flight Society and Sikorsky, 10 2016.

[4] AHS, "34th Annual AHS International Student Design Competition 2016-2017 Request for Proposals (RFP)," tech. rep., AHS, 2017.

[5] Alabrune, F., "Art of Aerial Transportation," 1942. U.S. Patent 2,298,912.

[6] Alabrune, F., "Transportation Method," 1945. U.S. Patent 2,373,086.

[7] ALFUS, "Autonomy Levels for Unmanned Systems (ALFUS) Framework Volume I : Terminology Unmanned Systems Working Group Participants 1," Tech. Rep. September, NIST, 2004.

[8] Anderson, J. D., *Aircraft Performance and Design*. mcgraw-hill ed., 1999.

[9] Anderson, V. R., "Method and Apparatus for Pick-Up and Delivery by Aircraft in Flight," 1942. U.S. Patent 2,295,537.

[10] Anderton, J., "$50,000 Prize for 24 Hours of Helicopter Hover," 2016. Engineering.com, accessed 9-10-2019.

[11] Ardema, M. D., "Computational singular perturbation method for dynamic systems," *Journal of Guidance, Control, and Dynamics*, vol. 14, pp. 661–664, 5 1991.

[12] Argatov, I. and Silvennoinen, R., "Efficiency of Traction Power Conversion Based on Crosswind Motion," in *Airborne Wind Energy: Advances in Technology Development and Research* (Schmehl, R., ed.), ch. 4, pp. 65–79, Berlin: Springer, 2013.

[13] Bass, J., Marois, F., Demers Bouchard, E., Bellochio, A., Murphy, A., Lacerda, M., Schrage, D., and Courtois, "Preliminary Design of a Highly Efficient VTOL System Based on Tethered Fixed-Wing Aircraft," in *Vertical Flight Society 75th Annual Forum & Technology Display*, (Philadelphia), Vertical Flight Society 75th Annual Forum & Technology Display, 2019.

[14] Berrios, M. G., Tischler, M. B., Cicolani, L. S., Engineer, A., and Powell, J. D., "Stability, Control, and Simulation of a Dual Lift System Using Autonomous R-MAX Helicopters," in *AHS 70th Annual Forum*, (Montreal, Quebec), AHS, 2014.

[15] Bir, G. S., "User's Guide to MBC3: Multi-Blade Coordinate Transformation Code for 3-Bladed Wind Turbines," tech. rep., National Renewable Energy Laboratory, Golden, 2010.

[16] Bir, G., "Multi-Blade Coordinate Transformation and its Application to Wind Turbine Analysis," in *46th AIAA Aerospace Sciences Meeting and Exhibit* (AIAA, ed.), no. January, (Reston, Virigina), American Institute of Aeronautics and Astronautics, 1 2008.

[17] Bosch, A., Schmehl, R., Tiso, P., and Rixen, D., "Nonlinear Aeroelasticity, Flight Dynamics and Control of a Flexible Membrane Traction Kite," in *Airborne Wind Energy: Advances in Technology Development and Research* (Schmehl, R., ed.), ch. 17, pp. 307–323, Berlin: Springer, 2013.

[18] Breukels, J., Schmehl, R., and Ockels, W., "Aeroelastic Simulation of Flexible Membrane Wings based on Multibody System Dynamics," in *Airborne Wind Energy: Advances in Technology Development and Research* (Schmehl, R., ed.), ch. 16, pp. 287–305, Berlin: Springer, 2013.

[19] Chapdelaine, B., Ledoux, G., and Rancourt, D., "Experimental Validation of Vertical Lifting Capabilities of Circling Tethered Fixed Wing UAVs," in *Vertical Flight Society 75th Annual Forum & Technology Display*, Vertical Flight Society, 2019.

[20] Chilowsky, C., "Method and Device for Establishing Communication between Aicraft in Full Flight and the Ground," 1931. U.S. Patent 1,829,474.

[21] Cicolani, L. S. and Kanning, G., "Equations of Motion of Slung Load Systems with Results for Dual Lift," tech. rep., NASA Ames Research Center, Moffett Field, 1990.

[22] Cormier, M., Rancourt, D., Demers Bouchard, E., and Mavris, D., "Optimization of the Forward Flight Operation for a Reconfigurable Rotor Concept," (San Francisco), American Helicopter Society International, 2016.

[23] Cotton, R. B., "Aerial Pick-up and Delivery System," 1967. U.S. Patent 3,351,325.

[24] Cummings, M. L., "Operator Interaction with Centralized Versus Decentralized UAV Architectures," in *Handbook of Unmanned Aerial Vehicles* (Valavanis, K. and Vachtsevanos, G., eds.), ch. 39, pp. 977–992, springer ed., 2015.

[25] Dalamagkidis, K., "Classification of UAVs," in *Handbook of Unmanned Aerial Vehicles* (Valavanis, K. and Vachtsevanos, G., eds.), ch. 5, pp. 83–91, Dordrecht: Springer, 2015.

[26] Datta, B. N., *Numerical methods for linear control systems : design and analysis*. San Diego: Elsevier Academic Press, 2004.

[27] Demers Bouchard, E., Rancourt, D., and Mavris, D. N., "Design Space Exploration of an Electric-Powered Reconfigurable Rotor VTOL Concept," in *AHS 71st Annual Forum of the American Helicopter Society*, (Virginia Beach), AHS International, 5 2015.

[28] Demers Bouchard, E., Rancourt, D., and Mavris, D. N., "Integration of Electric Propulsion in Efficient Heavy-Lift VTOL Concept," in *15th AIAA Aviation Technology, Integration, and Operations Conference*, (Reston, Virginia), pp. 1–10, American Institute of Aeronautics and Astronautics, jun 2015.

[29] Department of Defense, "Flying Qualities of Piloted Aircaft MIL-STD-1797A," tech. rep., 1997.

[30] Development, Advisory Group for Aerospace Research and Development, "Handling Qualities of Unstable Highly Augmented Aircraft," tech. rep., Advisory Group for Aerospace Research & Development, Neuilly sur Seine, 1991.

[31] Diehl, M., "Airborne Wind Energy: Basic Concepts and Physical Foundations," in *Airborne Wind Energy: Advances in Technology Development and Research* (Schmehl, R., ed.), ch. 1, pp. 3–22, Berlin: Springer, 2013.

[32] Drela, M., "QPROP Formulation," tech. rep., MIT, 2006.

[33] Droste, C. and Walker, J., *The General Dynamics Case Study on the F-16 Fly-By-Wire Flight Control System*. Reston ,VA: American Institute of Aeronautics and Astronautics, 1 2010.

[34] Erhard, M. and Strauch, H., "Theory and Experimental Validation of a Simple Comprehensible Model of Tethered Kite Dynamics Used for Controller Design," in *Airborne Wind Energy: Advances in Technology Development and Research* (Schmehl, R., ed.), ch. 8, pp. 141–165, Berlin: Springer, 2013.

[35] Etkin, B., *Dynamics of Atmospheric Flight*. Dover Publications, 2000.

[36] Fagiano, L., Nguyen-Van, E., Rager, F., Schnez, S., and Ohler, C., "Autonomous Takeoff and Flight of a Tethered Aircraft for Airborne Wind Energy," *IEEE Transactions on Control Systems Technology*, vol. 26, pp. 151–166, 1 2018.

[37] Fagiano, L., Zgraggen, A. U., and Morari, M., "On Modeling, Filtering and Automatic Control of Flexible Tethered Wings for Airborne Wind Energy," in *Airborne Wind Energy: Advances in Technology Development and Research* (Schmehl, R., ed.), ch. 9, pp. 167–180, Berlin: Springer, 2013.

[38] Fechner, U. and Schmehl, R., "Model-Based Efficiency Analysis of Wind Power Conversion by a Pumping Kite Power System," in *Airborne Wind Energy: Advances in Technology Development and Research* (Schmehl, R., ed.), ch. 14, pp. 249–269, Berlin: Springer, 2013.

[39] Fritz, F., "Application of an Automated Kite System for Ship Propulsion and Power Generation," in *Airborne Wind Energy: Advances in Technology Development and Research* (Schmehl, R., ed.), ch. 20, pp. 359–372, Berlin: Springer, 2013.

[40] Gamzon, E., "Method and system for supporting an airborne vehicle in space.," 1990. Eurpean Patent Application 90630056.1.

[41] Gamzon, E., "Method and System for Supporting an Airborne Vehicle in Space," 1991. U.S. Patent 5,074,489.

[42] Garmendia, D. C., *A Multi-Disciplinary Conceptual Design Methodology for Assessing Control Authority on a Hybrid Wing Body Configuration*. PhD thesis, Georgia Institute of Technology, 2015.

[43] Garmendia, D. C. and Mavris, D. N., "Alternative Trim Analysis Formulations for Vehicles with Redundant Multi-Axis Control Surfaces," 2015.

[44] Goldstein, L., "Airborne Wind Energy Conversion Systems with Ultra High Speed Mechanical Power Transfer," in *Airborne Wind Energy: Advances in Technology Development and Research* (Schmehl, R., ed.), ch. 13, pp. 235–247, Berlin: Springer, 2013.

[45] Gros, S. and Diehl, M., "Modeling of Airborne Wind Energy Systems in Natural Coordinates," in *Airborne Wind Energy: Advances in Technology Development and Research* (Schmehl, R., ed.), ch. 10, pp. 181–203, Berlin: Springer, 2013.

[46] Gros, S., Zanon, M., Vukov, M., and Diehl, M., "Nonlinear MPC and MHE for Mechanical Multi-Body Systems with Application to Fast Tethered Airplanes," 2012.

[47] Haimes, Y., Lasdon, L., and Wismer, D., "On a Bicriterion Formulation of the Problems of Integrated System Identification and System Optimization," *IEEE Transactions of Systems, Man and Cybernetics*, no. 1, pp. 296–296, 1971.

[48] Hansen, M., "Stability Analysis of Three-Bladed Turbines Using an Eigenvalue Approach," in *42nd AIAA Aerospace Sciences Meeting and Exhibit* (AIAA, ed.), (Reston, Virigina), American Institute of Aeronautics and Astronautics, 1 2004.

[49] Hirschberg, M., "JMR Technology Demonstration Update: The Road to Future Vertical Lift," *Vertiflite*, vol. 62, no. 1, pp. 22–27, 2016.

[50] Hoh, R. H., Heffley, R. K., and Mitchell, D. G., "Development of Handling Qualities Criteria for Rotorcraft with Externally Slung Loads," tech. rep., NASA Ames Research Center, Moffett Field, 2006.

[51] Horn, G., Gros, S., and Diehl, M., "Numerical Trajectory Optimization for Airborne Wind Energy Systems Described by High Fidelity Aircraft Models," in *Airborne Wind Energy: Advances in Technology Development and Research* (Schmehl, R., ed.), ch. 11, pp. 205–218, Berlin: Springer, 2013.

[52] How, J. P., Frazzoli, E., and Chowdhary, G. V., "Linear Flight Control Techniques for Unmanned Aerial Vehicles," in *Handbook of Unmanned Aerial Vehicles* (Valavanis, K. and Vachtsevanos, G., eds.), pp. xix–xxi, springer ed., 2015.

[53] Jacobs, D. H., Kamiya, E., and Spadomi, A., "Airborne tethered sensor system," 1998. U.S. Patent 5,722,618.

[54] Johnson, W., *Helicopter Theory*. Princeton, NJ: Princeton University Press, 1980.

[55] Johnson, W., "Airloads, Wakes, and Aeroelasticity," tech. rep., 1990.

[56] Johnson, W., *Rotorcraft Aeromechanics*. cambridge ed., 2013.

[57] Karsak, K., Meened, K. R., Meyers, D. N., and Piaseck, F. N., "Multi-Helicopter Heavy Lift System feasibility Study," tech. rep., 1972.

[58] Key, D. L., "Handling qualities specifications for U.S. Military helicopters," *Journal of Aircraft*, vol. 19, no. 2, pp. 138–144, 1982.

[59] Kluber, A., "Sikorsky and AHS International Offer 'Hover' Challenge, $50k," 2016. Rotor and Wing International, 2016.

[60] Kokotovic, P. V., "Singular perturbation techniques in control theory," in *Singular Perturbations and Asymptotic Analysis in Control Systems*, pp. 1–55, Berlin/Heidelberg: Springer-Verlag, oct 2005.

[61] Kokotovic, P. V., Bensoussan, A., and Blankenship, G. L., eds., *Singular Perturbations and Asymptotic Analysis in Control Systems*, vol. 90 of *Lecture Notes in Control and Information Sciences*. Berlin, Heidelberg: Springer Berlin Heidelberg, 1987.

[62] Kondak, K., Bernard, M., Caballero, F., Maza, I., and Ollero, A., "Cooperative Autonomous Helicopters for Load Transportation and Environment Perception," in *Advances in Robotics Research: Theory, Implementation, Application*, Springer, 2009.

[63] Leishman, G., *Principles of Helicopter Aerodynamics*. Campbridge University Press, 2006.

[64] Leloup, R., Roncin, K., Bles, G., Leroux, J.-B., Jochum, C., and Parlier, Y., "Estimation of the Lift-to-Drag Ratio Using the Lifting Line Method: Application to a Leading Edge Inflatable Kite," in *Airborne Wind Energy: Advances in Technology Development and Research* (Schmehl, R., ed.), ch. 19, pp. 339–355, Berlin: Springer, 2013.

[65] Makani Power, "The technology." Online reference, 6 2014.

[66] Maza, I., Ollero, A., Casado, E., and Scarlatti, A., "Classification of Multi-UAV Architectures," in *Handbook of Unmanned Aerial Vehicles* (Valavanis, K. and Vachtsevanos, G., eds.), ch. 38, pp. xix–xxi, springer ed., 2015.

[67] Michael, N., Fink, J., and Kumar, V., "Cooperative manipulation and transportation with aerial robots," *Autonomous Robots*, no. September 2010, pp. 1–14, 2010.

[68] Milanese, M., Taddei, F., and Milanese, S., "Design and Testing of a 60 kW Yo-Yo Airborne Wind Energy Generator," in *Airborne Wind Energy: Advances in Technology Development and Research* (Schmehl, R., ed.), ch. 21, pp. 373–386, Springer, 2013.

[69] Mittal, M., *Modeling and control of a twin-lift helicopter system.* PhD thesis, Georgia Institute of Technology, 1991.

[70] Moore, M. D., Selfridge, J. M., Brown, S., and Hodges, T., "Centrifugally Stiffened Rotor: Eternal Flight as the Solution for 'X' NIAC Phase I Final Report," tech. rep., NASA, 2014.

[71] Moorhouse, D. J. and Woodcock, R. J., "Background Information and User Guide for MIL-F-8785B, Military Specification - Flying Qualities of Piloted Airplanes," tech. rep., Wright-Patterson Air Force Base, 1982.

[72] Mozaffari, M., Saad, W., Bennis, M., Nam, Y.-H., and Debbah, M., "A Tutorial on UAVs for Wireless Networks: Applications, Challenges, and Open Problems," *IEEE Communications Surveys & Tutorials*, vol. 21, no. 3, pp. 2334–2360, 2019.

[73] Olson, G., "System and Method for Transporting Cargo Utilizing an Air Towing System That Can Acheive Vertical Take-Off and Vertical Landing," 2012. U.S. Patent 8,308,142.

[74] Padfield, G. D., *Helicopter Flight Dynamics.* Blackwell, 2007.

[75] Peletan, L., Baguet, S., Torkhani, M., and Jacquet-Richardet, G., "A comparison of stability computational methods for periodic solution of nonlinear problems with application to rotordynamics," *Nonlinear Dynamics*, vol. 72, no. 3, 2013.

[76] Poznyak, A. S., *Advanced Mathematical Tools for Control Engineers: Volume 1.* Elsevier Ltd, 2008.

[77] Rancourt, D., *Method for the flight path optimization of the electric-powered reconfigurable rotor (EPR2) VTOL concept.* PhD thesis, Georgia Institute of Technology, 11 2016.

[78] Rancourt, D. and Demers Bouchard, E., "Tethered wing structures complex flight path," 2016.

[79] Rancourt, D., Demers Bouchard, E., and Mavris, D. N., "Optimal Flight Path of the Tethered Airplanes in the EPR^2 VTOL Concept During Moderate Flight Velocity," in *AHS Technical Meeting on Aeromechanics*, (San Francisco), American Helicopter Society International, 2016.

[80] Rediess, H. A., "Impact of Advanced Control Concepts on Aircraft Design," in *ICAS Congress*, 1980.

[81] Selfridge, J. M., "Centrifugally Stiffened Rotor: A Complete Derivation and Simulation of the Inner Loop Controller," *AIAA Guidance, Navigation, and Control Conference*, 2015.

[82] Selfridge, J. M. and Tao, G., "A Complete Derivation of the Plant Model with Nonlinear Dynamics," *AIAA Aviation Technology, Integration, and Operations Conference*, 2015.

[83] Selfridge, J. M., *Tethered Uni-Rotor Network Design, Modeling, Control, and Simulation for a Novel Eternal Flight System.* PhD thesis, University of Virginia, 2017.

[84] Shabana, A. A., *Computational Dynamics*, vol. 53. Chichester, UK: John Wiley & Sons, Ltd, 1 2010.

[85] Skelton, R. E. and Han, J., "Systems Modeling And Model Reduction," in *Handbook of Smart Systems and Materials*, 2004.

[86] SKOP, R. A. and CHOO, Y. I., "The configuration of a cable towed in a circular path.," *Journal of Aircraft*, vol. 8, pp. 856–862, 11 1971.

[87] Smith, B. B., "Method and Apparatus for Cargo Loading and Discharging in Flight," 1939. U.S. Patent 2,151,395.

[88] Stol, K. A., Moll, H.-G., Bir, G., and Namik, H., "A Comparison of Multi-Blade Coordinate Transformation and Direct Periodic Techniques for Wind Turbine Control Design," in *47th AIAA Aerospace Sciences Meeting Including The New Horizons Forum and Aerospace Exposition*, AIAA, 2009.

[89] Strauss, M., "AHS International ' s Igor I . Sikorsky 24 Hour Hover Challenge," 2017.

[90] Sun, L., *Dynamic Modeling, Trajectory Generation and Tracking for Towed Cable Systems.* PhD thesis, Brigham Young University, 2012.

[91] Sun, L. and Castagno, J., "Parameter Estimation for Towed Cable Systems Using Moving Horizon Estimation," *IEEE Transactions on Aerospace and Electronic Systems*, vol. 512, pp. 1432–1446, 2015.

[92] Szal, A., "AT&T Deploys Temporary Cell Site via Helicopter in Puerto Rico," 2017. Wireless Week, accessed 9-10-2019, 2017.

[93] Terink, E. J., Breukels, J., Schmehl, R., and Ockels, W. J., "Flight Dynamics and Stability of a Tethered Inflatable Kiteplane," *Journal of Aircraft*, vol. 48, no. 2, 2011.

[94] Tischler, B., Colbourne, J. D., Morel, M. R., Biezad, D. J., Levine, W. S., and Moldoveanu, V., "CONDUIT A New Multidisciplinary for Flight Integration Environment Control Development," 1997.

[95] Tischler, M. B., Lee, J. A., and Colbourne, J. D., "Comparison of Flight Control System Design Methods Using the Conduit Design Tool," *Journal of Guidance, Control and Dynamics*, vol. 25, no. 3.

[96] Tischler, M., Colbourne, J. D., Morel, M. R., Biezad, D. J., Cheung, K. K., Levine, W. S., and Moldoveanu, V., "A multidisciplinary flight control development environment and its application to a helicopter," *IEEE Control Systems*, vol. 19, pp. 22–33, aug 1999.

[97] United States Army Aviation and Missile Command, "Ads-33e-Prf Aeronautical Design Standard Performance Specification Handling Qualities Requirements For Military Rotorcraft," tech. rep., 2000.

[98] Valavanis, K. P. and Vachtsevanos, G. J., "Networked UAVs and UAV Swarms: Introduction Kimon," in *Handbook of Unmanned Aerial Vehicles* (Valavanis, K. and Vachtsevano, G., eds.), ch. 81, pp. 1983–1985, springer ed., 2015.

[99] Vander Lind, D., "Analysis and Flight Test Validation of High Performance AirborneWind Turbines," in *Airborne Wind Energy: Advances in Technology Development and Research* (Schmehl, R., ed.), ch. 28, pp. 473–490, Berlin: Springer, 2013.

[100] Williams, P., Lansdorp, B., and Ockels, W., "Nonlinear Control and Estimation of a Tethered Kite in Changing Wind Conditions," *Journal of Guidance, Control, and Dynamics*, vol. 31, pp. 793–799, may 2008.

[101] Williams, P., Lapthorne, P., and Trivailo, P., "Circularly-Towed Lumped Mass Cable Model Validation from Experimental Data," in *AIAA Modeling and Simulation Technologies Conference and Exhibit*, (Reston, Virigina), American Institute of Aeronautics and Astronautics, aug 2006.

[102] Williams, P. and Ockels, W., "Dynamics of Towed Payload System Using Multiple Fixed-Wing Aircraft," *Journal of Guidance, Control, and Dynamics*, vol. 32, pp. 1766–1780, nov 2009.

[103] Williams, P. and Trivailo, P., "Dynamics and Equilibrium of a Twin-Aircraft-Cable System for Payload Retrieval," in *AIAA Atmospheric Flight Mechanics Conference and Exhibit*, (Reston, Virigina), American Institute of Aeronautics and Astronautics, aug 2006.

[104] Williams, P. and Trivailo, P., "Dynamics of Circularly Towed Aerial Cable Systems, Part 2: Transitional Flight and Deployment Control," *Journal of Guidance, Control, and Dynamics*, vol. 30, pp. 766–779, may 2007.

[105] Williams, P. and Trivailo, P., "Dynamics of Circularly Towed Cable Systems, Part 1: Optimal Configurations and Their Stability," *Journal of Guidance, Control, And Dynamics*, vol. 30, no. 3, 2007.

[106] Wilson, Jr., F. and Bennett, A., "New concept for low cost VTOL cargo delivery capability," in *Guidance and Control Conference*, (Reston, Virigina), American Institute of Aeronautics and Astronautics, 8 1983.

[107] Wilson Jr, F. M., "Aerial transport of payloads with vertical pick up and delivery," 1983.

[108] Yin, S.-K. and Hohenemser, K. H., "The Method Of Multiblade Coordinates In The Linear Analysis Of Lifting Rotor Dynamic Stability And Gust Response At High Advance Ratio," (Washington DC), 1971.

[109] Yudilevitch, G., Tischler, M., Levine, W., Lin, C., and Potter, P., "Rotorcraft flight control system design based on multi-criterion parametric optimization," in *Guidance, Navigation, and Control Conference*, (Reston, Virigina), American Institute of Aeronautics and Astronautics, 8 1995.

[110] Zanon, M., Gros, S., and Diehl, M., "Rotational start-up of tethered airplanes based on nonlinear MPC and MHE," in *2013 European Control Conference (ECC)*, (Zurich), pp. 1023–1028, 2018.

[111] Zanon, M., Gros, S., and Diehl, M., "Model Predictive Control of Rigid-Airfoil Airborne Wind Energy Systems," in *Airborne Wind Energy: Advances in Technology Development and Research* (Schmehl, R., ed.), ch. 12, pp. 219–233, Berlin: Springer, 2013.